

Copyright © 1996, by the author(s).
All rights reserved.

Permission to make digital or hard copies of all or part of this work for personal or classroom use is granted without fee provided that copies are not made or distributed for profit or commercial advantage and that copies bear this notice and the full citation on the first page. To copy otherwise, to republish, to post on servers or to redistribute to lists, requires prior specific permission.

**OXIDE CHARGING DAMAGE IN INTEGRATED
CIRCUIT PROCESSING INVESTIGATED WITH
A COUPLED PLASMA/IC DEVICE MODEL**

by

William George En

Memorandum No. UCB/ERL M96/35

18 May 1996

**OXIDE CHARGING DAMAGE IN INTEGRATED
CIRCUIT PROCESSING INVESTIGATED WITH
A COUPLED PLASMA/IC DEVICE MODEL**

Copyright © 1996

by

William George En

Memorandum No. UCB/ERL M96/35

18 May 1996

ELECTRONICS RESEARCH LABORATORY

College of Engineering
University of California, Berkeley
94720

**OXIDE CHARGING DAMAGE IN INTEGRATED
CIRCUIT PROCESSING INVESTIGATED WITH
A COUPLED PLASMA/IC DEVICE MODEL**

Copyright © 1996

by

William George En

Memorandum No. UCB/ERL M96/35

18 May 1996

ELECTRONICS RESEARCH LABORATORY

College of Engineering
University of California, Berkeley
94720

Abstract

Oxide Charging in Integrated Circuit Processing Investigated with a Coupled Plasma/IC Device Model

by

William George En

Doctor of Philosophy in Electrical Engineering and Computer Sciences

University of California at Berkeley

Professor Nathan W. Cheung, Chair

In both plasma and conventional ion implantation processing an important concern is oxide charging damage. As gate oxides reduce in thickness and plasma and implantation processes become more prevalent, oxide charging damage issues will continue to affect the yield and reliability of MOS devices in integrated circuits. By understanding the complex interactions between the plasma, device structure, and substrate bias, oxide charging damage can be controlled and minimized.

We have verified that the plasma currents generated during plasma immersion ion implantation (PIII) are accurately modeled with an analytical approach using only physical plasma parameters which are measured by Langmuir probe. Through the model, each of the four major current components (plasma ion, plasma electron, secondary electron, and displacement current) are individually determined for all time. By implementing the plasma model within the circuit simulator SPICE as a time-dependent non-linear element, the total plasma current model is coupled to include the interaction between the plasma, device structure, and substrate bias. Integrated circuit device structures are modeled using the large library of device models available in SPICE, and the substrate bias is modeled as either a simple voltage source or as a more complex set of equivalent circuit elements. The interactions within the system are modeled to determine the total charging damage induced.

The model shows how the shape and repetition rate of the substrate bias waveform can be optimized to minimize charging damage in PIII. Using a typical bias waveform, the repetition rate of the bias modulates the generated gate oxide voltage. The gate oxide voltage decreases in magnitude initially with increasing repetition rate; then increases rapidly at high repetition rates. The oxide voltage increases beyond the oxide breakdown voltage at the threshold frequency. Using a microsecond rectangular pulse at the maximum

allowable repetition rate, the charging damage can be minimized and the implantation rate optimized.

Since the simulation uses physical parameters in the plasma model, the model predicts the effect of the plasma conditions on oxide charging damage. The threshold frequency increases with decreasing electron temperature due to an increase in the electron current during the off time of the pulse waveform. Variation in the ion density has a minimal effect on the threshold frequency, implying that the ion density can be increased without increasing oxide charging damage in PIII. Using a distributed network approach, extreme plasma non-uniformity induces charging damage due to the local interaction of the floating gate and the global interaction of the wafer substrate.

Device structure also plays a crucial role in determining the charging damage. Fowler-Nordheim tunneling current through the gate oxide is implemented in the model as a non-linear element, allowing the model to determine the quantity of charge flowing through the oxide. Antenna structures enhance the charge deposited on the gate oxide during an implantation pulse. Also, the charge enhancement in antenna structures exposed to a plasma is shown to be reduced with the magnitude of the floating potential of the plasma.

We have also extended the plasma model to simulate both reactive ion etching (RIE) and beam-line conventional ion implantation. The coupled charging model approach is demonstrated to determine accurately the currents generated by a pulsed RF bias up to 4MHz. The model is shown to be applicable to conventional ion implantation by allowing the plasma to vary with time to simulate the motion of the ion beam with respect to the wafer. To model plasmas with multiple ion species, an adapted model for multiple ions has been developed. Through the coupled charging damage approach, an understanding of mechanisms for charging damage has been achieved.

date

Table of Contents

List of Figures	vii
List of Tables	x
CHAPTER 1. Introduction	1
1.1. Oxide Charging Damage in IC Processing.....	1
1.2. IC Processing Trends	1
1.3. Implant and Etching Concerns	2
1.4. Oxide Charging Damage Investigation	3
References	4
CHAPTER 2. Background	5
2.1. Introduction	5
2.2. Charging Damage Effects	5
2.3. Oxide Stressing Mechanisms	9
2.4. Oxide Damage Induced by Plasma Processing	10
2.5. Device Area Dependence of Oxide Charging during RIE (Antenna Effect).....	12
2.6. Perimeter Length Dependence of Oxide Charging during RIE	12
2.7. Conclusions	13
References	13
CHAPTER 3. Oxide Charging Damage Measurement Techniques	15
3.1. Introduction	15
3.2. C-V Measurement of Damage.....	15
3.3. MOSFET Device Parameter Measurements	23
3.4. Q_{bd} and Breakdown Voltage Measurement Techniques.....	26
3.5. CHARM-2 Test Vehicle.....	27
3.6. Conclusions	28
References	28
CHAPTER 4. Plasma Diagnostics	30
4.1. Introduction	30
4.2. Langmuir Probe Measurement Technique	30
4.3. Optical Emission Spectroscopy (OES).	35
4.4. Mass Spectroscopies	37
4.5. Secondary Electron Measurements	44
4.6. Conclusions	49
References	50

CHAPTER 5. Plasma Immersion Ion Implantation	52
5.1. Introduction	52
5.2. PIII Concept	52
5.3. UC Berkeley Reactor Configuration	53
5.4. PIII Applications	55
5.5. Conclusions	61
References	61
CHAPTER 6. Coupled Plasma & IC Structure Model	64
6.1. Introduction	64
6.2. Plasma Model	64
6.3. Background on Plasma Modeling	64
6.4. PIII Model	65
6.5. Phases of Plasma Currents During PIII	68
6.6. Experimental Results	70
6.7. Conclusions	78
6.8. Coupled Model	79
6.9. SPICE Implementation of Plasma Model	80
6.10. Concept of Modeling IC Circuit and Bias Interactions	80
6.11. Concept of Modeling 2-D Effects	81
6.12. Conclusions	82
References	83
CHAPTER 7. Substrate Bias Effects	85
7.1. Introduction	85
7.2. Theory of Oxide Charging in PIII	85
7.3. Equilibration Time in PIII	87
7.4. Oxide Voltage Variation Due to PIII	89
7.5. Pulse shape effects	91
7.6. Comparison Between Simulation and Experiment	94
7.7. Conclusions	95
References	97
CHAPTER 8. Device Structure Effects	98
8.1. Introduction	98
8.2. IC Device Structures of Interest	98
8.3. Conclusions	104
References	105
CHAPTER 9. Effects of Plasma Characteristics on PIII	106
9.1. Introduction	106
9.2. Plasma Electron Temperature Dependence	106
9.3. Plasma Ion Density Dependence	107

9.4.	Plasma Uniformity Effects	109
9.5.	Implications on the Choice of Plasma Sources	111
9.6.	Conclusions	111
	References	112
CHAPTER 10. Additional Damage Effects in Plasma Processing		114
10.1.	Introduction	114
10.2.	Coupled Antenna Effect	114
10.3.	Damage Enhancement due to Nitride and Oxide Deposition.....	117
	References	126
CHAPTER 11. Extension of Coupled Charging Model to Other Processes....		127
11.1.	Introduction	127
11.2.	Pulsed RF Bias Modeling.....	127
11.3.	Conventional Beam-line Ion Implantation Modeling	134
11.4.	Conclusions	137
	References	137
CHAPTER 12. Conclusions.....		139
	References	142
Appendix A: OES peaks		143
A.1	Introduction	143
Appendix B: Plasma Model Implementation in SPICE		149
B.1	Introduction	150
B.2	Model Equation Conversion to SPICE.....	150
B.3	SPICE Input Deck:	154
Appendix C: Multiple Ion Species Plasma Model		156
C.1	Introduction	156
C.2	Multiple Ion Species Derivation	157
C.3	Discussion	161
Appendix D: Derivation of Equilibration Time After Implant Pulse		162
D.1	Equilibration Time	162
Appendix E: Derivation of Oxide Voltage Dependence on PIII Bias		165
E.1	Oxide Voltage Derivation	165

List of Figures

Figure 2-1.	“Volcano” extreme charging damage	6
Figure 2-2.	I-V characteristics of thin oxides.....	10
Figure 2-3.	Non-uniformity inducing charging damage	11
Figure 3-1.	Measured and theoretical quasi-static C-V curves.	17
Figure 3-2.	Measured and theoretical high frequency C-V curves	18
Figure 3-3.	C-V equivalent circuits.....	19
Figure 3-4.	D_{it} extraction using quasi-static and high frequency C-V.....	21
Figure 3-5.	Q_{it} versus Q_{stress}	22
Figure 3-6.	Cross section of typical antenna structures and equivalent circuit model.....	24
Figure 3-7.	Diode protection circuit.....	26
Figure 3-8.	Fuse protection circuit	27
Figure 4-1.	Diagram of a Langmuir probe	31
Figure 4-2.	Typical langmuir probe I-V	32
Figure 4-3.	Optical emission spectroscopy setup.....	35
Figure 4-4.	OES spectrum of H_2 plasma.....	36
Figure 4-5.	OES spectra of a BF_3 plasma	37
Figure 4-6.	Schematic of large mass spectrometer.....	38
Figure 4-7.	Mass spectrum of BF_3 plasma neutrals	39
Figure 4-8.	Mass spectrum of BF_3 plasma ionized species	40
Figure 4-9.	Energy spectrum of B^+ ions	40
Figure 4-10.	BF_3 Mass spectrum with Ferran micropole.....	41
Figure 4-11.	Schematic diagram of magnetic quadrant mass spectrometer.....	42
Figure 4-12.	BF_3 mass spectrum using magnetic quadrant.....	43
Figure 4-13.	Measured bias and total current density of an aluminum target in an argon plasma.....	46
Figure 4-14.	Secondary electron yield for aluminum.	48
Figure 4-15.	Extracted secondary electron yield.....	49
Figure 5-1.	PIII concept	53
Figure 5-2.	PIII reactor schematic.....	54
Figure 5-3.	Conformal trench doping.....	56
Figure 5-4.	Pd seeding for electroless copper plating	57
Figure 5-5.	SRP of sub-100nm p^+/n junction.....	58
Figure 5-6.	Uniformity of PIII.....	60
Figure 5-7.	SPIMOX	61
Figure 6-1.	Charge flow during a PIII Pulse	69
Figure 6-2.	3kV waveform and model comparison.....	72

Figure 6-3.	Sheath for 3kV waveform	73
Figure 6-4.	5kV waveform and model comparison.....	74
Figure 6-5.	Sheath dynamics for 5kV pulse	75
Figure 6-6.	Plasma condition variation simulation and experiment.....	76
Figure 6-7.	Single reflected pulse waveform	77
Figure 6-8.	Double reflected pulse waveform	78
Figure 6-9.	Unusually shaped PIII pulse simulation	79
Figure 6-10.	Plasma/IC circuit model concept.....	81
Figure 6-11.	Plasma non-uniformity modeling	82
Figure 6-12.	CMOS structure model.....	83
Figure 7-1.	Schematic of capacitor test structure	86
Figure 7-2.	Multiple pulse effect concept	87
Figure 7-3.	Oxide voltage variation due to single pulse	88
Figure 7-4.	Multiple pulse effect in PIII.....	91
Figure 7-5.	Oxide voltage dependence on pulse rate	92
Figure 7-6.	Oxide voltage dependence on fall time	93
Figure 7-7.	Effect of fall time on threshold frequency.....	94
Figure 7-8.	Effect of pulse width on charging damage	95
Figure 7-9.	Simulation & experiment on the multiple pulse effect.....	96
Figure 8-1.	Thin oxide modeling.....	99
Figure 8-2.	Fowler-Nordheim I-V characteristics.....	100
Figure 8-3.	F-N tunneling model.....	101
Figure 8-4.	ESD in PIII	102
Figure 8-5.	Antenna structure.....	104
Figure 9-1.	Electron temperature dependence.....	107
Figure 9-2.	Ion density dependence on pulsing.....	108
Figure 9-3.	Ion density dependence on throughput.....	109
Figure 9-4.	Schematic diagram of 2-D plasma modeling	110
Figure 9-5.	Simulation of plasma non-uniformity	110
Figure 9-6.	Plasma sources phase space of ion density and electron temperature	112
Figure 10-1.	Load line of plasma and oxide for antenna effect	115
Figure 10-2.	Stressing current dependence on antenna ratio	116
Figure 10-3.	Backend plasma process steps investigated	118
Figure 10-4.	Change in V_t versus stress time.....	120
Figure 10-5.	Charging damage for 65k:1 antenna ratio devices	121
Figure 10-6.	Charging damage for 5k:1 antenna ratio devices	122
Figure 10-7.	Charging damage in diode protected 65k:1 antenna ratio devices	123

Figure 10-8. Charging damage in diode protected 5k:1 antenna ratio devices	124
Figure 10-9. Diode protected device stressing	125
Figure 11-1. Schematic of pulsed RF bias coupled charging model.....	129
Figure 11-2. 300KHz pulsed RF experiment	130
Figure 11-3. 1MHz pulsed RF bias simulation	131
Figure 11-4. 4MHz RF pulsed bias simulation	132
Figure 11-5. Close-up of 4MHz pulsed RF bias simulation	133
Figure 11-6. Time dependent plasma and ion beam model.....	135
Figure 11-7. Total currents for conventional ion implantation model	136
Figure 12-1. Circuit diagram of pulse network for the PIII system	141
Figure B-1. Sheath thickness circuits.....	150
Figure B-2. Circuit converting S^3 to S	151
Figure B-3. Circuits solving for the displacement current.....	153
Figure B-4. Total current output of model	153
Figure C-1. Dual ion species PIII: ion density variation during an implant pulse.....	160

List of Tables

Table 1-1.	Projected MOSFET scaling trends	2
Table 6-1.	Default plasma parameters used in the simulation	71
Table 6-2.	Comparison of theoretical and experimental sheaths for 7kV waveform	77
Table 6-3.	Comparison of peak current for 14kV waveform.....	78

Acknowledgments

I would like to thank all of the professors and colleagues who have helped me throughout my graduate career. I would like to thank Professors Nathan W. Cheung, Mike A. Lieberman, Chenming Hu, and David B. Graves for serving on my thesis committee. From the relentless discussions with Professor Nathan Cheung, I learned how to critically think through challenges in my research. He gave me the chance to learn on my own while giving guidance when needed. The additional guidance and advice provided by Professors Chenming Hu and Mike Lieberman helped me to establish the foundation for my project and refine it with many later adjustments.

The many discussions and interactions with colleagues at conferences and visits have proved to be an invaluable asset toward my graduate career. I would like to thank Larry Larson, Michael Current, Wes Lukazek, and Sue Felch for their insightful advice and helpful interactions which provided me with new ideas and directions for my work. I would also like to thank Arye Shapiro of Sematech for providing with the Ferran micropole equipment and Larry Larson for facilitating the initial contact.

My life at Berkeley has been made far more rewarding by the members of Nathan's lab. Kaustav Banerjee, James Chan, Tracy Fu, Seongil Im, Sundar Kumar Iyer, Tao Jiang, Erin Jones, Meng-Hsiung Kiang, Barry Linder, Jingbao Liu, Xiang Lu, Professor Min, William Wong, and Crid Yu have all made the many deadlines more bearable. From the first day I began working as a graduate student, Erin has been a constant foil to bounce ideas off of and to refine my thoughts. Tracy provided invaluable insight into my innumerable fundamental questions. I would also like to thank Barry for putting up with my incessant comments and questions on charging damage. Chris Lee and Vivien Talghader have both provided me with sanity checks through many breaks and hallway discussions. I would especially like to thank Vivien for the many hours of arguments over homework and projects that proved extremely valuable in my coursework. I could not have performed my experimental work without the guidance of John Benasso. John assisted me in setting up much of the apparatus I used and taught me how to function in the lab.

Finally, I would like to thank Josephine for her support throughout the dissertation writing experience and for her detailed editing.

1 Introduction

1.1. Oxide Charging Damage in IC Processing

Oxide charging damage is a process where a large electric field induced across a thin oxide results in current flow through the oxide. This stressing current degrades the quality of the oxide or causes complete oxide failure. In integrated circuit processing, oxide charging damage has been and will continue to be an issue of concern. Processes such as ion implantation and plasma etching have been shown to cause charging damage [1.1,1.2]. These processes are essential in current integrated circuit processing: ion implantation for formation of well junctions, source/drain junctions, and doping of polysilicon; as well as plasma etching for the feature size control and selectivity required.

1.2. IC Processing Trends

The historical trend of device scaling is expected to continue well into the future. Using the channel length of MOSFETs as the primary scale, projections show that the current 0.35 μm technology will be scaling down to sub 0.1 μm devices in the future. Along with the scaling of the channel length, other device parameters will need to scale as well as shown in Table 1-1 [1.3]. An understanding of the mechanisms of charging damage will help to determine the charging damage issues that may arise with scaled down devices.

Depending on the mechanism by which the charging damage occurs, scaled down MOSFETs will either be more or less sensitive to the charging damage. As gate oxide thicknesses decrease to below 7nm, the charge to breakdown increases while the voltage necessary to generate charging damage decreases. The increase in charge to breakdown implies that for the same stressing current, the thinner oxide will be less damaged. However, with a lower breakdown voltage and lower voltage to induce damage, the plasma pro-

Minimum feature size (μm)						
	0.5	0.35	0.25	0.18	0.13	0.09
High-speed scenario						
Year of introduction	1992	1995	1998	2001	2005	2010
V_{dd} (V) (+10% for max V_{dd})	5	3.3	3.3	3.3	2.2	2.2
MOSFET gate oxide (nm)	15	9	8	7	4.5	4
Junction Depth (μm)	0.15	0.15	0.1	0.08	0.08	0.07
NMOS I_{dsat} at $V_{gs}=V_{dd}$ (mA/ μm)	0.56	0.48	0.55	0.65	0.51	0.62
PMOS I_{dsat} at $V_{gs}=V_{dd}$ (mA/ μm)	0.27	0.22	0.26	0.32	0.24	0.32
Low-power scenario						
V_{cc} (V) (+10% for max V_{cc})	3.3	2.2	2.2	1.5	1.5	1.5
MOSFET gate oxide (nm)	12	7	6	4.5	4	4
NMOS I_{dsat} at $V_{gs}=V_{cc}$ (mA/ μm)	0.35	0.27	0.31	0.17	0.24	0.29
PMOS I_{dsat} at $V_{gs}=V_{cc}$ (mA/ μm)	0.16	0.11	0.14	0.07	0.11	0.13

Table 1-1. Projected MOSFET scaling trends

Projected MOSFET scaling trends by C. Hu for both low power and high speed applications [1.3].

cess can generate more easily the voltage needed to induce failure. Thus in plasma processes where a fixed current flows, thinner oxides will be better. However, in plasma processes that induce a fixed voltage, the thinner oxides will be more susceptible to damage. By understanding the charging damage mechanisms, the viability of thinner oxides in future MOSFET devices can be determined.

1.3. Implant and Etching Concerns

For plasma etching concerns, the aspect ratio needed for future processes will increase. For contact and via holes, the thickness of the inter-metal oxide will not decrease due to capacitance concerns resulting in higher aspect ratios to make the smaller minimum hole. The higher aspect ratio requirements imply that stricter etching conditions may be required, reducing the process window allowed. Hopefully, with the use of low dielectric constant materials instead of oxide in the inter-metal dielectric the aspect ratio may be stabilized, but other reliability issues may arise.

For ion implantation, the smaller device dimensions will require more and more complex implants. More complex source/drain engineering with more complex LDD structures is needed for punchthrough protection and for hot electron suppression. Higher throughput also requires higher ion beam current which can create high instantaneous charge or voltage over the thin oxide.

Advanced metallization adds more concerns for oxide charging damage. With larger packing densities, more metal layers are required to provide the ground, clock, supply, and device interconnects in advanced microprocessors. For each metal layer several plasma processes are required, such as plasma ashing of photoresist, plasma etching of metal lines, plasma etching of contact vias, and plasma TEOS oxide deposition.

1.4. Oxide Charging Damage Investigation

This work studies the physical dependencies of charging damage through experiments and an analytical model of the interactions of the plasma, devices, and substrate bias. Toward that goal, the research began by developing a simple non-destructive damage measurement technique. The damage was measured using area capacitors with an oxide thickness of 10nm. To quantify the damage, both high frequency and quasi-static C-V measurements were used to determine the interface state density. Then, a variety of plasma diagnostic tools were developed to measure the plasma conditions inducing the charging damage. Some of the diagnostic tools used were: Langmuir probe, mass spectroscopy, and optical emission spectroscopy. An emerging process called Plasma Immersion Ion Implantation (PIII) was used as one of the test vehicles for studying charging damage. PIII both exposes the wafer to a plasma and implants ions into the wafer, resulting in a unique process for studying charging damage. To aid in our understanding of the physical mechanisms of charging damage, an analytical model of the plasma currents, IC devices, and substrate bias was developed. Since the model simulates the interactions of the entire system, it was used to study the effect of substrate bias, device structure, and plasma characteristics on charging damage. Finally, the model was expanded to investigate the effect of RF bias on charging damage and was adapted to simulate the charging currents in conventional ion implantation.

References

- [1.1] I.-W. Wu, R. H. Bruce, G. B. Anderson, M. Koyanagi, and T. Y. Huang, "Damage to gate oxides in reactive ion etching," *Proc. SPIE*, vol. 1185, pp. 284-295, 1989.
- [1.2] Implant damage Paper
- [1.3] C. Hu, "Ultra-large-scale integration device scaling and reliability," *Journal of Vacuum Science & Technology B (Microelectronics and Nanometer Structures)*, vol. 12, no.6, pp. 3237-3241, 1994.

2 Background

2.1. Introduction

Oxide charging damage has affected integrated circuit processing ever since the first ion implanters were used [2.1,2.2]. A variety of different damage effects have been observed. The types of damage range from complete device destruction to much more subtle oxide reliability degradation. In addition, reactive ion etching studies have observed the effect of plasma non-uniformity and device structure on charging damage [2.3].

2.2. Charging Damage Effects

Oxide charging damage effects have varied from the early “volcanos” where the device was destroyed to more subtle charge to breakdown effects. The decrease in the severity of the damage being studied follows the increase in the general understanding of charging damage. The charging damage effects observed in current devices affect both the oxide reliability and the device characteristics, similar to the effects observed in both ion implantation and plasma processing.

2.2.1. Early damage studies

Early reports of charging damage were of extreme device failures. As Figure 2-1 shows, the induced damage caused such a high electric field across the oxide that arcing induced catastrophic failure [2.4]. This failure was called “volcanos” for obvious reasons. Oxide failure due to “volcanoes” completely destroyed the device and could easily be detected both visually and electrically.

Fortunately, this type of catastrophic charging damage has not been observed for typical processes today. However, with greater awareness of charging damage, more subtle

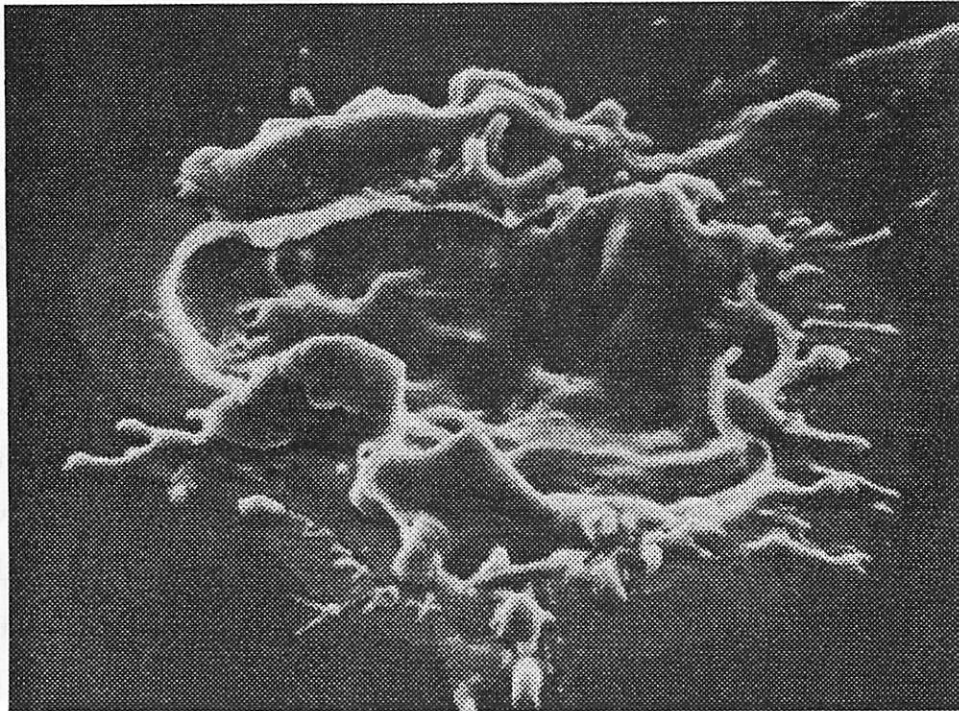


Figure 2-1. "Volcano" extreme charging damage

SEM of extreme charging damage in a conventional ion implanter resulting in complete oxide failure due to crater formation [2.5]

charging damage effects have been observed. These effects categorized as device and oxide reliability effects.

2.2.2. Charging effects on device performance

Charging damage has been observed to directly affect the MOSFET device characteristics. The device characteristic changes due to charging damage have been attributed to the high energy electrons tunneling through the oxide which either charge traps inside the oxide or generate charged states at the oxide/silicon interface. The fixed oxide traps and interface states directly affect the device performance.

2.2.2.1. Fixed oxide traps

One of the first non-catastrophic charging damage effects observed was the generation of fixed oxide traps [2.6]. Early MOSFETs had gate oxide thicknesses greater than 20nm. The charge passing through the gate oxide could get trapped inside the oxide or could generate positively charged traps. These charged traps inside the oxide cause the

threshold voltage to shift. For a given oxide thickness (t_{ox}) and trap charge in the oxide, the threshold voltage shifts as:

$$\Delta V_t = -\int_0^{t_{ox}} q x Q_f(x) dx \quad [2-1]$$

where q and $Q_f(x)$ are the unit charge and fixed oxide charge at position x , with $x=0$ at the silicon oxide interface.

Typically the threshold voltage should be well controlled within 0.1V and for current technologies below 50mV. If the threshold voltage shifts to a lower value, the leakage current will increase, causing the power consumption to increase. The current advent of low power circuit applications with battery power is making power consumption an increasingly important issue. If the threshold voltage increases, then the current driving capability of the device will decrease, causing the device to switch slower, slowing down the circuit. With clock speeds in the hundreds of MHz and continuing to increase, switching speed is extremely important.

Current MOSFETs are not as affected by fixed oxide traps because of decreasing gate oxide thickness [2.7]. A thinner gate oxide does not influence the threshold voltage as much for a given fixed oxide charge. Effectively, the maximum distance the charge can be from the oxide/gate interface is decreased reducing the effect the charge has on the threshold voltage. Also, with a thinner gate oxide, both the space where fixed traps can form is smaller and the time during which the electrons have to interact with the gate oxide is decreased. Thus, the fixed oxide traps are not as much a concern with future gate oxides which are scaling down from the current 7nm thickness.

2.2.2.2. Interface states

Interface states are also generated by charging damage. Interface traps are thought to be broken interface bonds [2.8]. Since the density of interface traps being investigated is on the order of $10^{10}/\text{cm}^2$, which is a small fraction of the approximately $10^{15}/\text{cm}^2$ bonds at the interface, electrical methods are the only way to measure the number of interface states easily.

Interface traps have a variety of effects on the characteristics of a MOSFET. The interface states, like the fixed oxide traps, also affect the threshold voltage. The interface states either provide additional charge, which lowers the threshold voltage or cause more charge to be needed to overcome the charge in the interface states, which increases the threshold voltage [2.9]. As with the fixed oxide traps, the threshold voltage shift has the same detrimental effects of device performance. In addition to the shift in threshold voltage, the interface states also degrade the mobility of the MOSFET. Effectively, the interface states act as additional scattering centers to charge flow across the gate. The reduction in mobility reduces the current driving capability of the device, causing the device to switch slower in a digital circuit. Thus, interface trap generation is very detrimental to the MOSFET device characteristics.

2.2.2.3. Other effects

In addition to the threshold voltage and mobility degradation, charging damage has also been attributed to causing other device parameters to degrade. The subthreshold swing has been reported to increase with charging damage [2.10]. Subthreshold swing is the change in drain voltage per decade change in drain current. Ideal subthreshold swing is 60mV/decade, which increases with charging damage. Increasing subthreshold swing results in higher leakage current for the device, causing higher power consumption. Also, the drain $1/f$ noise has been shown to increase with increasing charging damage [2.11]. The $1/f$ noise has been correlated with the charging and discharging of interface traps. In addition, charging damage has been associated with low level leakage currents (Stress Induced Leakage Currents (SILC)). This effect causes an increase in the leakage current at low electric field strengths ($3\text{-}6\text{MV}/\text{cm}^2$). Also, SILC is only observed for extremely thin gate oxides typically below 6nm. For a gate oxide of 9nm, SILC induces only a very slight change in the leakage current. However, for a gate oxide of 5.4nm, the leakage current increases several orders of magnitude due to SILC [2.12]. SILC is theorized to be induced by neutral trap generation [2.13]. Therefore, as a result of the trend toward thinner oxides, SILC will grow in importance as a charging damage mechanism.

2.2.3. Oxide reliability effects

In addition to affecting the device performance, charging damage also affects the reliability of the gate oxide. Charging damage physically affects the gate oxide, reducing the lifetime of the oxide. TDDB studies show that devices which have charging damage have lower Q_{bd} versus similar devices that have not [2.14]. Thus, the damaged devices will not last as long in operation as undamaged ones, resulting in failures either during burn-in or early in device operation.

2.3. Oxide Stressing Mechanisms

2.3.1. Fowler-Nordheim tunneling

An electric field across the gate oxide above 6MV/cm can induce Fowler-Nordheim (F-N) tunneling [2.15]. The charge that flows through the oxide via F-N tunneling is the charge that generates the charging damage. The thin oxide between the gate and silicon substrate is a potential barrier to charge flow. At low fields (below 5MV/cm), the potential barrier is high enough to prevent any measurable charge from tunneling through. As the voltage across the barrier increases, the barrier thins and the probability of tunneling increases.

2.3.2. Direct tunneling

As the thickness of the oxide reduces to below 4nm, direct tunneling can take place. Unlike F-N tunneling which goes through a triangular energy barrier, direct tunneling goes straight through the oxide and sees a trapezoidal barrier. As Figure 2-2 [2.16] shows, direct tunneling increases the tunneling current several orders of magnitude higher than F-N theory predicts at low electric fields. For 2-4nm oxides, direct tunneling stress damage appears to be similar to that seen in F-N stressed oxides [2.17]. Thus, even for direct tunneling, the damage mechanisms in the oxide remain the same. The enhanced stressing current due to direct tunneling could potentially enhance the charging damage induced at such thin oxides.

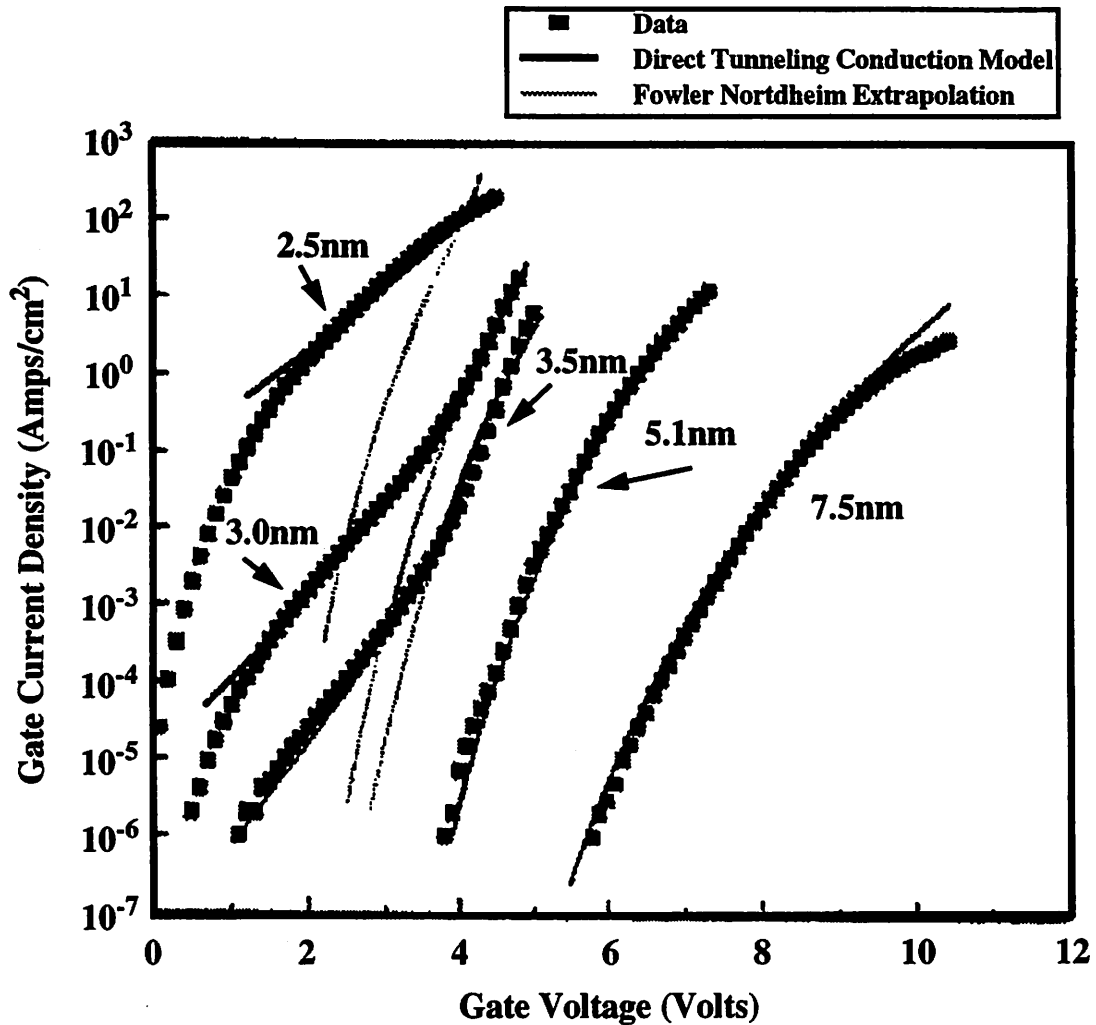


Figure 2-2. I-V characteristics of thin oxides

Scaling of oxide below 4nm will result in large direct tunneling current even at low voltage [2.16].

2.4. Oxide Damage Induced by Plasma Processing

2.4.1. Spatially non-uniform plasma density

One source of charging damage is plasma non-uniformity. Plasma non-uniformity induces charging damage by generating a charge imbalance between one portion of the wafer and another. This charge imbalance can be sufficient to generate current across the wafer, causing charging damage to occur [2.18]. Since the current flows from one portion of the plasma through the wafer and back to another portion of the plasma, a complete cir-

cuit exists between the plasma and the wafer which can generate charging damage as shown in Figure 2-3.

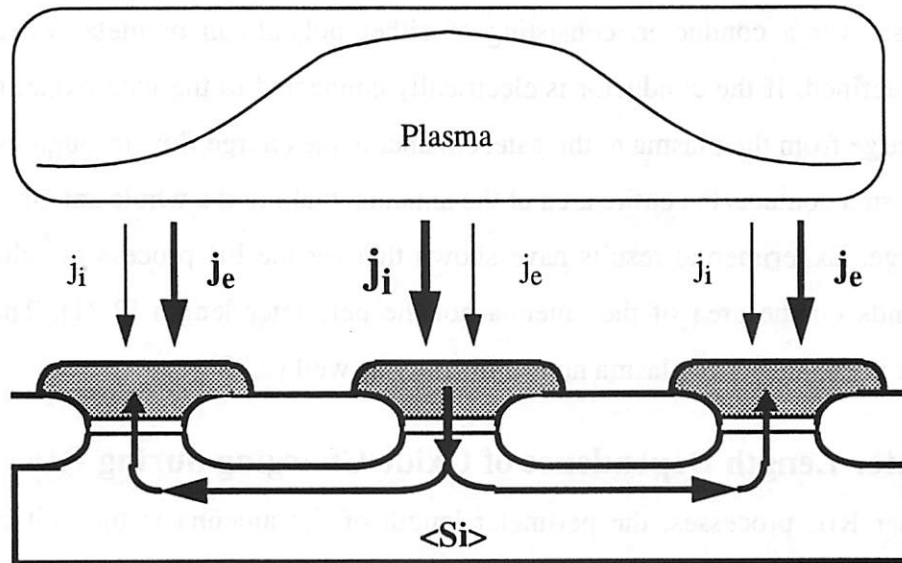


Figure 2-3. Non-uniformity inducing charging damage

The more dense portion of the plasma can locally induce more ion current which flows to the edges of the wafer where locally more electron current flows.

A variety of experiments have been done which illustrate non-uniformity charging damage effects. By inducing a strong non-uniform plasma with a magnet behind the wafer holder, non-uniform charging damage patterns were generated which followed the shape of the magnet [2.19]. After the magnet was removed and the plasma was allowed to become more uniform, the damage went away [2.19]. Also, non-uniform charging damage effects were seen in a MERIE (Magnetically Enhanced Reactive Ion Etcher) when the rotating magnet under the wafer holder was held stationary [2.20]. Hence, with a highly non-uniform plasma, the imbalance in the plasma can be strong enough to generate currents across the wafer and through the plasma to induce charging damage in the gate oxides on the wafer.

2.5. Device Area Dependence of Oxide Charging during RIE (Antenna Effect)

In RIE, the plasma damage is found to be dependent on the pattern area when the pattern area is exposed directly to the plasma. For example, a PR ashing process removes the photoresist over a conductor, consisting of either polysilicon or metal which has already been defined. If the conductor is electrically connected to the gate oxide, then it can funnel charge from the plasma to the gate, enhancing the charge flow through the gate oxide. The plasma contacts the entire area of the antenna, making the whole antenna a collector of charge. Experimental results have shown that for the PR process the charging damage depends on the area of the antenna not the perimeter length [2.21]. The area antenna effect is enhanced by plasma non-uniformity as well [2.22].

2.6. Perimeter Length Dependence of Oxide Charging during RIE

In other RIE processes, the perimeter length of the antenna is the collector of charge. This type of charging damage has been observed in both poly and aluminum etching [2.23]. The PR used to define the pattern acts to shield the area of the antenna from charging damage. The edges, which are exposed to the plasma, collect the charge and funnel it to the gate oxide. Experiments using perimeter length intensive antennas show charging damage correlates with the perimeter length when the antenna area is insulated [2.24]. So for etches where the area of the antenna is insulated from the plasma and only the perimeter is directly exposed to the plasma, the antenna perimeter length determines the charging damage enhancement.

2.6.1. Transient effects

A variety of transient charging damage effects have also been reported as avenues where damage can occur. One transient damage mechanism is due to stringers formed during the etch of polysilicon or metal lines. Since the etch is anisotropic, the contours associated with the topography will create corners with larger vertical dimensions due to conformal deposition. These stringers act as antennas and can direct plasma charge to a gate oxide. When the etch completes, the stringers disappear and the damage ceases. Charging damage associated with the end of an etch has been reported in polysilicon etch

cases as well as aluminum etches [2.25,2.26]. This type of transient charging damage phenomena can be alleviated in more advanced processes where the metal lines are made planar by chemical mechanical polishing of the underlying dielectric. However, polysilicon lines will still have topography to them because the poly lines need to be over both the gate oxide and the field oxide.

2.7. Conclusions

Oxide charging damage has been reported in virtually all plasma etch processes. Etching damage can come from initial transients, during the etch process, at the end of the etch process, or during the over etch phase. Essentially, whatever the plasma source of the damage is, the plasma has to induce sufficient charge across the gate oxide to induce tunneling current. In order to understand oxide charging damage, it must be observed, the sources of damage determined, and the damage must be quantified and measured.

References

- [2.1] R. G. Wilson and G. R. Brewer, Ion beams with applications to ion implantation, Wiley-Interscience, Chichester, Sussex, UK, 1973.
- [2.2] K. H. Nicholas, "Implantation damage in silicon devices," *Journal of Physics D*, vol. 10, no. 4, pp. 393-407, 1977.
- [2.3] S. Fang and J. P. McVittie, "Model for oxide damage from gate charging during magnetron etching," *Applied Physics Letters*, vol. 62, no. 13, pp. 1507-1509, 1993.
- [2.4] F. Schwirzke, "Unipolar arc model," *Journal of Nuclear Materials*, vol. 128-129, pp. 609-612, 1984.
- [2.5] C. M. McKenna, in program for Wafer charging effects in ion implantation processing, UC Berkeley Extension Short Course, 1993.
- [2.6] D. M. Fleetwood, P. S. Winokur, R. A. Reber Jr., and T. L. Meisenheimer, "Effects of oxide traps, interface traps, and 'border traps' on metal-oxide-semiconductor devices," *Journal of Applied Physics*, vol. 73, no. 10, pp. 5058-5074, 1993.
- [2.7] Y. Roh and L. Trombetta, "A comprehensive model for the formation of interface traps in MOS devices," *Microelectronic Engineering*, vol. 28, pp. 23-26, 1995.
- [2.8] K. P. Cheung and C. P. Chang, "Plasma-charging damage: a physical model," *Journal of Applied Physics*, vol. 75, no. 9, pp.4415-4426, 1994.
- [2.9] E. H. Nicollan and J. R. Brews, MOS (Metal Oxide Semiconductor) Physics and Technology. John Wiley & Sons, New York, 1982.
- [2.10] H. Shin, Ph. D. Thesis, UC Berkeley, 1993.

- [2.11] Z. J. Ma, H. Shin, P. K. Ko, and C. Hu, "Effects of plasma charging damage on the noise performance of thin-oxide MOSFET's," *IEEE Electron Device Letters*, vol. 15, no. 6, pp. 224-226, 1994.
- [2.12] M. Kimura, H. Koyama, "Stress-induced Low-Level Leakage Mechanism in Ultrathin Silicon Dioxide Films Caused by Neutral Oxide Trap Generation," *IEEE IRPS*, pp. 167-172, 1994.
- [2.13] D. J. DiMaria, "Stress Induced Leakage Currents in Thin Oxides," *Microelectronic Engineering*, vol. 28, pp. 63-66, 1995.
- [2.14] X. Li, J. T. Hsu, P. Aum, D. Chan, J. Rembetski, and C. R. Viswanathan, "Plasma-damaged oxide reliability study correlating both hot-carrier injection and time-dependent dielectric breakdown," *IEEE Electron Device Letters*, vol. 14, no. 2, pp. 91-93, 1993.
- [2.15] M. Lenzlinger and E. Snow, "Fowler-Nordheim Tunneling into Thermally grown SiO₂," *Journal of Applied Physics*, vol. 40, no. 1, pp. 278-283, 1969.
- [2.16] K. F. Schuegraf, C. C. King, and C. Hu, "Ultra-thin silicon dioxide leakage current and scaling limit," *1992 IEEE Symposium on VLSI Technology*, pp. 18-19, 1992.
- [2.17] P. Lundgren, M. O. Andersson, K. R. Farmer, and O. Engstrom, "Electrical instability of ultrathin thermal oxides on silicon," *Microelectronic Engineering*, vol. 28, pp. 67-70, 1995.
- [2.18] S. Fang and J. P. McVittie, "Oxide damage from plasma charging: breakdown mechanism and oxide quality," *IEEE Transactions on Electron Devices*, vol. 41, no. 6, pp. 1034-1039, 1994.
- [2.19] S. Fang and J. P. McVittie, "Model for oxide damage from gate charging during magnetron etching," *Applied Physics Letters*, vol. 62, no. 13, pp. 1507-1509, 1993.
- [2.20] H. Shin, K. Noguchi, X. Y. Qian, N. Jha, and C. Hu, "Spatial distributions of thin oxide charging in reactive ion etcher and MERIE etcher," *IEEE Electron Device Letters*, vol. 14, no. 2, pp. 88-90, 1993.
- [2.21] H. Shin, C. King, and C. Hu, "Thin oxide damage by plasma etching and ashing processes," *30th IRPS Proceedings 1992*, pp. 37-41, 1992.
- [2.22] S. Fang and J. P. McVittie, "The role of antenna structure on thin oxide damage from plasma induced wafer charging," *Materials Reliability in Microelectronics II Symposium. MRS Symp. Proc.*, vol. 265, pp. 231-236, 1992.
- [2.23] H. Shin and C. Hu, "Plasma etching antenna effect on oxide-silicon interface reliability," *Solid-State Electronics*, vol. 36, no. 9, pp. 1356-1358, 1993.
- [2.24] K. Noguchi and K. Okumura, "The effect of plasma-induced oxide and interface degradation on hot carrier reliability," *IEEE IRPS*, pp. 232-237, 1994.
- [2.25] C. T. Gabriel and J. P. McVittie, "Effect of plasma overetch of polysilicon on gate oxide damage," *JVST-A*, vol. 13, no. 3, pp. 900-904, 1995
- [2.26] H. Shin and C. Hu, "Dependence of plasma-induced oxide charging current on Al antenna geometry," *IEEE Electron Device Letters*, vol. 13, no. 12, pp. 600-602, 1992.

3 Oxide Charging Damage Measurement Techniques

3.1. Introduction

Both direct and indirect methods have been developed to quantify and monitor charging damage. Direct methods measure either device parameter variation or oxide reliability reduction. Indirect methods use other parameters such as the threshold voltage in a CHARM-2 device, which are then correlated back to device parameter variation or oxide reliability reduction. The sensitivity of the measurement techniques is increased by several different damage enhancement structures among which the antenna structure is the most common one. Also, to prevent charging damage in devices for generating control test devices, charge protection structures are employed, such as protection diodes or fuses.

3.2. C-V Measurement of Damage

Several non-destructive C-V techniques are available to extract the interface trap density in MOS capacitors [3.1]. For our studies, the method that has the best accuracy uses both the quasi-static and high frequency C-V measurements. This chapter discusses how the quasi-static and high frequency C-V measurements are made and how the interface traps can be extracted from the C-V measurements.

3.2.1. Quasi-static C-V measurement method

The quasi-static C-V measurement uses a constant voltage ramp to determine the C-V curve of the test capacitor. If the MOS capacitor has a negligible parallel leakage path for the applied voltages, then the current measured is proportional to the capacitance at the applied voltage, with the proportionality factor being the voltage ramp rate:

$$I = C \frac{dV}{dt} \quad [3-1]$$

In order to get an accurate quasi-static C-V measurement, the voltage ramp rate must be fast enough to keep the displacement current much greater than the parallel leakage current. However, if the ramp rate is faster than a characteristic response time for the interface traps, the traps will not respond to the bias, creating error in the measurement. The quasi-static C-V measurement must keep all of the interface traps in equilibrium with the applied voltage. For the majority of interface traps the response time can range from microseconds to many milliseconds. For our measurements, a voltage ramp rate of 1V/sec is slow enough to let the traps to remain in equilibrium throughout the voltage ramp; yet is fast enough so that the displacement current generated is many orders of magnitude greater than the leakage current.

3.2.2. High-Frequency C-V measurement method

The high frequency C-V measurement applies a test voltage to the capacitor. On top of the test voltage a high frequency sinusoidal signal is applied. From the phase information the capacitance of the test MOS capacitor can be determined at the applied voltage.

In the high frequency C-V measurement, we do not want the interface traps to respond to the high frequency sinusoidal applied signal. Therefore the frequency of the applied signal must be faster than the response time of the traps. A frequency of 3-7MHz was used for our experiments.

3.2.3. D_{it} extraction methods

Several different methods have been developed to extract the interface trap density from C-V measurements. Three different methods are outlined along with their relative merits and problems of each are found. From this survey of extraction techniques, the method of using both the quasi-static and high frequency C-V measurements was determined to be the best for our purposes.

3.2.3.1. D_{it} extraction using only quasi-static C-V

This method [3.2] compares the measured quasi-static C-V curve with a theoretical quasi-static C-V curve generated using the measured oxide thickness, capacitor area, and substrate dopant concentration. The theoretical curve is generated assuming there are no interface traps. The differences in the two curves are the result of interface traps. The interface traps cause the capacitance to increase in the depletion region of the C-V curve. In addition, the interface traps cause the voltage range of the depletion region to stretch out. From the differences of the two curves, the interface trap density can be determined (Figure 3-1).

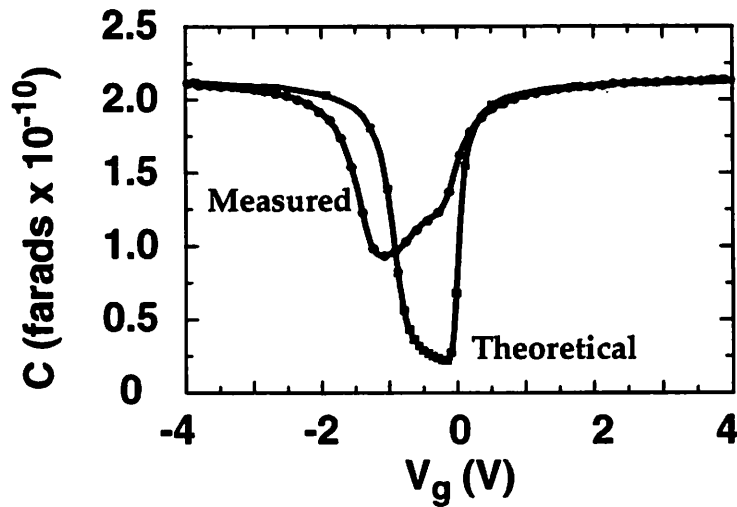


Figure 3-1. Measured and theoretical quasi-static C-V curves.

The measured curve has interface traps and the theoretical curve contains no interface traps.

The major drawback of this method is that it depends on the theoretical curve to determine the interface traps. The inherent errors in the actual oxide thickness and in the dopant density strongly affect the theoretical C-V curve. In addition, the dopant concentration under the oxide is usually not constant with depth, which is extremely difficult to take into consideration in the theoretical curve.

Another method that uses only the quasi-static C-V measurement was developed by Shin [3.3]. This method compares the quasi-static C-V curves for both electrically

stressed capacitors and plasma charging damage stressed capacitors. If the shape of the quasi-static C-V curves for the electrical stress is the same as the one for the plasma stress then the plasma stress is the same as the electrical stress. Thus the damage induced can be quantified.

3.2.3.2. D_{it} extraction using only high frequency C-V

This method [3.4] compares the measured high frequency C-V measurement with the theoretical high frequency C-V measurement. Though the interface traps do not respond to the sinusoidal applied signal, they do respond to the applied DC bias. This results in a stretch out of the voltage range of the depletion region of the C-V curve. As in the quasi-static only method, the difference in the two C-V curves determines the interface trap density (Figure 3-2).

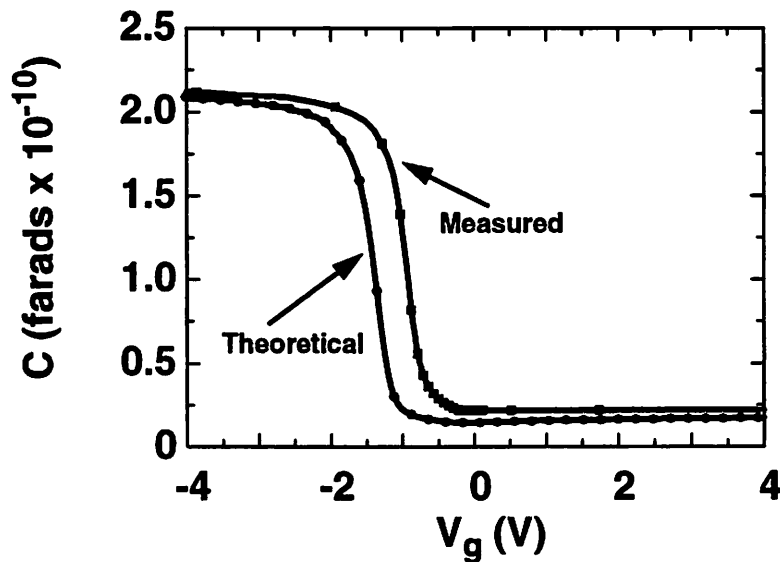


Figure 3-2. Measured and theoretical high frequency C-V curves

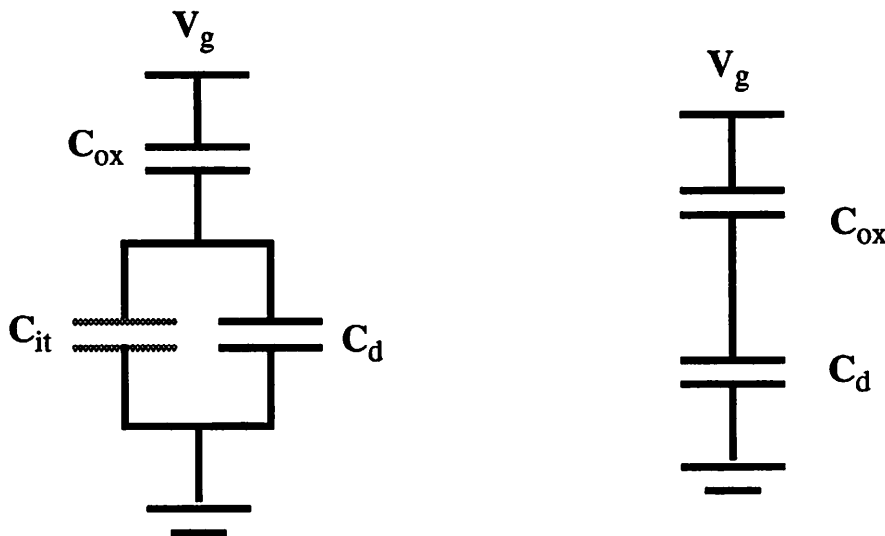
The measured curve has interface traps and the theoretical curve contains no interface traps.

The major drawback of this method is the use of the theoretical reference curve as in the quasi-static only method. Also the difference between the two curves can be induced by both interface states and fixed oxide traps, and cannot be distinguished from each other.

In addition, all of the problems seen in the quasi-static only method are applicable here as well.

3.2.3.3. Quasi-static and High Frequency Method

This method [3.5] uses the difference in the capacitance values of the quasi-static and high frequency C-V curves. For the quasi-static and the high frequency C-V measurements an equivalent circuit of MOS capacitor can be drawn to show the capacitances that contribute to the total capacitance (Figure 3-3).



Quasi-Static Equivalent Circuit High Frequency Equivalent Circuit

Figure 3-3. C-V equivalent circuits

Schematics of the equivalent circuit for both the quasi-static and high frequency C-V measurements.

In both measurements the capacitance due to the oxide and the depletion capacitance remains the same. The quasi-static C-V measurement allows the interface traps to respond to the applied bias, and the variation of the interface trap charge is measured as an equivalent capacitance. However, the high frequency C-V measurement does not allow the interface traps to respond to the sinusoidal test signal and therefore, the interface traps do

not contribute to the capacitance. From this difference, the interface trap capacitance can be extracted as a function of applied voltage:

$$C_{it}(V_g) = \left\{ \left(\frac{1}{C_{qs}(V_g)} - \frac{1}{C_{ox}} \right)^{-1} - \left(\frac{1}{C_{hf}(V_g)} - \frac{1}{C_{ox}} \right)^{-1} \right\} \quad [3-2]$$

where C_{it} , C_{qs} , C_{ox} , C_{hf} , and q are the interface trap capacitance, quasi-static C-V capacitance, oxide capacitance, high frequency C-V capacitance and electron charge respectively. From the interface trap capacitance, D_{it} can be determined. D_{it} is the interface trap density per eV of surface potential:

$$D_{it}(V_g) = \frac{C_{it}(V_g)}{qA} \quad [3-3]$$

where A is the area of the capacitor.

To get a quantitative interface trap density the surface potential (Φ_s) must be determined as a function of applied bias. The surface potential is the potential relative to ground at the oxide-silicon interface. The surface potential can be determined using Berglund's Method [3.2] (Figure 3-4).

$$\Phi_s(V_g) = \int_{V_{fb}}^{V_g} \left(1 - \frac{C_{qs}}{C_{ox}} \right) dV \quad [3-4]$$

By integrating across the mid-gap region of the surface potential of the D_{it} versus Φ_s curve, Q_{it} (interface trap density) is extracted. The traps at the edges of the bandgap are not included because the error becomes very large in those regions. In addition, the mid-gap traps are the most detrimental of the traps to MOSFET performance in terms of mobility degradation.

Unlike the other two methods, the quasi-static and high frequency C-V interface trap extraction method does not require a theoretical reference curve. Any variation in oxide thickness or non-uniformities in the dopant concentration will be taken into account in both the quasi-static and high frequency measurements and will cancel out in the extraction.

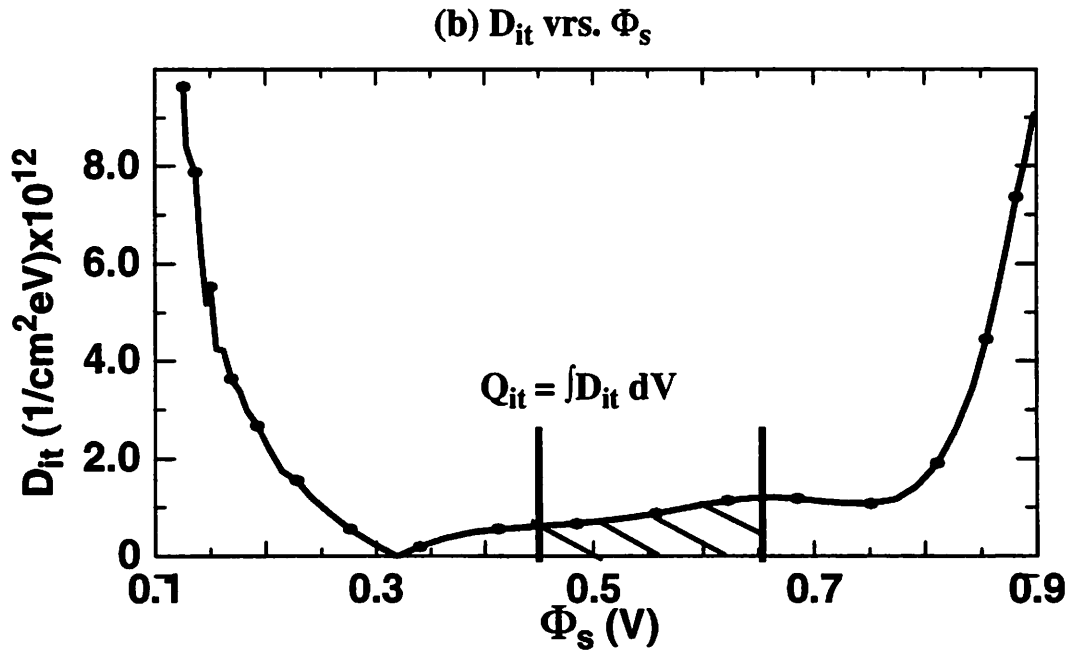
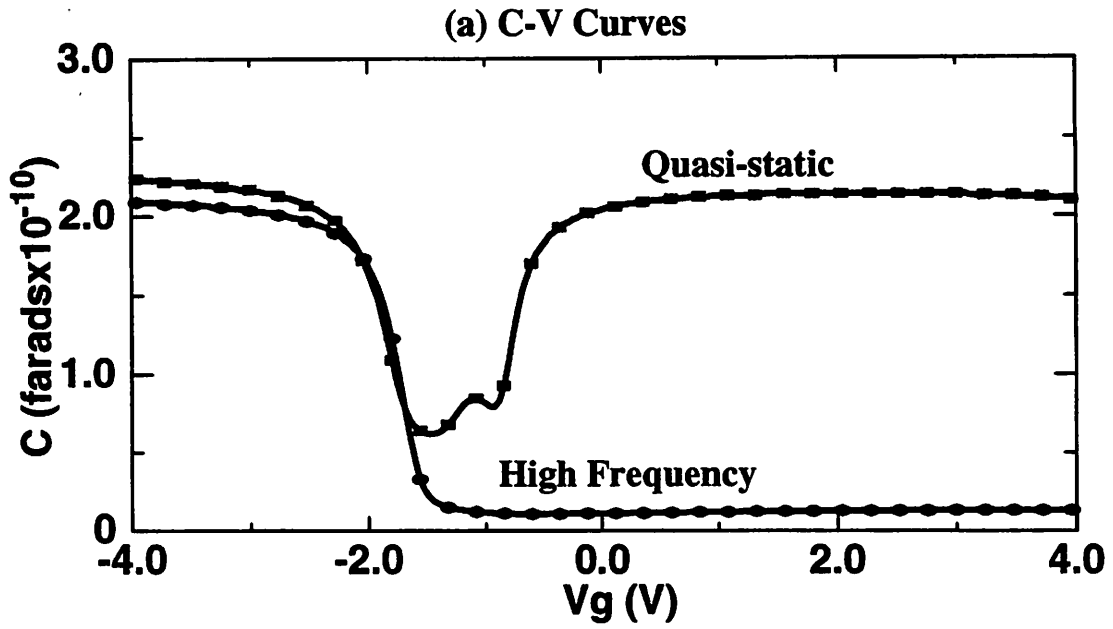


Figure 3-4. D_{it} extraction using quasi-static and high frequency C-V

(a) Quasi-static and high frequency C-V measurements of the same MOS capacitor with interface traps. (b) Interface trap density curve extracted from the C-V curves.

Using C-V curves to extract the interface trap density allows a non-destructively damage measurement of the test capacitors. The method of using both the quasi-static and high frequency C-V measurements was chosen because it does not require a theoretical reference curve and thus has the least error of the three possible methods.

3.2.4. D_{it} and device damage relationship

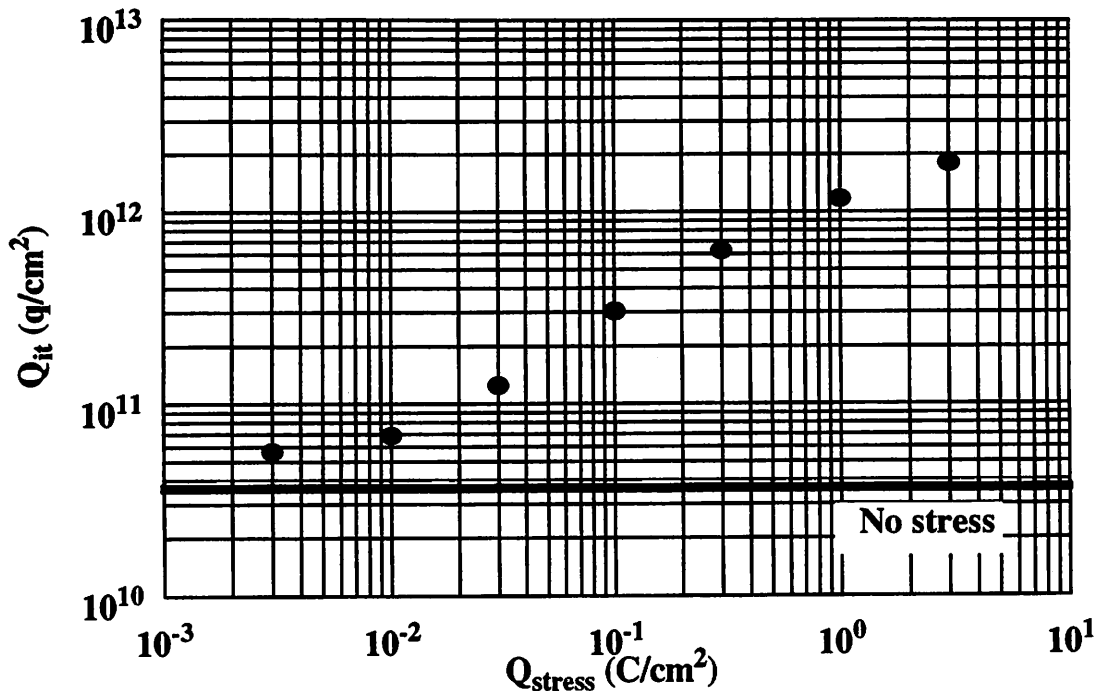


Figure 3-5. Q_{it} versus Q_{stress}

Electrical stressing 10nm thick gate oxide capacitors (area = 250x250 μm) causes the interface trap density to increase with larger Q_{stress} . Without electrical stress a finite Q_{it} exists due to defects in the Si/SiO₂ interface formed during oxide growth [3.6].

By using electrical stress, the interface trap density (Q_{it}) can be correlated to the stressing charge (Q_{stress}). After a range of different stressing currents were applied to test capacitors of 10nm gate oxide thickness the resulting Q_{it} was measured. Figure 3-5 [3.6] shows the results of the electrical stressing and the measured Q_{it} values. By correlating Q_{it} to Q_{stress} , Q_{it} can be used to quantitatively determine the amount of charge that passed through the gate oxide during a given process.

3.3. MOSFET Device Parameter Measurements

A more direct method of measuring charging damage is through the use of complete MOSFETs. By using MOSFETs, the degradation of actual device parameters can be measured. Charging damage detrimentally shifts a variety of different device characteristics; such as the threshold voltage, mobility, sub-threshold swing, and $1/f$ noise. In addition charging damage has been observed to increase the variation of these parameters across the wafer. Thus, by measuring the change in the device parameters or the distribution of the device parameters, the induced charging damage can be found.

3.3.1. Damage enhancement structures

For isolated MOSFET structures, the charging damage may be small or difficult to measure. To enhance the charging damage and to simulate actual conditions for MOSFETs connected in an integrated circuit, several charging damage enhancement structures have been developed.

3.3.1.1. Antenna structure

The most common charging damage enhancement structure used is the antenna structure. The antenna structure consists of a large conductor over either field oxide or inter-metal dielectric which is connected to the gate as shown in Figure 3-6. The antenna acts to collect charge from the plasma, funneling it to the gate oxide which enhances the charging damage. The antenna structure exists on a typical integrated circuit as the poly over the field oxide or the metal lines electrically connected to the poly gate. A wide variety of antenna type structures, from simple large area antennas to long perimeter intensive structures, are used as test vehicles.

3.3.1.2. Damage enhancement in antenna structures

The antenna structure can enhance the charging damage in two ways. First, the antenna can act to enhance the voltage drop across the oxide. The antenna structure can be modeled as two capacitors in parallel: one capacitor for the gate and another for the antenna as shown in Figure 3-6. If a uniform charge per unit area (Q) is placed on the surface then, by using the capacitive divider formula, the induced voltage across the oxides can be deter-

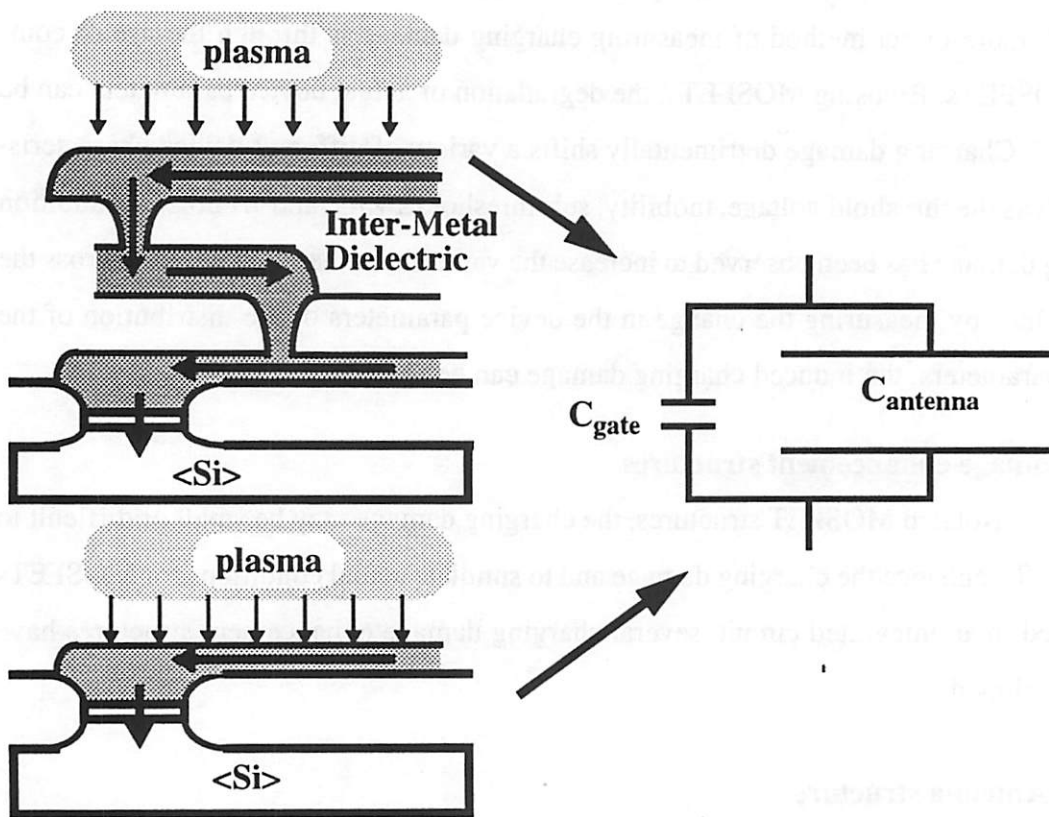


Figure 3-6. Cross section of typical antenna structures and equivalent circuit model

Antenna structures can occur at both the poly level or at the metal level. The antenna structure can be modeled as two capacitors in parallel, with one capacitor representing the antenna and the other representing the gate oxide.

mined. Since the antenna has a lower capacitance per unit area than the gate oxide, more voltage will be induced across it than the gate. Charge will flow down the potential difference, enhancing the charge on the gate oxide.

3.3.1.3. Area and perimeter antennas

Antenna structures can take advantage of either area or perimeter charging damage mechanisms by changing the shape of the antenna. To examine area intensive charging damage, square or rectangular antennas are preferred because they maximize the effect of area charging damage over perimeter charging damage. To maximize the effect of perimeter charging damage, elongated structures or structures with multiple fingers are used to

maximize the perimeter length to area ratio. These two antenna structures are the most common in investigating charging damage.

3.3.1.4. Contact and via arrays

Another method to enhance the charging damage in insulator etch processes is to use arrays of contacts or vias. During the dielectric etch process, the insulator prevents charge from reaching the gate oxide to induce charging damage. However, when the etch finishes, the insulator is removed from the contact or via hole, allowing the plasma to directly contact the underlying metal or polysilicon which is electrically connected to the gate. To magnify the effect of the damage by this mechanism, large arrays of contact or via holes act like an antenna to collect the charge from the plasma and funnel it down to the gate oxide.

3.3.2. Damage reduction structures

In addition to enhancing damage, structures have been developed that can reduce or eliminate charging damage. These structures either short out the gate capacitor to prevent any damaging voltage from being developed or drain away plasma charging currents through leakage paths. These structures can be used to prevent charging damage from occurring in a process or can be used to isolate individual steps in a process flow with many steps suspected of inducing charging damage.

3.3.2.1. Diode protection

Diode protected devices have a diode placed in parallel with the gate oxide to shunt charging currents away from the gate oxide as illustrated in Figure 3-7. Either the diode acts as a short across the oxide or carries sufficient current to prevent any charge from building up to the point where oxide charging damage occurs [3.7]. To prevent the diode from disrupting the operation of the MOSFET, it is connected reversed biased during normal device operation. During plasma processing, light from the plasma enhances the leakage current of the reverse-biased diode to improve the charging damage protection. However, for packing density concerns, elimination of the charging damage during processing is preferred over this interim type solution.

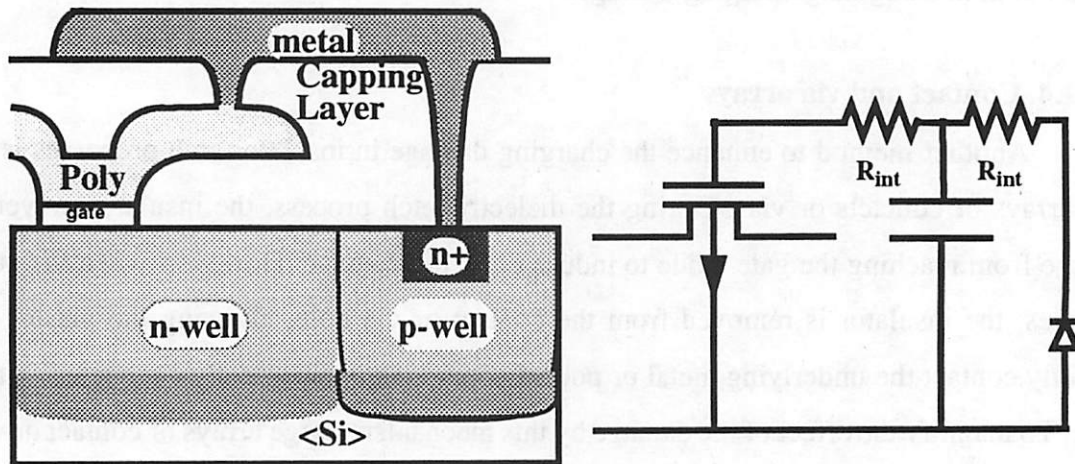


Figure 3-7. Diode protection circuit

Schematic diagram of both the vertical cross-section and circuit diagram of a MOSFET protected from charging damage by a reverse biased diode.

3.3.2.2. Fuse protection

Another method of protecting devices is through fuse structures. The fuse consists of a thin metal wire connecting the polysilicon gate to the substrate as shown in Figure 3-8. The metal wire shorts out the gate capacitor, preventing any damaging voltage from developing across the gate oxide. To operate the device, the fuse must be blown and turned into an open circuit. The fuse blowing is typically done by grounding the substrate contact and gate contact while biasing the fuse blowing pad, which avoids any charging damage due to the fuse blowing. Unfortunately, this method of device protection is not practical for actual integrated circuits because the large area required for the contact pads and the extra time required to blow the fuses are too expensive for a production process. However, fused devices allow both the study of specific process steps and the study of damage caused by other mechanisms besides charging damage.

3.4. Q_{bd} and Breakdown Voltage Measurement Techniques

In addition to device performance degradation, oxide reliability is also an indicator of charging damage. By using Time Dependent Dielectric Breakdown (TDDB) measure-

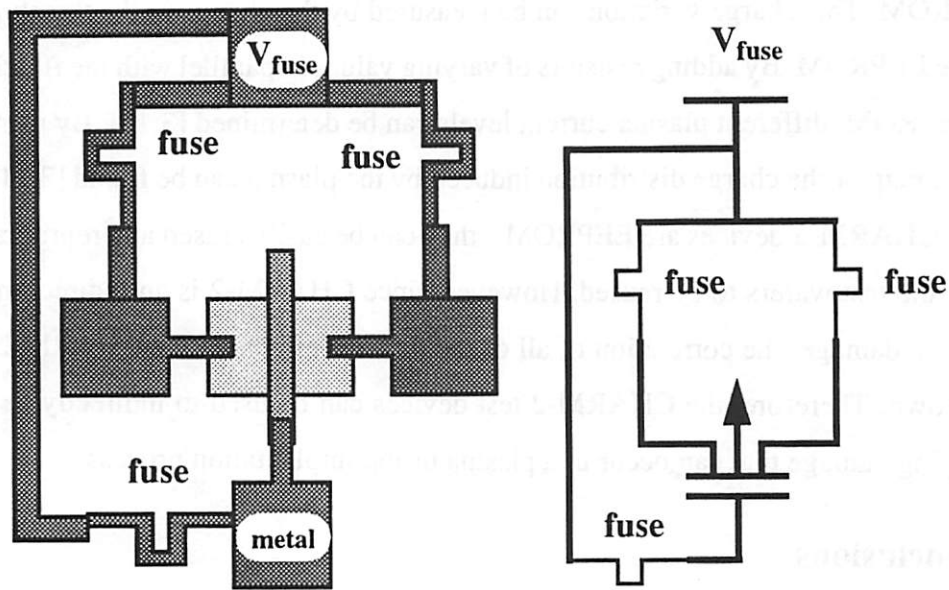


Figure 3-8. Fuse protection circuit

A plan view and circuit diagram of a MOSFET protected from charging damage by fuse structures.

ments, the reduction in the lifetime of the oxide is a direct method of determining the damage induced [3.8]. Since oxide charging damage directly affects the reliability of the oxide which in turn concerns the reliability of the integrated circuit, the TDDDB measurement is a good method for determining charging damage [3.9].

However, TDDDB measurements are time intensive. To speed up the measurement of the oxide reliability, voltage ramp to breakdown measurements can be done. Voltage ramp to breakdown measurements apply a fast voltage ramp to the oxide and determine the breakdown voltage. From this quick measurement, the reliability of the oxide can be inferred because damaged oxides have lower breakdown voltages as compared to undamaged oxides.

3.5. CHARM-2 Test Vehicle

In addition to measuring conventional devices, specialized test structures for monitoring charging damage have been developed. One such test vehicle is called CHARM-2. CHARM-2 uses a double gated EEPROM to collect the charge induced by the plasma.

Since the EEPROM is programmable, the plasma either enhances or drains the charge on the EEPROM. This charge variation can be measured by the change in the threshold voltage of the EEPROM. By adding resistors of varying values in parallel with the floating gate of the EEPROM, different plasma current levels can be determined [3.10]. By using these devices, a map of the charge distribution induced by the plasma can be found [3.11]. Also, since the CHARM-2 devices are EEPROMs, they can be easily erased and reprogrammed, allowing the test wafers to be reused. However, since CHARM-2 is an indirect measurement of the damage, the correlation of all of the damage effects to the CHARM-2 results is not known. Therefore, the CHARM-2 test devices can be used to indirectly determine the charging damage that can occur in a plasma or ion implantation process.

3.6. Conclusions

Both destructive and non-destructive measurement techniques have been developed to monitor charging damage. These techniques measure either interface traps, MOSFET parameters, or oxide reliability degradation to quantify the damage. Antenna type structures are used to increase the sensitivity of the measurements. Direct measurement techniques, such as TDDB, allow accurate determination of the degradation, but are destructive procedures. Alternative methods, such as CHARM-2, are reusable but determine the damage indirectly.

References

- [3.1] E. H. Nicollian and J. R. Brews, MOS (metal oxide semiconductor) physics and technology, John Wiley and Sons, New York, 1982.
- [3.2] C. N. Berglund, "Surface states at steam grown silicon-silicon dioxide interfaces," IEEE Trans. Electron Devices, vol. 13, pp. 701-710, 1966.
- [3.3] H. Shin, C. C. King, R. Moazzami, T. Horiuchi and C. Hu, "Characterization of thin oxide damage during aluminum etching and photoresist ashing processes," Proc. of International Symposium on VLSI Technology, Systems, and Applications, pp. 210-213, 1991.
- [3.4] L. M. Terman, "An investigation of surface states at a silicon/silicon-oxide interface employing metal-oxide-silicon diodes," Solid State Electronics, vol. 5, pp. 285-299, 1962.

- [3.5] R. Castagne and A. Vapaille, "Description of the SiO₂-Si Interface Properties by Means of Very Low Frequency MOS Capacitance Measurements," *Surface Sci.*, vol. 28, pp. 157-193, 1971.
- [3.6] B. Shieh, personal correspondence.
- [3.7] H. Shin, Z. Ma, and C. Hu, "Impact of plasma charging damage and diode protection on scaled thin oxide," *IEDM 1993, IEEE*, pp. 467-470, 1993.
- [3.8] R. Moazzami, and C. Hu, "Projecting gate oxide reliability and optimizing reliability screens," *IEEE Transactions on Electron Devices*, vol. 37, no. 7, pp. 1643-1650, 1990.
- [3.9] X. Li, J. -T. Hsu, P. Aum, and D. Chan, "Plasma-damaged oxide reliability study correlating both hot-carrier injection and time-dependent dielectric breakdown," *IEEE Electron Device Letters*, vol. 14, no. 2, pp. 91-93, 1993.
- [3.10] W. Lukaszek, J. Reedholm, M. I. Current, and N. Tripsas, "CHARM-2: A new tool for characterization of wafer charging in ion and plasma-based IC processing equipment," *SPIE*, vol. 2336, pp. 208-216, 1994.
- [3.11] W. Lukaszek, W. Dixon, M. Vella, and C. Messick, "Characterization of wafer charging mechanisms and oxide survival prediction methodology," *1994 IEEE IRPS Proceedings*, pp. 334-338, 1994.

4 Plasma Diagnostics

4.1. Introduction

Charging damage generated by plasma processing is directly related to the physical condition of the plasma. A number of different measurement techniques are available for plasma monitoring. This section discusses four different plasma measurement tools used in this work: Langmuir probe, optical emission spectroscopy, mass spectroscopy, and secondary electron yield measurement. Each of these measurement techniques examines different aspects of the plasma and determines different plasma parameters.

4.2. Langmuir Probe Measurement Technique

The Langmuir probe is an elegant and simple measurement technique that can provide vital information of the plasma characteristics. In our experiments the Langmuir probe was used to determine the ion density, electron density, plasma potential, floating potential, and electron temperature. In addition to these parameters, the Langmuir probe can provide information about the electron energy distribution, which was not measured in our experiments.

4.2.1. Description of probe dimensions and materials

Langmuir probes come in a variety of different shapes and sizes. The simplest type is the single cylindrical probe which is used most frequently in our experiments. To simplify the extraction of the plasma parameters and to minimize the perturbation of the plasma due to the measurement, a cylindrical probe with a very small diameter was used. When this type of probe is used, a collision-less sheath can be assumed.

As Figure 4-1 illustrates, the Langmuir probe consists of two parts: the probe body and the probe tip. The probe body supports the probe tip, contains the vacuum seal, and

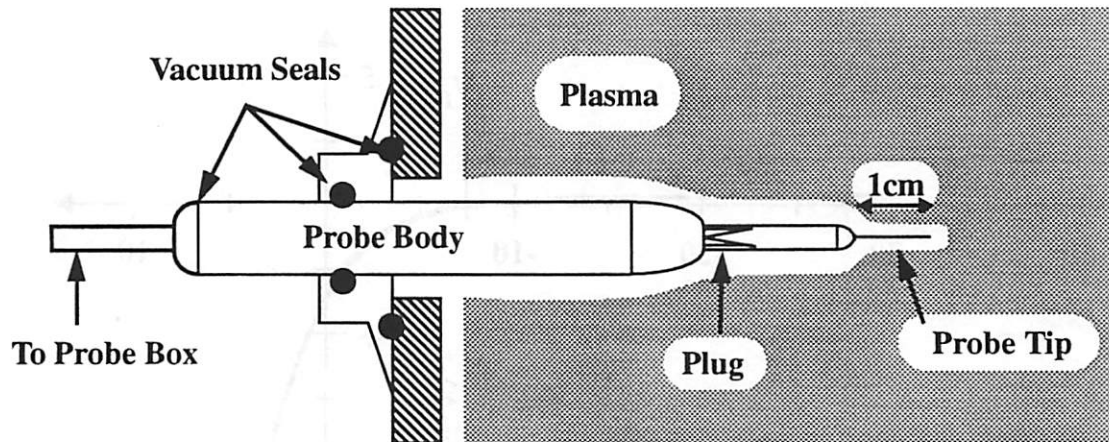


Figure 4-1. Diagram of a Langmuir probe

Typical single Langmuir probe setup used in system. Probe body vacuum seal is outside plasma to avoid degradation of the seal due to plasma exposure.

insulates the bias from the chamber wall. The probe body consists of a stainless steel cylinder with a wire running through the center. A vacuum seal is placed on the end outside the plasma to prevent plasma exposure damage. A ceramic cement is used on the plasma end to hold the plug in place and to taper down the probe body diameter to the plug diameter. The probe tip consists of a ceramic cylinder with a very thin ($\sim 0.07\text{mm}$ diameter) tungsten wire. Whenever corrosive gases are used, such as BF_3 , platinum wire is used instead of tungsten.

4.2.2. Measurement technique

For the Langmuir probe measurements, a computer controlled probe box was set to apply the voltage bias and measure the induced current. Figure 4-2 shows a typical I-V characteristic, acquired by using the Langmuir probe in an argon plasma. In the negative bias regime plasma ions are collected, and in the positive bias regime plasma electrons are collected.

To determine the plasma characteristics from the Langmuir probe I-V sweep several assumptions need to be made. First, the probe must be cylindrical. To meet that goal, the probe is made to be much longer than its diameter (probe length/ probe diameter = $1\text{cm}/0.07\text{mm}$). Second, the probe sheath is assumed to be collision-less, which is achieved by

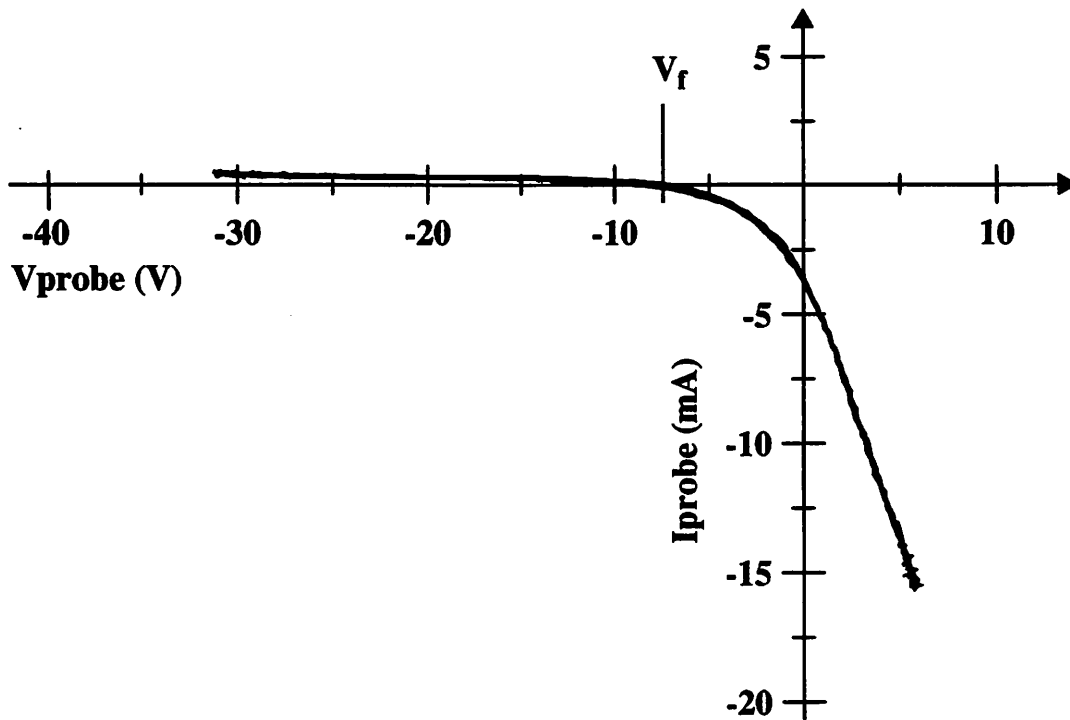


Figure 4-2. Typical langmuir probe I-V

I-V from a Langmuir probe with 1cm probe length and 0.07mm probe diameter. The plasma measured used 1mtorr argon feed gas and 900W microwave power.

making the plasma density relatively high ($\sim 10^{10}/\text{cm}^3$) and pressure low (1-5mtorr). Using these assumptions, the plasma characteristics can be extracted from the I-V curve.

4.2.2.1. Determination of the floating and plasma potentials

The simplest plasma characteristics to be determined are the floating and plasma potentials. The floating potential (V_f) is the bias built up on a floating surface in the plasma, and is determined by the equal flux of ions and electrons to the probe. Therefore, from the I-V characteristics, V_f is the potential where no current flows. The plasma potential (V_p) is also very easy to determine from the I-V characteristics. V_p is defined as the potential of the plasma with respect to ground. In the I-V characteristics, V_p is the potential larger than V_f where the first derivative is maximum. Experimentally, V_p is determined by the zero crossing of the second order derivative of the current with respect to the applied voltage.

In this way both the floating and plasma potentials can be found directly from the I-V curve.

4.2.2.2. Determination of the ion density

The ion density can be determined from the ion saturation current in the negative bias region of the probe I-V sweep. Since the probe is cylindrical, the ion current collected increases along with the negative bias due to the expanding sheath. In the ion saturation region the ion current follows the relation:

$$I_{\text{sat}} = 2qn_o a d \left(\frac{2q|V_p - V_{\text{app}}|}{m} \right)^{1/2} \quad [4-1]$$

where q , n_s , a , d , m , V_{app} , and I_{sat} are the electron charge, ion density, probe radius, probe length, ion mass, applied voltage, and ion saturation current respectively. From Equation 4-1, the ion density can be determined by plotting I_{sat}^2 versus $-V_{\text{app}}$ and the slope of the curve in the ion saturation regime is proportional to n_s^2 . However, the ion density calculation may have error due to a variety of sources such as collisions in the sheath and anisotropy of the distribution of the ions at the sheath edge. At one extreme the results of the ion density calculation can be off by almost a factor of two.

4.2.2.3. Determination of the electron density

The electron density should be determined and compared with the calculated ion density since the electron and ion densities are the same in a plasma. Similar numbers between the electron and ion density calculations indicate accurate results. The electron density can be determined from the electron saturation current when V_{app} is larger than V_p . As with the ion density calculation, the electron saturation current (I_{esat}) follows Equation 4-1 but the ion mass is replaced with the electron mass. The electron density can be determined by plotting I_{esat}^2 versus $-V_{\text{app}}$. In the electron saturation regime, the slope of the curve is proportional to n_e^2 where n_e is the electron density. Thus the electron density can be determined from the I-V curve.

4.2.2.4. Determination of the electron temperature

Within the plasma, the electrons are heated and collide with neutral atoms to form electron-ion pairs. As a result, the electrons are at a much higher energy than the ions, which have an energy typically close to room temperature values in the bulk of the plasma.

To determine the electron temperature, the region of the I-V curve between V_p and V_f is used. In this region, the electron current is modulated by the applied bias:

$$I_e = \frac{1}{4} q n_o v_e A \exp\left(\frac{V_{app} - V_p}{T_e}\right) ; v_e = (8qT_e/\pi m_e)^{1/2} \quad [4-2]$$

where T_e and m_e are the electron temperature in units of volts and electron mass respectively. The electron temperature can be found by plotting $\ln(I_e)$ versus V_{app} . The inverse of the slope of the curve is equal to T_e .

4.3. Optical Emission Spectroscopy (OES).

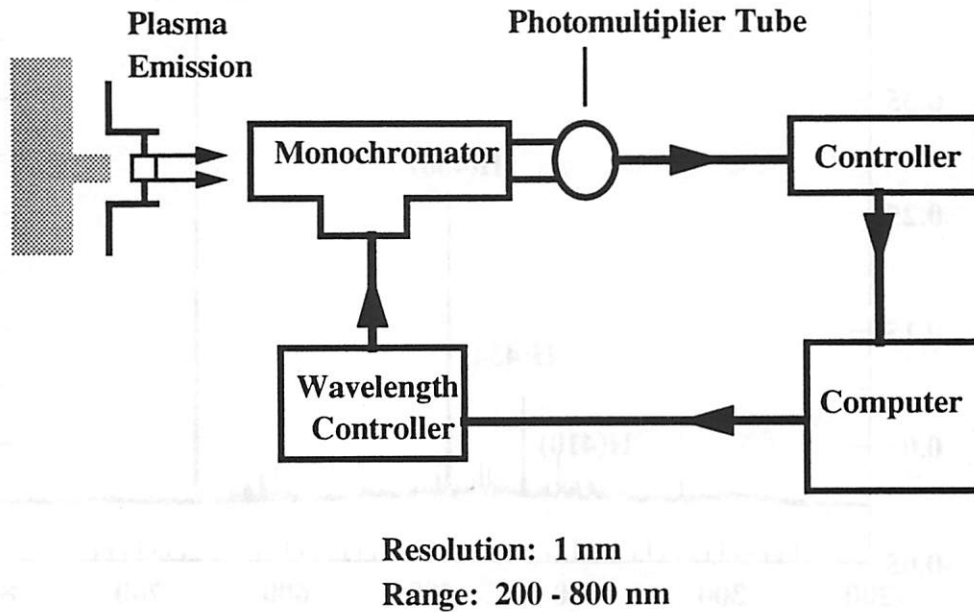


Figure 4-3. Optical emission spectroscopy setup

Schematic of the OES setup used to monitor the spectra of light being emitted from the plasma

Optical Emission Spectroscopy (OES) is another diagnostic tool that provides a non-invasive method of studying the plasma. Unlike the Langmuir probe, OES will not perturb the plasma or alter the plasma from the actual process conditions. Unfortunately, OES does not provide quantitative information about the plasma as the Langmuir probe measurement. OES uses a monochromator to filter out a specific wavelength and a photomultiplier tube to enhance the optical signal and convert it to an electrical signal. This signal is then converted to a number and stored in the computer as illustrated in Figure 4-3.

Many of the collisions between an electron and a neutral species do not result in ionization. Instead, the electron transfers some of its energy to the neutral atom by raising one of the electrons to a higher energy level. The excited electron then falls down in energy emitting light in the process. Since each atom has a unique set of energy levels, each species will emit a different spectra of light. The same happens for ionized species, though the light emitted is much less due to the lower density of ionized species to neutral species.

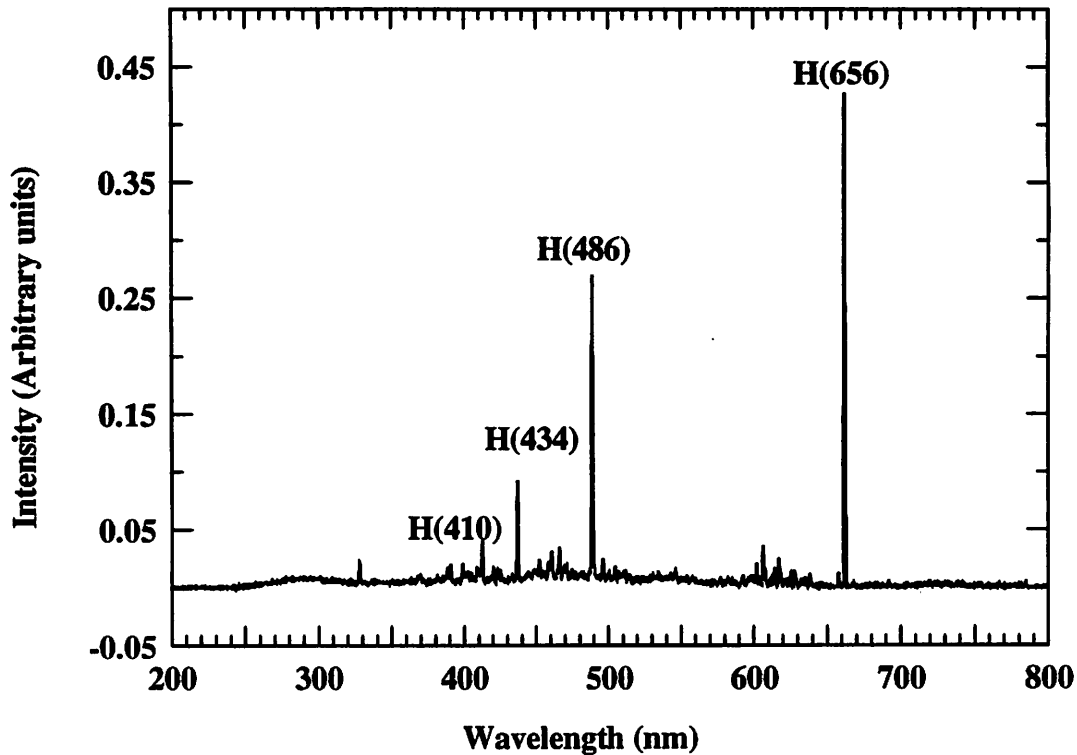


Figure 4-4. OES spectrum of H₂ plasma

H₂ plasma at 1mtorr 900W microwave power. Spectrum shows only H not H₂ peaks.

OES monitors the plasma by measuring the spectra of light being emitted. From the wavelengths of the intensity peaks, the various ion and neutral species in the plasma can be identified.

A good example of how OES can determine the species in the plasma is with a hydrogen plasma. In the plasma, the hydrogen can be ionized or dissociated from H₂ to H atoms. From the OES spectrum (Figure 4-4), the four major peaks are associated with H atoms. In addition to identifying the peaks, the ratio of the intensity of the peaks follows the expected ratios for an H atom, with the peak ratio being 2000:1200:400:150, from longest to shortest wavelength. Thus, this OES spectrum clearly shows the presence of H in the plasma.

Unfortunately, most OES spectra of process plasmas are more complicated. A typical BF₃ spectra (Figure 4-5) shows a broad peak from about 300nm to 480nm. This broad

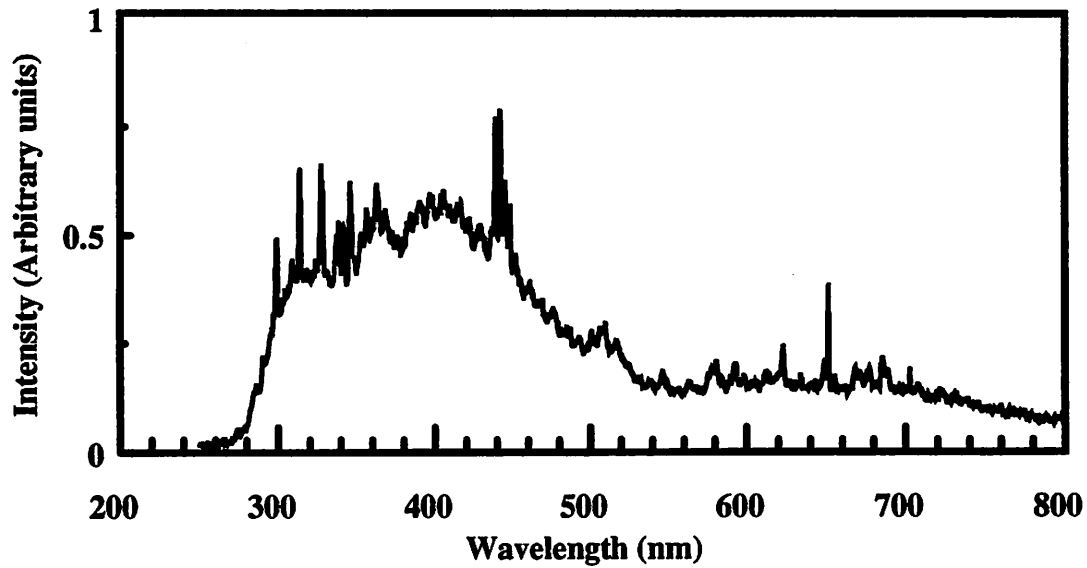


Figure 4-5. OES spectra of a BF_3 plasma

BF_3 optical emission spectrum for a 1mtorr 900W plasma.

peak is attributed to the fact that many of the neutral species in the plasma are molecules, and both the rotational and vibrational states of the atomic bonds in the molecules broaden the peaks. Mixed in with the background broad peak are many single transition peaks. Appendix A lists some of the identified peaks for BF_3 and its decomposed species [4.6]. For such complex spectra, quantitative data is difficult to acquire. Instead, OES can be used to fingerprint each process condition used and a change in the spectra can indicate if something has affected the plasma.

OES provides a quick and non-invasive measurement of the species in the plasma. For typical process plasmas with complex emission spectra, OES can provide a method of checking run to run consistency.

4.4. Mass Spectroscopies

Another method of determining the species present in the plasma is with a mass spectrometer. Mass spectroscopy can provide information about each of the neutral species in the plasma and the relative concentrations of each. One mass spectrometer can also provide the energy distribution and relative concentration of ionized species in the plasma. In

our experiments, three different mass spectrometers were used. One is an external commercial mass spectrometer using a quadrupole and an energy analyzer. Another is also a commercial mass spectrometer whose quadrupole mass analyzer is placed inside the plasma. The third mass spectrometer consists of a homemade magnetic quadrant analyzer placed inside the plasma.

4.4.1. CMA/Quadrupole mass spectrometer

The most accurate mass spectrometer used is a commercial system with both a qua-

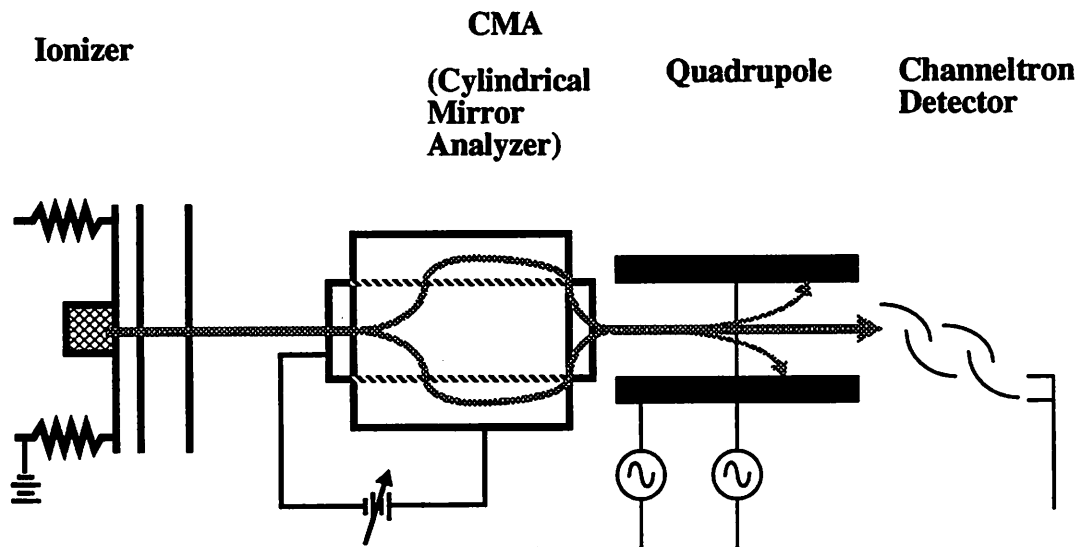


Figure 4-6. Schematic of large mass spectrometer

Schematic of mass spectrometer showing quadrupole mass analyzer and cylindrical energy analyzer

drupole mass analyzer and cylindrical energy analyzer as illustrated in Figure 4-6. This mass spectrometer can monitor the neutral species in the plasma by ionizing them with a filament. As shown in Figure 4-7, this mass spectrometer can determine the neutral species in a BF_3 plasma. The filament can be turned off to allow the mass spectrometer to analyze the ionized species in the plasma. Since the signal is much weaker for the ionized species, the pressure range at which the mass spectrometer can operate in this manner is reduced to below 1mtorr. At higher gas pressures collisions in the system interfere with the signal. The distribution of ionized species can be very different from the neutral species as seen in

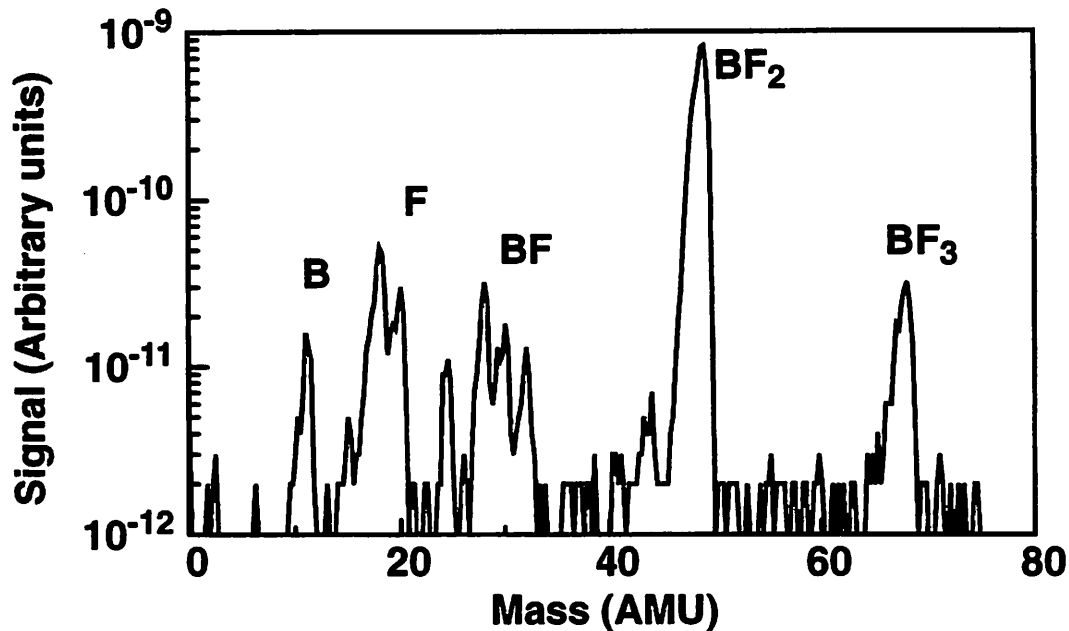


Figure 4-7. Mass spectrum of BF_3 plasma neutrals

Mass spectrum of neutral species in BF_3 plasma at 1mtorr 900W microwave power.

Figure 4-8. The differences are due to different ionization cross-sections for the various neutral species. With the cylindrical mirror analyzer, this mass spectrometer can also determine the energy spectrum of a particular ionized species. As Figure 4-9 shows, the energy of the B^+ ions peaks at 24eV which is approximately the plasma potential.

Using this mass spectrometer, the relative concentrations of the neutral and ionized species in the plasma as well as the energy spectra of the ionized species can be determined. However, one major drawback of this mass spectrometer is its relatively large size (about 1 meter long from entrance port to channeltron) resulting in some collisions due to background gas and a relatively large amount of wall losses for the ionized species. As a result, this mass spectrometer cannot easily measure the ionized species for plasmas with feed gas pressures above 1mtorr, even with differential pumping.

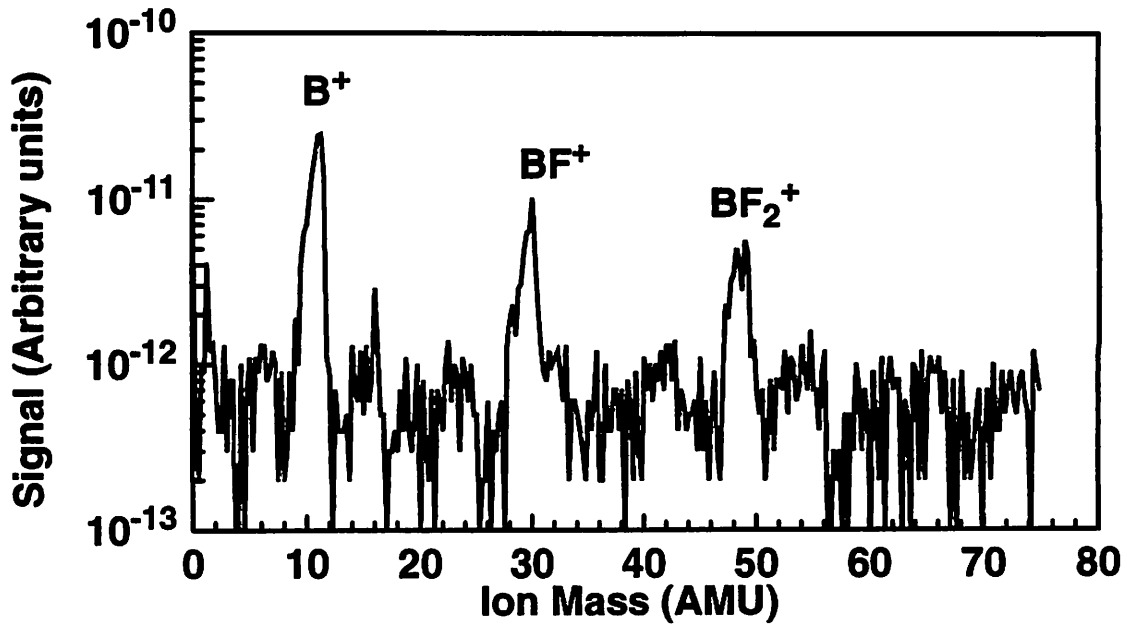


Figure 4-8. Mass spectrum of BF_3 plasma ionized species

Mass spectrum of ionized species in a BF_3 plasma at 1mtorr 900W microwave power.

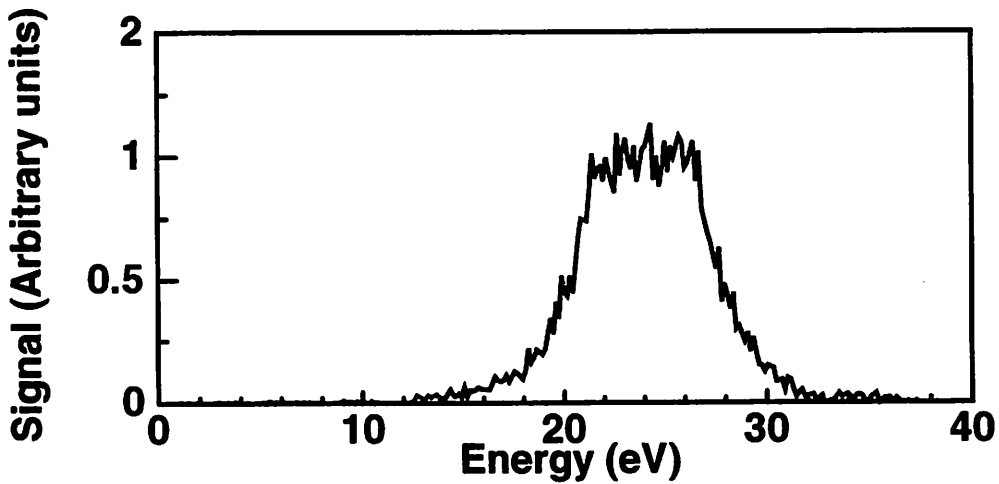


Figure 4-9. Energy spectrum of B^+ ions

The energy spectrum of B^+ ions in a BF_2 plasma at 1mtorr and 900W microwave power.

4.4.2. Ferran micropole mass spectrometer

Another mass spectrometer used was the Ferran Micropole. The Ferran Micropole

is a quadrupole mass spectrometer of only 1cm in length. This allows the micropole to operate without differential pumping up to pressures as high as 5 mtorr. Using this small mass spectrometer, the mass spectra of BF_3 neutrals can be determined as shown in Figure 4-10. The ionized spectrum is similar to the spectrum obtained by the CMA mass spectrometer in Figure 4-7. One drawback of this system is that it cannot measure the energy spectra of the species and cannot detect the ionized species in the plasma because the ionizer cannot be turned off and the system is biased to a potential too high for any plasma ions to enter into the system.

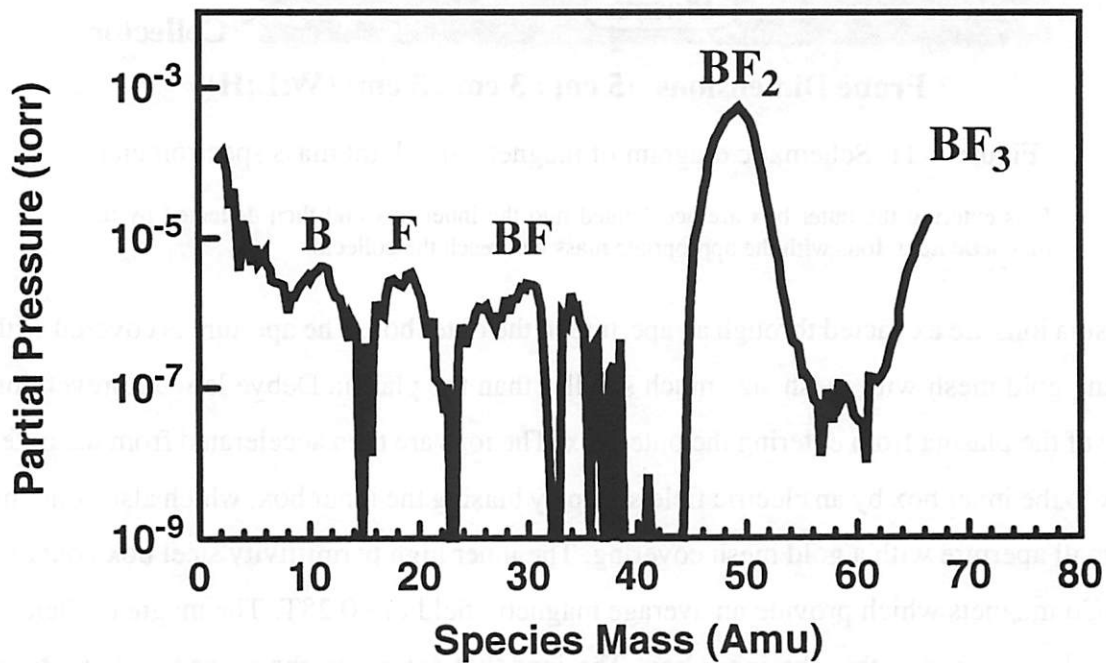
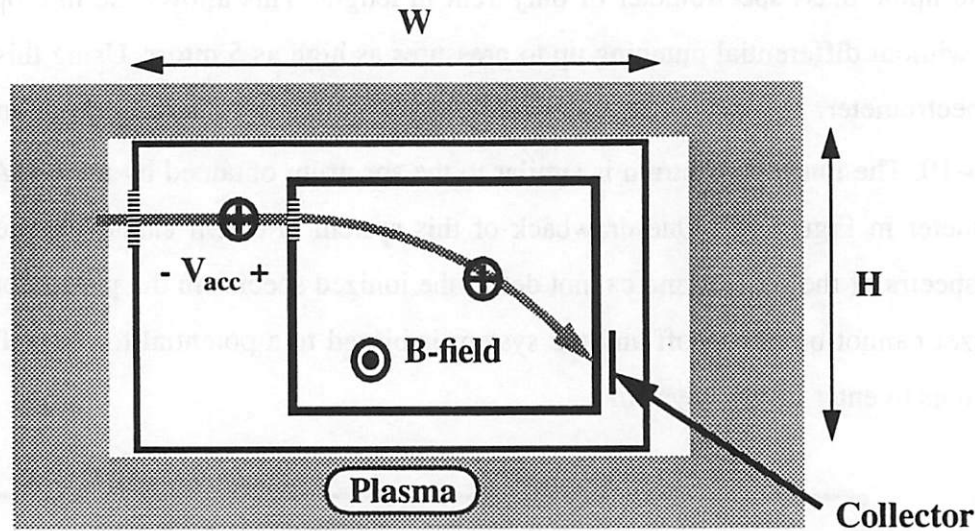


Figure 4-10. BF_3 Mass spectrum with Ferran micropole

Neutral species mass spectrum for a BF_3 plasma 1mtorr 900W microwave power.

4.4.3. Magnetic sector mass spectrometer

A third mass spectrometer was assembled to monitor the ionized species from within the plasma at relatively high pressures (up to 5mtorr). This mass spectrometer was constructed after a design by Tuzewski with some modifications [4.7]. As illustrated in Figure 4-11, this mass spectrometer consists of two metallic boxes separated by teflon insulation. The outer aluminum box is grounded and acts as a shield for the inner box. The



Probe Dimensions: (5 cm : 3 cm : 3 cm) (W:L:H)

Figure 4-11. Schematic diagram of magnetic quadrant mass spectrometer

Ions entering the outer box are accelerated into the inner box and then deflected by the magnetic field. Ions with the appropriate mass will reach the collector.

plasma ions are extracted through an aperture in the outer box. The aperture is covered with a fine gold mesh with mesh size much smaller than the plasma Debye length, preventing any of the plasma from entering the outer box. The ions are then accelerated from the outer box to the inner box by an electric field set up by biasing the inner box, which also contains a small aperture with a gold mesh covering. The inner high permittivity steel box contains SmCo magnets which provide an average magnetic field of $\sim 0.28\text{T}$. The magnetic field is entirely confined within the inner box. The ions that enter into the inner box have been accelerated and are bent by the perpendicular magnetic field. The radius of curvature of the ions follows:

$$\rho = 0.144 (EA/Z)^{1/2}/B \quad [4-3]$$

where ρ , E , A , Z , and B are the radius of curvature (mm), Ion Energy ($E = V_{\text{acc}}$ (Volts)), ion to proton mass ratio, charge state of the ion, and magnetic field strength (Tesla) respectively. For this mass spectrometer, when the ion to proton mass ratio times the accelerating voltage is equal to $\sim 960\text{V}$, then the ions will reach the collector at the far side of the inner box. A scan of the ion masses is obtained by scanning V_{acc} . Figure 4-12 shows the mass

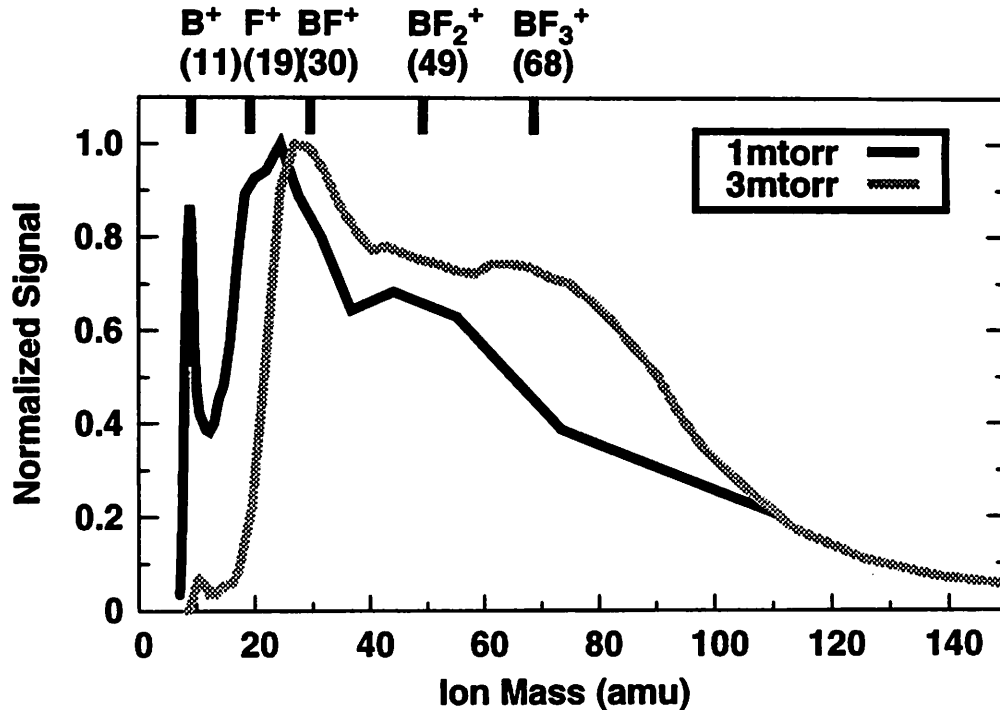


Figure 4-12. BF_3 mass spectrum using magnetic quadrant

The mass spectrum for 1mtorr and 3mtorr BF_3 plasmas both with 900W microwave power.

spectrum collected for a BF_3 plasma at 1mtorr and 3mtorr for 900W microwave power. At higher pressure, the B^+ ion concentration is reduced while BF_2^+ and BF_3^+ relative ion concentrations are increased. The 1mtorr spectrum is similar in shape to the 1mtorr ionized spectrum obtained with the CMA mass spectrometer in Figure 4-8.

This mass spectrometer allows direct measurement of the relative ion densities in the plasma. Unfortunately, as Figure 4-12 shows, this mass spectrometer works best at low ion masses below 20 amu. Above this level, the mass resolution degrades rapidly, making the relative ion concentrations difficult to determine.

4.4.4. Conclusions

By using a variety of different mass spectrometers, the plasma species and energies can be observed. Using the large external mass spectrometer, the ion energy spectra and both neutral and ionized species spectra can be determined at low pressure. The Ferran

micropole system can quickly determine the neutral species in the plasma by using a miniature quadrupole mass analyzer. The magnetic sector system can directly measure the ions in the plasma, but it suffers from low mass resolution at high ion masses.

4.5. Secondary Electron Measurements

4.5.1. Introduction

Plasma processing, whether etching or deposition, uses ion bombardment of solids which can generate secondary electrons. The secondary electrons generated on plasma exposed surfaces can play an important role in determining the charging damage that occurs. One way to quantify the secondary electron emission is through the secondary electron yield (γ), defined as the average number of electrons emitted per incident ion.

A variety of studies have measured the secondary electron yield of various materials [4.8,4.9,4.10]. Most use atomically clean surfaces in ultra high vacuum to eliminate the effect of the surface condition. However, for plasma exposed surfaces, the plasma changes the surface and typically increases the secondary electron yield as compared to an atomically clean surface [4.11]. For plasma exposed surfaces, studies by Rocca and Szapiro measured the secondary electron yield for a variety of materials in cold cathode discharges using argon, neon, or helium carrier gases [4.12,4.13]. Also, the secondary electron yields of metallurgical materials were measured during plasma implantation of nitrogen or oxygen [4.14].

Most secondary electron measurement techniques so far use a single ion energy and determine the secondary electron yield at that energy. To determine the dependence of the secondary electron yield on ion energy, the experiment must measure the secondary electron yield for each energy of interest. From a single measurement, our new procedure determines the dependence of the secondary electron yield on ion energy for a range of ion energies.

Plasma implantation is a process where a target, immersed into a plasma, gets implanted by the ion species in the plasma. A high voltage negative bias applied to the target provides an accelerating potential for the plasma ions, giving them the necessary

energy to implant. Many potential applications for this technology exist in both metallurgical [4.15,4.16] and semiconductor areas [4.17,4.18]. To predict the implantation dose from a measurement of the target current, the secondary electron yield and its dependence on ion energy are required.

4.5.2. Secondary electron yield measurement

Our procedure determines the secondary electron yield of a plasma exposed material by applying a high voltage negative pulse to a target with unknown secondary electron yield. The measured current due to the pulse contains current components from the impinging ions and the secondary electrons. Therefore, if the ion current can be predicted and the two components are separated from the measured data, then the secondary electron yield as a function of ion energy can be determined.

Using a model of the plasma currents, the secondary electron yield can be extracted from the measured voltage and current waveforms. The analytical plasma model, which will be discussed in Chapter 6, analytically determines the plasma ion, plasma electron, and displacement currents [4.19,4.20]. If the secondary electron yield is known a-priori, then the model can accurately determine the total current generated.

For an unknown surface, the only current component not known is the secondary electron current. Using the plasma model the plasma ion, electron and displacement currents can be removed from the measured current waveform, leaving behind the secondary electron current. And from the secondary electron current and the voltage waveform, the secondary electron yield can be found.

Extracting the secondary electron yield requires several steps. The first step is the measurement of the current generated by the negative voltage applied to the target material. Figure 4-13 shows the measured bias and current for a film of sputtered aluminum on a silicon wafer in an argon plasma. This bias waveform is then input into the plasma model to determine the ion, electron, and displacement currents. The relations for the ion current density and displacement current density are independent of the target material, and thus do not require knowledge of the secondary electron yield of the material. The only other

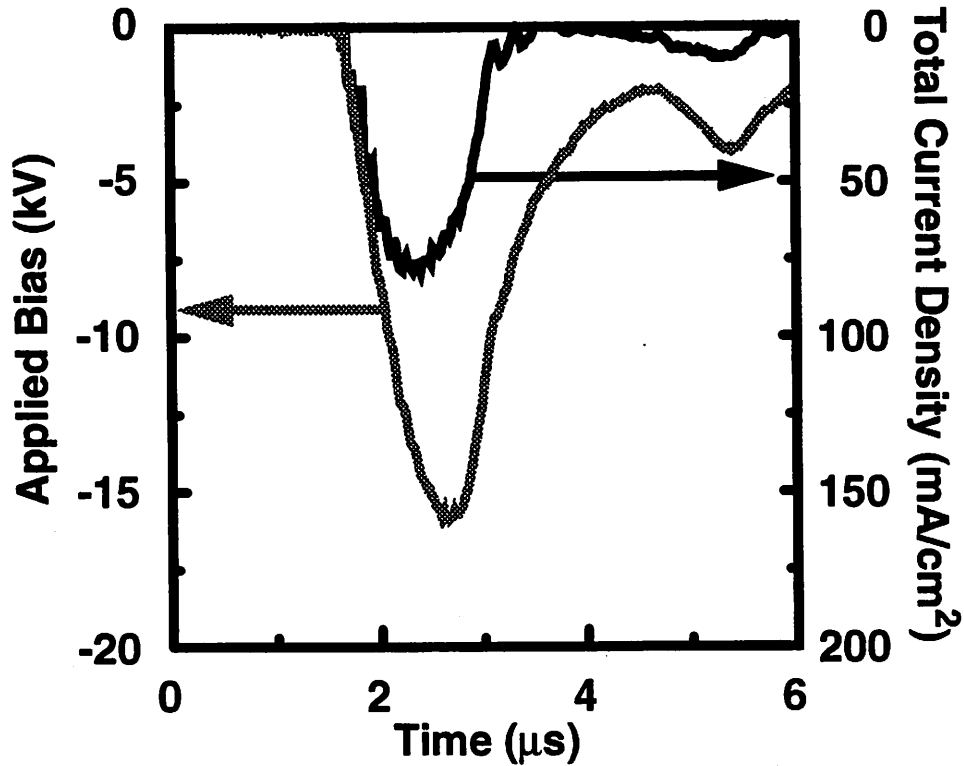


Figure 4-13. Measured bias and total current density of an aluminum target in an argon plasma

Measured applied bias and total current density for an evaporated aluminum target. The argon plasma conditions are: ion density = $4 \times 10^{10} \text{cm}^{-3}$, electron temperature = 4 eV, plasma potential = 18V, and floating potential = -6V.

parameters required are from the plasma which are the ion density (n_i), electron temperature (T_e), plasma potential (V_p), and floating potential (V_f). By using only the measured plasma condition and the measured applied voltage, the ion current and displacement current as a function of time are determined.

The large negative applied bias generates a large potential barrier to all electrons in the plasma, preventing them from reaching the target. Therefore, the plasma electron current remains negligible in the determination of the secondary electron yield. However, the plasma electron current is included in the formalism for completeness.

Once the model calculates the plasma ion, displacement, and plasma electron currents, the secondary electron current as a function of time can be extracted by subtracting all of the known components from the measured total current density:

$$j_{\text{sec}}(t) = j_{\text{total}}(t) - j_i(t) - j_{\text{disp}}(t) - j_e(t) \quad [4-4]$$

Then to extract the secondary electron yield, the secondary electron current density and plasma ion current density are used:

$$\gamma(t) = j_{\text{sec}}(t) / j_i(t) \quad [4-5]$$

Now, the ion energy as a function of time must be determined. The ion energy as a function of time equals the sheath voltage as a function of time:

$$E_{\text{ion}}(t) = qV_{\text{sheath}}(t) = q(V_{\text{bias}}(t) - V_p) \quad [4-6]$$

Since the secondary electron yield and the ion energy are known as functions of time, the secondary electron yield as a function of ion energy results from using time as a parametric parameter.

4.5.3. Experimental results

The aforementioned technique has been used to determine the secondary electron yield of several electronic materials used in the semiconductor industry. As an initial test, the measured secondary electron yield of aluminum with argon ions was compared to previous secondary electron yield results by Rocca [4.13]. The test used a 100mm diameter silicon wafer with 1 μ m of sputter deposited aluminum as a planar target to measure the total current and applied voltage pulse. To reach a surface in equilibrium with the argon implantation, the target requires several minutes of implantation. To check that the surface reaches equilibrium, multiple measurements of the current pulse over several minutes were compared. Then using the measured plasma parameters, the simulator determined the ion energy, ion current, and secondary electron current for the applied voltage pulse. From the simulator results, Figure 4-14 shows the extracted secondary electron yield as a function of ion energy. Experimental data from Szapiro and Rocca's experiment with aluminum exposed to an argon discharge correlates with the experimental data.

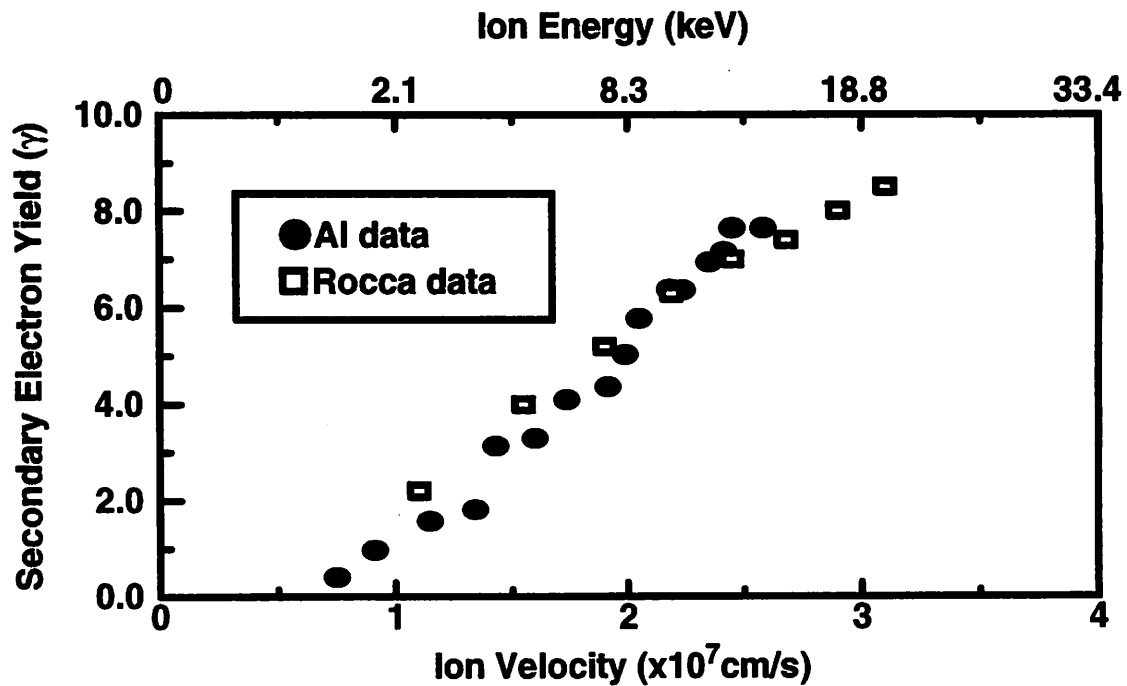


Figure 4-14. Secondary electron yield for aluminum.

Extracted secondary electron yield for sputtered aluminum shows good agreement with previous experimental data reported by Rocca [4.13]. Plasma conditions are the same as in Figure 4-13.

The secondary electron yield was also measured for three other materials: single-crystal <100> silicon, silicon dioxide, and titanium nitride due to argon bombardment. The single-crystal silicon sample consisted of a bare silicon wafer dipped in HF to remove the native oxide. The SiO₂ and TiN targets consisted of a film of 200nm thermally-grown oxide on a silicon wafer and of a film of sputter-deposited TiN on a silicon wafer respectively. Figure 4-15 shows the secondary electron yield of each material as a function of ion velocity. For these measurements of the secondary electron yield the error was found to vary from 55% to 6% as calculated from the measured variance in the total current and ion density. The error decreased with increasing ion energy, having a minimum at the peak ion energy.

The ion energy of the Si, Al, and TiN targets is equated to the difference between the plasma potential and the surface potential because the applied voltage is directly con-

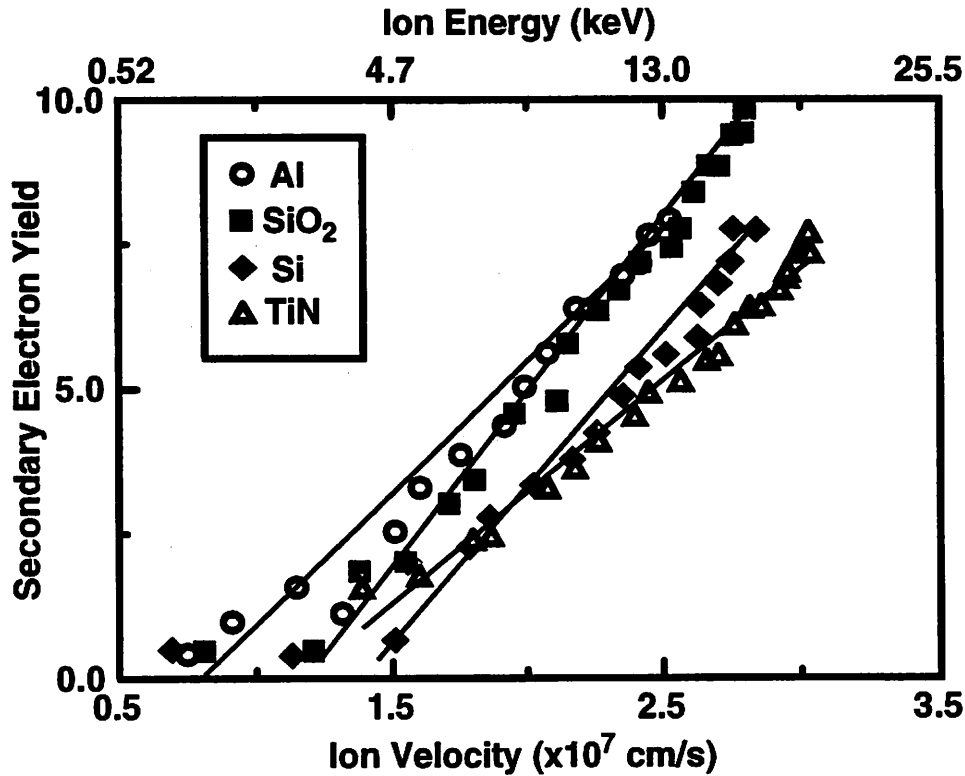


Figure 4-15. Extracted secondary electron yield.

Extracted secondary electron yield for aluminum, silicon dioxide, silicon, and titanium nitride as a function of ion velocity. Plasma conditions are the same as in Figure 4-13.

nected to the conducting surface. However with the SiO₂ target, some of the applied voltage drops across the capacitance of the insulating oxide, reducing the sheath voltage and the ion energy. This reduction is taken into account by the model since it uses the calculated sheath voltage as the ion energy instead of the applied bias.

Previous studies of the secondary electron yield of materials have shown that the secondary electron yield depends linearly on the ion velocity for the energy range used in this study [4.21]. For all of the materials used in this study, the secondary electron yield as a function of ion velocity correlated to a linear fit (Table I).

4.6. Conclusions

By using several measurement techniques, a comprehensive picture of the plasma characteristics can be developed. The simple common Langmuir probe technique is used

to determine such plasma parameters as ion density, electron density, plasma potential and floating potential from probe I-V characteristics. The plasma neutral and ion composition can be qualitatively found by the non-invasive technique of optical emission spectroscopy. For quantitative neutral and ion composition results, mass spectrometers with varying capabilities have been employed. A method of determining the secondary electron yield of materials exposed and bombarded by a plasma is developed. This method is useful for characterizing the secondary electron yield in low pressure processes, such as those used in many high density sources: ICP, ECR, Helicon, and Helical Resonator. This technique can also be used to extract the secondary electron yield of fresh samples and determine the evolution of the secondary electron yield during plasma processing. All of these techniques will be utilized in the following chapters as we analyze the physical mechanisms of charging damage.

References

- [4.1] M. Suto, C. Ye, and L.C. Lee, "Photoabsorption and fluorescence spectroscopy of BF_3 in the extreme-vacuum-ultraviolet region", The American Physical Society, vol. 42, no. 1, pp. 424 - 431, 1990.
- [4.2] E. Hesser and K. Dressler, "Radiative Lifetimes of Ultraviolet Emission Systems Excited in BF_3 , CF_4 , and SiF_4 ", The Journal of Chemical Physics, vol. 47, no. 9, pp. 3443-3450, 1967.
- [4.3] J.C. Creasey, et. al., "Vacuum UV fluorescence excitation spectroscopy of BF_3 in the range 45-125nm", Molecular Physics, vol. 78, no. 4, pp. 837-854, 1993.
- [4.4] Th. Glenewinkel-Meyer, et. al., "Emission spectra and electronic structure of group IIIa monohalide cations", Journal of Chemical Physics, vol. 89, no. 12, pp. 7112-7125, 1988.
- [4.5] J. Reader and C.H. Corliss, Wavelengths and Transition Probabilities for Atoms and Atomic Ions. Part I, NSRDS-NBS 68 (1980)
- [4.6] B Shieh, internal correspondence
- [4.7] M Tuzewski, "A Compact Mass Spectrometer for Plasma Discharge Ion Analysis" submitted to Review of Scientific Instruments.
- [4.8] E. V. Alonso, R. A Baragiola, J. Ferron, M. M. Jakas, and A. Oliva-Florio, "Z Dependence of Ion-Induced Electron Emission from Aluminum", Physical Review B, vol 22, pp. 80-87, 1980.
- [4.9] M. Delaunay, M. Fehringer, R. Geller, D. Hitz, P. Varga, and H. Winter, "Electron Emission from a Metal Surface Bombarded by Slow highly Charged Ions", Physical Review B, vol. 35, pp. 4232-4235, 1987.

- [4.10] B. Svensson and G. Holmen, "Electron Emission from Ion-Bombarded Aluminum", *J. Applied Physics*, vol. 52, no. 11, pp. 6928-6931, 1981.
- [4.11] J. Ferron, E.V. Alonso, R. A. Baragiola and A. Oliva-Florio, "Ion-electron Emission: The Effect of Oxidation", *Surface Science*, vol. 120, pp. 427-434, 1982.
- [4.12] B. Szapiro, J. J. Rocca, and T. Prabhuram, "Electron Yield of Glow Discharge Materials under Helium Ion Bombardment", *Applied Physics Letters*, vol. 53, no. 5, pp. 358-360, 1988.
- [4.13] B. Szapiro and J. J. Rocca, "Electron Emission from Glow-discharge Cathode Materials due to Neon and Argon Ion Bombardment," *J. Applied Physics*, vol. 65, no. 9, pp. 3713-3716, 1989.
- [4.14] J. R. Conrad, "Plasma Source Ion Implantation: A New Approach to Ion Beam Modification of Materials," *Proceedings of the 6th International Conference on Surface Modification of Metals by Ion Beams*, Rival del Garda, Italy, pp. 197-203, 1988.
- [4.15] J. R. Conrad and T Castagna, "Plasma Source Ion Implantation for Surface Modification," *Bull. Am. Phys. Soc.*, vol. 31, no. 9, p. 1479, 1986.
- [4.16] M. M. Shamim, J. T. Scheuer, R. P. Fetherston, and J. R. Conrad, "Measurement of Electron Emission Due to Energetic Ion Bombardment in Plasma Source Ion Implantation", *J. Applied Physics*, vol. 70, no. 9, pp. 4756-4759, 1991.
- [4.17] N. W. Cheung, "Plasma Immersion Ion Implantation for ULSI Processing," *Nuclear Instruments & Methods in Physics Research, Section B*, vol. B55, pp. 811-820, 1991.
- [4.18] N. W. Cheung, W. En, E. C. Jones and C. Yu, "Plasma Immersion Ion Implantation of Semiconductors," *MRS Symp. Proc. Boston, MA*, 1992.
- [4.19] W. En, M. A. Lieberman, and N. W. Cheung, "Comparison of Experimental Target Currents with Analytical Model Results for Plasma Immersion Ion Implantation," *IEEE Transactions on Plasma Science*, vol. 23, no. 3, pp. 415-421, 1995.
- [4.20] W. En and N. W. Cheung, "Analytical Modeling of Plasma Immersion Ion Implantation Target Current using the SPICE Circuit Simulator," *J. Vac. Sci. and Tech. B*, pp. 956-9612, 1994.
- [4.21] E. V. Alonso, R. A. Baragiola, J. Ferron, M. M. Jakas, and A. Oliva-Florio, "Z Dependence of Ion-Induced Electron Emission from Aluminum", *Physical Review B*, vol. 22, pp. 80-87, 1980.

5 Plasma Immersion Ion Implantation

5.1. Introduction

In our study of oxide charging damage, we examined an emerging implantation process called Plasma Immersion Ion Implantation (PIII). PIII was chosen because it both implants ions and exposes the devices to a plasma, allowing us to examine the effect of the plasma, ion implantation, and their interactions on charging damage. In addition, this new process allows us to examine the phase-space for PIII conditions where charging damage can be minimized or eliminated.

5.2. PIII Concept

PIII offers a variety of unique features as compared to conventional ion implantation. Some of the advantages of PIII include non-line-of-sight implantation, high current capability at low ion energy, and simple machine design.

Conventional ion implantation is a standard doping technique used in semiconductor manufacturing. Implantation has also been used to modify the surface properties of materials to improve their resistance to wear, corrosion and fatigue. However, conventional ion implanters require complex optics to scan a narrow ion beam across the target to achieve implantation uniformity.

The PIII process, on the other hand, implants the entire wafer simultaneously by immersing the target into a plasma containing the ion species to be implanted. The ions are extracted from the plasma directly and are accelerated by applying negative high-voltage pulses to the target as illustrated by Figure 5-1. The plasma forms a small ion sheath around the target to maintain a steady-state equilibrium of charge flow with the target. High voltage negative pulses applied to the target cause the sheath to expand rapidly and the uncov-

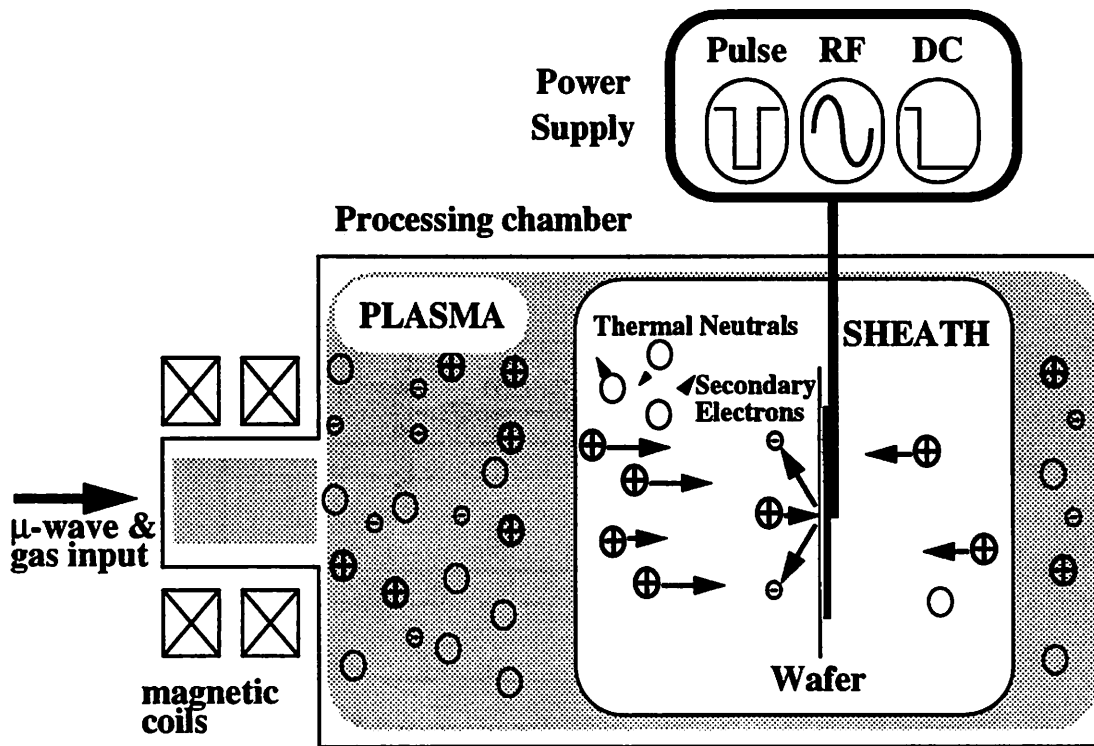


Figure 5-1. PIII concept

Schematic of plasma immersion ion implantation showing conformity of the plasma sheath to the wafer surface. Ions from the plasma accelerate across the sheath and implant.

ered ions accelerate across the sheath and implant into the target. By repeating the pulses, the required dose is implanted. Both metallurgical [5.1,5.2] and semiconductor [5.3,5.4] implantation processes have been demonstrated using PIII.

5.3. UC Berkeley Reactor Configuration

The PIII reactor developed in the Plasma Assisted Materials Processing Lab is shown schematically in Figure 5-2. Microwave power from a 2.45 GHz, 1500W microwave power supply is routed by waveguides, and is fed through a TE_{10} rectangular to TM_{01} circular mode converter into the ECR source chamber through a quartz window. The plasma is generated inside the source chamber. Surrounding the source chamber are two magnets in a mirror configuration. Within the source chamber, there is a zone at 875 gauss which is the magnetic field needed for the electrons to resonate with the 2.45Ghz micro-

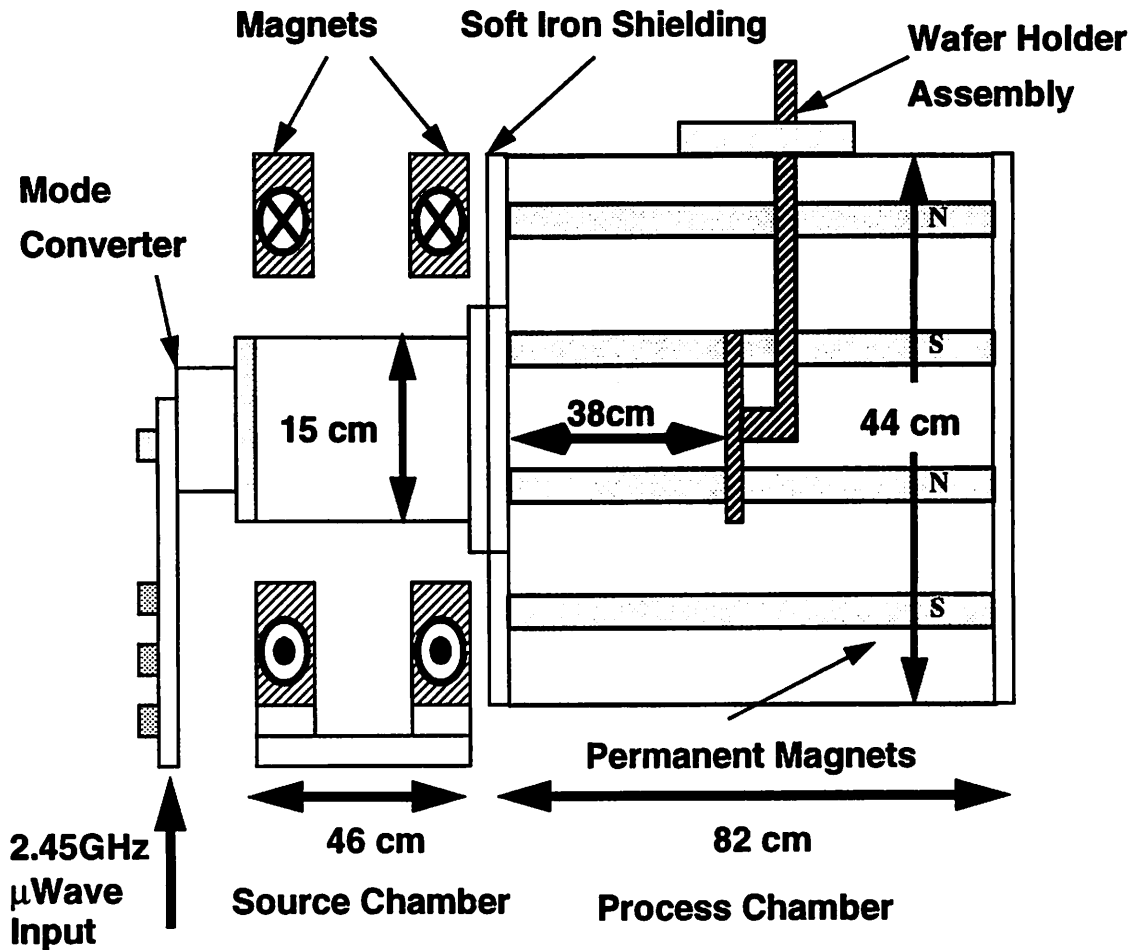


Figure 5-2. PIII reactor schematic

Schematic of PIII system at UC Berkeley Plasma Assisted Materials Processing Lab.

waves. The plasma density is varied by altering the microwave power, process gas pressure, or magnetic field configuration. The plasma flows from the source chamber into an 44cm diameter processing chamber surrounded by lines of permanent magnets to create a magnetic bucket on the chamber walls to improve the uniformity of the plasma and to reduce the wall losses. Uniformity of the ion density of an Ar plasma has been measured by Langmuir probe measurements as $\pm 2\%$ across 8 inches [5.5]. Process gas enters near the quartz microwave input window via a ring of pinholes and the gaseous by-products leave the chamber through turbomolecular and mechanical pump systems. The chamber has a base pressure of 10^{-7} torr before processing. Typical process gas pressures used in this study are in the 0.2 to 5 mTorr range. Single or multiple-wafer holders up to 25 cm in

diameter can be located 20-45 cm away from the source chamber in the 82 cm long process chamber allowing the system to be compatible with both single wafer cluster tools and large-area implantation.

5.4. PIII Applications

A wide variety of applications have been developed for PIII, from metallurgical applications, such as nitridation of artificial hip joints, to semiconductor applications, such as shallow junction formation. These applications take advantage of PIII's ability to implant conformally and at low energy with high dose rate.

5.4.1. Metallurgical origins

The concept of plasma implantation began with Conrad et al. with metallurgical applications in the late 1980s [5.1,5.2]. Nitrogen was conformally implanted into drill bits and other non-planar metal objects to harden the surface by nitridation[5.6]. PIII can easily provide the high energy (~100keV) and high doses (10^{16} - $10^{18}/\text{cm}^2$) necessary to form the nitride surface layer.

5.4.2. Semiconductor applications (trenches, Cu plating, doping, TFTs SOI)

In addition to metallurgical applications, PIII has also been used for semiconductor applications. Some of the processes investigated with PIII include conformal trench doping, palladium seeding for selective electroless copper plating, shallow junction formation, and buried oxide formation.

5.4.2.1. Conformal trench doping

High aspect ratio trenches provide a large surface area for charge storage in DRAM applications and still allow very high packing densities. For conventional ion implantation, implanting such a trench is a challenge. Since conventional implantation is line of sight, complex tilt and rotation of the wafer is necessary to implant all sides of the trench without shadowing.

PIII has been demonstrated to conformally dope extremely high aspect ratio trenches. Conformal trench doping was first demonstrated by Qian et al. in 1991 [5.7]. Uni-

form doping of both sidewalls and bottom of trenches was achieved for trenches with 6:1 aspect ratio. Later work demonstrated conformal doping of trenches with 12.5:1 aspect ratio as shown in Figure 5-3 [5.8].

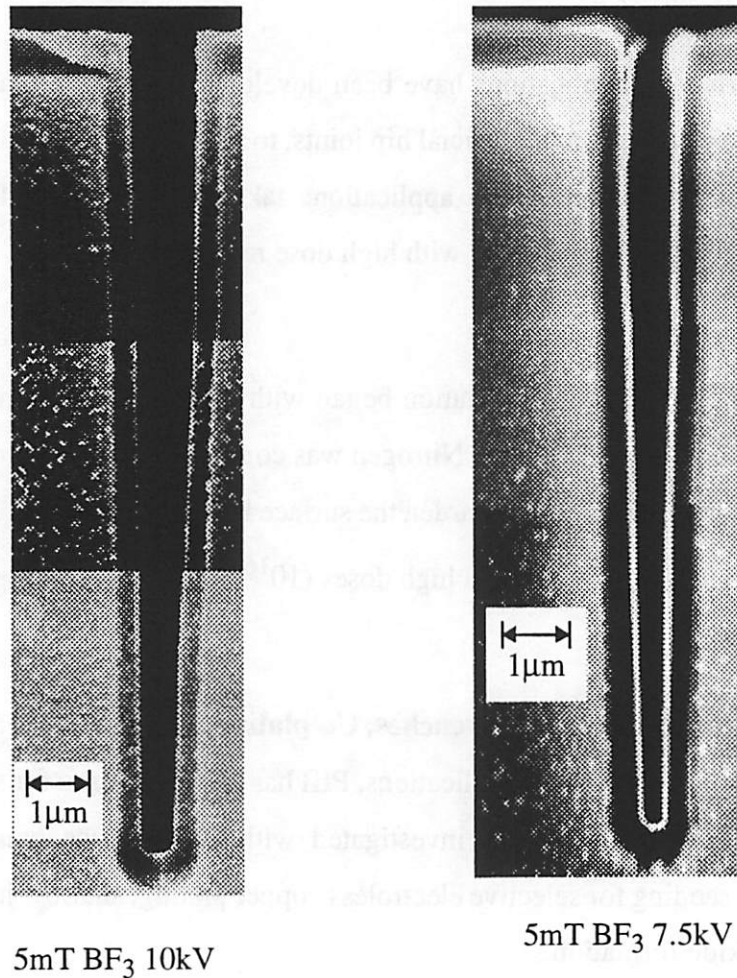


Figure 5-3. Conformal trench doping

SEM angled lapped cross-section of 12.5:1 aspect ratio trenches showing conformality of the doping

5.4.2.2. Pd seeding for selective electroless copper plating

As IC interconnects continue to scale down, smaller interconnect lines will be needed to reduce line delays due to parasitic capacitances. Current aluminum alloys are limited in minimum line width by resistance and electromigration concerns. An alternative interconnect metal is copper. Copper has much better electromigration properties [5.9] and

lower impedance than Al/Cu/Si alloys. Unfortunately, copper is difficult to plasma etch because of the lack of volatile etch products. Instead, copper interconnect lines must be selectively deposited to avoid the need for patterning a blanket copper layer.

PIII has been demonstrated to form a Pd seed layer in oxide trenches, allowing selective electroless copper plating to fill the trench [5.10]. To make the copper lines, the PIII system is setup in a triode fashion to allow sputtering of a Pd plate by argon ions as shown in Figure 5-4. The sputtered Pd is ion mixed at the bottom of the oxide trench. Sub-

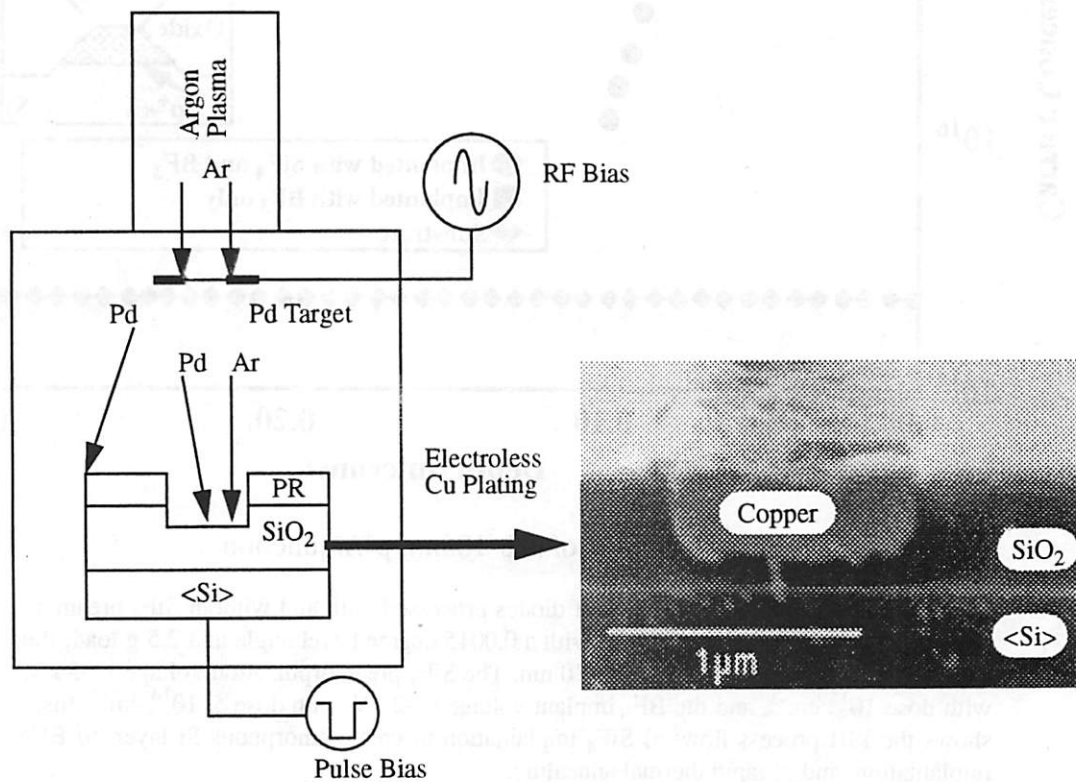


Figure 5-4. Pd seeding for electroless copper plating

By using the PIII system in a triode fashion, Pd atoms can be sputtered off a Pd target using an argon plasma. The Pd atoms are ion mixed at the bottom of the SiO₂ trench.

sequently, the Pd layer at the bottom of the trench acts as a seed layer for electroless copper plating, forming a copper interconnect as shown in Figure 5-4. Good electrical and mechanical characteristics were found for the copper layer [5.11].

5.4.2.3. Shallow junction formation.

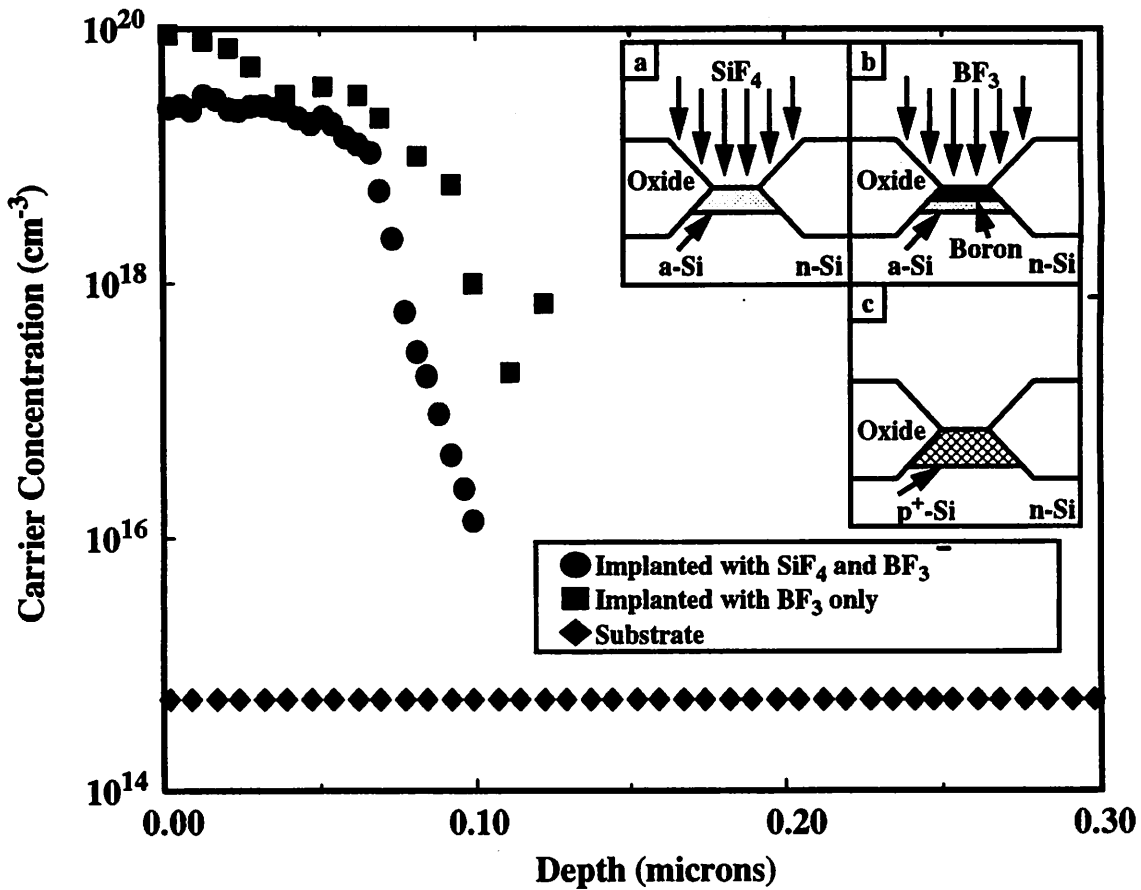


Figure 5-5. SRP of sub-100nm p⁺/n junction

Spreading resistance (SRP) profiles of diodes processed with and without SiF₄ preamorphization step. SRP analysis is done with a 0.0015 degree bevel angle and 2.5 g load; the expected error in junction depth is 3-10 nm. The SiF₄ preamorphization voltage is -5 kV, with dose 10¹⁵ cm⁻³, and the BF₃ implant voltage is -2 kV, with dose 5x10¹⁴ cm⁻³. Inset shows the PIII process flow: a) SiF₄ implantation to create amorphous Si layer, b) BF₃ implantation, and c) rapid thermal annealing.

As devices continue to scale down, shallower source and drain junctions will be needed. Conventional ion implantation cannot easily implant ions below 10keV due to low beam currents. Unfortunately implantation must be around 1-5 keV to form sub-100nm junctions, which will be needed for sub-0.18 μm channel IC technologies and beyond.

A variety of alternative methods have been developed to form the necessary shallow junctions. Dopants can be introduced into an overlayer of polysilicon and diffused to form the junction [5.12,5.13,5.14,5.15]. Also, molecular layer doping [5.16,5.17] and laser

techniques such as pulsed excimer laser deposition, gas immersion laser doping (GILD), and projection-gas immersion laser doping (P-GILD) have shown promising results [5.18,5.19].

PIII has also been used to form p+/n shallow junctions. PIII can implant large doses with high throughput at energies from 1-5keV down to as low as 50eV. Sub-100nm junctions have been demonstrated using PIII. Qian et al. demonstrated sub-100nm p⁺/n junctions using a SiF₄ plasma preamorphization implant and a BF₃ plasma implant [5.20]. In latter work in 1992, by Jones et al., low area leakage 80nm p⁺/n junctions were formed as shown by spreading resistance profiling (SRP) in Figure 5-5 [5.21]. The total area reverse bias leakage current was 3nA/cm² at -5V reverse bias. For the PIII implant conditions used, the implant dose of 2x10¹⁵/cm² could be theoretically done in about 10sec. Therefore, PIII has been shown to form high quality shallow junctions and can form those junctions with higher throughput than conventional ion implantation.

5.4.2.4. Uniformity of the PIII implant

Since PIII implants the entire wafer simultaneously, the uniformity of the implant is achieved by having a uniform implant current over the entire wafer. A conventional implanter achieves uniformity by scanning the ion beam across the wafer, which cannot be done with PIII. By ensuring a uniform plasma, Felch et al. has shown that the PIII process can consistently achieve an implant with 1.5% uniformity and 2.4% wafer to wafer standard deviation as shown in Figure 5-6 [5.22]. Thus PIII can achieve comparable uniformity as a conventional ion implanter.

5.4.2.5. SPIMOX

Silicon on insulator (SOI) type devices offer a variety of advantages over conventional junction isolated ones. The advantages include alpha particle radiation hardness and latch-up immunity [5.23]. The first devices of this type were fabricated on silicon on sapphire (SOS) wafers. Due to high expense, this technique is not used for commercial purposes. Recently, SOI wafers have been fabricated using conventional ion implantation of oxygen and subsequent high temperature annealing, which is called Separation by IMplan-

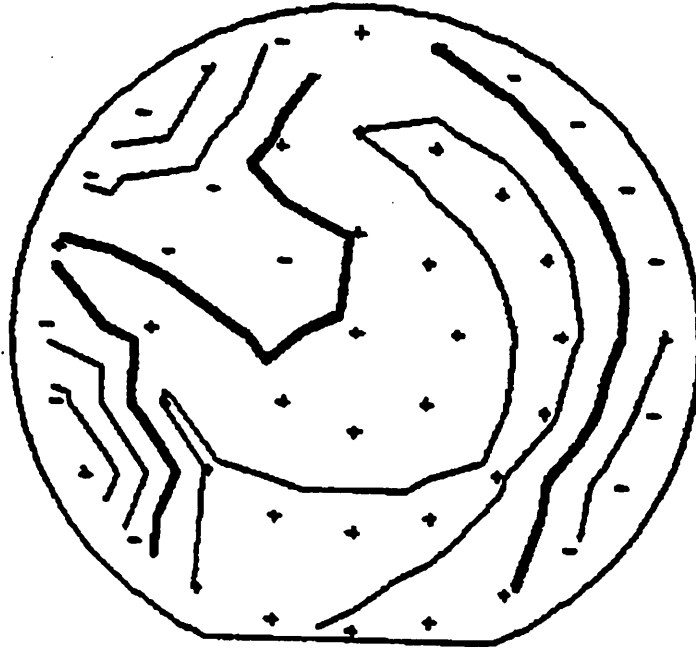


Figure 5-6. Uniformity of PIII

Spreading resistance map of BF_3 implant on an 8" wafer, with measurements out to 7.5" diameter. (Mean = $362 \Omega/\text{sq.}$, Standard Deviation = 1.32%, Wafer to wafer = 2.4%)

tation of OXYgen (SIMOX). Single crystal silicon overlayers with very uniform thickness have been made [5.24,5.25]. However, long implant times are required to implant the necessary dose of 10^{17} to $10^{18}/\text{cm}^2$, resulting in high cost per wafer. The implantation time will increase with larger wafer sizes.

PIII has been demonstrated to form single crystal silicon over a buried oxide layer using a process called Separation by Plasma IMplantation of OXYgen (SPIMOX) [5.26,5.27]. PIII can implant the entire wafer simultaneously which allows a constant implant time for larger wafer sizes, resulting in an increasing time savings over conventional implantation with larger wafer sizes. By implanting with a DC bias the necessary dose of $10^{16}/\text{cm}^2$ can be implanted in about 2 minutes. Figure 5-7 shows a TEM of the SPIMOX formed so far at UC Berkeley [5.28].

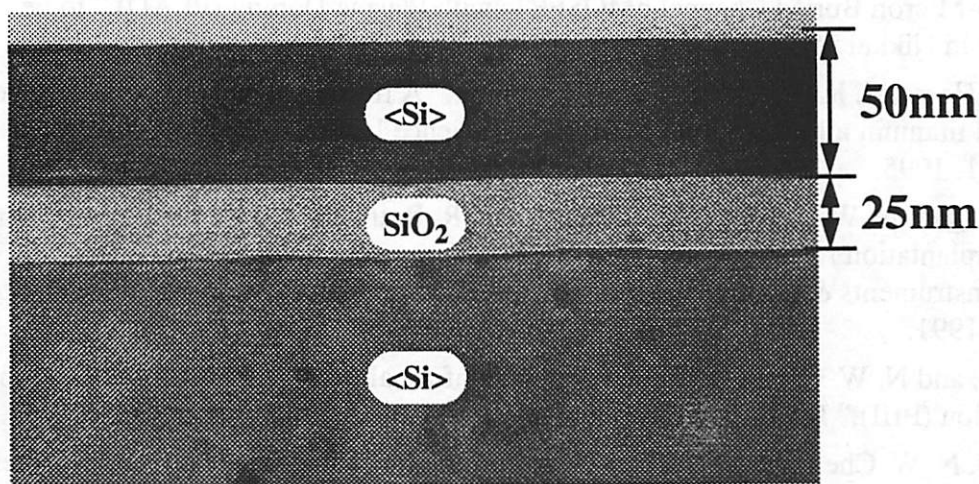


Figure 5-7. SPIMOX

TEM of buried oxide layer formed by 60keV bias O₂ plasma and 3 hrs 1300°C N₂ anneal.

5.5. Conclusions

So PIII can provide a uniform, high dose, and high throughput implant for semiconductor applications. Moving on from its metallurgical origins, PIII has been shown to have a variety of semiconductor applications. Conformal doping of high aspect ratio trenches as well as Pd seeding for selective electroless copper plating have been demonstrated. Shallow junction formation has also been demonstrated and is currently being converted into a commercial product for this purpose. In addition, current work in fabrication of SOI wafers is promising. To fully develop PIII, the charging damage issues must be understood.

References

- [5.1] J. R. Conrad, and T Castagna, "Plasma Source Ion Implantation for Surface Modification," Bull. Am. Phys. Soc., vol. 31, no. 9, pp.1479, 1986.
- [5.2] M. M. Shamim, J. T. Scheuer, R. P. Fetherston, and J. R. Conrad, "Measurement of Electron Emission Due to Energetic Ion Bombardment in Plasma Source Ion Implantation," J. Applied Physics, vol. 70, no. 9, pp. 4756-4759, 1991.
- [5.3] N. W. Cheung, "Plasma Immersion Ion Implantation for ULSI Processing," Nuclear Instruments & Methods in Physics Research, Section B, vol. B55, pp. 811-820, 1991.
- [5.4] N. W. Cheung, W. En, E. C. Jones, and C. Yu, "Plasma Immersion Ion Implantation of Semiconductors," MRS Symp. Proc. Boston, MA, pp. 297-306, 1992.

- [5.5] S. B. Felch, D. P. Brunco, A. Ahmad, K. Prall, and D. L. Chapek, "Formation of Deep Sub-Micron Buried Channel pMOSFETs with Plasma Doping (PLAD)," to be published in *Nikkei Microdevices* 1996.
- [5.6] N. C. Horswill, K. Sridharan, and J. R. Conrad, "A fretting wear study of a nitrogen implanted titanium alloy," *Journal of Materials Science Letters*, vol. 14, no. 19, pp. 1349-1351, 1995.
- [5.7] X. Y. Qian, N. W. Cheung, M. A. Lieberman, R. Brennan, and M. I. Current, "Conformal implantation for trench doping with plasma immersion ion implantation," *Nuclear Instruments & Methods in Physics Research, Section B*, vol. B55, no. 1-4, pp. 898-901, 1991.
- [5.8] C. Yu, and N. W. Cheung, "Trench doping conformality by plasma immersion ion implantation (PIII)," *IEEE Electron Device Letters*, vol. 15, no. 6, :pp. 196-198 1994.
- [5.9] J. Tao, N. W. Cheung, and C. Hu, "Electromigration characteristics of copper interconnects," *IEEE Electron Device Letters*, vol. 14, no. 5, pp. 249-251, 1993.
- [5.10] M-H. Kiang, M. A. Lieberman, N. W. Cheung, and X. Y. Qian, "Pd/Si plasma immersion ion implantation for selective electroless copper plating on SiO₂," *Applied Physics Letters*, vol. 60, no. 22, pp. 2767-2769, 1992.
- [5.11] M-H. Kiang, J. Tao, W. Namgoong, C. Hu, M. A. Lieberman, N. W. Cheung, H. K. Kang, and S. S. Wong, "Planarized copper interconnects by selective electroless plating," *Advanced Metallization and Processing for Semiconductor Devices and Circuits - II. Symposium. Mater. Res. Soc*, pp. 745-755, 1992.
- [5.12] D. L. Kwong, Y. H. Ku, S. K. OLee, E. Louis, N. Alvi, and P. Chu, "Silicided shallow junction formation by ion implantation of impurity ions into silicide layers and subsequent drive-in," *Journal of Applied Physics*, vol. 61, no. 11, pp. :5088-5088, 1987.
- [5.13] C. M. Osburn, S. Chevacharoenkul, Q. F. Wang, and K. Markus, "Materials and device issues in the formation of sub-100-nm junctions," *NIM-B*, vol. B74, no. 1-2, pp. 53-59, 1993.
- [5.14] H. Jiang, C. M. Osburn, P. Smith, and Z. Xiao, "Ultra shallow junction formation using diffusion from silicides. Silicide formation, dopant implantation and depth profiling," *Journal of the Electrochemical Society*, vol. 139, no. 1, pp. 196-206, 1992.
- [5.15] T. Y. Hsieh, H. G. Chun, D. L. Kwong, and D. B. Spratt, "Shallow junction formation by dopant diffusion from in situ doped polycrystalline silicon chemically vapor deposited in a rapid thermal processor," *Applied Physics Letters*, vol. 56, no. 18, pp. 1778-1780, 1990.
- [5.16] J. Nishizawa, K. Aoki, and T. Akamine, "Ultrashallow, high doping of boron using molecular layer doping," *Applied Physics Letters*, vol. 56, no. 14, pp. 1334-1335, 1990.
- [5.17] C. M. Ransom, T. N. Jackson, J. F. DeGelormo, and C. Zeller, "Shallow n+ junctions in silicon by arsenic gas-phase doping," *Journal of the Electrochemical Society*, vol. 141, no. 5, pp. 1378-1381, 1994.
- [5.18] E. Ishida, K. J. Kramer, T. W. Sigmon, and K. H. Weiner, "Doping of and outdiffusion from tungsten silicide films using gas immersion laser doping," *SPIE*, vol. 1804, pp. 87-93, 1993.

- [5.19] K. H. Weiner, and A. M. McCarthy, "Fabrication of sub-40-nm p-n junctions for 0.18 μm MOS device applications using a cluster-tool-compatible, nanosecond thermal doping technique," SPIE, vol. 2091, pp. 63-70, 1994.
- [5.20] X. Y. Qian, N. W. Cheung, M. A. Lieberman, and S. B. Felch, "Plasma immersion ion implantation of SiF_4 and BF_3 for sub-100 nm p+/n junction fabrication," Applied Physics Letters, vol. 59, no. 3, pp. 348-350, 1991.
- [5.21] E. C. Jones, and N. W. Cheung, "Characteristics of sub-100-nm p/sup +//n junctions fabricated by plasma immersion ion implantation," IEEE Electron Device Letters, vol. 14, no. 9, pp. 444-446, 1993.
- [5.22] S. B. Felch, to be published in Nikkei Microdevices
- [5.23] S. Christoloveanu and S. S. Li, Electrical Characterization of Silicon-On-Insulator Materials and Devices, Kluwer Academic Publishers Boston, pp. 1-4, 1995.
- [5.24] J. B. Liu, S. Iyer, J. Min, P. Chu, and N. W. Cheung, "Synthesis of buried oxide by plasma implantation with oxygen and water plasma," 1995 IEEE International SOI Conference Proceedings, pp. 166-167, 1995.
- [5.25] J. Liu, S. Iyer, J. Min; P. Chu, and N. W. Cheung, "Competitive oxidation during buried oxide formation using separation by plasma implantation of oxygen (SPIMOX)," Film Synthesis and Growth Using Energetic Beams. Symposium. Mater. Res. Soc, pp. 385-391, 1995.
- [5.26] J. Liu, S. Iyer, C. Hu, and N. W. Cheung, "Formation of buried oxide in silicon using separation by plasma implantation of oxygen," Applied Physics Letters, vol. 67, no. 16, pp. 2361-2363, 1995.
- [5.27] J. Min, P. K. Chu, Y. C. Cheng, J. B. Liu, and N. W. Cheung, "Buried oxide formation by plasma immersion ion implantation," Materials Chemistry and Physics, vol. 40, no. 3, pp. 219-222, 1995.
- [5.28] S. Iyer, to be published.

6 Coupled Plasma & IC Structure Model

6.1. Introduction

Through our coupled plasma model the physical mechanisms of oxide charging damage in PIII can be found. The model accurately determines the plasma charging currents using only measured physical relations of all the components of the plasma currents. Since the device structure and substrate bias affect the plasma charging currents, models of these are coupled to the plasma to allow the simulation to determine the effect of each and the interactions between them to generate the oxide charging damage.

6.2. Plasma Model

A physical model of the plasma currents during PIII has been developed. The model provides a description of the physical currents and sheath dynamics that occur when the high voltage bias is applied in PIII. From this model, we can determine the total charging currents generated in PIII.

6.3. Background on Plasma Modeling

Previous analytical and numerical models of PIII [6.1,6.2,6.3] have been developed to determine the implantation current, implanted dose, and energy distribution of the implanted ions. The model presented here includes secondary electron current and electron current from the plasma. These additional relations allow our model to simulate the total current that is collected by a target and thus allow us to test the validity of the model with experiment.

The transient sheath expansion has been studied in mercury arc rectifiers by Chester [6.4]. Additional work in PIII transient sheaths, has been investigated experimentally and theoretically by Shamim et al. for spherical and cylindrical geometry [6.5]. The model presented here not only investigates the sheath expansion but also the collapse of the sheath after the voltage pulse has been turned off.

We chose the circuit simulator SPICE [6.6] as the platform to implement the model. SPICE has built-in differential equation solving routines that allow a modular and flexible model to be implemented. In addition, the integrated circuit modeling capabilities of SPICE allow us to calculate the voltages and currents across device structures in the wafer during implantation.

6.4. PIII Model

A negative voltage waveform is applied to a target immersed in a uniform plasma of density n_0 , pushing the electrons away from the target and uncovering positively charged ions. The uncovered ions see the applied voltage and are accelerated to the target. When the waveform is turned off, the sheath collapses, replenishing the depleted plasma in front of the target.

To model the time-varying currents and potentials induced in the plasma before, during and after an applied voltage waveform, we make the following assumptions. A planar geometry is used to model the PIII reactor. Ions within the sheath are accelerated to hundreds of eV, making the transit time on the order of nanoseconds for typical PIII conditions. Therefore the sheath transit time for the ions will be considered to be instantaneous because the voltage pulse time scale is on the order of microseconds. Also, the model assumes a collision-less sheath which is valid at the low neutral gas pressure conditions used (~ 1 mtorr). Since the sheath voltage is much greater than the electron temperature, we will assume that a quasi-static Child Law sheath exists for all times and the ion current is spatially constant within the sheath.

6.4.1. Ion current

The basis of our model is an analytical model by Lieberman and Stewart [6.2]. The Child Law [6.7] current density j_i for a voltage V_s across a collision-less sheath of thickness s is:

$$j_i = \frac{4}{9} \epsilon_0 (2q/M)^{1/2} V_s^{3/2} / s^2 \quad [6-1]$$

where ϵ_0 , q , and M are the free-space permittivity, ion charge, and ion mass respectively. The ion current at the sheath edge is due to the uncovering of ions by the moving sheath and the motion of ions toward the sheath boundary at velocity v_s , which is the ion velocity at the sheath edge normal to the sheath edge:

$$qn_o \left(\frac{ds}{dt} + v_s \right) = j_i \quad [6-2]$$

In this work, we do not use the Bohm velocity for v_s . In the UC Berkeley reactor and magnetic field geometry, the plasma expands outward from the source chamber into the process chamber. This expansion generates an ion density gradient that is known as a distributed sheath. Using the concept of a distributed sheath [6.8,6.9], the ion velocity v_s can be determined using the magnetic field expansion from the ECR ion source to the wafer holder, the distance of the wafer holder from the ECR source (x_w), and the mean free path for ion neutral collisions (λ_o):

$$v_s = \sqrt{v_b^2 + \frac{2T_e}{M} \left(\frac{\lambda_o}{x_w} \right) \ln \left(\frac{v_s A_s}{v_b A_o} \right)} \quad [6-3]$$

where v_b , T_e , and M are the Bohm velocity, electron temperature in units of volts and ion mass respectively. For an argon gas pressure of 1mtorr and our reactor geometry, we get the sheath edge ion velocity to be about 1.2 times the Bohm velocity. In our case, the sheath thickness is much less than the spacing of the target from the plasma source. Thus we can approximate v_s to be constant for all time.

Balancing the ion current with the quasi-static collision-less Child law current enables us to obtain a first-order differential equation that can be solved for the sheath thickness:

$$qn_o \left(\frac{ds}{dt} + v_s \right) = \frac{4}{9} \epsilon_o (2q/M)^{1/2} V_s^{3/2} / s^2 \quad [6-4]$$

Once the sheath thickness is determined, the ion current can be acquired from the Child Law.

6.4.2. Secondary electron current

In order to model the total current drawn from the target, additional current components must be added to the Lieberman and Stewart model. The first additional term is the secondary electron current. At high ion energies, the secondary electron current can dominate the total current. The secondary electron yield as a function of the ion energy has been measured for targets processed in a glow discharge [6.10], at conditions similar to that present during PIII. The measured data were empirically fitted to model the secondary electron yield as a function of ion energy. A multiplicative factor α is introduced such that the secondary electron current is αj_i . Our empirical fit yields:

$$\alpha \approx k \sqrt{V_s} \quad [6-5]$$

where $k = 0.0696$ for an argon ion incident on an aluminum wafer holder.

Though the secondary electron current can be several times greater than the ion current, the ionization of neutrals by secondary electrons in the sheath region is negligible for the following reasons: the neutral density is low at 1mtorr, the maximum sheath thickness is only ~ 1 cm, and the electron transit time is on the order of picoseconds. Thus the probability of secondary electron ionization in the sheath is small. For which this effect is ignored in the model.

6.4.3. Plasma electron current

The plasma electron current is also included in our model to take into consideration voltages on the order of tens of volts during the time period before and after the voltage waveform is applied. We assume that the surface potential is always more negative than the plasma potential. We assume that the electrons have a single Maxwellian distribution with temperature T_e . Thus the electron current j_e is modeled as an exponential function with respect to the sheath voltage:

$$j_e = -\frac{1}{4}qn_0u_e e^{-V_s/T_e} \quad [6-6]$$

where $u_e = (8qT_e/\pi m_e)^{1/2}$ is the average electron velocity, n_0 is the electron density, and T_e is the electron temperature in units of volts.

6.4.4. Displacement current

Since the sheath has a capacitance (C_s), the variation of the applied voltage and the time variation of C_s results in displacement currents. For typical applied voltages and sheath capacitances in PIII, the displacement current is relatively negligible, but for completeness it is included in the model [6.11]:

$$j_{disp} = C_s \frac{dV_s}{dt} + V_s \frac{dC_s}{dt} \quad [6-7]$$

In each region of operation, before, during, and after the applied waveform, various parts of this model will dominate and others will be negligible. Figure 6-1 illustrates the three regions of operation in this model. However, when this model is implemented, all relations are used in every region of operation, making this model continuous for all conditions under consideration. The total current density is:

$$j_{total}(V_s, t) = j_i(V_s, t) [\alpha(V_s) + 1] + j_e(V_s) + j_{disp}(V_s, t) \quad [6-8]$$

6.5. Phases of Plasma Currents During PIII

Using the analytical plasma model developed, the breakdown of the various current components in PIII can be determined. Since PIII uses high voltage pulses, the current phases can be broken down into three stages. First, the quiescent stage is before the applied bias turns on. Second, the sheath expansion stage is where the applied bias turns on and causes the sheath to expand. And finally, the sheath collapse stage is where the applied bias decreases in magnitude and the sheath collapses back down and the system eventually reaches back to the quiescent stage.

6.5.1. Quiescent stage

Assuming the plasma is initially in steady-state, the initial condition of the plasma at low voltages is determined. In the steady-state low voltage condition, the sheath is

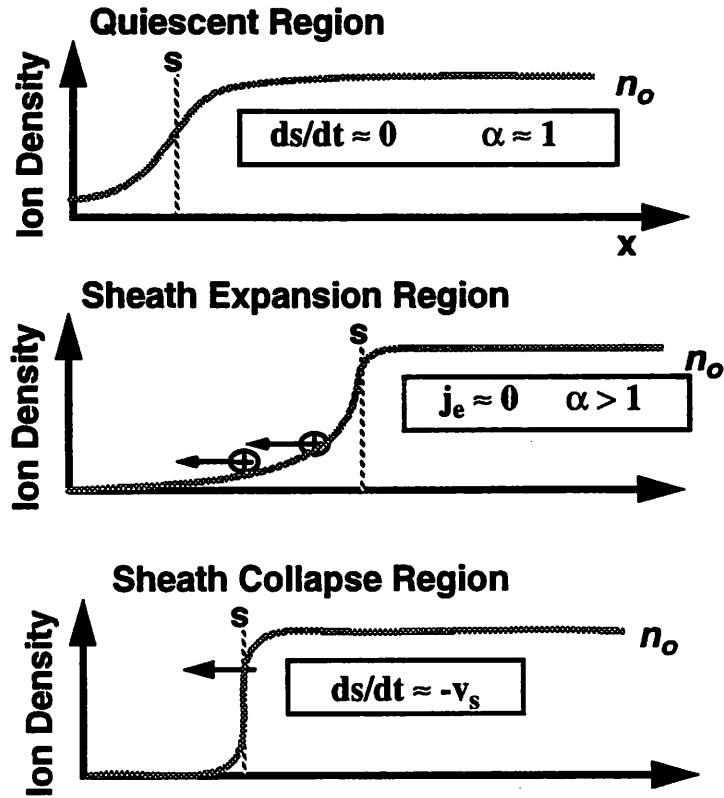


Figure 6-1. Charge flow during a PIII Pulse

Diagram showing various regions of operation for the analytical SPICE model. The model is continuous and all relations operate in all regions of operation.

motionless, making the ion current a constant: $j_i = qn_0v_s$ (e.g. $ds/dt = 0$). This sets an initial plasma thickness before the voltage is applied. At such low voltages, the secondary electron yield is negligible. In the case where the conductive target is in direct contact with the plasma, the DC potential applied to the target (usually grounded) sets the voltage drop across the sheath. This causes a net DC current to be drawn from the plasma. If the surface of the target is insulated or if the supply is capacitively coupled to the plasma, then the balancing of the ion and electron fluxes to the surface sets the voltage drop across the plasma. In addition, if there is an integrated circuit element on the surface of the target, then the sheath voltage drop is set by balancing the net current from the plasma with the current flowing through the integrated-circuit element.

6.5.2. Sheath expansion stage

Once the voltage waveform is applied, the sheath begins to expand and the ion current is no longer a constant. The applied voltage is so large that no electrons from the plasma pass through the V_s voltage barrier, making the electron current essentially zero. In this region, secondary electrons become significant in determining the total current.

6.5.3. Sheath collapse stage

After the applied voltage is turned off, the field supporting the sheath no longer exists and the sheath will collapse. When the applied voltage drops, the ion current decreases. Setting the ion current to approximately zero in Equation 6-2, we obtain the sheath collapse speed:

$$\frac{ds}{dt} \approx -v_s \quad [6-9]$$

For PIII conditions, the collapse of the sheath will only take several microseconds. If the time between pulses is comparable, then the plasma will not have time to reach steady state and the ion current of the subsequent pulse will be decreased [6.12,6.13]. The effects of the sheath collapse on the total current of multiple pulses and unusually shaped pulses are examined in our experiments and simulations.

6.6. Experimental Results

To test the validity of the model, a 100mm diameter aluminum disk was implanted using PIII in an ECR argon plasma. The plasma parameters used in the simulation were measured using a Langmuir probe placed ~1cm in front of the disk at the center. The default plasma conditions and probe results are given in Table 6-1.

For our experimental setup, the plasma density behind the disk was measured to be several orders of magnitude lower than in front. Thus we ignored the plasma behind the target for the simulation. This assumption is verified experimentally by having the backside of the disk insulated by a thick quartz cover, and no significant change in current was observed with or without the cover. Various pulse waveforms and plasma conditions were used in our experiments. The voltage pulse waveform was measured using a high voltage probe and simultaneously the current drawn was measured using a Rogowski loop. The

Parameter	Value
Feed Gas	Argon
Base Pressure	1 mtorr
Ion Density	$4.5 \times 10^{10} \text{ cm}^{-3}$
Electron Temperature	4V
Floating Potential	-6V
Plasma Potential	18.3V

Table 6-1. Default plasma parameters used in the simulation

(These parameters were extracted using Langmuir probe measurements.)

Rogowski loop was installed close to the wafer holder so that the measured current is the same as the actual total current going to the wafer holder. The measured pulse waveform was input as a piece-wise linear time-varying voltage source in SPICE, and the total current drawn was obtained from the simulator.

Figure 6-2 shows a 3kV voltage pulse and the resulting measured and simulated currents. In Figure 6-3, we illustrate the corresponding sheath dynamics for the 3kV pulse. We can look at the plasma dynamics during the voltage pulse by dividing the pulse into three time domains. In region 1, the applied bias is rapidly increasing, and the sheath responds by rapidly expanding. This induces a large ion current drawn to the target consisting mainly of ions uncovered by the moving sheath. In region 2, the voltage rise slows considerably. The onset of region 2 corresponds to the peak in the collected current. Though the voltage is still increasing its time rate of change has decreased considerably. This results in a decrease in the velocity of the sheath edge. The current drops because the sheath uncovers fewer ions per unit time than before. Therefore, it is not the voltage but its rate of change that most strongly affects the current drawn. Eventually the current becomes almost constant due to the sheath approaching equilibrium.

In region 3, the applied bias decreases with time. Due to the non-equilibrium state of the system, the sheath initially continues to increase because it is still smaller than the steady-state thickness for the voltage at that time. The finite time required for the sheath to reach equilibrium is slower than the voltage ramp rate. However, the voltage drops eventually to the point where the sheath is larger than the steady-state thickness. This causes the

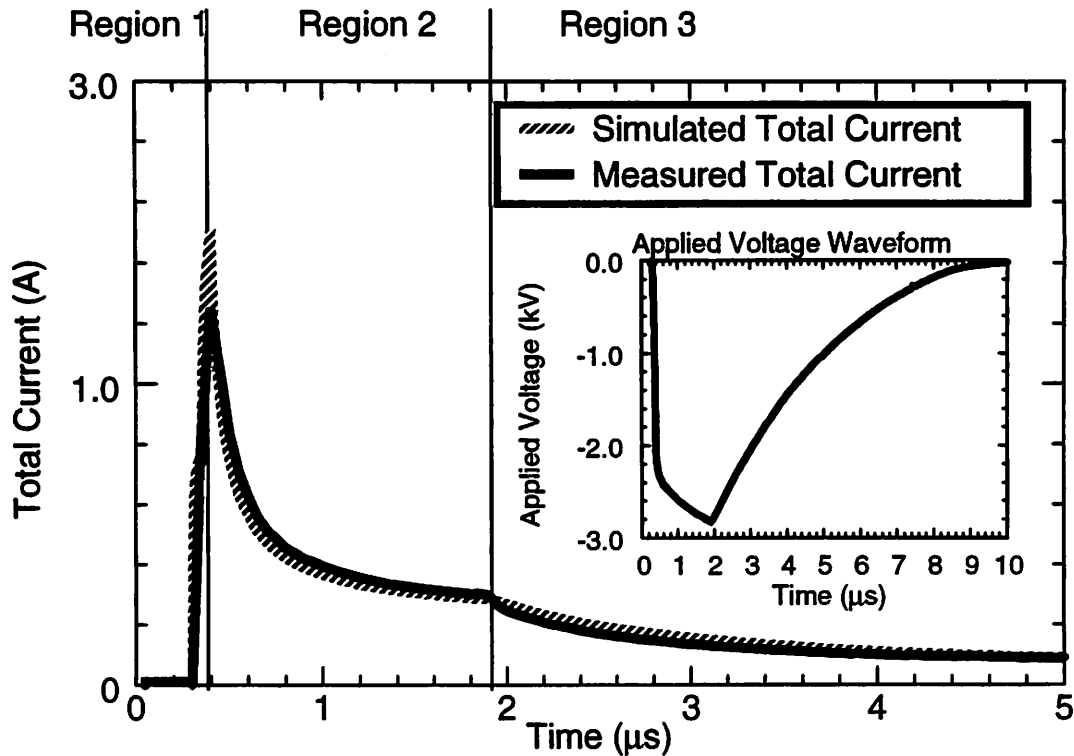


Figure 6-2. 3kV waveform and model comparison

Comparison of measured total current and simulated total current for a 3kV pulse using the conditions shown in Table 6-1. Insert shows the applied voltage waveform.

sheath to start collapsing. As the voltage decreases faster than the sheath can equilibrate to, the sheath will collapse at the maximum possible velocity, which is the velocity of the ions at the sheath edge, v_s . Hence, the slope of the sheath thickness as a function of time in region 3 is v_s while the voltage is decreasing. The current drops off rapidly in this region because no more ions are being uncovered by the sheath. Eventually the collected current becomes negligible.

6.6.1. Voltage dependence

When the peak pulse voltage is increased from 3kV to 5kV, we get a corresponding increase in the collected current. Figure 6-4 shows the comparison of the measured and simulated currents for the 5kV pulse. Both theory and experiment show that the current is much larger than would be expected for a linear voltage response. The ion current increases approximately sub-linear with respect to the voltage because the sheath expansion is sub-

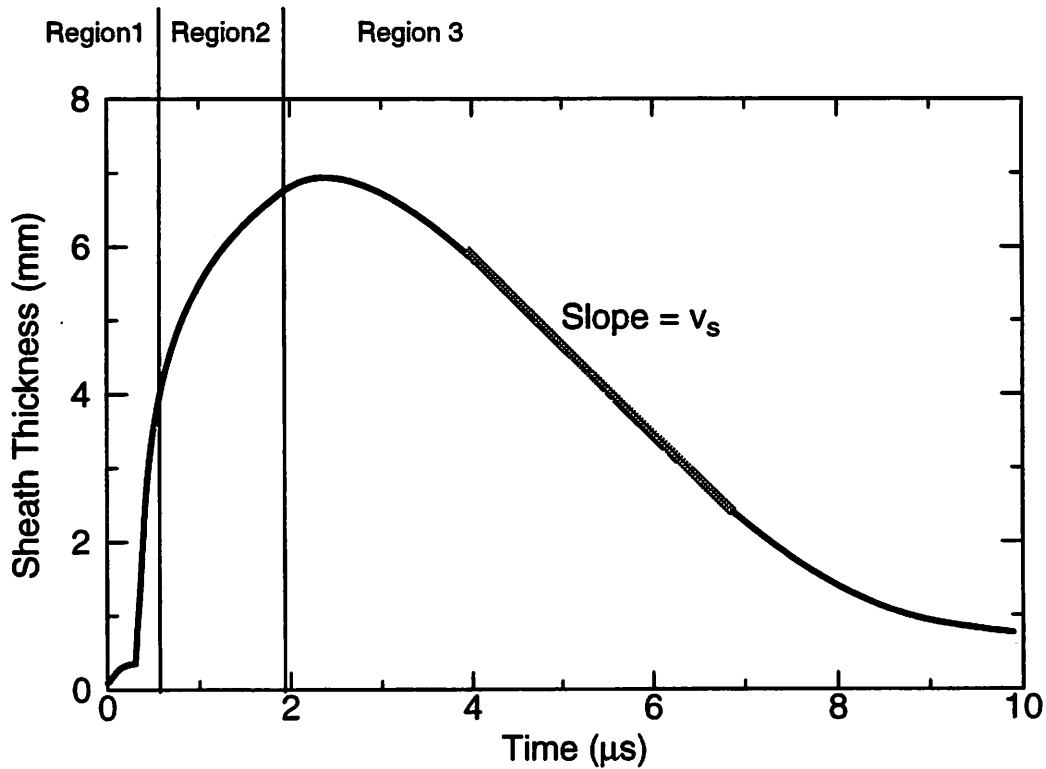


Figure 6-3. Sheath for 3kV waveform

Simulated sheath dynamics during the 3kV pulse waveform.

linear with voltage. Though the ion current does not increase linearly, the secondary electron current increases dramatically due to the larger number of secondary electrons generated per impinging ion, which accounts for much of the increase in total current. Another effect of the higher bias is that the plasma takes longer to reach steady-state. As shown in Figure 6-5, the sheath dynamics for the 5kV pulse are similar to the 3kV pulse. However, the sheath expands to a larger maximum thickness, and as a result it takes longer to reach steady-state than for the 3kV pulse.

6.6.2. Gas pressure effect

To test the validity of the model in various plasma conditions, we also varied the feed gas pressure. To maintain a collision-less sheath, we increased the pressure from 1mtorr to 2mtorr. The change in feed gas pressure caused all of the other plasma parame-

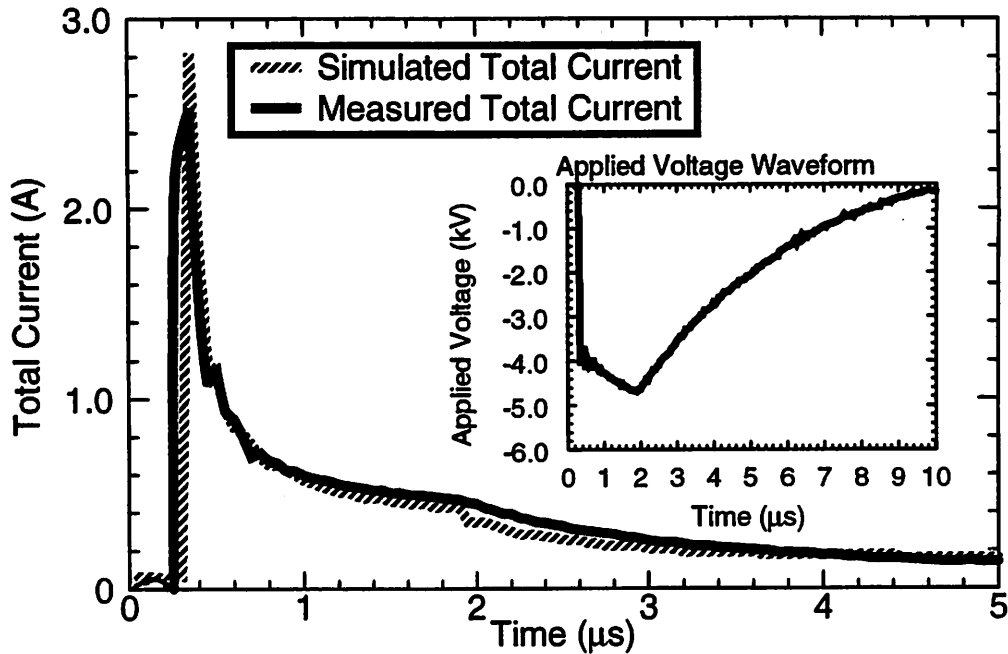


Figure 6-4. 5kV waveform and model comparison

Comparison of measured total current and simulated total current for a 5kV pulse using the conditions in Table 6-1. Insert shows the applied voltage waveform.

ters to change. Figure 6-6 illustrates the good agreement even when the plasma conditions are varied within the limits of the approximations used.

6.6.3. Reflected pulse effect

If an impedance mismatch between the pulse line and the plasma and between the pulse line and the pulse generator is induced, reflected pulses can be created with a delay of several microseconds. The delay between the initial pulse and the first reflected pulse is shorter than the time required for the plasma to reach the equilibrium stage. Thus the model of the sheath collapse can be tested using reflected pulses. Figure 6-7 illustrates the voltage pulse and the good agreement between measured and simulated currents.

To test the sensitivity of the current to various possible sheath dynamics, we simulated two additional possible scenarios and compared their peak currents in Table 6-2. In the first scenario, we used our full model which showed good agreement with the experimental results. As for the second scenario, the plasma did not have time to collapse during

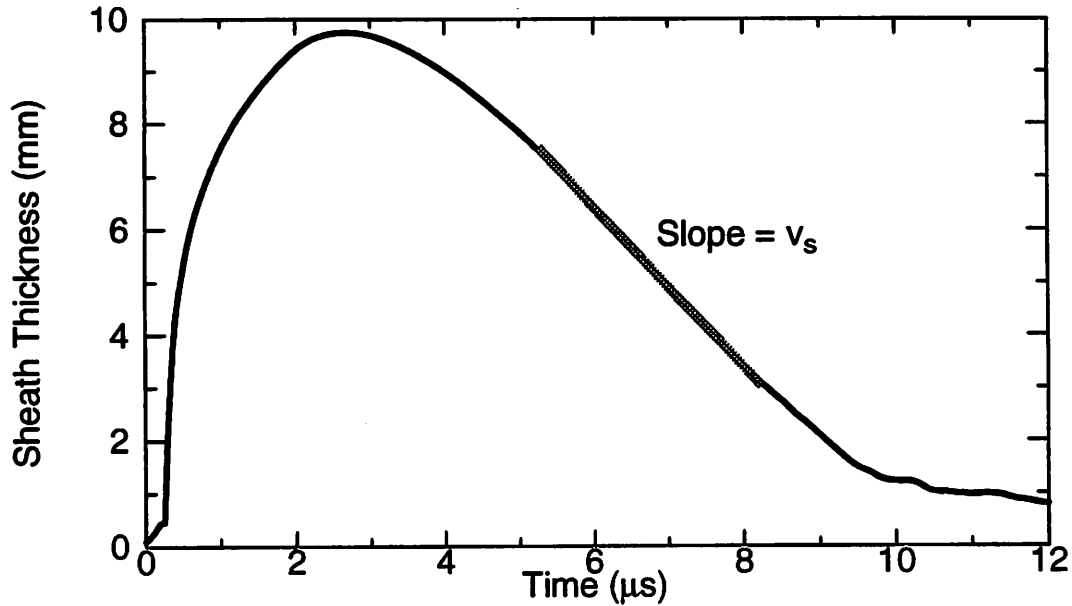


Figure 6-5. Sheath dynamics for 5kV pulse

Simulated sheath dynamics during the 5kV pulse waveform.

the interval between the initial pulse and the reflected pulse, resulting in a significant drop in the peak current of the second pulse is seen because of the inverse square dependence of the ion current on the sheath thickness. The third scenario assumed that the plasma had time to completely equilibrate in the time between pulses, giving a peak current of the second pulse much higher than the experimental value. Thus the model of the sheath collapse has a significant effect on the shape of the time-varying current, and has to be modeled correctly to describe the actual PIII currents. .

To test the model with varying pulse delay times, we increased the voltage of the initial pulse to 15kV. This allowed a second reflected pulse to be visible at 5.4 μs after the initial pulse. Figure 6-8 illustrates the waveform used and the current results. Once again we obtained good correlation for different temporal spacings of the reflected pulses, with

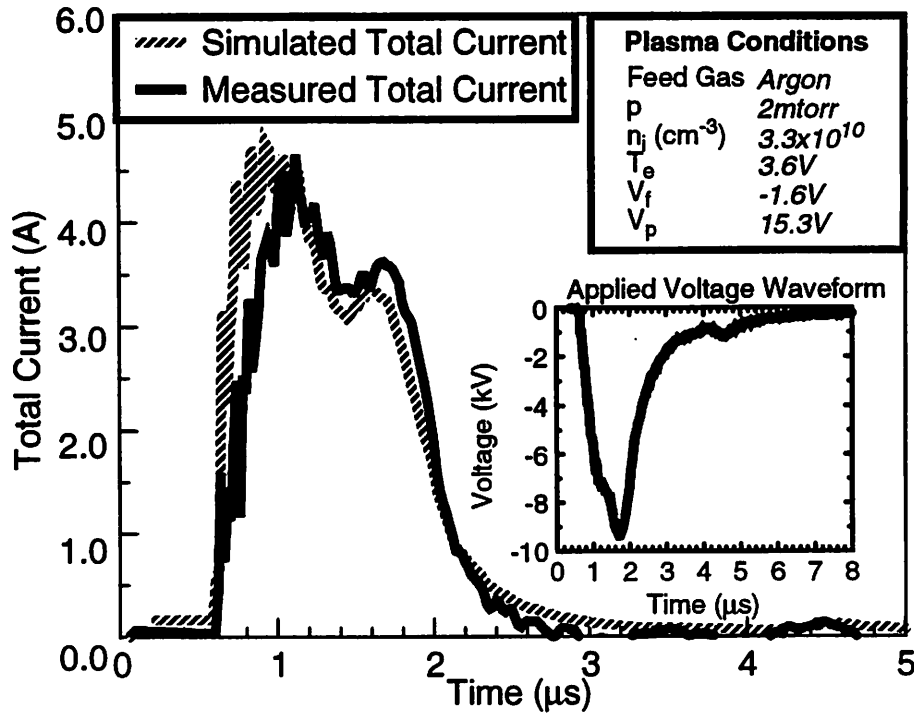


Figure 6-6. Plasma condition variation simulation and experiment

Comparison of measured total current and simulated total current for a 10kV pulse. Insert shows the applied voltage waveform. The ECR plasma conditions used were 2mtorr and 700W of microwave power with argon as the feed gas. A short table of the plasma parameters is inserted.

good correlation between initial and each reflected peak currents as shown in . Table 6-3. Finally, we tested the model against unusually shaped pulses. We chose a pulse that dipped midway through the voltage pulse. The dip in the voltage pulse results in a complex current

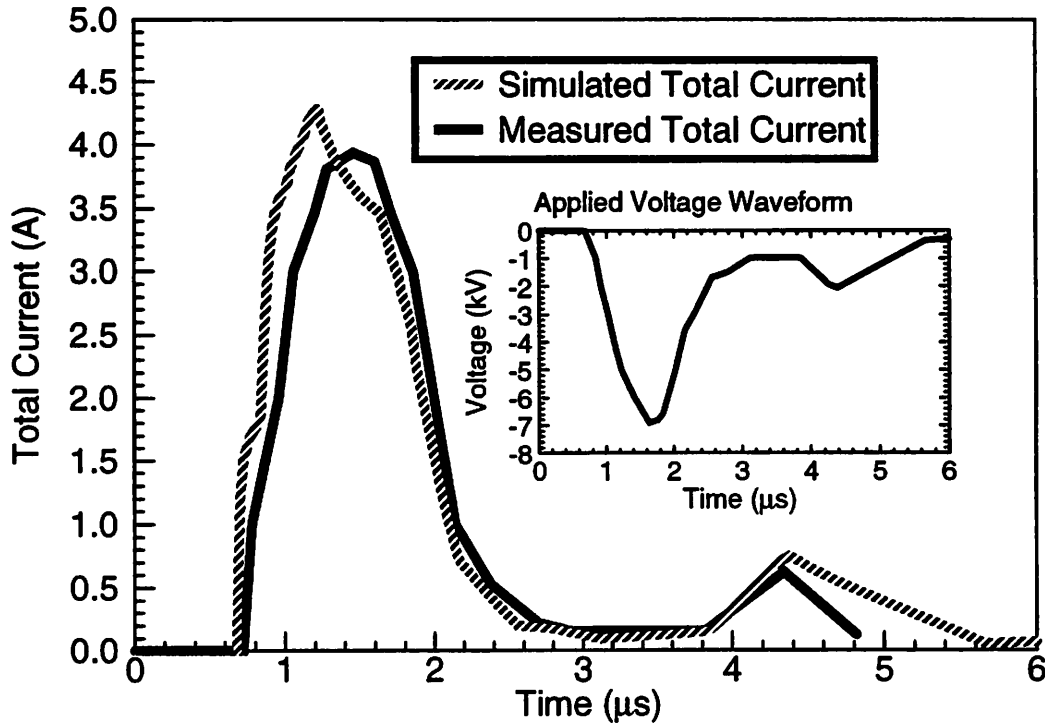


Figure 6-7. Single reflected pulse waveform

Comparison of measured total current and simulated total current including reflected pulse for 7kV waveform. Insert of applied voltage waveform. Peak voltage of initial pulse is 7kV. Peak Voltage of reflected pulse is 2kV.

Parameters	Model with sheath collapse	Model without sheath collapse †	Model of fast sheath collapse*	Experiment
Sheath thickness at second voltage peak	6.0mm	10.7mm	4.8mm	_____
Second peak current	0.75 A	0.24 A	1.2 A	0.7 A

Table 6-2. Comparison of theoretical and experimental sheaths for 7kV waveform

† v_s term was removed from simulation preventing the sheath from collapsing. The current for the initial pulse was not affected significantly.

* Sheath is forced to collapse rapidly to the equilibrium value very soon after the initial pulse.

waveform. Figure 6-9 illustrates that the model correlates well with experiment for any shape voltage pulse that can be generated.

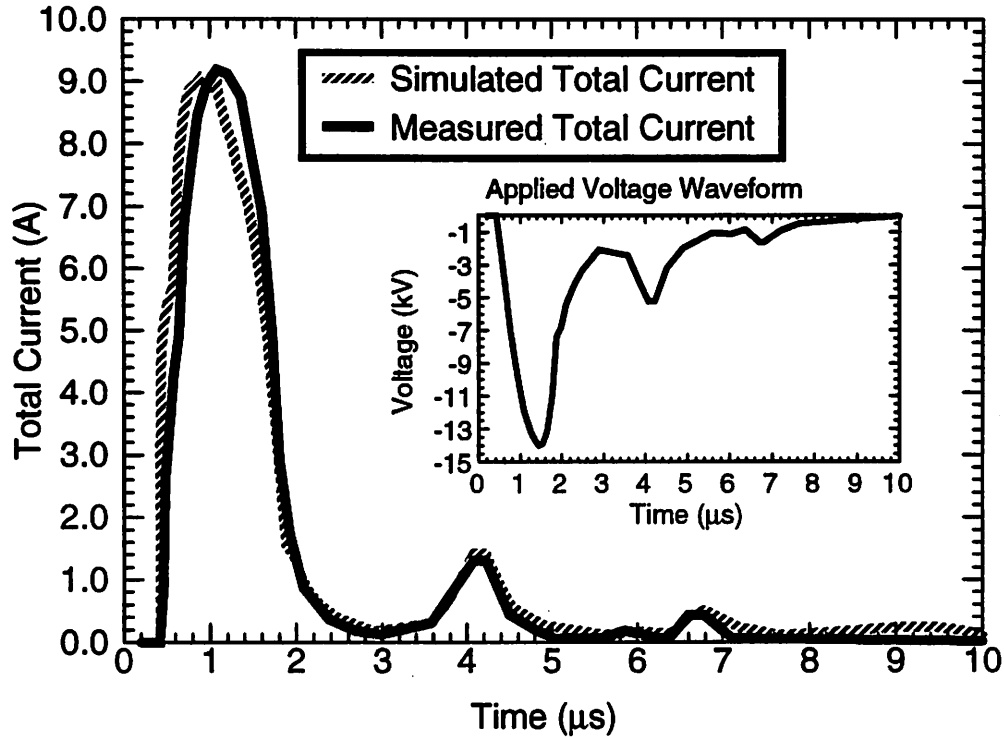


Figure 6-8. Double reflected pulse waveform

Comparison of measured total current and simulated total current for 14kV waveform. Insert of applied voltage waveform. Initial pulse peak voltage is 14kV. First reflected pulse peak voltage is 5.2kV. Second reflected pulse peak voltage is 1.7kV.

Parameter	Model	Experiment
Initial Pulse	9.0 A	9.1 A
First Reflected Pulse	1.4 A	1.4 A
Second Reflected Pulse	0.5 A	0.45 A

Table 6-3. Comparison of peak current for 14kV waveform

6.7. Conclusions

An analytical plasma model has been developed which does not require any fitting parameters to accurately describe the plasma currents during PIII. The model was implemented using the circuit simulator SPICE platform. This model allows easy experimental verification by extracting a few simple plasma parameters (n_i , T_e , V_p , V_f) from a single Langmuir probe measurement. Results show that the sheath collapse mechanism can significantly affect the target current, especially for high repetition rates, and has to be prop-

erly accounted for in the PIII model. Comparison of model and experimental results shows that our model of the sheath collapse correlates well. Our findings also verify the significance of secondary electrons. In addition, we have shown that a plasma in our reactor configuration will equilibrate by a sheath collapse at a maximum constant rate v_s .

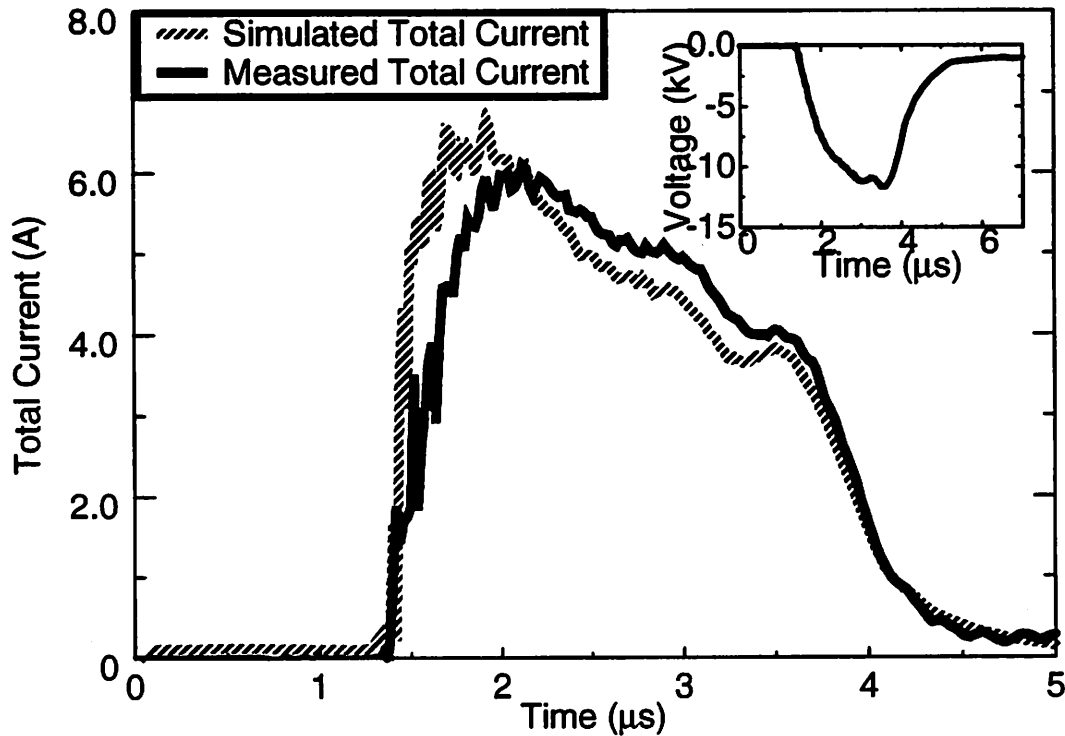


Figure 6-9. Unusually shaped PIII pulse simulation

Comparison of measured total current and simulated total current for a 12kV pulse using conditions shown in Table 6-1. Insert shows the applied voltage waveform.

6.8. Coupled Model

With an accurate model of the plasma currents, we can couple it to I-V characteristics of device structures and substrate biases, allowing charging damage effects to be modeled. The plasma model provides an accurate description of all the current components making up the total plasma current. A convenient platform to integrate the plasma model with device structures and substrate bias is SPICE [6.14]. Since the plasma model consists of a set of analytical relations and since SPICE contains a robust differential equation solver, the plasma model can be easily integrated into SPICE as a set of non-linear and

time-dependent elements. These elements can be grouped together to form a single non-linear time-dependent element representing the plasma. In addition to the plasma, device structures existing on the wafer can be modeled as discrete circuit elements. In addition, the substrate bias can be represented as either a voltage source or as a more complex source with inductance, capacitance, and resistance. By combining all of the above elements together, the interactions that induce charging damage can be modeled.

6.9. SPICE Implementation of Plasma Model

The implementation of the coupled charging model in SPICE requires a rearrangement of the equations to convert the plasma equations into equivalent circuit elements. First, the Child Law ion current relation (Equation 6-1) and the ion charge per unit time crossing the sheath boundary (Equation 6-2) are equated. This relation is rearranged to solve for the sheath thickness:

$$V_s^{3/2}(t) = \frac{qn_o}{\frac{4}{9}\epsilon_o(2q/M)^{1/2}} \left(\frac{1}{3} \frac{d(s(t))^3}{dt} + (s(t))^2 v_s \right) \quad [6-10]$$

where s is the sheath thickness and V_s is the voltage drop across the sheath. In this form, the relation can be implemented in SPICE as an equivalent circuit. Once the sheath thickness is calculated, the ion current from the plasma can be determined. By adding the plasma electron (Equation 6-6), the secondary electron (Equation 6-5), and the displacement currents (Equation 6-7) to the ion current, the total current is determined. The conversion of the entire plasma model is described in Appendix B.

6.10. Concept of Modeling IC Circuit and Bias Interactions

The second portion of the model is the IC circuit. The integrated circuit on the wafer is modeled as a set of discrete IC devices in order to determine the currents and voltages generated during a plasma process. For example, the thin gate oxide can be modeled as a capacitor in parallel with the Fowler-Nordheim tunneling model. Lastly, the substrate bias must be added to complete the total charging environment. The substrate bias can be modeled as either a current or voltage source, and if necessary, more complex bias supply models, using elements such as transmission lines, can be incorporated. For our implemen-

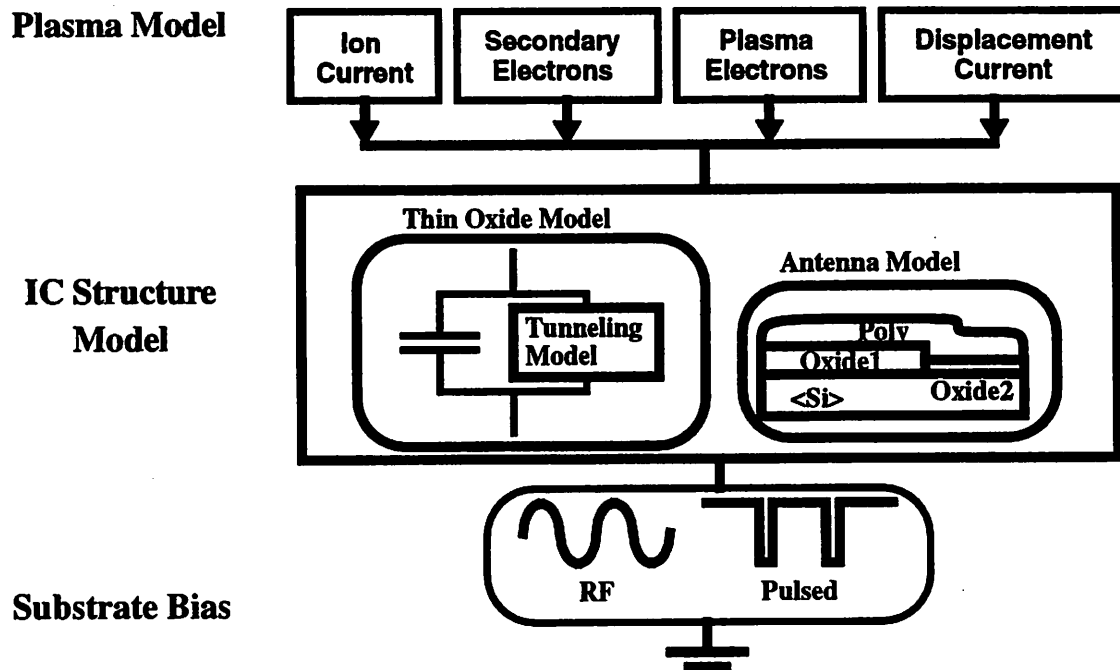


Figure 6-10. Plasma/IC circuit model concept

Schematic of interaction of plasma model with SPICE IC structure circuit and substrate bias.

tation of the model, the bias is modeled as a piece-wise linear voltage source, using measured values of the voltage waveform over time. The coupling between the plasma model, the wafer, and the substrate bias is illustrated in Figure 6-10.

6.11. Concept of Modeling 2-D Effects

The model can be extended to examine two dimensional plasma and IC structure effects. A non-uniform plasma can be modeled using a distributed network of plasma models as shown in Figure 6-11. Each plasma model in the distributed network represents a section of the plasma, and is scaled to the area it represents. Since each plasma element can use different plasma parameters the non-uniformity of any of the plasma parameters can be modeled.

Also, two dimensional device structures can be modeled. A network of device elements can represent the device structure. For each separate surface conductor a separate plasma element can represent the connection of the plasma to that electrode. For example,

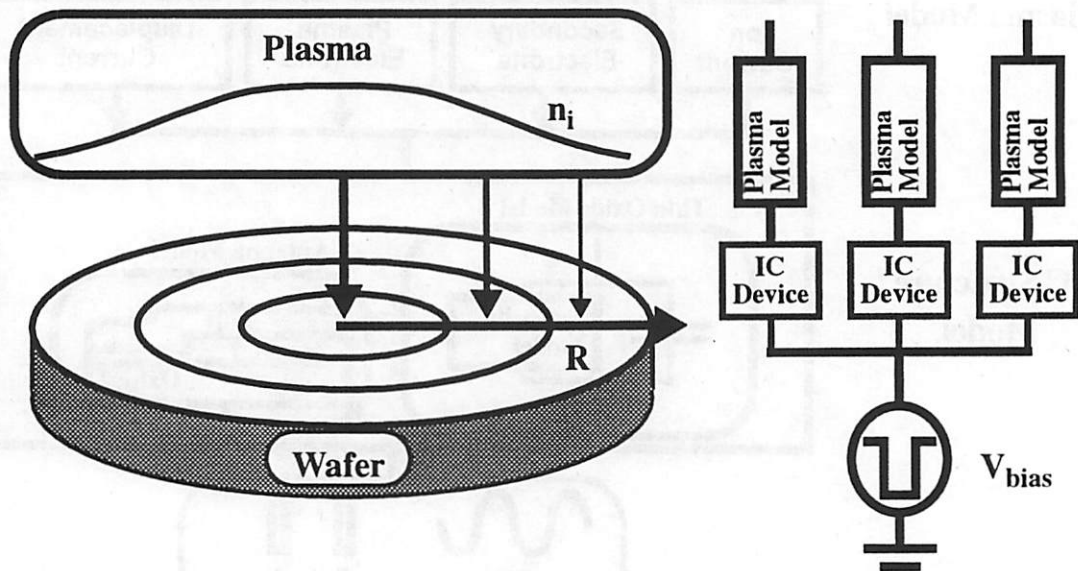


Figure 6-11. Plasma non-uniformity modeling

Concept for modeling plasma non-uniformity by dividing the plasma into discrete sections and using a distributed network of plasma models, with each model varying in plasma parameters to simulate non-uniformities in the plasma.

a CMOS inverter can be simulated as illustrated in Figure 6-12. In addition to the desired elements, additional parasitic elements, such as bipolar devices and capacitances can be modeled to form a complete picture of the interactions.

6.12. Conclusions

Through the use of this coupled plasma IC device structure model, the charging damage effect, due to any component of the system as well as to interactions between the components, can be determined. By using a distributed network approach, plasma non-uniformity effects and two dimensional device structures can be modeled and the charging damage effects can be determined.

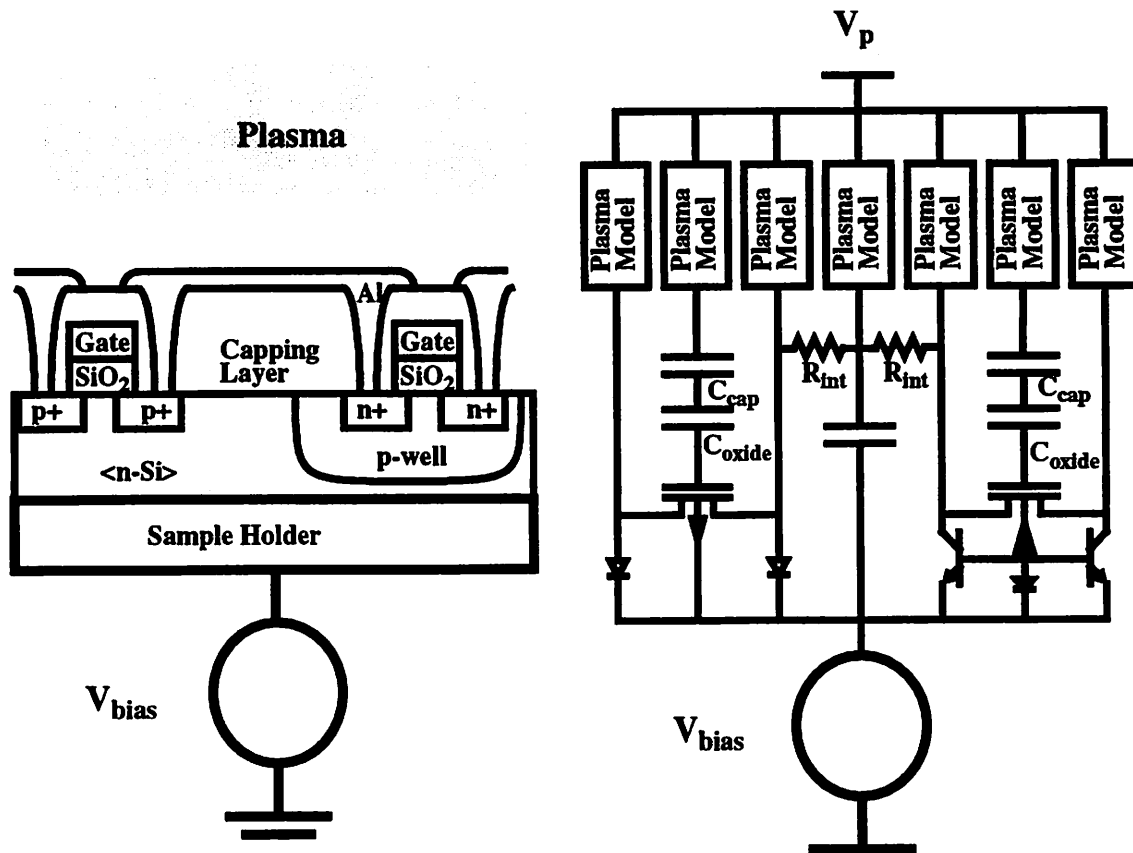


Figure 6-12. CMOS structure model

Concept for modeling of 2-D device structures in charging damage model.

References

- [6.1] M. A. Lieberman, "Model of Plasma Immersion Ion Implantation," *J. Applied Physics*, vol. 66, no. 7, pp. 2926-2929, 1989.
- [6.2] R. A. Stewart, and M. A. Lieberman, "Model of Plasma Immersion Ion Implantation for Voltage Pulses with Finite Rise and Fall Times," *J. Applied Physics*, vol. 70, no. 7, pp. 3481- 3487, 1991.
- [6.3] J. T. Scheuer, M. Shamim, and J. R. Conrad, "Model of Plasma Source Ion Implantation in Planar, Cylindrical, and Spherical Geometries," *J. Applied Physics*, vol. 67, pp. 1241-1245, 1990.
- [6.4] J. K. Chester, "Effects of Expanding Sheaths on the Operation of Mercury-Arc Rectifiers", *Journal of Science and Technology*, vol. 37, no. 1, pp. 2-10, 1970.

- [6.5] M. Shamim, J. T. Scheuer, and J. R. Conrad, "Measurements of Spatial and Temporal Sheath Evolution for Spherical and Cylindrical Geometries in Plasma Source Ion Implantation," *J. Applied Physics*, vol. 69, pp. 2904-2908, 1991.
- [6.6] P. Antognetti, and G. Massobrio, *Semiconductor Device Modeling with SPICE*, 1st ed. Mc Graw-Hill, New York, 1988.
- [6.7] C. D. Child, "Discharge From Hot CaO," *Phys. Rev.*, vol. 32, pp. 492-511, 1911.
- [6.8] M. Hussein, and G. A. Emmert, "Numerical Simulation of ECR Microwave Plasma Stream," *IEEE International Conference on Plasma Science* New York, NY, pp. 147, 1989.
- [6.9] M. A. Lieberman, "Design of High Density Plasma Sources for Materials Processing," *Physics of Thin Films*, vol. 18, M. Francombe and J. Vossen eds., Academic Press, 1994.
- [6.10] B. Szapiro, and J. J. Rocca, "Electron Emission from Glow-discharge Cathode Materials due to Neon and Argon Ion Bombardment," *J. Applied Physics*, vol. 65, no. 9, pp. 3713-3716, 1989.
- [6.11] B. P. Wood, "Displacement Current and Multiple Pulse Effects in Plasma Source Ion Implantation," *J. Applied Physics*, vol. 73, no. 10, pp. 4770-4778, 1994.
- [6.12] W. En, and N. W. Cheung, "Analytical Modeling of Plasma Immersion Ion Implantation Target Current Using the SPICE Circuit Simulator," *J. Vac. Sci and Tech. B*, vol. 12, no. 2, pp. 833-837, 1994.
- [6.13] W. G. En, M. A. Lieberman, and N. W. Cheung, "Comparison of experimental target currents with analytical model results for plasma immersion ion implantation," *IEEE Transactions on Plasma Science*, vol. 23, no. 3, pp. 415-421, 1995.
- [6.14] P. Antognetti and G. Massobrio, *Semiconductor Device Modeling with SPICE*, 1st ed. Mc Graw-Hill, New York, 1988.

7 Substrate Bias Effects

7.1. Introduction

Using the coupled model of charging damage the effect of substrate bias on charging damage can be explored. Both the effects of the shape as well as the frequency of the pulses affect the oxide voltage. By understanding the relationship between the pulsing bias and damage, the bias can be optimized to minimize charging damage. Thus, a physical understanding of the effects of the bias can be found through the model.

Oxide charging mechanisms in PIII can be modeled or measured using area capacitor test devices. The plasma model previously described, the thin oxide capacitor, and the applied voltage bias are placed in series in the simulation as shown in Figure 7-1. We will use this system to explain various aspects of charging damage in PIII.

7.2. Theory of Oxide Charging in PIII

Since the plasma model can determine all of the current components generated in PIII, the evolution of the currents during the first applied voltage pulse can be studied carefully. The time-varying bias can be separated into three distinct regimes: before, during, and after the pulse, as shown in Figure 7-2. In each regime different currents dominate and different potentials are generated.

Before the voltage pulse begins (Figure 7-2a), the plasma brings the floating surface of the thin gate oxide to the floating potential. Since the plasma electrons are faster than the ions, a net charge must be setup on the surface to retard the electrons and balance the fluxes. This equilibrium surface voltage is called the floating potential (V_f).

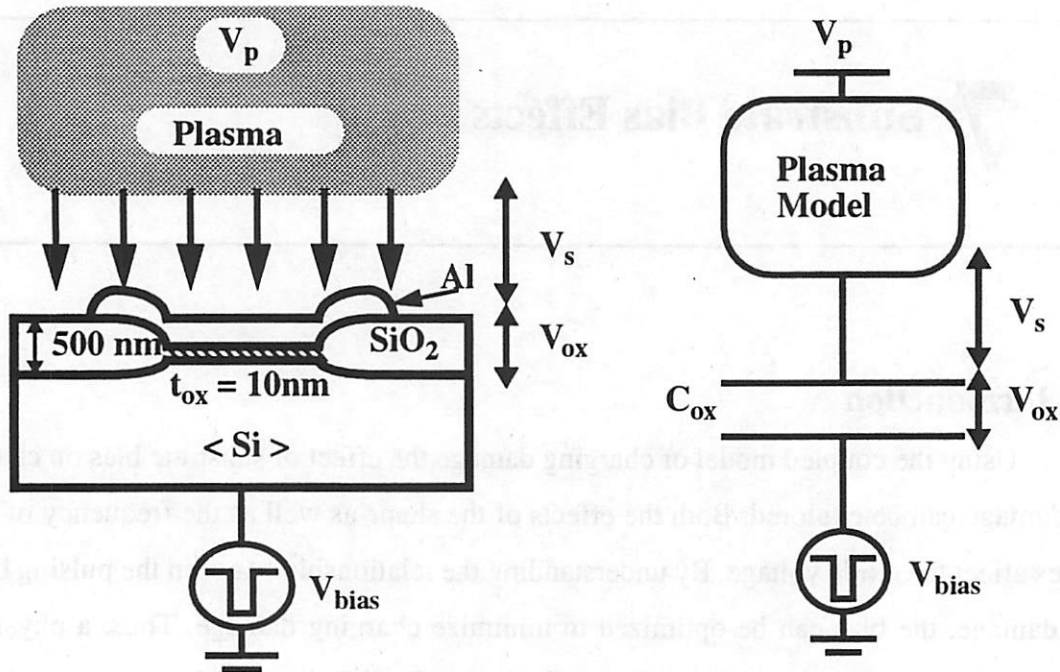


Figure 7-1. Schematic of capacitor test structure

Schematic of example charging scenario used throughout the paper. On the left, is a schematic of the structure modeled by the circuit diagram on the right.

When the high voltage pulse turns on (Figure 7-2b) with a peak voltage from a few hundred volts to one hundred kilovolts, ions implant into the surface. The plasma electrons are repelled away from the surface by the negative bias, and the plasma ions are accelerated to the surface. Since the capacitance of the sheath (C_s) is extremely low, all of the applied bias drops across the sheath, providing the accelerating potential for the implanting ions. The implanting ions generate secondary electrons which increase the net positive charge on the surface as the secondary electrons accelerate away. The combined ion and secondary electron currents induce a small perturbation in the oxide voltage (V_{ox}) as shown in Figure 7-3.

After the applied bias is turned off (Figure 7-2c), plasma electrons will eventually bring the surface back to equilibrium at the floating potential. Since the potential barrier by the applied bias is gone, the positive shift of the oxide voltage increases the voltage-sensitive electron current over the ion current, generating a net negative current to remove the charge deposited during the implantation. For a typical plasma condition, many millisec-

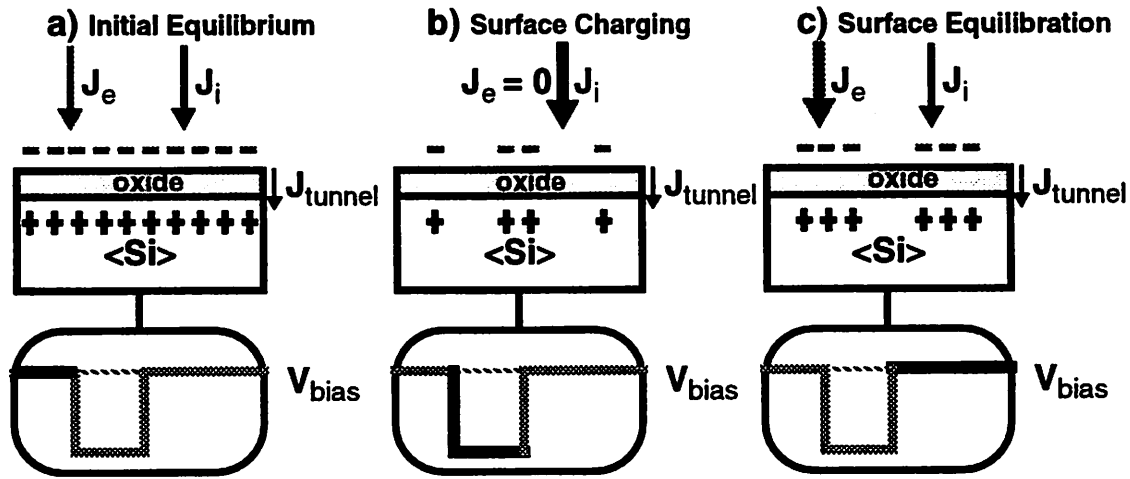


Figure 7-2. Multiple pulse effect concept

Pictorial illustration showing the evolution of oxide charges in PIII. (a) initial equilibrium with a net negative charge (b) implantation that reduces the net negative charge (c) surface equilibration where the surface returns to the initial equilibrium after an equilibration time.

onds are required for the plasma electrons to return the surface back to the floating potential.

7.3. Equilibration Time in PIII

Using the analytical relations of the plasma, the equilibration time can be determined for a floating surface after an implantation pulse. For the positive charge generated in a PIII pulse, the equilibration time is independent of the charge per pulse because of the exponential dependence of the electron current. If the charge deposited increases, the neutralizing electron current increases too. However, the equilibration time does depend on the plasma condition and oxide thickness. The equilibration time due to a voltage pulse derives from the net current after the pulse due to the positive charge deposited (See Appendix D):

$$t_{\text{equil}} = \frac{C_{\text{ox}} T_e}{q n_o v_s} \ln \left(\frac{1}{|\delta|} \right) \quad [7-1]$$

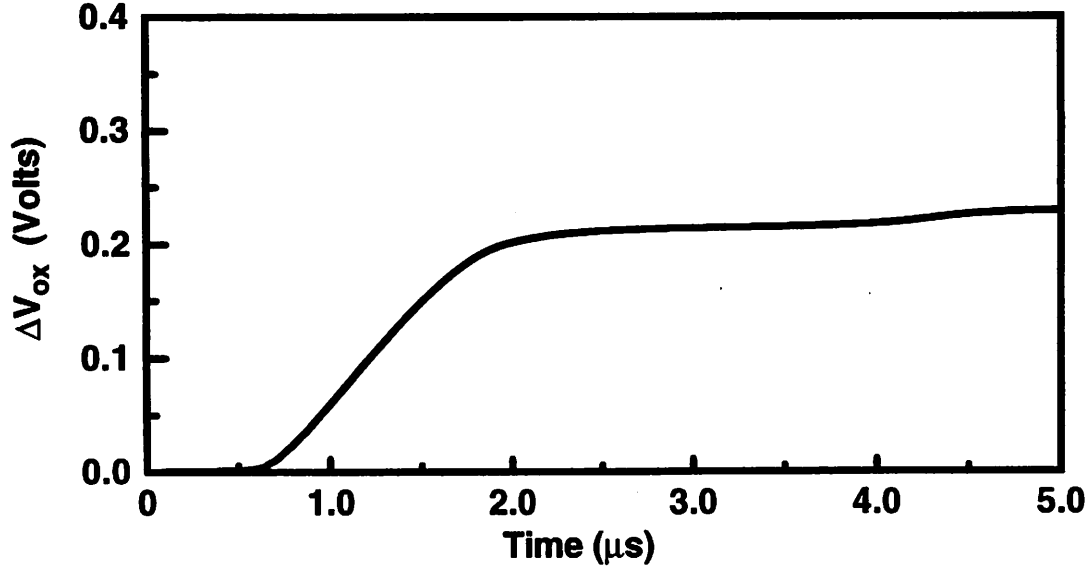


Figure 7-3. Oxide voltage variation due to single pulse

Simulation showing the variation of the voltage drop across a 10nm gate oxide for a single 10kV voltage pulse caused by the implanted charge and the secondary electrons.

where δ is a dimension-less number less than unity representing a characteristic fraction of the electron temperature, T_e . As shown in Appendix D, when the charge deposited is positive, t_{equil} does not depend on the deposited charge (ΔQ_{ox}), to the first order.

The equilibration time can be decreased by changes in the device and plasma conditions. A lower t_{equil} is better for charging damage because the pulsing repetition rate can be made much higher without accumulating charge from multiple pulses on the oxide. By lowering the electron temperature (T_e), a square root decrease in t_{equil} can be achieved since v_s is proportional to $T_e^{1/2}$; however, since T_e can only vary by at most a factor of 2 in a typical process plasma, very little benefit can be gained. An increase in the ion density (n_0) can have a significant effect on t_{equil} since n_0 can vary by several orders of magnitude. t_{equil} decreases with increasing n_0 because more electron flux is available to compensate the charge per pulse. Finally, t_{equil} can also be reduced by decreasing C_{ox} (i.e. increasing the oxide thickness). However, since the current trend is toward thinner oxides with higher

C_{ox} in MOSFETs, this avenue cannot be pursued to reduce t_{equil} . Thus, the best method of reducing t_{equil} is by increasing the ion density. Since a higher ion density has other benefits, such as higher throughput in PIII, multiple benefits can be gained at the same time.

For PIII, the implant pulses deposit positive charge on the surface, resulting in a fixed equilibration time. Using typical values of oxide thickness ($x_{ox} = 10\text{nm}$), electron temperature in units of volts ($T_e = 4\text{V}$), ion density ($n_o = 5 \times 10^{10} \text{ cm}^{-3}$), ion velocity ($v_s = 5 \times 10^5 \text{ cm/s}$), and constant δ ($\delta = 0.1$); the time required to equilibrate is 17.3ms. For a typical pulse waveform, the plasma requires a much longer time to equilibrate than a pulsing rate of several kHz allows. Thus for typical pulse repetition rates, which are in the kHz range, large voltages can be generated by the accumulation of many pulses with very little charge per pulse.

7.4. Oxide Voltage Variation Due to PIII

Since the wafer surface requires such a long time to equilibrate, the charge deposited during PIII can accumulate over many pulses at repetition rates above a few tens of Hertz. This accumulation of charge due to t_{equil} causes the DC surface potential to shift away from the floating potential, equilibrating to a new potential based on the PIII implantation conditions. Since each individual pulse causes only a small variation in the surface potential, the new equilibrium after many pulses can be considered to be effectively dc. Using this approximation and the analytical relations of the model, a simple calculation shows the dependence of the new dc oxide voltage on the applied voltage pulsing (See Appendix E):

$$V_{ox}(t) \approx \langle V_{ox} \rangle = V_f + T_e \ln \left(\frac{1}{1 - fT_{on}} \right) + T_e \ln \left(1 + \frac{\beta Q_i f}{qn_o v_s} \right) \quad [7-2]$$

where T_{on} , f , Q_i , and β are the pulse on time, pulse repetition frequency, ion charge deposited per pulse, and the effective secondary electron yield for the pulse ($\beta \equiv Q_{se}/Q_i$; Q_s is the total secondary electron charge generated by the pulse) respectively.

Several observations can now be made with respect to the effects of pulsing on the surface potential. The term fT_{on} is the duty factor of the pulsing. To minimize the change in $\langle V_{ox} \rangle$, Equation 7-2 requires the duty factor be minimized. Also, the third term in Equation 7-2 contains the term $(Q_i f / q n_0 v_s)$ which is the fraction of the total flux of ions reaching the wafer that implants (i.e. the efficiency of the implant). Note that ions continually bombard the wafer surface while it is exposed to the plasma; however, only the ions that are accelerated during the pulse get implanted. To maximize the implant rate, the efficiency of the implant must be maximized.

From Equation 7-2, we can maximize the efficiency of the implant to minimize the charging damage. Minimizing the electron temperature reduces $\langle V_{ox} \rangle$ through the effects of duty factor and implantation efficiency. In principle, reducing the secondary electron yield (β) allows a higher efficiency for the same change in surface potential. Unfortunately, the secondary electron yield is a function of the target material and the impinging ion species which are factors not easily changed for a given implant energy.

With a simple square pulse waveform, Figure 7-4 illustrates the change of V_{ox} for a 10nm thick oxide from its initial equilibrium to a new steady-state for several pulse repetition rates. The charge balance due to the plasma charge flux generates the initial equilibrium V_{ox} . As the repetition rate increases, the charge builds up with multiple pulses shifting V_{ox} . For the 1kHz case, only a small voltage variation occurs because the plasma has almost enough time to equilibrate between pulses. In support of this simulation result, previous experimental work has shown that low repetition rates does not affect the charging damage to thin oxides [7.1]. As the pulse repetition rate increases, the plasma no longer fully equilibrates between pulses. As a result, charge from the implantation pulses accumulates over multiple pulses, shifting V_{ox} until the plasma electron current increases enough to discharge the increased positive current. Thus, the voltage pulsing can significantly alter V_{ox} , changing the charging damage that occurs.

Another way to look at the charging effect is to plot V_{ox} as a function of the pulsing repetition rate for an ideal square pulse shape (Figure 7-5). Initially the floating potential

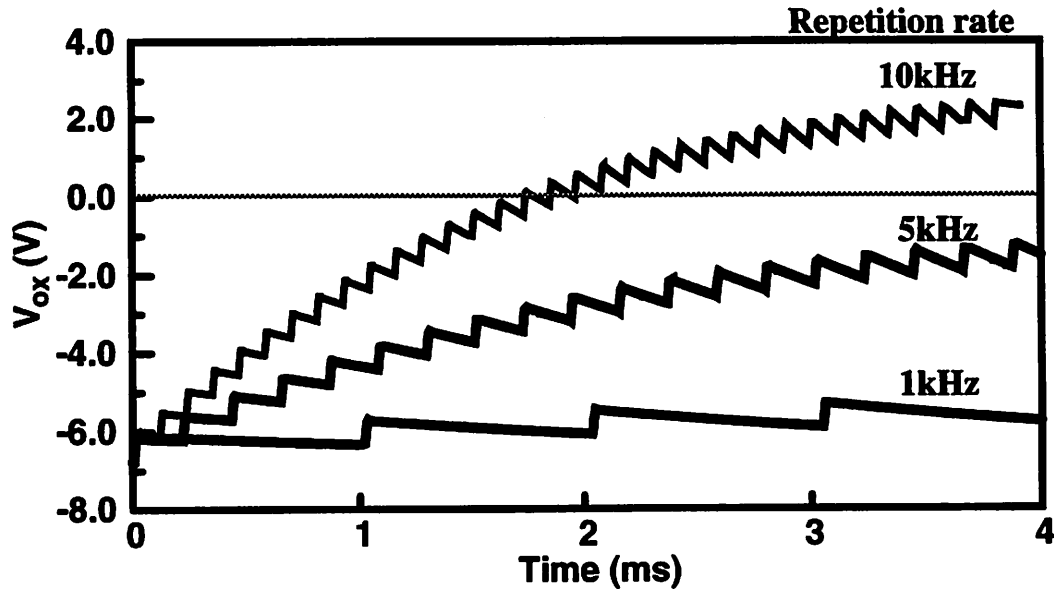


Figure 7-4. Multiple pulse effect in PIII

Multiple pulse effect for three different pulse repetition rates (1kHz, 5 kHz, and 10kHz) using an ideal $1\mu\text{s}$ square pulse shape. The respective duty factors for the three conditions are 10^{-3} , 5×10^{-3} , and 10^{-2} . Initially all three conditions are at the same equilibrium, but after several milliseconds of pulsing, they shift to three different steady-states. The plasma conditions are the same as in Table 6-1.

sets up a negative V_{ox} as electrons accumulate on the surface. The magnitude of the voltage drop across the oxide decreases initially as the repetition rate of the pulses increases because the average positive current increases due to the secondary electrons and the average negative electron current decreases. Eventually, the sign of the accumulated charge on the surface changes from negative charge to positive charge, and the magnitude of the voltage drop across the oxide increases rapidly, exceeding the breakdown voltage of the oxide. The frequency at which this rapid increase in voltage occurs is defined as the threshold frequency. Thus charging during PIII limits the maximum pulse repetition rate allowed.

7.5. Pulse shape effects

As the previous calculations show, the millisecond time-scale which the plasma requires to equilibrate after an implantation pulse, affects the wafer surface potential during PIII. If the voltage pulses are too close together then the charge builds up, and a new equilibrium surface potential is reached. The shape of the pulse, which affects the pulse on

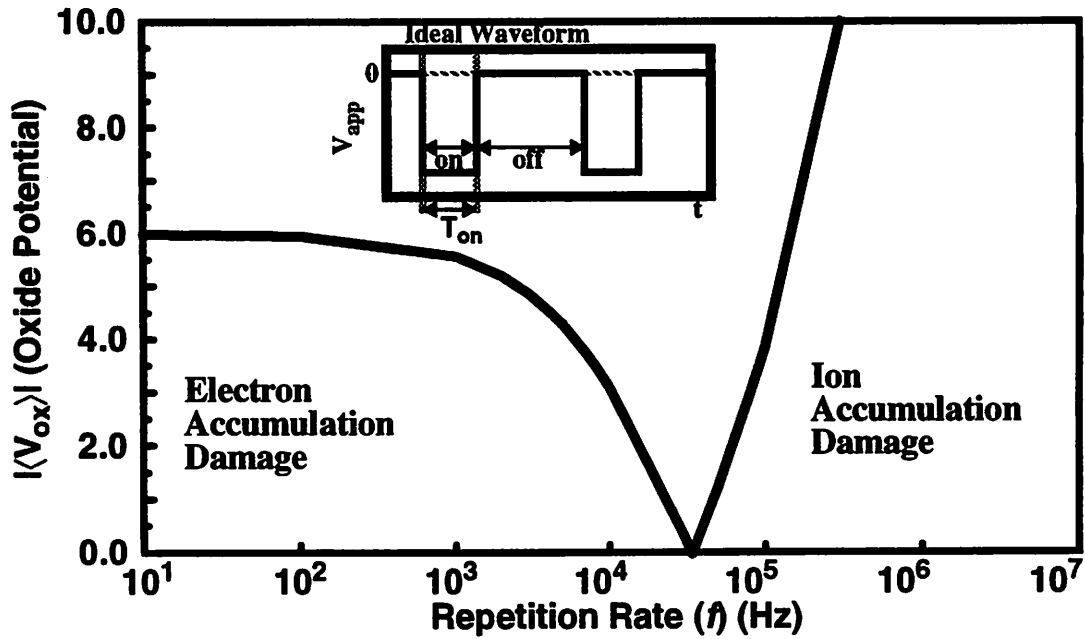


Figure 7-5. Oxide voltage dependence on pulse rate

Frequency dependence of the steady-state time-averaged oxide voltage ($\langle V_{ox} \rangle$) for a 10nm oxide with an ideal square waveform. The shape of the waveform is shown in the insert. The threshold frequency (f_t) is defined as the frequency where $\langle V_{ox} \rangle$ reaches zero, as shown.

time and the implant charge per pulse, changes the parameters in Equation 7-2 altering the total charging behavior. The effect of the pulse shape on charging is shown by examining the general dependencies of charging on two control parameters (the fall time and the pulse width) of the pulse shape.

The fall time of the voltage pulse begins when the applied voltage drops from the peak voltage. When the implantation voltage drops, the ion and secondary electron currents decrease significantly, while the electron current remains negligible since the bias is still negative. Therefore, during the fall time little net current flows. In Equation 7, the fall time causes an increase in the pulse width (T_{on}) and little change in the total charge per pulse. As Figure 7-6 illustrates, the oxide voltage drops at an earlier frequency, and the threshold frequency decreases from that of the ideal square waveform. With larger fall times the threshold frequency decreases, reducing the maximum allowable implantation

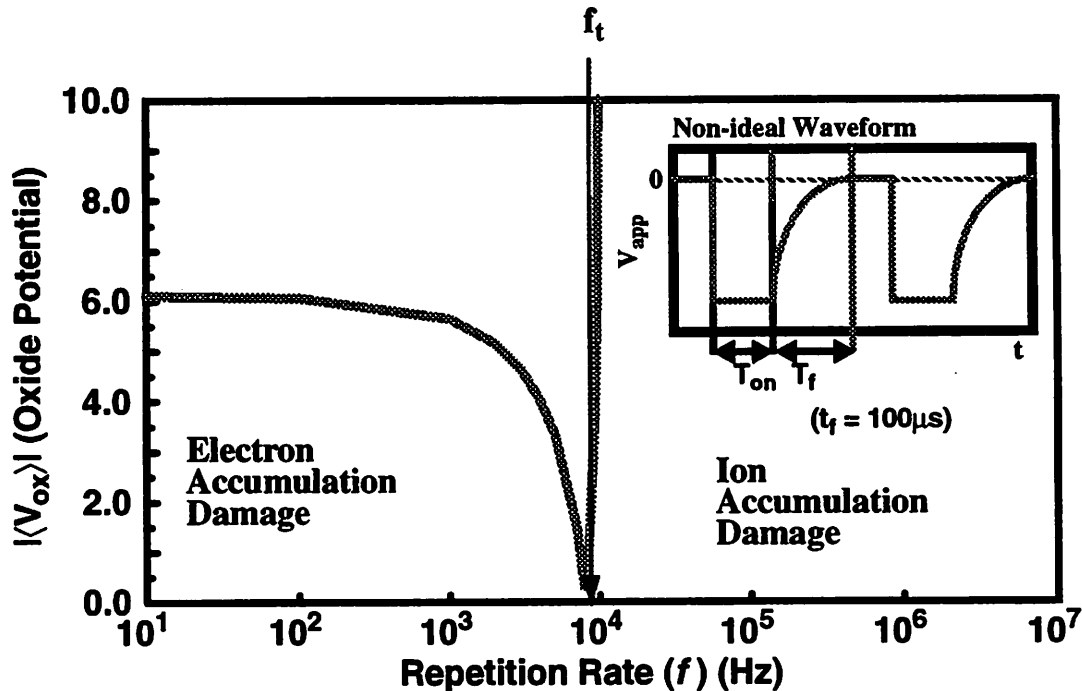


Figure 7-6. Oxide voltage dependence on fall time

Frequency dependence of the steady-state time-averaged oxide voltage ($\langle V_{ox} \rangle$) for a 10nm oxide for a waveform containing a fall time tail. The shape of the waveform is shown in the insert. $\langle V_{ox} \rangle$ is negative in magnitude in the electron accumulation region and positive in ion accumulation.

rate (Figure 7-7). Thus for an optimized implantation pulse, the fall time should be minimized.

The pulse width of the applied bias also affects charging. A longer pulse width increases both the ion charge implanted per pulse (Q_i) and T_{on} . A larger T_{on} decreases the threshold frequency; however, a larger Q_i increases the dose rate at lower repetition rates. The best measure of the optimal pulse width is the average dose rate over one pulse cycle ($1/f$). Figure 7-8 shows the normalized time-averaged implantation current as a function of the repetition rate for three pulse widths: 10ms, 100 μs , and 2 μs . As the pulse width decreases, higher pulse repetition rates are needed to generate the same implant current because shorter pulse widths generate less charge per pulse. However, the threshold frequency for each of these pulse widths shows that the maximum implantation rate occurs

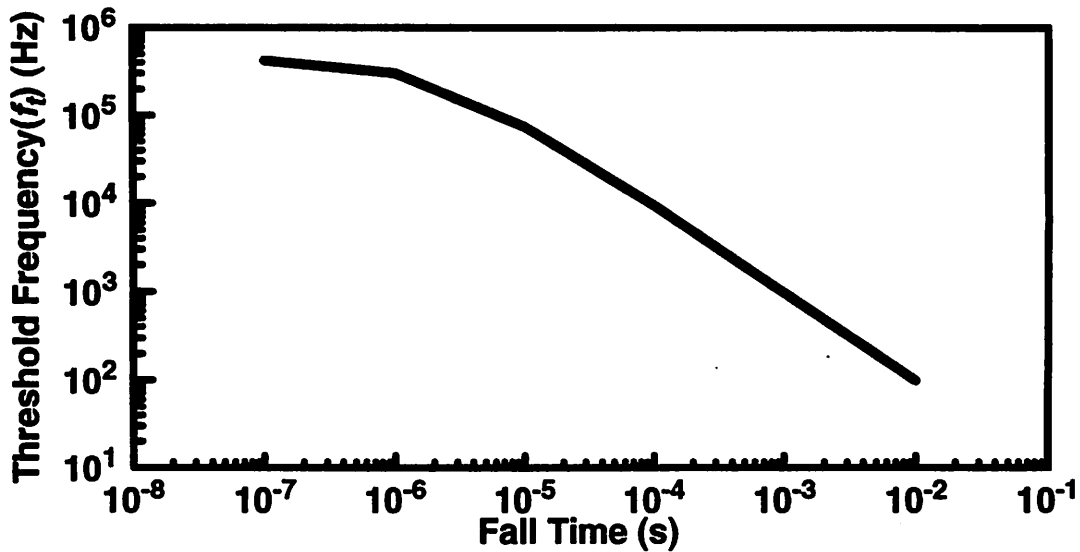


Figure 7-7. Effect of fall time on threshold frequency

Variation of threshold frequency (f_t) as a function of the fall time tail (T_f).

with shorter pulse widths, without exceeding the threshold frequency. To minimize the implantation time for a given implant dose, shorter pulse widths are necessary.

7.6. Comparison Between Simulation and Experiment

Using test capacitors, experiments confirmed the predicted dependence of charging damage on pulsing repetition rate. For a set of six samples, the repetition rate of the PIII pulse waveform was varied from zero to 10 kHz under identical argon plasma conditions for five minutes. For each pulse frequency, we determined the damage induced by measuring the interface trap density using C-V techniques. The test capacitors consisted of 10nm thick gate oxide with 500nm LOCOS (local oxidation) field oxide. The gate electrode was made of evaporated aluminum with an area of 250 μ m by 250 μ m.

The simulator used measured plasma parameters and voltage waveform to determine the oxide voltage (V_{ox}) generated by each process run. Without any implantation pulsing, the simulator predicted that V_{ox} was 6V, which is enough to generate a small quantity of tunneling charge through the oxide and cause oxide reliability degradation. As Figure 7-9 shows, the simulator predicts that the magnitude of V_{ox} decreases with increasing repetition rate until the threshold frequency is about 8kHz. As the pulse repetition rate

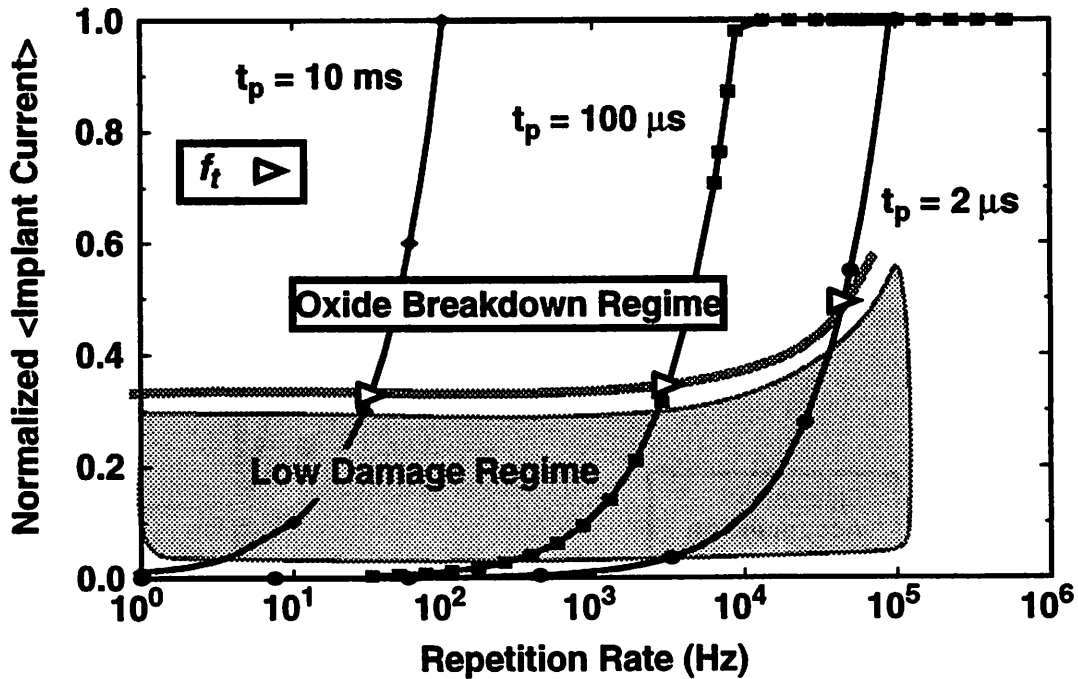


Figure 7-8. Effect of pulse width on charging damage

Normalized, steady-state, and time-averaged implant current as a function of repetition rate for three different pulse widths. All pulses are ideal with no fall time tail. The threshold frequency (f_t) of each pulse waveform is plotted as a threshold boundary for severe oxide damage.

increases beyond the threshold frequency, the magnitude of V_{ox} increases rapidly above the oxide breakdown voltage. Experimentally, the samples show a decrease in the interface trap density (Q_{it}) up to the threshold frequency. Beyond the threshold frequency, the rapid increase in the oxide voltage causes complete oxide failure in the samples. Thus, the experimental results show the same charging damage trend as predicted by simulation, demonstrating that the simulator can predict charging damage trends in PIII.

7.7. Conclusions

The time-dependent charging damage in PIII is accurately simulated by using a few basic plasma relations for the relevant plasma current components. Due to the finite plasma currents, the plasma is shown to require many milliseconds to re-equilibrate a floating surface after a voltage pulse. This equilibration time is not dependent on the quantity of charge deposited per pulse, implying that the equilibration time cannot be reduced significantly by

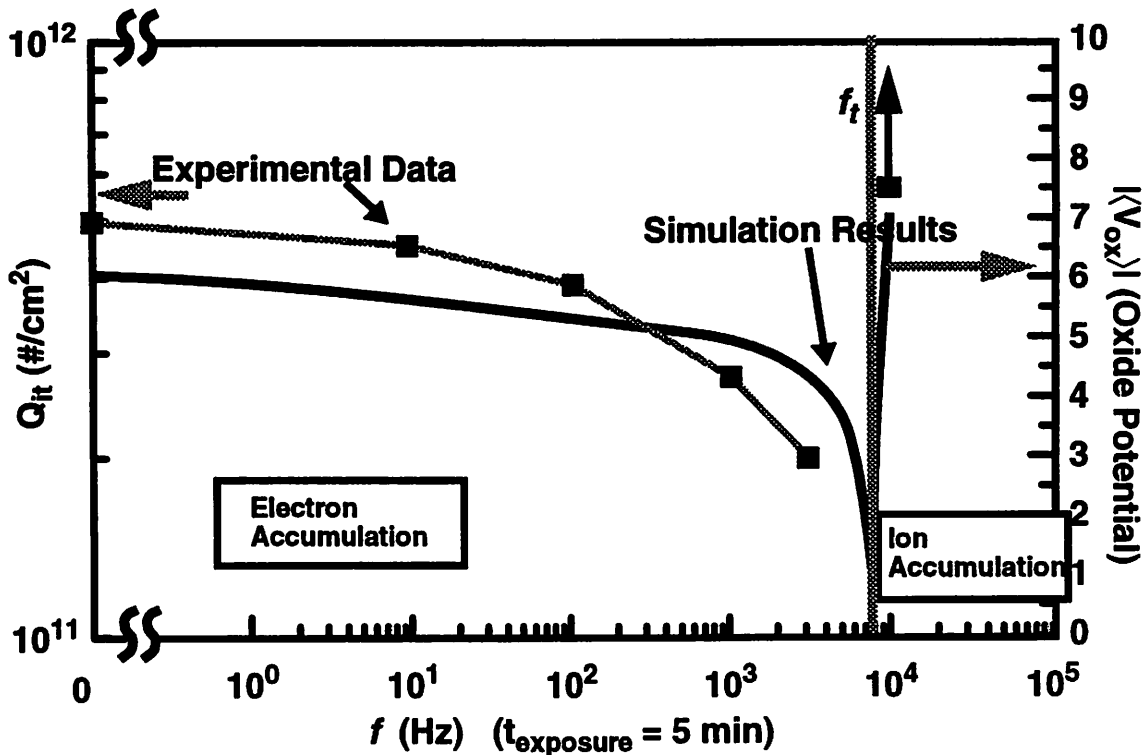


Figure 7-9. Simulation & experiment on the multiple pulse effect

Comparison between simulation and experiment for the dependence of oxide charging damage on pulse repetition rate. Simulation curve shows relation of $\langle V_{ox} \rangle$ for a 10nm gate oxide as a function of pulse repetition rate, and the experimental curve of the interface trap density (Q_{it}) for six different pulse repetition rates correlates qualitatively with the simulation results.

changing the shape of the pulse. The long equilibration time causes V_{ox} to shift at pulse repetition rates above several Hz. For a given pulse shape and plasma condition, a maximum pulse repetition rate exists, which delineates the electron and ion accumulation regions. Beyond this threshold frequency the oxide fails because V_{ox} increases rapidly with respect to the pulsing frequency, exceeding the oxide breakdown voltage. Simulation results of the dependence of V_{ox} on pulsing repetition rate are correlated with experimental data. In addition, the simulation predicts that lower electron temperature, short pulse widths around $2\mu\text{s}$, and rectangular pulse shape will minimize the charging damage and maximize the allowable implantation rate for PIII processing.

References

- [7.1] W. En and N. W. Cheung, "Wafer charging monitored by high frequency and quasi-static C-V measurements," Nucl. Instr. and Meth. in Phys. Res., B74, pp. 311-313, 1993.

8 Device Structure Effects

8.1. Introduction

Oxide charging damage in thin gate dielectrics is consistently a concern for integrated circuit processing. As gate oxide thicknesses decrease with future generations of integrated circuits, the voltage necessary to induce charging damage will decrease, potentially enhancing the oxide charging problem. Since experimental results have shown device structure affects charging damage, the model described in this work can be used to examine the mechanisms by which the structures enhance or reduce the damage induced.

8.2. IC Device Structures of Interest

A variety of IC device structures are of interest in studying charging damage. The simplest device to fabricate is the MOS (Metal Oxide Silicon) capacitor. To determine the charging damage in the MOS capacitor, the I-V characteristics of the oxide must be known. In addition, several structures common to IC circuits can enhance the damage induced, which are the antenna structure and local metal lines for electro-static discharge. All of these device structure effects are implemented in the coupled charging model.

8.2.1. Simple MOS capacitor

The simulations begin with a simple MOS capacitor. The simulation shows how the potential drop across the oxide varies with the time varying potential. Initially, when the voltage pulse is applied to the substrate, virtually all of the voltage drop falls across the plasma. This occurs because the plasma acts as a very small capacitor in series with the much larger MOS capacitor. The large negative potential attracts ions from the plasma and the surface charges up. A voltage drop is generated across the oxide due to the current coming from the plasma. The charge induced on the capacitor by the implantation pulse is

a combination of positive implant charge and secondary electrons which leave positive charge behind. The amount of charge deposited, and hence the voltage generated across the gate oxide depends on the applied bias. If the applied bias is left on for a long time, the oxide will eventually charge up to the point where breakdown occurs [8.1]. If the voltage pulse is kept short enough then there will be no significant change in voltage drop across the MOS capacitor. Figure 8-1 shows the change in potential drop across a 10nm oxide

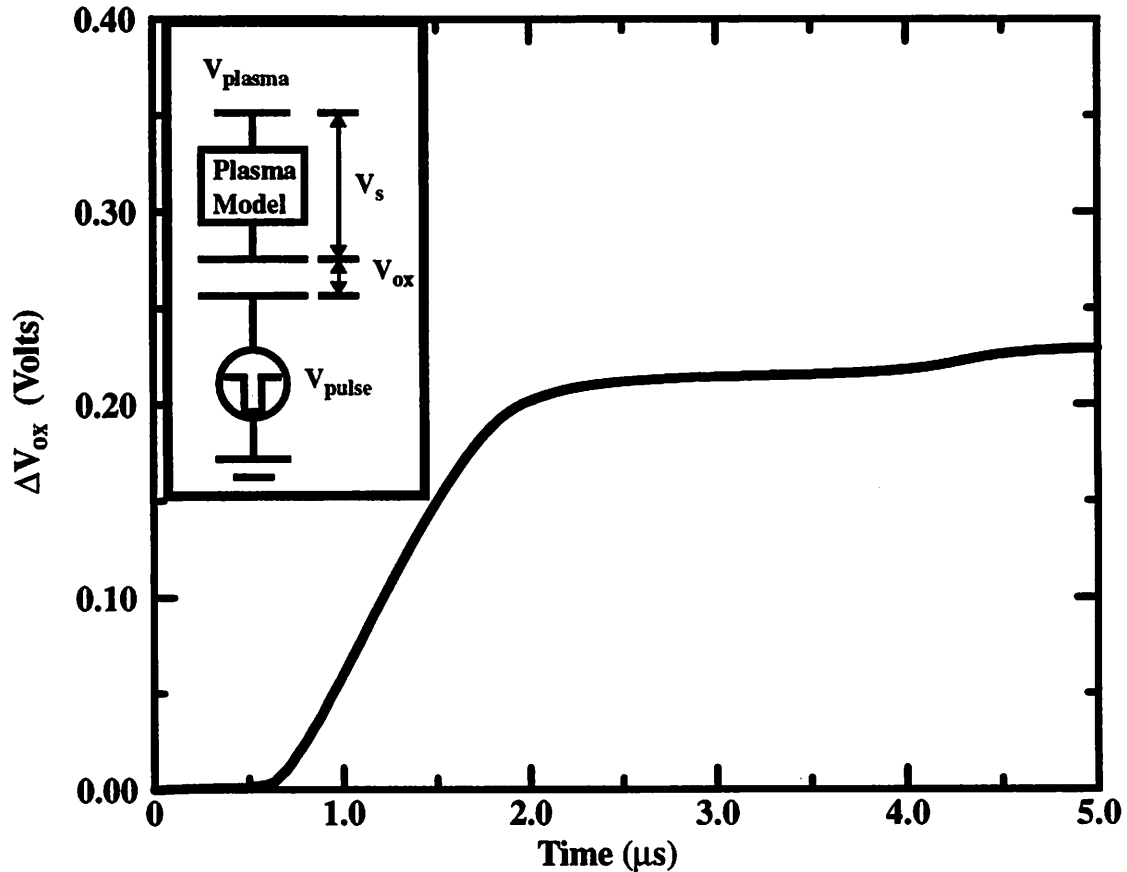


Figure 8-1. Thin oxide modeling

Simulation of a plasma coupled with a MOS capacitor representing a 10nm gate oxide. The change in surface potential is due to a 10kV implantation pulse

after a 10kV pulse is applied. We see that for this case, due to the voltage pulse, there is only a 0.2 volt change in potential, which is insufficient to cause charging damage by itself. Previous experimental work has shown that such pulses at low repetition rates do not induce damage to the oxide [8.2]. Either multiple pulses at high repetition rate accumulat-

ing large positive charge on the surface, or a net dc voltage offset induced by the plasma (i.e. the surface floating potential) is needed to cause damage.

8.2.2. Fowler-Nordheim tunneling current through gate dielectric

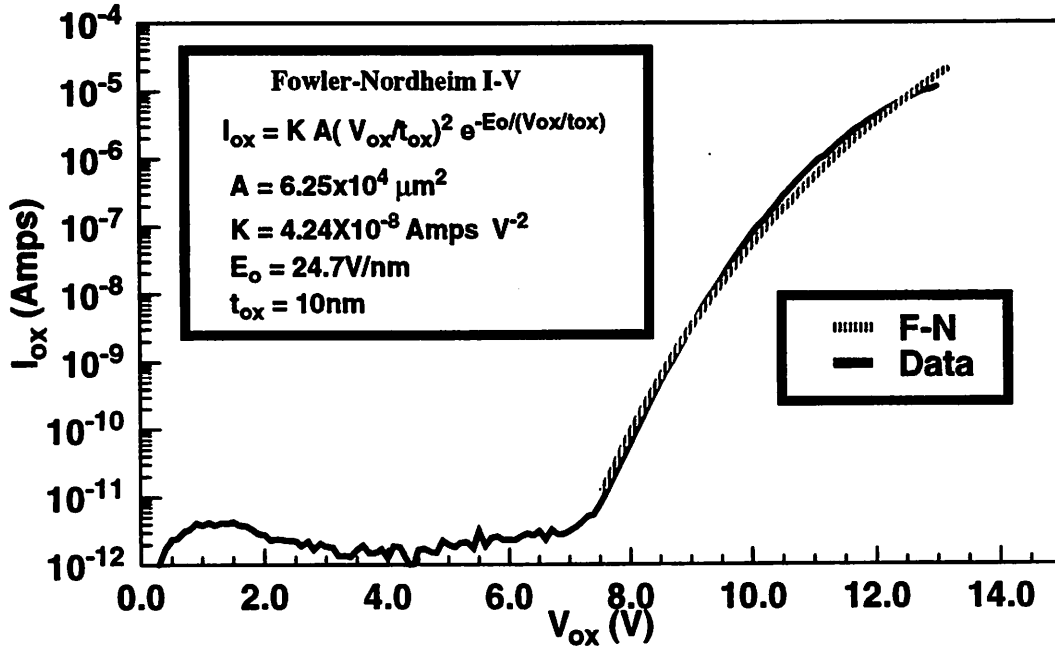


Figure 8-2. Fowler-Nordheim I-V characteristics

10nm oxide I-V characteristics correlates with Fowler-Nordheim tunneling theory.

To quantify the damage induced by the implantation, we need to include the Fowler-Nordheim tunneling current through the gate oxide. The Fowler-Nordheim tunneling current has been identified as the mechanism by which thin oxides are degraded. Following the concept of charge to breakdown, the charge that tunnels through the oxide can be used to determine how much damage has occurred [8.3,8.4,8.5]. The Fowler-Nordheim tunneling mechanism has been well characterized and a universal analytical I-V relation is known:

$$I_{F-N}(V_{ox}) = KA (V_{ox}/t_{ox})^2 e^{-E_0/(V_{ox}/t_{ox})} \quad [8-1]$$

where V_{ox} , t_{ox} , A , K , and E_0 are the voltage drop across the oxide, the oxide area, the oxide thickness, and universal constant coefficients related to the oxide material respectively.

The I-V characteristics of our 10 nm oxides are measured, and correlate well to the Fowler-Nordheim I-V characteristics of 10nm oxide, as shown in Figure 8-2. Thus the analytical I-V relation of the Fowler-Nordheim tunneling can be used as an additional non-linear circuit element in parallel with the gate oxide capacitance, which allows the determination of the current that flows through the oxide during PIII. Figure 8-3 shows how the addition of

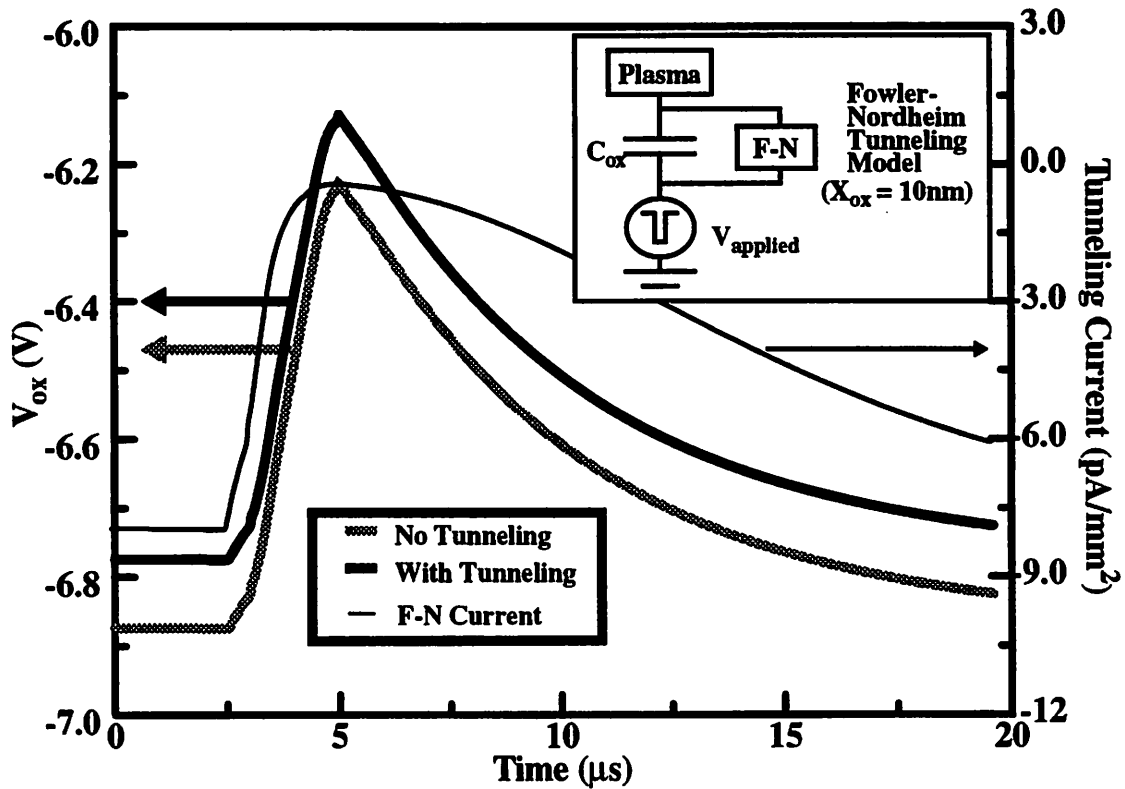


Figure 8-3. F-N tunneling model

Simulation of a plasma coupled with a MOS capacitor representing a 10nm gate oxide. The Fowler-Nordheim tunneling model is included in parallel with the capacitor. A dc voltage shift is observed between the surface potential with the tunneling model and the surface potential without the tunneling model.

the Fowler-Nordheim relation to the oxide model reduces the magnitude of the voltage drop across the oxide during PIII. Since a net current flows through the oxide, the surface potential shift has to shift from the floating potential. Due to the non-linear nature of the Fowler-Nordheim current, a rapid drop occurs in the magnitude of the tunneling current through the gate oxide during the application of a voltage pulse because of the small drop

in the magnitude of the bias. Thus, for this plasma condition, the tunneling current during the pulse is low because of the drop in the magnitude of the oxide voltage.

8.2.3. Electro-static discharge

One of the simplest device structures to examine Electro-Static Discharge (ESD) effects is two conductive interconnects on different oxide thicknesses very close to each other. Such IC structures can occur when polysilicon interconnects over thick field oxide come close to polysilicon gates over thin gate oxide. The polysilicon interconnect over the thick oxide can charge up to a much higher potential than the polysilicon gate. We modeled this structure as two capacitors with different capacitances. Figure 8-4 illustrates the effect

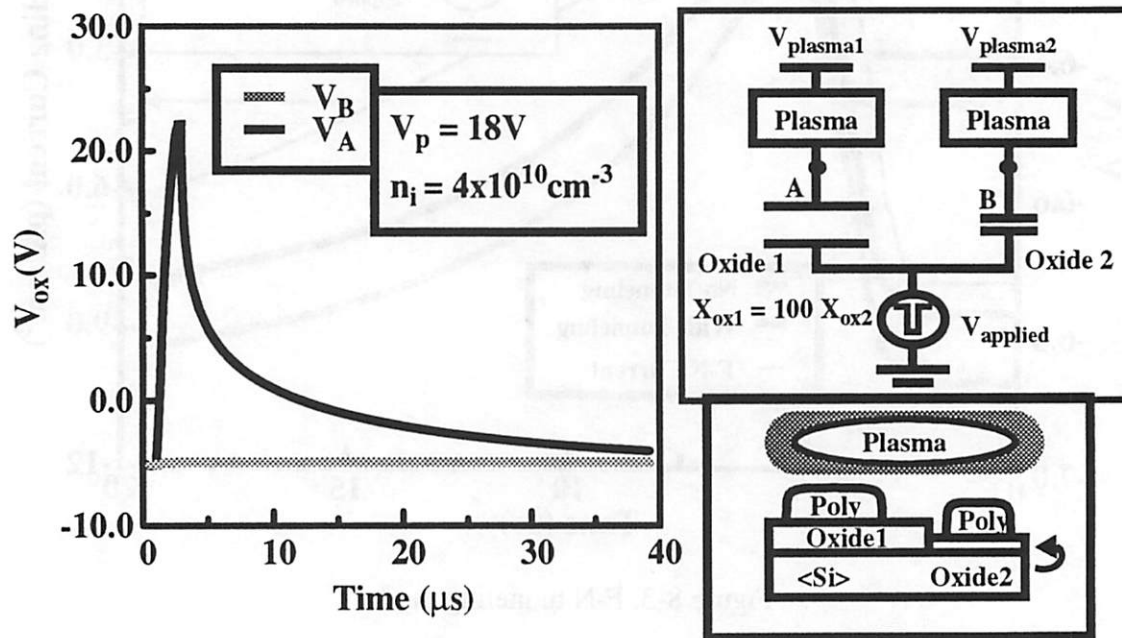


Figure 8-4. ESD in PIII

Simulation of two polysilicon interconnect lines on different oxide thicknesses in close proximity. Oxide 1 and Oxide 2 are 100nm and 10nm thick respectively. Included is a non-uniform plasma ion density. The ion density over oxide 1 (n_{i1}) and oxide 2 (n_{i2}) are $4 \times 10^{10} \text{ cm}^{-3}$ and $2 \times 10^{10} \text{ cm}^{-3}$ respectively. V_A and V_B denote the potential at nodes A and B respectively.

of a single voltage pulse has on the voltage of the polysilicon over the thick oxide (V_A) and over the thin oxide region (V_B). The voltage pulse generates a large voltage difference between V_A and V_B with a maximum of 27 volts. The electric field generated between the

lines could be large enough to induce arcing which would transfer charge to the thin gate oxide, increasing the oxide voltage. The electric field generated will increase with decreasing interconnect spacing, exacerbating the problem. Thus, a potential charging problem with ESD is found through the model.

8.2.4. Antenna effect on oxide charging

An antenna structure occurs in IC layouts when a conductor on thick dielectric is electrically connected to the poly gate. This structure can occur in an IC layout when the polysilicon gate over the gate oxide continues over the field oxide to interconnect with the rest of the circuit. Or the antenna structure could be a metal line over inter-metal dielectric connected through vias and other metal lines to the poly gate. The conductor over the thick oxide acts like an antenna collecting charge for the gate oxide. Charge can flow between the antenna and the polysilicon over the thin gate oxide to create an equipotential surface. An antenna structure can be modeled as two capacitors in parallel connected by a resistor (R_I) between them. The resistor represents the average impedance the charge sees as it is transferred between the field oxide region and the gate oxide region. As devices are scaled down, the gate areas will decrease. However, antenna area is not expected to scale as fast as the gate area, which implies the ratio of antenna area to gate area will increase as devices are scaled down.

The following example illustrates the antenna effect. The field oxide was made $1\mu\text{m}$ thick, one hundred times the thickness of the 10nm gate oxide since a larger oxide thickness difference will increase the charge transfer between the thick oxide and the thin oxide. Also the ratio of antenna area to gate area was set at one hundred because a larger field oxide area will create a larger collection area, which will funnel more charge to the gate oxide. Figure 8-5 shows the simulation results for the antenna structure. The primary difference between this simulation and the ESD simulation is the inclusion of R_I . We observe that the voltage drop across the field oxide decreases, as compared to the ESD case, and the voltage drop across the gate oxide increases dramatically. This is due to the charge sharing between the two capacitors. The voltage variation between the two capacitors is induced due to the finite impedance between them. Initially, as the surfaces are

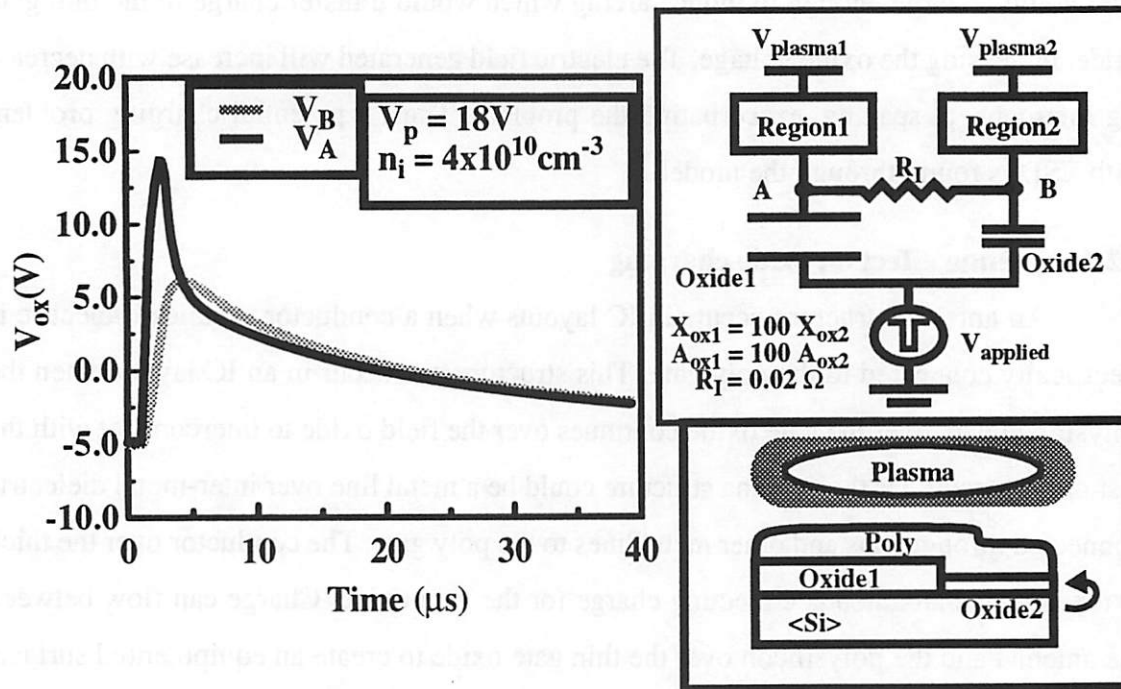


Figure 8-5. Antenna structure

Simulation of an antenna structure. Oxide 1 and oxide 2 are 1mm and 10nm thick respectively. Included is a non-uniform plasma ion density. The ion density over oxide 1 (n_{i1}) and oxide 2 (n_{i2}) are $4 \times 10^{10} \text{ cm}^{-3}$ and $2 \times 10^{10} \text{ cm}^{-3}$ respectively. V_A and V_B denote the potential at nodes A and B respectively. Initially current flows from the field oxide to the gate oxide. During discharge, current flows from the gate oxide to the field oxide.

charged up by the implantation, current flows from the field oxide to the gate oxide. After the implantation pulse is turned off, the field oxide region discharges faster than the gate oxide region and thus the current reverses and flows from the gate oxide to the field oxide. The voltage drop across the gate oxide can become large with the antenna, resulting in potential significant charging due to a single pulse.

8.3. Conclusions

Both the plasma and the device structures can be coupled together in order to study the charging effects induced by PIII. The simple IC structures indicate how oxide charging is affected by device geometrical factors. Antenna structures can enhance the charge induced per pulse due to charge flow from the antenna to the thin oxide. Also, nearby lines on thick oxide can attain much higher potentials than the thin oxide region due to a single

pulse resulting in potential electrostatic discharge effects. By incorporating the Fowler-Nordheim tunneling model, the oxide damage induced during PIII can be quantified.

References

- [8.1] T. Sheng, S. B. Fetch, and C. B. Cooper III., "Characteristics of a plasma doping system for semiconductor device fabrication," *Journal of Vacuum Science & Technology B*, vol. 12, no. 2, pp. 969-72, 1994.
- [8.2] W. En and N.W. Cheung, "Wafer charging monitored by high frequency and quasi-static C-V measurements," in *Nuclear Instruments & Methods in Physics Research, Section B*, vol. B74, no.1-2, pp. 311-313, 1993.
- [8.3] R. Moazzami, J. Lee, I. C. Chen, and C. Hu, "Projecting the minimum acceptable oxide thickness for time-dependent dielectric breakdown," *International Electron Devices Meeting. Technical Digest*, pp. 710-713, 1988.
- [8.4] T. Kusaka, Y. Ohji, and K. Mukai, "Time-dependent dielectric breakdown of ultra-thin silicon oxide," *IEEE Electron Device Letters*, vol. 8, no. 2, pp. 61-63, 1987.
- [8.5] P. P. Apte and K. C. Saraswat, "Correlation of trap generation to charge-to-breakdown (Q_{bd}): a physical-damage model of dielectric breakdown," *IEEE Transactions on Electron Devices*, vol. 41, no. 9, 1595-1602, 1994.

9 Effects of Plasma Characteristics on PIII

9.1. Introduction

Using the coupled charging damage model the effect of plasma conditions on damage can be simulated. Since measured physical plasma parameters are used in the relations for the plasma currents, those parameters can be varied and the effect of each plasma parameter can be determined. Thus, for the typical ranges of the electron temperature and ion density, the optimal plasma condition for charging damage in PIII was found. In addition to examining the effect of plasma parameters, the effect of the uniformity of the plasma on charging damage can be modeled.

9.2. Plasma Electron Temperature Dependence

For typical plasma sources, the electron temperature varies from about 2eV to 8eV. However, the exponential dependence of the plasma electron current on the electron temperature implies that even small variations in the electron temperature can cause large variations in the charging damage.

The effects of the electron temperature on charging are best illustrated by observing the changes in the oxide voltage versus bias repetition rate curve. For higher electron temperatures, the voltage drop across the oxide decreases faster and starts to decrease at a lower repetition rate. This occurs because the higher electron temperature causes a corresponding increase in the plasma potential making a larger barrier to the flux of electrons. This larger barrier slows down the electrons, thus causing the faster drop in the voltage at lower repetition rates. The increase in the magnitude of the voltage drop occurs at a lower repetition rate for higher T_e for the same reason. To illustrate the effect of the electron tem-

perature on charging damage, Figure 9-1 shows the variation of the magnitude of the volt-

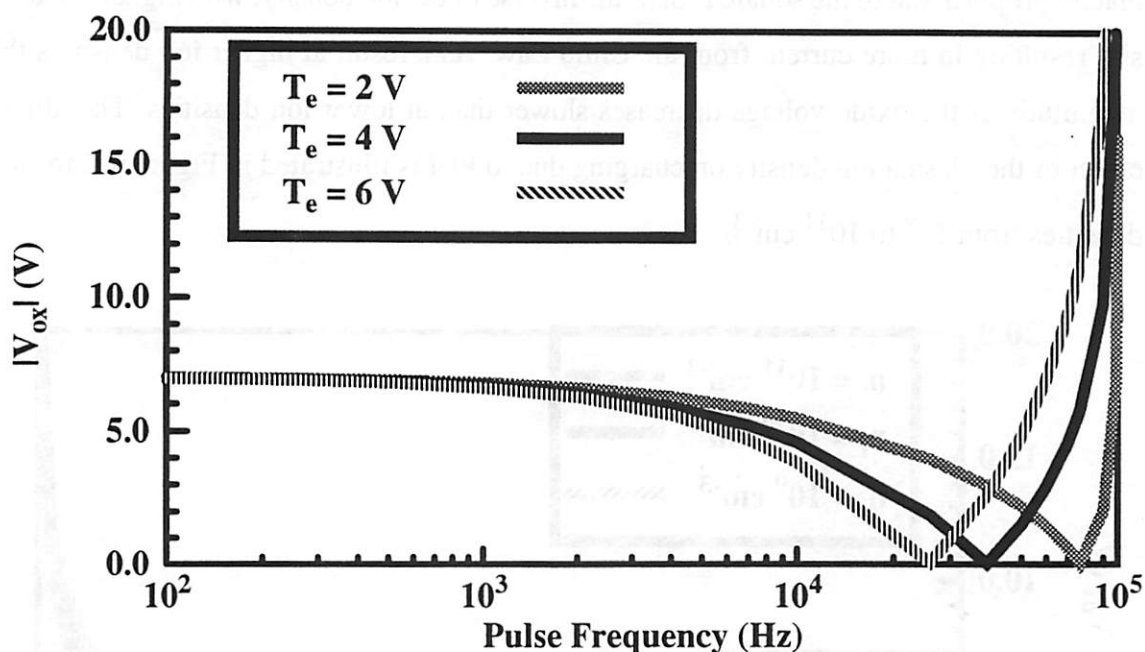


Figure 9-1. Electron temperature dependence

The voltage drop across a 10nm gate oxide as a function of the applied voltage pulse frequency. The pulse width is 1ms and peak voltage of -5kV. Three different electron temperatures are used, 2, 4 and 6 V, holding all other parameters constant. The constant plasma conditions are $n_i = 10^{10} \text{cm}^{-3}$ and $V_f = -7\text{V}$.

age drop across the oxide as a function of the repetition rate of the waveform for electron temperatures of 2, 4 and 6 eV.

9.3. Plasma Ion Density Dependence

The plasma ion density indirectly affects charging in PIII. To first order, the plasma ion density is linearly proportional to the implanted charge per pulse. The condition that an individual pulse does not induce charging by itself still holds for even the maximum ion density is investigated. In the bulk of a plasma, the ion density is equal to the electron density. Therefore, the increase in charge per pulse generated by the increase in ion density is associated with an increase in the plasma electron current. Thus, the equilibration rate is the same for all ion densities of interest. However, a second order non-linear effect causes the charge per pulse to increase slightly sub-linearly with respect to the ion density. This

second order effect is due to a small reduction in the sheath thickness, which is approximately proportional to the square root of the inverse of the ion density, with higher ion density resulting in more current from the Child Law. As a result at higher ion densities the magnitude of the oxide voltage decreases slower than at lower ion densities. This direct effect of the plasma ion density on charging due to PIII is illustrated in Figure 9-2 for ion densities from 10^9 to 10^{11} cm^{-3} .

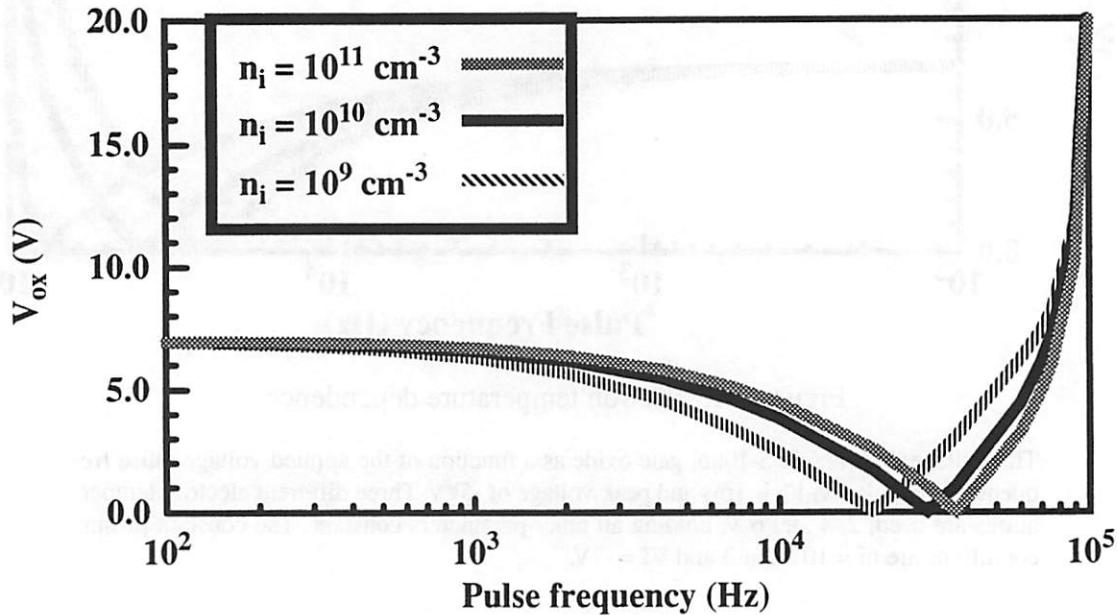


Figure 9-2. Ion density dependence on pulsing

The voltage drop across a 10nm gate oxide as a function of the applied voltage pulse frequency. The pulse width is 1ms and peak voltage of -5kV. Three different ion densities are used, 10^{11} , 10^{10} , and 10^9 cm^{-3} holding all other parameters constant. The constant plasma conditions are $T_e = 4\text{eV}$, $V_p = 20\text{V}$, and $V_f = -7\text{V}$. The effect of the ion density variation on the voltage drop versus pulse frequency curve is illustrated.

More important than the direct effect is the relation of the ion density, implant rate and charging to each other. An increase in the ion density increases the implant rate significantly, reducing the implantation time required for a given dose. A shorter implantation time reduces the oxide damage due to plasma exposure. Figure 9-3 shows that at higher ion densities, the PIII process can achieve much higher implant rates with less oxide damage than at lower ion densities.

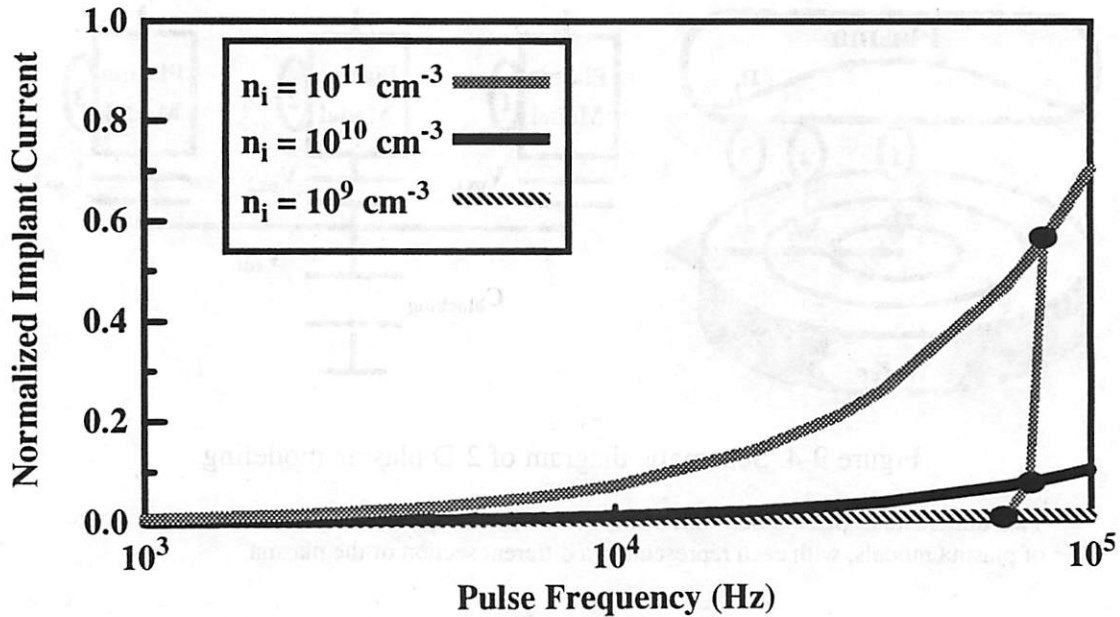


Figure 9-3. Ion density dependence on throughput

Normalized implant current as a function of the applied voltage pulse frequency. The implant current is normalized to the maximum physical implant rate for an ion density of 10^{11} cm^{-3} . The voltage pulse is 1ms wide. Three different ion densities are used (10^{11} , 10^{10} , and 10^9 cm^{-3}) while holding all other parameters constant. For any given pulse frequency, a higher ion density provides a higher implant rate. The three solid circles indicate the maximum allowable dose rate for a given oxide stress condition of 8V

9.4. Plasma Uniformity Effects

Another source of charging damage is plasma non-uniformity. Previous experimental results have shown enhanced charging damage in non-uniform plasmas [9.1]. Current theory suggests that the non-uniform plasma can induce charging damage by generating current loops across the wafer and into the plasma. Using the coupled charging damage model the effect of plasma non-uniformity can be observed.

The non-uniformity effect can be modeled by using the distributed network approach as shown in Figure 9-4. Each plasma element in the model represents a section of the plasma. In this example, the plasma has been divided into concentric rings, representing a plasma with radial non-uniformity, which is the most common non-uniformity observed. Since the plasma has been divided into concentric rings, each plasma element can be weighted by the wafer surface area it represents. For each plasma element, all of the

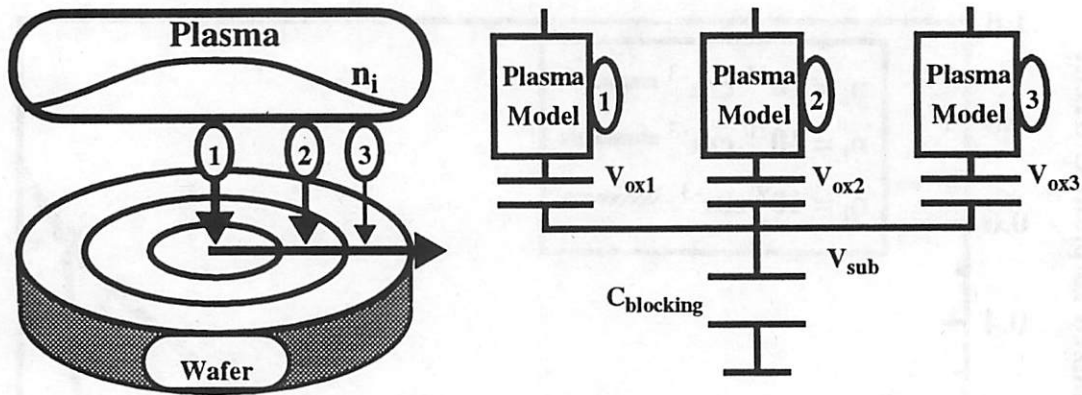


Figure 9-4. Schematic diagram of 2-D plasma modeling

Two dimensional plasma non-uniformity effects are modeled using a distributed network of plasma models, with each representing a different section of the plasma.

plasma parameters can be varied, representing the actual variation of the plasma characteristics due to the non-uniformity.

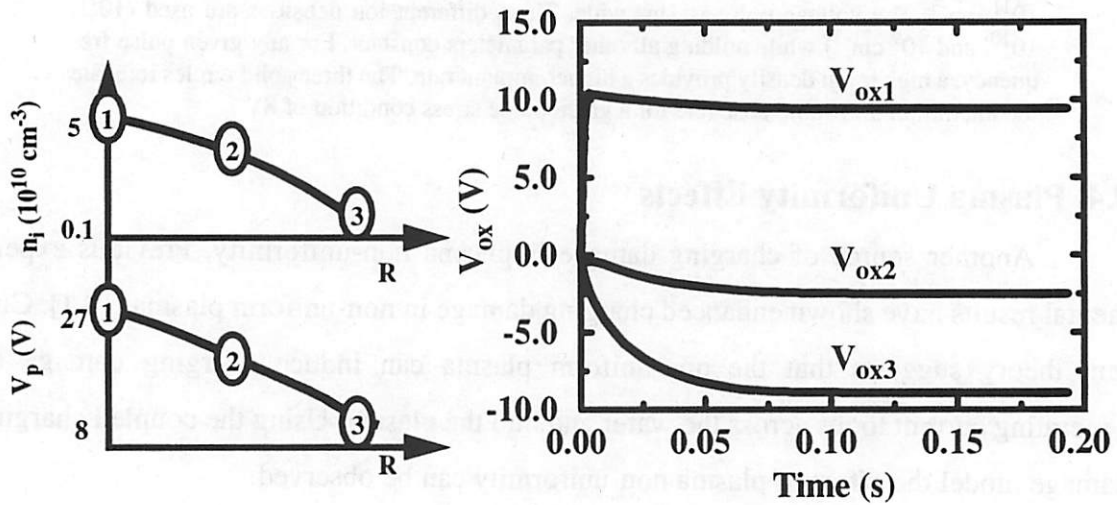


Figure 9-5. Simulation of plasma non-uniformity

Simulation of radial ion density and plasma potential variation, showing positive charging damage in the center and negative damage on the edge of the wafer.

As an example, Figure 9-5 shows a non-uniformity in the ion density and the corresponding non-uniformity in the plasma potential which reflects the density variation. As

a result of the plasma non-uniformity, the oxide voltage in the center of the wafer charges positively and the oxide voltage at the edge of the wafer charges negatively. This voltage variation induces a current flow from the center of the wafer to the edge.

The oxide voltage variation arises from the fact that the substrate of the wafer is exposed to the entire plasma where the floating gate of the oxide is only exposed to a local portion of the plasma. The substrate effectively averages the plasma and is biased to a mean potential. However, since each of the capacitors only sees the local plasma, they are biased either positively or negatively with respect to the substrate. Thus, current can flow from the center of the wafer to the edge of the wafer and through the plasma.

9.5. Implications on the Choice of Plasma Sources

Currently there are a myriad of different high density plasma sources available for use in PIII. The two plasma parameters of interest in terms of charging are the ion density and the electron temperature. Figure 9-6 surveys the phase space for a variety of high density plasma sources as a function of ion density and electron temperature [9.2,9.3,9.4,9.5,9.6]. For comparison, a parallel plate RIE plasma is included. Though the reported data shows small differences, these differences may just be due to the limits of the particular operation conditions used, and may not represent the full capabilities of each source. Essentially, all of these decoupled plasma sources are capable of generating high ion density and a range of electron temperatures. Our simulation work clearly indicates the preference for low electron temperature for low oxide charging damage. The plasma ion density has been shown to have only a second order effect on oxide damage. However, using a high ion density reduces the PIII processing time which will reduce the length of time that the devices are being stressed.

9.6. Conclusions

The dependence of oxide charging on the plasma parameters during PIII is illustrated by the coupled charging model. This model has been shown to accurately determine the time dependent current generated in PIII and the charging trends due to variations in the applied voltage waveform. A lower electron temperature is shown to reduce the charging damage induced by PIII. Ion density is shown to be only a second order effect on charg-

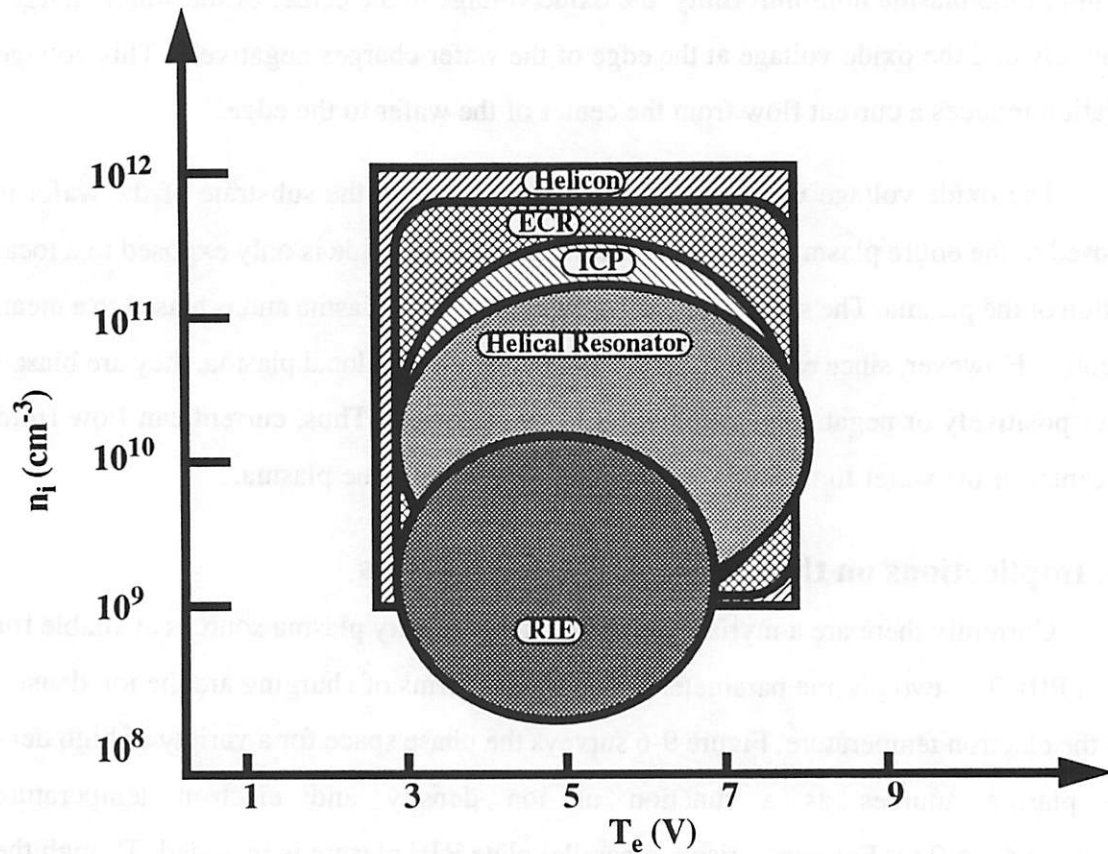


Figure 9-6. Plasma sources phase space of ion density and electron temperature

Phase space of ion density versus electron temperature for various high density sources that could be used in PIII. The phase space for an RIE reactor is shown for comparison.

ing damage in PIII. However, a higher ion density decreases the implant time which reduces oxide damage due to plasma exposure time. Finally, the non-uniformity of the plasma has also been shown to induce charging damage by generating currents within the wafer and through gate oxide capacitors from high plasma potential regions to low plasma potential regions.

References

- [9.1] S. Fang and J. P. McVittie, "Oxide damage from plasma charging: breakdown mechanism and oxide quality," IEEE Transactions on Electron Devices, vol. 41, no. 6, pp. 1034-1039, 1994.

- [9.2] J. Hopwood, C.R. Guarnieri, S. J. Whitehair, and J. J. Cuomo, "Electromagnetic fields in a radio-frequency induction plasma," *Journal of Vacuum Science & Technology A*, vol. 11, no. 1, pp.147-151, 1993.
- [9.3] J. Hopwood, C.R. Guarnieri, S. J. Whitehair, and J. J. Cuomo, "Langmuir probe measurements of a radio frequency induction plasma," *Journal of Vacuum Science & Technology A*, vol. 11, no. 1, pp.152-156, 1993.
- [9.4] A. J. Perry, D. Vender, and R. W. Boswell, "The application of the helicon source to plasma processing," *Journal of Vacuum Science & Technology B*, vol. 9, no. 2, pp.310-317, 1991.
- [9.5] K. Niazi, A. J. Lichtenberg, M. A. Lieberman, and D. L. Flamm, "Operation of a helical resonator plasma source," *Plasma Sources, Science and Technology*, vol. 3, no. 4, pp. 482-95, 1994.
- [9.6] V. A. Godyak and N. Sternberg, "Dynamic model of the electrode sheaths in symmetrically driven RF discharges," *Physical Review A*, vol. 42, no. 4, pp. 2299-2312. 1990.

10 Additional Damage Effects in Plasma Processing

10.1. Introduction

Charging damage effects are not only limited to current interactions between the plasma, device structure and substrate bias. Though interactions in the system induce the damage, other mechanisms can enhance the charging damage effects. These additional charging damage effects illustrate the interactive nature of charging damage and the many possible sources.

10.2. Coupled Antenna Effect

The device structure described in Chapter 8 shows the antenna effect as a result of pulsing in PIII. However, even without the pulsed bias, the antenna structure can still enhance charging damage. The severity of this aspect of the antenna effect depends on the plasma condition as well as the antenna ratio. Thus, it is a good example of how charging damage effects depend on the interaction between the plasma, device structure, and substrate bias.

10.2.1. Mechanisms of antenna effect

An antenna structure electrically connected to a thin gate oxide can collect charge from the plasma and enhance the charging damage on the device. This antenna effect can be described by a load line. The I-V characteristics of the thin gate oxide are described by the Fowler-Nordheim Tunneling model. For this example a 10nm thick gate oxide with out any antenna is used with the substrate grounded. The I-V characteristics of the plasma (I_{no} antenna) are shown in Figure 10-1 along with the I-V characteristics of the oxide. The inter-

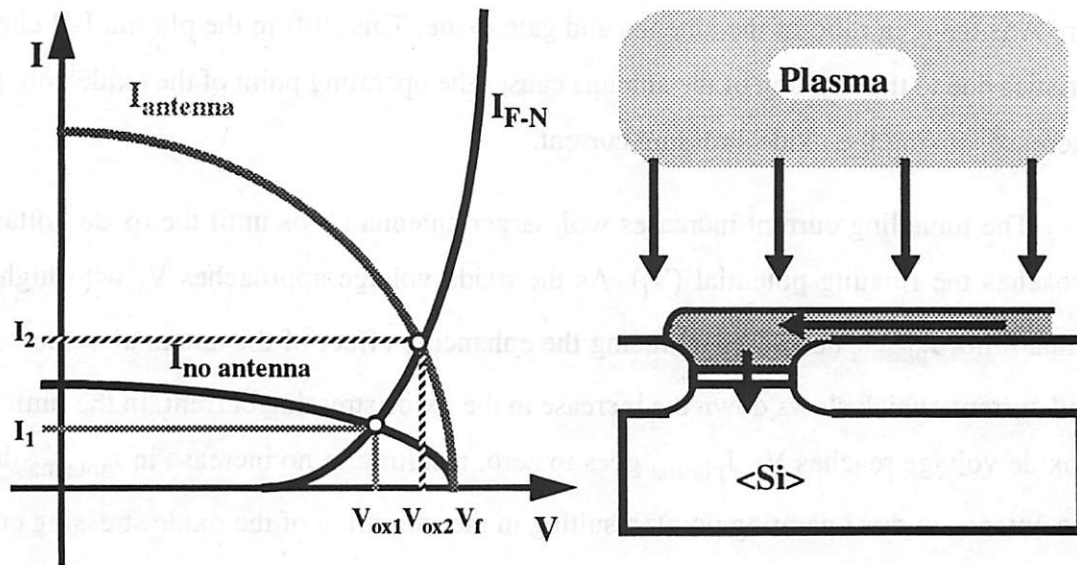


Figure 10-1. Load line of plasma and oxide for antenna effect

The plasma I-V characteristics shift when the antenna ratio increases, resulting in a higher oxide voltage and higher tunneling current.

section of the two curves defines the operating point for the particular plasma and thin oxide combination with V_{ox1} and I_1 as the stressing voltage and current respectively.

When an antenna is connected to the thin gate oxide, the magnitude of the I-V characteristics of the plasma increases inducing more charging damage. For a uniform plasma, the current collected by a surface is proportional to the area. So the I-V characteristics for the antennaless case is:

$$I_{no\ antenna} = A_1 J_{plasma} \quad [10-1]$$

where A_1 and J_{plasma} are the area of the oxide and the plasma current density. With an antenna of area A_{ant} electrically connected to the gate electrode, the plasma current becomes:

$$I_{antenna} = (A_{ant} + A_1) J_{plasma} \quad [10-2]$$

By combining Equation 10-1 and Equation 10-2 the relation between the antenna ratio and plasma current can be found:

$$I_{\text{antenna}} = (A + 1) I_{\text{no antenna}} \quad [10-3]$$

where A is the area ratio of the antenna and gate oxide. This shift in the plasma I-V characteristics due to the addition of the antenna causes the operating point of the oxide voltage to increase, raising the oxide stressing current.

The tunneling current increases with larger antenna ratios until the oxide voltage approaches the floating potential (V_f). As the oxide voltage approaches V_f with higher antenna ratio, J_{plasma} decreases, reducing the enhancing effect of the antenna on the collected current, which slows down the increase in the oxide stressing current. In the limit as the oxide voltage reaches V_f , J_{plasma} goes to zero, resulting in no increase in I_{antenna} due to the antenna at this operating point, resulting in the saturation of the oxide stressing current.

The effect of the antenna on the tunneling current is illustrated in Figure 10-2. The

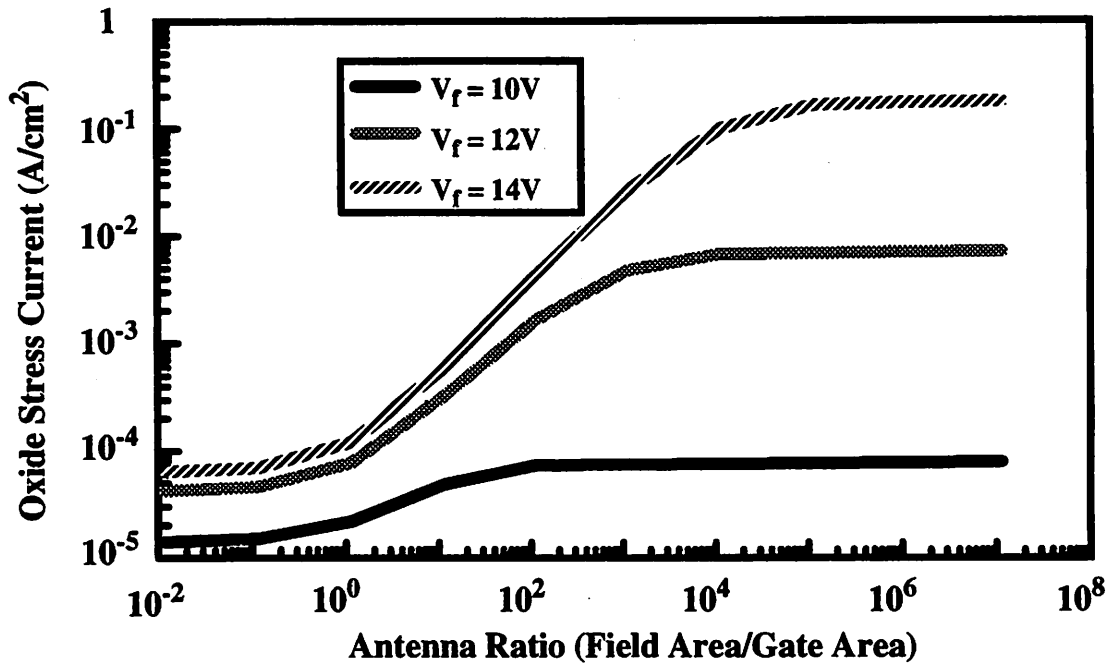


Figure 10-2. Stressing current dependence on antenna ratio

Increasing antenna ratio increases stressing current until current saturates. The stressing current decreases with lower floating potential (V_f) and saturates at a lower value.

larger the antenna ratio, the larger the current until the voltage saturates at the floating

potential. Thus, the antenna can increase the charging damage by multiplying the magnitude of the effective plasma I-V characteristics.

10.2.2. Conclusions

The plasma conditions and the antenna structure combine together to induce the antenna charging damage effect. The interdependence of the two implies that by varying the plasma conditions, the charging damage for a given antenna ratio can change. If the plasma condition can be changed such that the floating potential is low, then even a large antenna ratio will be acceptable. However, if the plasma condition is restricted by other constraints, such as etch rate, preventing the floating potential from being low, then the maximum allowable antenna ratio will be restricted by charging damage constraints. This interaction between the plasma condition and the device structure means a trade-off must be made between a large plasma condition phase space and allowable antenna ratio.

10.3. Damage Enhancement due to Nitride and Oxide Deposition

In this study, charging damage effects are studied in backend plasma process steps. Using antenna MOSFET test structures, the damage after plasma etch and deposition steps is quantified by measuring the threshold voltage. From wafer splits at six different plasma steps, deposition is found to enhance damage by increasing hydrogen trapping, and etching is found to cause damage after the oxide is etched to the metal. From these experimental results, direct charging damage is attributed to the etching processes while charging damage enhancement is attributed to the deposition processes.

Charging damage has been reported in etching processes for many years. Recently plasma deposition processes have also been attributed to charging damage. Through a factorial process optimization, damage in an oxide deposition process was found to increase with plasma power [10.1]. So essentially whatever the plasma process, etching or deposition, if the plasma charges can induce sufficient voltage across a gate oxide, then charging damage will occur.

10.3.1. Experiment

This study investigates charging damage effects in a variety of backend plasma processes. Using a typical metallization process, six different plasma process steps were chosen for investigation: metal etch, oxide deposition 1, oxide etch, oxide deposition 2, nitride deposition, nitride/oxide etch, as shown in Figure 10-3. These six process steps are

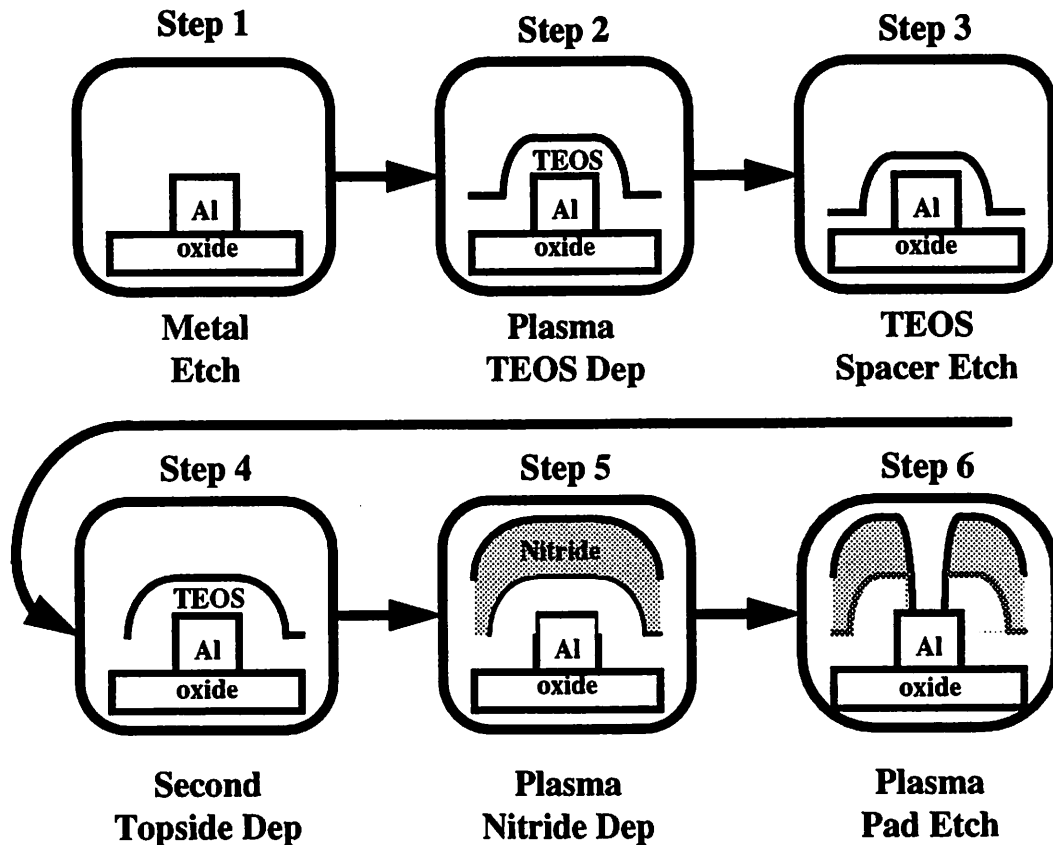


Figure 10-3. Backend plasma process steps investigated

Schematic of the six backend processing steps investigated: step 1 plasma etch of metal, step 2 plasma TEOS oxide deposition, step 3 plasma oxide etch, step 4 plasma oxide deposition, step 5 plasma nitride deposition, step 6 plasma nitride and oxide etch. The six steps represents a typical backend process from the final metal layer to a finished device.

the basic plasma etch and deposition steps required for metallization.

To determine the charging damage, a batch of six test wafers is processed together through to metal etch. At each of the six process steps of interest a wafer was pulled from the flow. Thus the quantity of damage induced up to each of the six steps could be deter-

mined, providing a picture of the damage for each of the steps as well as for the entire process.

To enhance the charging damage, antenna structures in the metal layer were attached to the gate oxide. Two different antenna ratios were used: 65k:1 and 5k:1. By using two different antenna ratios, any increase in damage with antenna ratio could be observed.

In addition, on the same die, identical devices with protection diodes were monitored to determine the effect of the diode on charging damage. The protection diodes are placed in parallel with the gate oxide and are reversed biased during normal circuit operation. Leakage current from the protection diodes should prevent damaging charge from accumulating across the gate oxide, in order to eliminate charging damage for the protected device. Thus, the diode protected devices provide characteristics of devices without charging damage.

The damage was quantified using test MOSFET devices with antenna structures. The test MOSFETs allowed the measurement of several device parameters to determine the effect of charging damage. Three device parameters were focused on: threshold voltage (V_t), sub-threshold swing (S), and transconductance ($g_m = dI_d/dV_g$). For each of these parameters the quantity used to quantify the charging damage is the percent change of the parameter from the nominal or undamaged value. Since the diode protected devices do not show any charging damage, the parameter values of the diode protected devices determined the nominal values for each corresponding die. Since some of the damage can be passivated by hydrogen bonding, a small ($\sim 1\text{mC}/\text{cm}^2$) amount of charge was passed through the oxide to activate the damage. This amount of charge is sufficient to activate the damage but not to induce any measurable damage by itself. Five dies across the wafer were measured to determine the variation of the damage.

10.3.2. Results

From measurements of the three device parameters for all six splits, charging damage effects are found in both deposition and etching steps. The damage for both the

deposition and etch depended on the thickness of the deposited material and the material type. As expected, the charging damage increased with antenna ratio.

The charging damage causes the sub-threshold slope (S) to increase and the transconductance (g_m) to decrease. However, the threshold voltage (V_t) first decreases and then increases with charging damage as seen in Figure 10-4. Thus, for the threshold voltage a small amount of charging damage can cause it to decrease, but further damage will cause it to increase.

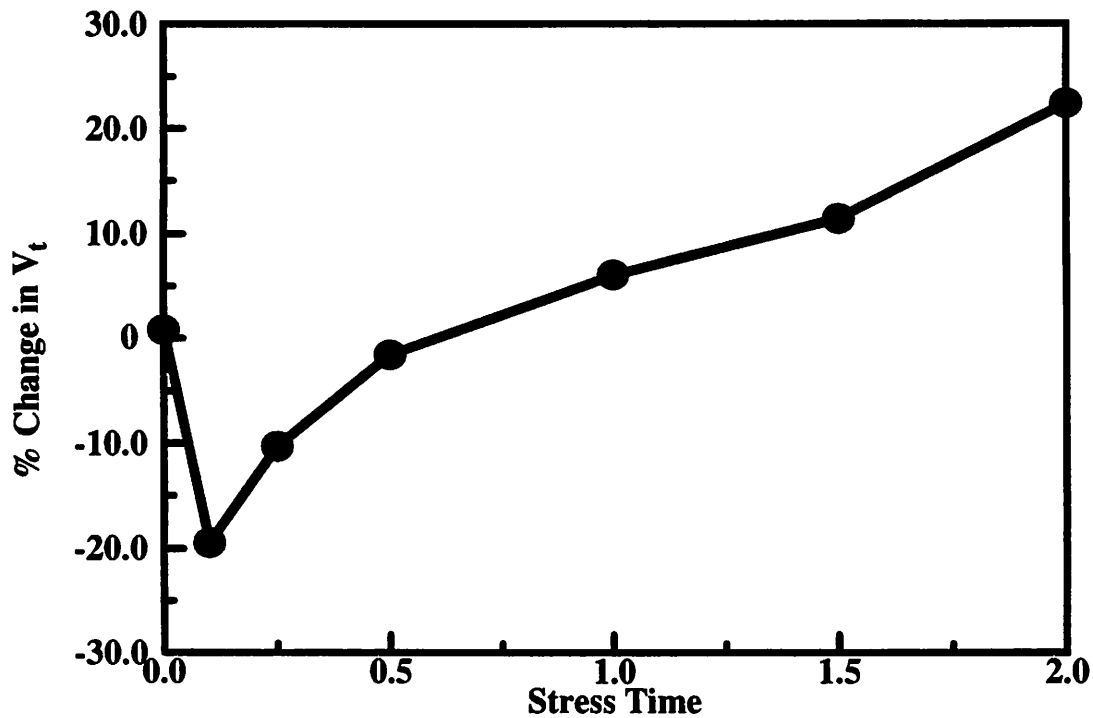


Figure 10-4. Change in V_t versus stress time

Percent change in threshold voltage as a function of stress time for a good gate oxide. Charging damage is seen to first induce a negative V_t shift and then a positive shift.

The damage was found to be uniform across the wafer with variation from 2% to 20% variation. The variation in the damage increased with more charging damage. As a result, the charging damage for each wafer is represented by averaging the percent change for the five measured devices per wafer. For the 65k:1 antenna ratio MOSFET, Figure 10-

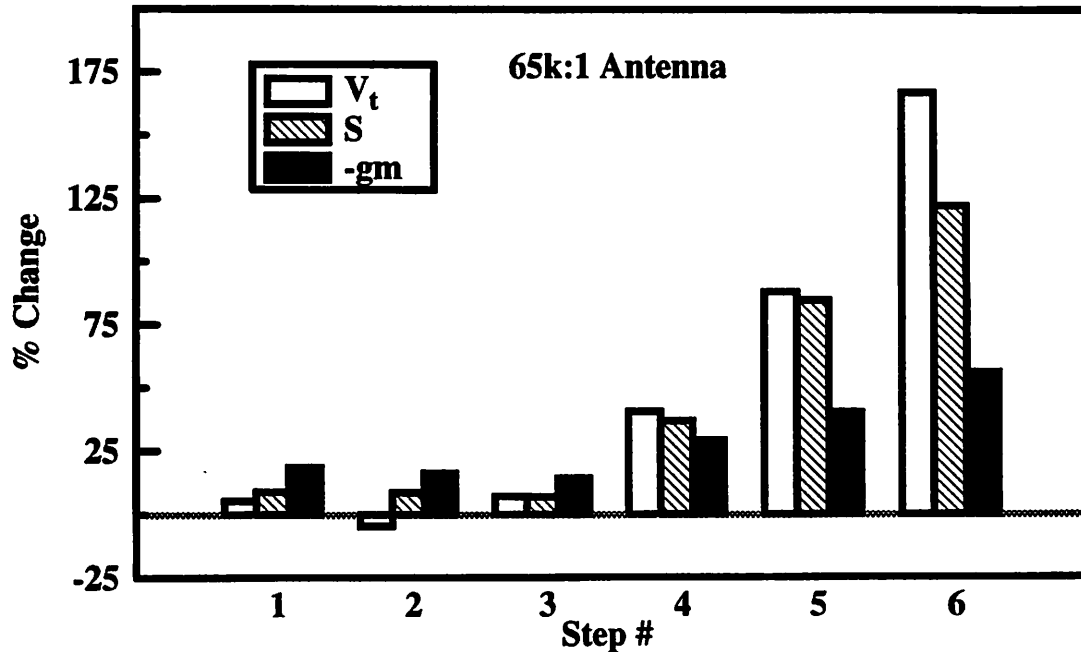


Figure 10-5. Charging damage for 65k:1 antenna ratio devices

Percent change of threshold voltage (V_t), sub-threshold swing (S), and - transconductance (-gm) for 65k:1 antenna ratio MOSFETs for wafers stopped after each of the six process steps. The same damage trends are observed in all three parameters.

5 shows the average % change in V_t , S, and gm, and Figure 10-6 shows the same for the 5k:1 antenna ratio device.

The oxide deposition damage was found to be dependent on the thickness of the oxide deposited. Step 2 (oxide deposition 1) deposited 200nm of oxide and step 4 deposited 800nm of oxide. Correspondingly, the damage for step 2 is minimal as seen by the small drop in V_t , small increase in S, and small drop in gm. With thicker oxide deposition more damage is observed. And corresponding to the thicker deposited oxide in step 4, the damage is much larger than in step 2.

Step 5, nitride deposition, shows even more damage than the oxide deposition steps. For the 65k:1 antenna ratio device, the nitride deposition causes about a 40% change in V_t and about half that for the 5k:1 device, with corresponding changes in S and gm. The effect on the device parameters for the nitride deposition is larger than that of step 4, second oxide deposition. So nitride deposition has a significant effect on the device parameters.

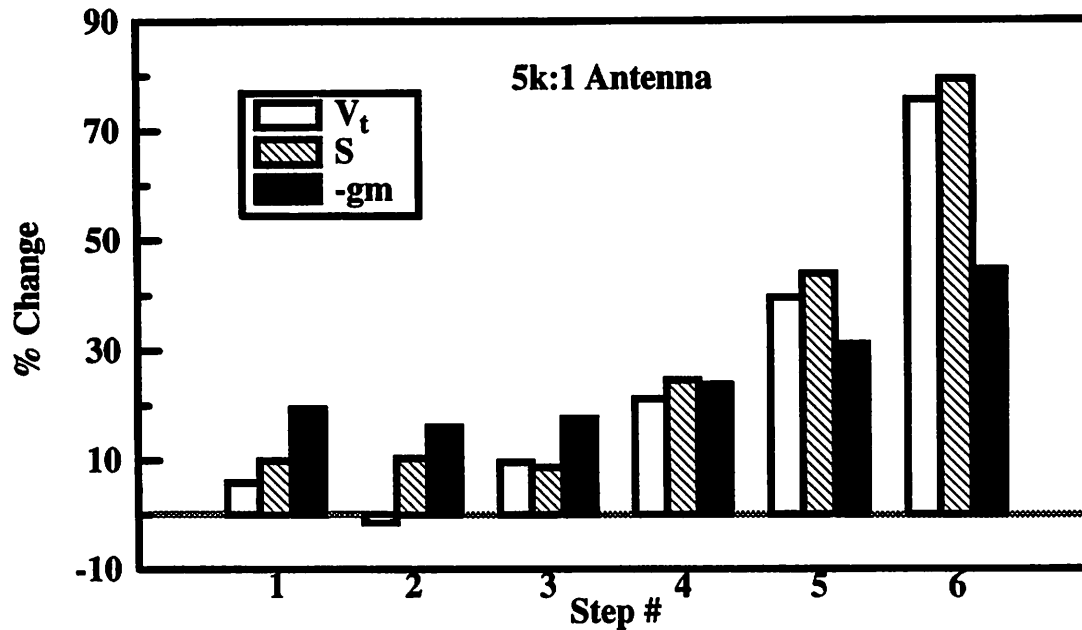


Figure 10-6. Charging damage for 5k:1 antenna ratio devices

Percent change of threshold voltage (V_t), sub-threshold swing (S), and - transconductance (-gm) for 5k:1 antenna ratio MOSFETs for wafers stopped after each of the six process steps. The same damage trends are observed in all three parameters. Damage trends are also similar to the 65k:1 antenna ratio devices but with a smaller magnitude.

In both etching processes, charging damage was measured. For the first etching process, step 3, a very small variation in the parameters occurred. However, for the second etch step, step 6, more damage than any other process step was observed. In this step a very long over etch is required to ensure that all of the oxide is removed for the contact pads, resulting in a long plasma exposure of the metal pads.

Finally, no measurable damage was observed with the diode protected devices. Figure 10-7 and Figure 10-8 show the percent variation of the three measured device parameters for the 5k:1 and 65k:1 devices respectively. Here the percent variation is determined by the variation of the device parameter after $1\text{mC}/\text{cm}^2$ of stressing charge passed through the gate oxide. As Figure 10-9 shows, very little parameter variation occurs for the diode protected devices unlike the unprotected ones.

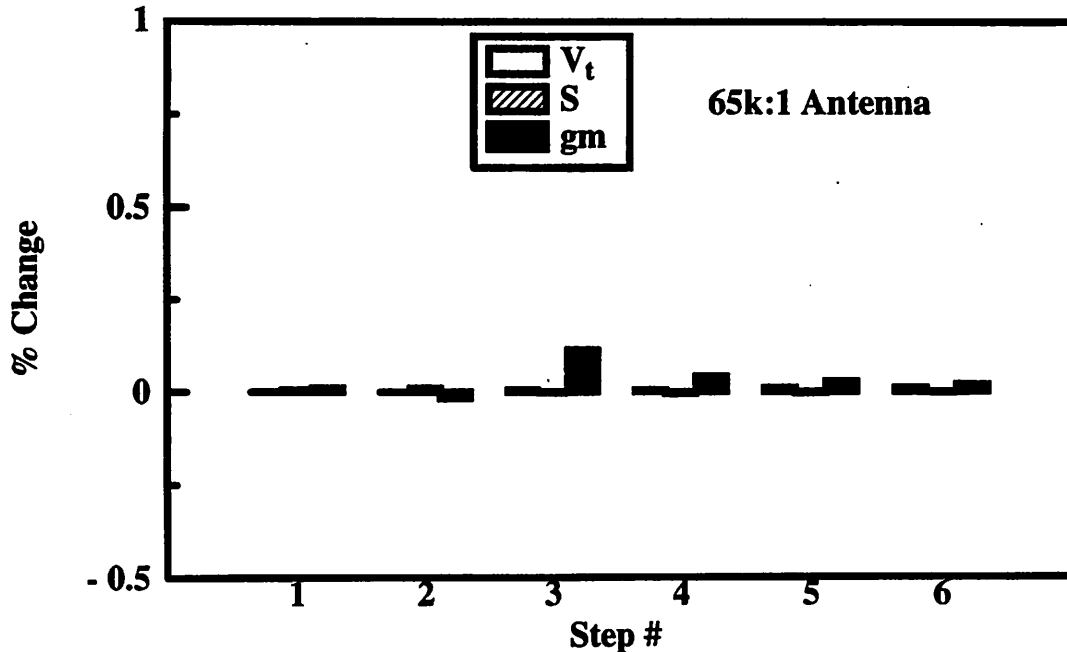


Figure 10-7. Charging damage in diode protected 65k:1 antenna ratio devices

Percent change of threshold voltage (V_t), sub-threshold swing (S), and transconductance (g_m) for 65k:1 antenna ratio MOSFETs with diode protection in parallel with the gate oxide. Within error, no change was observed in all three parameters. Thus, no charging damage was observed for devices stopped after each of the six process steps.

10.3.3. Discussion

The charging damage observed can be explained by two different mechanisms. The observed etching damage follows the conventional pattern charging damage as expected. However, for the deposition damage, the insulating material being deposited prevents the plasma charge from reaching the oxide. Thus, another mechanism, which is theorized to involve damage enhancement by either water or hydrogen trapping, must be occurring.

The parameter shifts attributable to the deposition steps can be considered damage enhancement rather than damage inducement. Since the plasma does not have direct electrical contact to the gate oxide, it cannot directly charge up the gate oxide to induce damage. However, damage enhancement in hot electron degradation has been experimentally observed due to the trapping of hydrogen for many years [10.2,10.3,10.4]. Moreover, water trapping has recently been proposed as an alternative source for damage enhancement [10.5]. Nitride is impermeable to water and hydrogen, trapping them near the gate

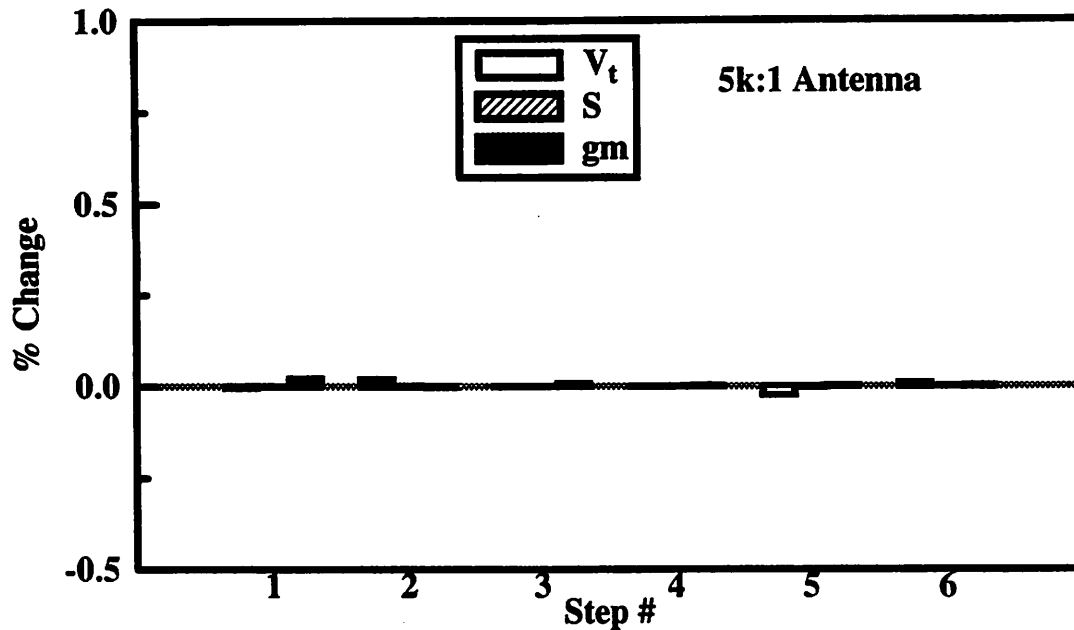


Figure 10-8. Charging damage in diode protected 5k:1 antenna ratio devices

Percent change of threshold voltage (V_t), sub-threshold swing (S), and transconductance (g_m) for 5k:1 antenna ratio MOSFETs with diode protection in parallel with the gate oxide. Within error, no change was observed in all three parameters. Thus, no charging damage was observed for devices stopped after each of the six process steps.

oxide. Deposited oxide can be a source for the hydrogen or water for damage enhancement. Hence, for the oxide deposition steps, the thinner oxide would have less damage because it contains less hydrogen or water and also because it does not trap them as well as a thicker oxide. In addition, the nitride deposition step would have more damage than the oxide steps because the nitride is a much better barrier to water or hydrogen. Damage enhancement by hydrogen or water trapping is therefore consistent with the damage trends seen in Figure 10-5.

Damage enhancement by water or hydrogen trapping may occur when charging damage partially stresses interface bonds. Charging damage has been thought to break interface bonds when generating interface states [10.6]. In addition to breaking bonds, charging damage may also stress some interface bonds, weakening them and forming partially stressed bonds. These partially stressed interface bonds are weaker than a good bond, but not weak enough to be activated during the damage measurement. However, these par-

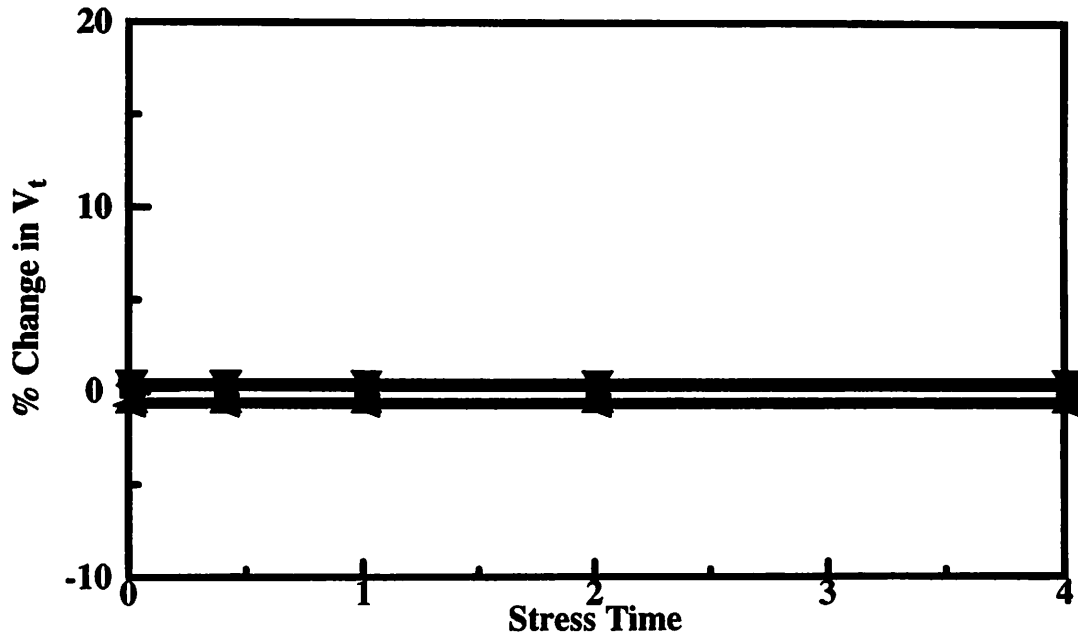


Figure 10-9. Diode protected device stressing

Under the same stressing conditions as the non-diode protected devices, no V_t shift was observed for the devices indicating that no measurable charging damage occurred.

tially stressed bonds are weakened further by the presence of the hydrogen or water at the interface and are now observed in the damage measurement.

Unlike the deposition damage, the etching process induced damage follows a more conventional damage pattern. In step 6, the etching reached the metal layer providing a direct path for the plasma currents to charge and damage the gate oxide. The damage from the first etch step, step 3, is much smaller than the damage from step 6 because it does not have a long over etch step, where the charge can be continuously delivered to the exposed metal layer.

10.3.4. Conclusions

From this study of several backend plasma processes, charging damage effects were found in both deposition and etching steps. The damage, as characterized by percent changes in three device parameters, was induced by two different methods. The first process consisted of typical charging damage and was induced during the etching steps. The second process, which occurred during the deposition steps, was due to hydrogen or water

trapping enhancing the formation of interface traps, enhancing the damage observed. The observed damage for both processes was enhanced by increasing the antenna size from 5k:1 to 65k:1, indicating charging damage occurred rather than other mechanisms.

All of the charging damage effects seen in the test structures were eliminated by the protection diode. Thus, the protection diode provides a structural method for eliminating the charging damage in the backend process. The protection diode allows the damage causing processes to have a much wider process window without restrictions due to charging damage. As a result, though charging damage effects are observed in all of the plasma steps investigated, the use of protection diodes can prevent the damage from occurring.

References

- [10.1] S. Bothra, C. T. Gabriel, S. Lassig, and D. Pirkle, "Control of plasma damage to gate oxide during high density plasma chemical vapor deposition," *Journal of the Electrochemical Society*, vol. 142, no. 11, pp. L208-L211, 1995.
- [10.2] R. C. Sun, J. T. Clemens, and J. T. Nelson, "Effects of Silicon Nitride Encapsulation on MOS Device Stability," in *18th Annual Proceedings of Reliability Physics*. (Las Vegas, NV, USA, 8-10 April 1980), pp. 244-251, 1980.
- [10.3] W. G. Meyer and R. B. Fair, "Dynamic Behavior of the Buildup of Fixed Charge and Interface States During Hot-carrier Injection in Encapsulated MOSFETs," *IEEE Transactions on Electron Devices*, vol. ED-30, no. 2, pp. 96-103, 1983.
- [10.4] R. B. Fair and R. C. Sun, "Threshold-voltage Instability in MOSFETs due to Channel Hot-hole Emission," *IEEE Transactions on Electron Devices*, vol. ED-28, no. 1, pp. 83-94, 1981.
- [10.5] M. Shimaya, "Water Diffusion Model for the Enhancement of Hot-carrier-induced Degradation due to Silicon Nitride Passivation in Submicron MOSFET's," in: *1995 IEEE International Reliability Physics Proceedings* (Las Vegas, NV, USA, 4-6 April 1995), pp. 292-296, 1995.
- [10.6] K. P. Cheung and C. P. Chang, "Plasma-charging damage: a physical model," *Journal of Applied Physics*, vol. 75, no. 9, pp.4415-4426, 1994.

11 Extension of Coupled Charging Model to Other Processes

11.1. Introduction

Since the coupled plasma charging model is not limited to pulsed biases, the model can be extended to other applications such as RF substrate biases used in RIE, PECVD and conventional ion implantation processing. These extensions of the model provide a test of the limits of the assumptions in the model and the accuracy of the model results. In addition, by extending the model, the potential for this methodology to examine charging damage in a variety of processes is illustrated.

11.2. Pulsed RF Bias Modeling

For a typical RIE or PECVD system, the most common substrate bias applied is an RF bias. To study the model's ability to determine the plasma currents generated by an RF bias, we used several frequencies from 300kHz up to 4MHz. To study the turn-on, turn-off, and steady state operation of the RF bias, a pulsed RF bias was chosen.

From these studies the model was found to provide inaccurate results for positive voltage biases above the plasma potential (V_p) and for bias frequencies above 1MHz. Thus, limits of the present model have been identified.

The modulated RF bias is also being investigated to improve etch and deposition processes. By modulating the RF bias, the etching can be maintained or even improved while the charging damage can potentially be reduced. Many studies using capacitively coupled plasmas have modulated both the plasma and substrate bias to improve the etch rate and the profile of the etch [11.1,11.2]. These time-modulated plasmas have been measured [11.3,11.4,11.5,11.6] and simulated [11.7,11.8]. With the advent of decoupled

sources, such as the inductively coupled and electron cyclotron resonance sources, modulating only the bias has also been examined [11.9]. Studies have shown that a time-modulated RF bias can improve the anisotropy of silicon trench etching [11.10].

As the applied bias increases in frequency, some assumptions of the present plasma model may not be valid. The equations for the ion current assume that the ions respond instantaneously to the applied bias. For the pulses used in the PIII case the frequency components of the bias are slow enough to allow the ions to completely cross the sheath before the applied voltage changes significantly. However, as the frequency of the bias increases, the voltage can change so rapidly that the ions do not have time to cross the sheath before the applied bias changes to significantly alter the electric field in the sheath. An upper limit for the maximum frequency at which the ions can respond is the ion plasma frequency:

$$\omega_{pi} = \frac{1}{2\pi} \left(\frac{q^2 n_o}{\epsilon_o M} \right)^{1/2} \quad [11-1]$$

where q , ϵ_o , n_o , and M are the unit charge, permittivity of free space, ion density and ion mass respectively. For a typical ion density of $1 \times 10^{10}/\text{cm}^3$ and M of $6.68 \times 10^{-26} \text{kg}$ (argon ion), the ion plasma frequency is about 3.3MHz. To simulate above the ion plasma frequency, the ion current equations in the model must be modified. At the extreme end, where the bias frequency is much larger than ω_{pi} , the ion current model can be easily modified to become a constant current source because the ions will no longer respond to the instantaneous voltage. At the intermediate frequencies, an ion crossing the sheath would see a time varying electric field due to the variation of the applied bias during the transit of the ion. Instead of being dependent on the instantaneous voltage, the instantaneous ion current would need to be dependent on an integration of the voltage over the ion transit time.

Fortunately, the current trend in ion sources is toward higher ion densities which will allow the current model to be valid at higher frequencies. For example if the ion density is increased to $10^{12}/\text{cm}^3$ then ω_{pi} increases to 33MHz, an order of magnitude increase bringing the standard 13.5MHz frequency well within the range of the model.

11.2.1. Comparison of simulation and experiments

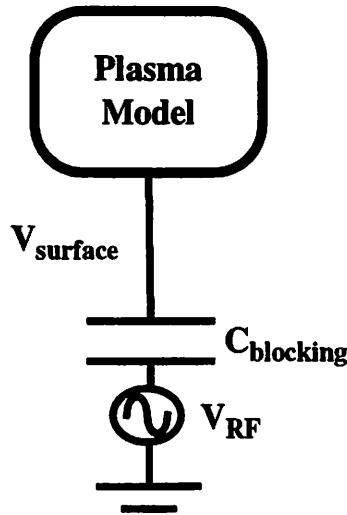


Figure 11-1. Schematic of pulsed RF bias coupled charging model

The pulsed RF bias is placed in series with a blocking capacitor and the plasma model.

To implement the pulsed RF bias requires little change in the model and only a few changes in the experimental setup. In the experiment, the high voltage pulsing system was replaced with an RF pulsed signal generator, RF amplifier, matching network, and blocking capacitor. Since the plasma model remains unchanged, the implementation of the RF bias requires only a change in the applied voltage model. To isolate the RF amplifier a blocking capacitor ($1\mu\text{F}$) was placed in series. These changes in the voltage system are reflected in the simulation by the addition of a capacitor and the plasma, as shown in Figure 11-1.

The experimental conditions of the plasma consisted of 1mtorr argon feed with 900W of input microwave power. This condition is the same as the one used in Chapter 6, resulting in the same plasma characteristics.

Using the measured plasma condition and the measured pulsed RF bias the model was shown to accurately describe the current waveform for a 300kHz pulsed RF bias as shown in Figure 11-2. Since 300kHz is well below the ion plasma frequency, the ions had sufficient time to respond to the bias, keeping the model assumptions valid. The model

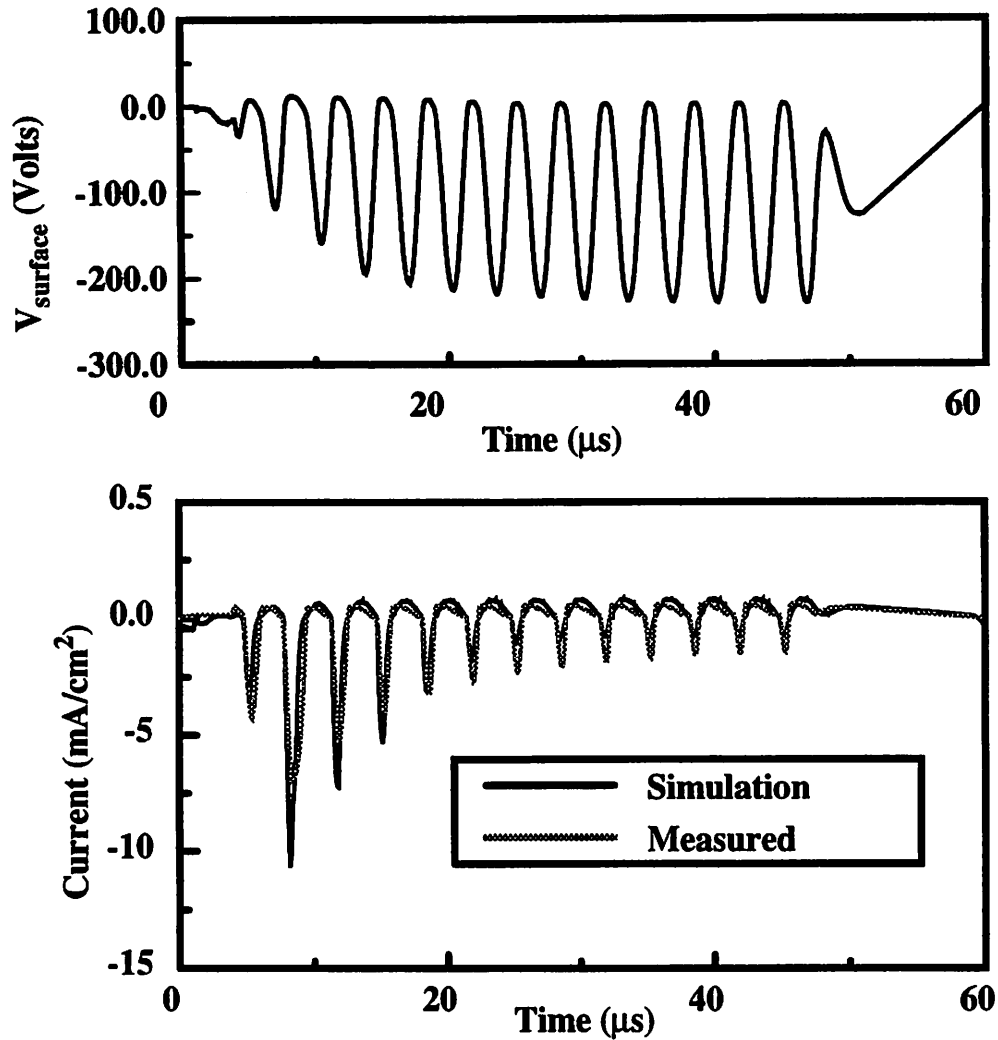


Figure 11-2. 300KHz pulsed RF experiment

Measured voltage and current for a 300KHz RF pulsed bias in a 1mtorr 900W Argon plasma. Good correlation between the simulation and measurement of the current for a 300kHz pulsed RF bias.

accurately describes the entire current waveform, from the initial turn on, to the steady-state, and finally the turn-off current.

When the bias frequency is increased to 1MHz the ion current is still well described by the model. However as Figure 11-3 shows, the 1MHz bias results in a much higher electron current than was expected. The excessive electron current is due to the positive swing of the bias exceeding the plasma potential. Also, the negative current is divided into two spikes due to high displacement current resulting from the small sheath thickness during

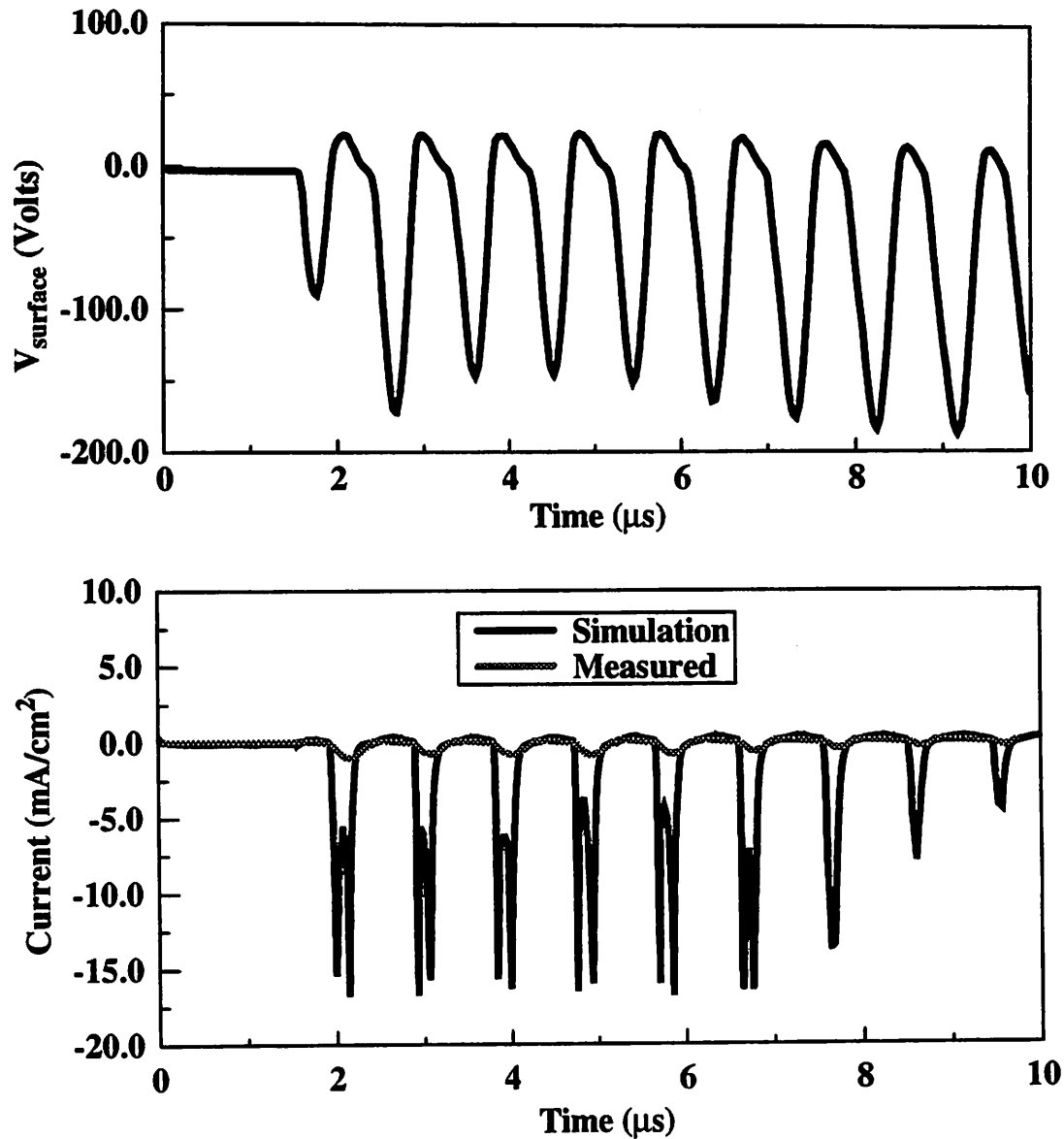


Figure 11-3. 1MHz pulsed RF bias simulation

Measured voltage and current of a 1MHz RF pulsed bias. Simulation results show increased electron current as compared with the experimental results.

this portion of the RF cycle. The exponential relation of the electron current is only valid below the plasma potential. Above the plasma potential, the electron current saturates for a planar surface. Though the electron current during the positive swing of the bias is not described well, the negative bias swing with the ion current is well described by the plasma

model. Thus the ion current model is still valid at 1MHz, though the model of the electron current breaks down due to excessive positive bias.

At 4MHz, the model fails to predict the plasma ion and electron currents during both the negative and positive swing of the bias. As Figure 11-4 shows the measured neg-

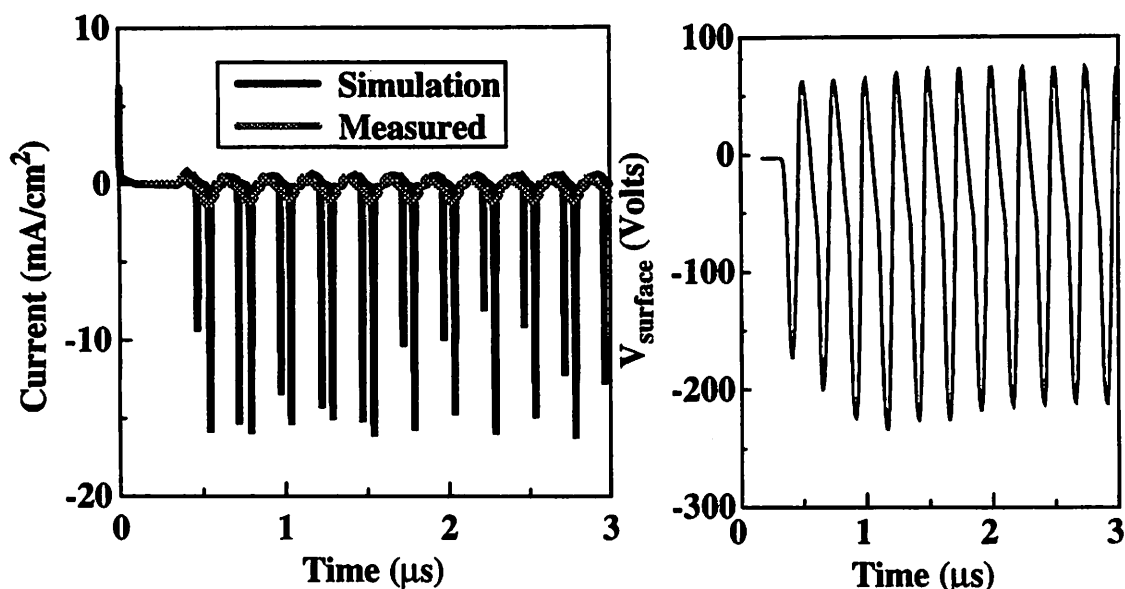


Figure 11-4. 4MHz RF pulsed bias simulation

Good correlation between the simulation and measured data for the positive swing of the current. The simulation does not predict the negative current swing. Included is the applied bias waveform.

ative swing of the current waveform is much less than the simulation predicts. As with the 1MHz pulse, the positive swing of the bias exceeds the plasma potential. The model's prediction of the ion current fails because the assumption that the plasma ions respond instantaneously to the varying voltage bias no longer holds. The failure of this assumption results in a much higher positive swing of the simulated current waveform as compared to the measured waveform as shown in Figure 11-5. The increase in the ion current by the simulation occurs because of the assumption that the ions respond completely to the bias. Since the ions cannot respond fast enough to the variation in the applied bias, the ions partially average out the potential variations, creating a less peaked ion current and more spread out

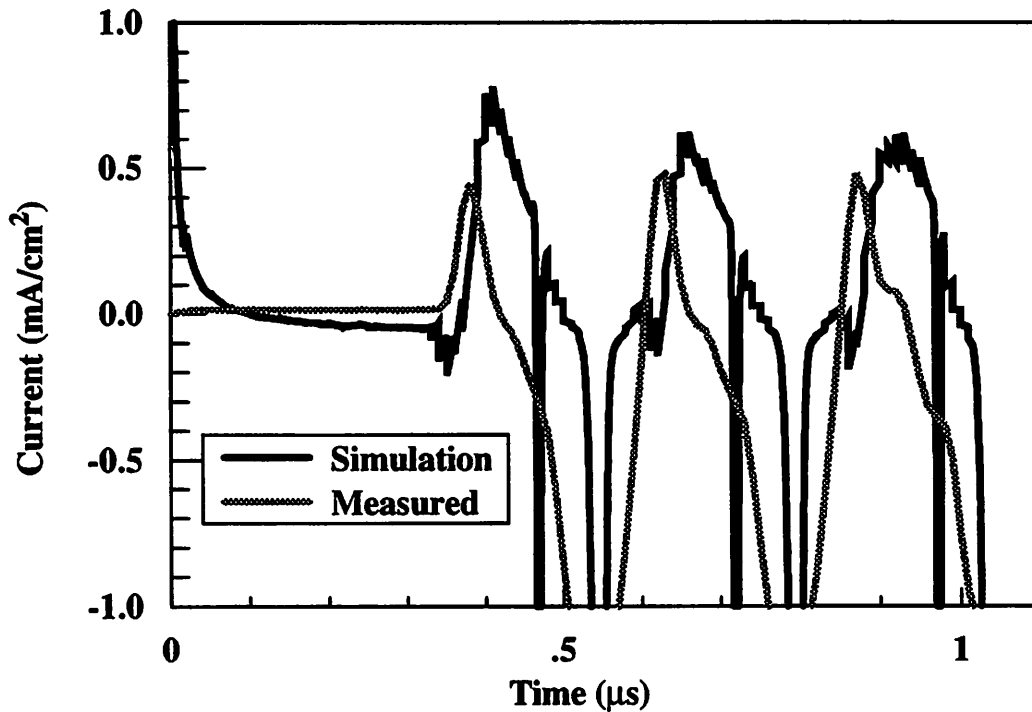


Figure 11-5. Close-up of 4MHz pulsed RF bias simulation

Close-up view of current waveform for 4MHz pulsed RF bias. Simulation results are off in magnitude, phase, and general shape.

over each voltage cycle. This results in the lower peak value of the ion current as seen in the experimental results. In addition to the peak value, the phase of the ion current waveform is different between the measured and simulated results. Therefore, at 4MHz the model no longer accurately determines the plasma currents.

11.2.2. Conclusions

The coupled plasma model can be extended to determine the plasma currents for an RF bias waveform. The pulsed RF bias waveform has potential applications as a method of modulating the etching bias to change the etch characteristics and control charging damage.

For the ion density of $3 \times 10^{10}/\text{cm}^3$ used in the experiments, the model's assumptions are valid for pulse frequencies up to 1MHz, but fail at 4MHz because the voltage changes too rapidly for the ions to respond. Also, the plasma electron current model fails

when the voltage swings more positively than the plasma potential. Though the model is limited in frequency to below 4MHz for the conditions used in the experiment, higher ion density sources will increase the valid frequency range for this present model.

11.3. Conventional Beam-line Ion Implantation Modeling

The coupled charging damage model can be converted to describe the charging damage in a conventional beam-line ion implantation system. By using this analytical model approach for conventional ion implantation, the charging damage mechanisms can be simulated and similar predictions about the charging damage in conventional ion implantation can be done as for PIII.

11.3.1. Conventional ion implanter system

A conventional ion implantation system can be broken down into four basic components. An implanter begins with an ion source which generates the ions and forms the ion beam. Next, the ion beam goes through a mass selector to form an ion beam with only a single ion specie. Then the ion beam is accelerated in an accelerator column. Finally, the beam reaches the end station where the wafers are. In a conventional ion implantation system, the wafers are placed in wafer holders on the end of spokes on a rotating wheel. The wheel is rotated at many hundreds of revolutions per second, allowing inertia to hold the wafers in place. Since a typical ion beam is only a couple of centimeters in area, the beam must be scanned to implant the entire wafer. The beam scanning is achieved by holding the beam stationary and sliding the rotating wheel back and forth across the beam.

Several similarities exist between a conventional ion implantation system and PIII. The ion beam in a conventional ion implanter consists of accelerated ions with a sea of low energy electrons to maintain beam integrity. In addition, many conventional implant systems use either an electron or plasma flood gun at the end station to reduce charging damage. The plasma flood gun creates a low density plasma near the wafer. So, the effective plasma of the ion beam as well as the plasma of the flood gun can be modeled like the plasma in the PIII system. However, unlike the PIII system, the plasma and ion beam are time-varying in the reference frame of the wafer since the wafer is rotating in and out of the beam.

11.3.2. Model implementation

To implement the conventional ion implantation system several changes must be made to the model. To accommodate the rotating wafer, the plasma parameters must be allowed to vary with time. From the reference frame of the wafer, the ion beam appears and disappears, taking a few milliseconds to pass. Therefore the model must allow the plasma parameters to vary with time to account for the time varying plasma. The ion beam current can be modeled as a time dependent current source. Since the ions in the beam are accelerated to high energies, they will be insensitive to the small potential variations on the wafer.

Using the time dependent model of the plasma, a test case was setup. The ion density and the plasma potential were allowed to vary as shown in Figure 11-6. Moreover, the

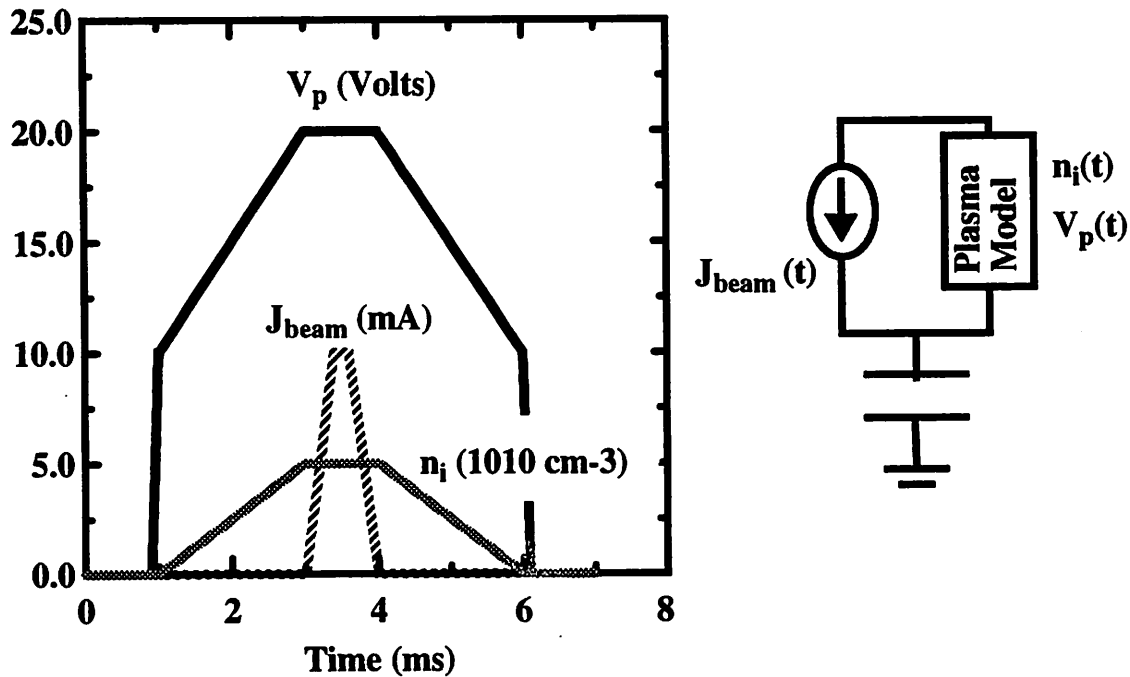


Figure 11-6. Time dependent plasma and ion beam model

Test case for modeling the plasma and ion beam in a conventional ion implanter. The plasma and ion beam are made time-dependent to model the rotation of the wafer through the beam. Also included is a schematic of the model and capacitor used.

ion beam current was allowed to peak in the middle of the plasma. The ion density and

plasma potential have a peaked symmetric profiles to simulate a typical plasma profile. On the wafer side, a simple 10nm thick oxide was used to collect the current from the plasma, with the backside grounded.

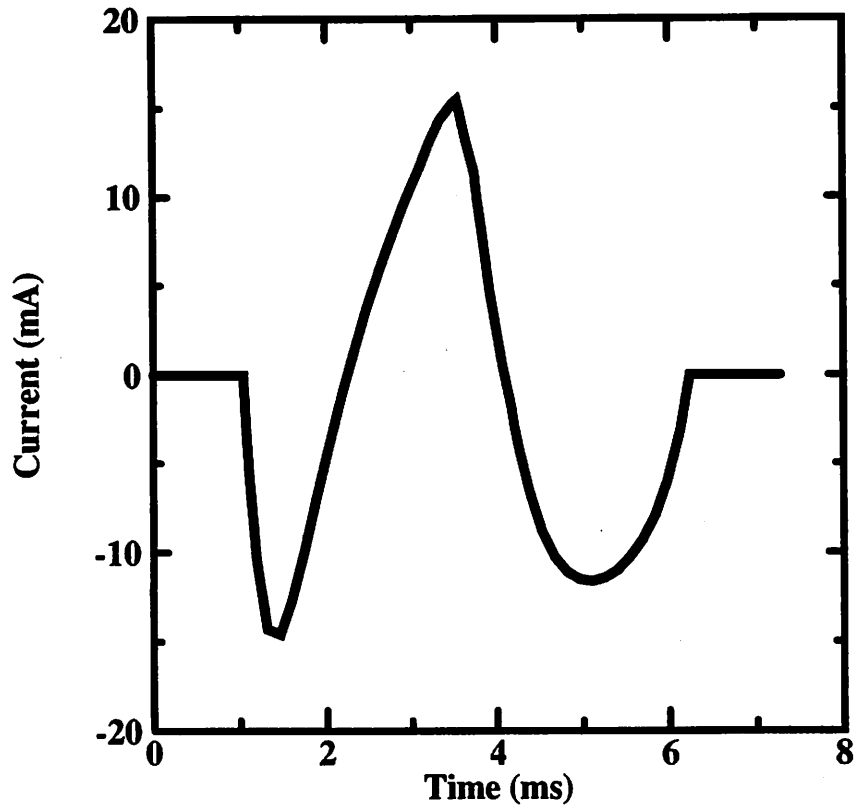


Figure 11-7. Total currents for conventional ion implantation model

Test current is similar to curve observed in current measurements in conventional implantation system.

Using the time dependent model and the test case conditions, the total currents generated over an oxide are found as shown in Figure 11-7. The currents generated go through three stages. First, the plasma electrons flood to the oxide generating the negative current. The flood of electrons occurs because the plasma electrons are more energetic than the plasma ions in this non-equilibrium state. Then, the ion beam hits the oxide and a flood of positive charge generates a net positive current. Finally, the beam turns off and the plasma electrons flood back to the oxide to reduce the positive charge placed by the ion beam. This

shape of the implanter current has been observed in measurements of conventional implanter systems [11.11].

11.3.3. Conclusions

Through the use of a time dependent plasma and ion beam current source, a model of the currents from a conventional ion implantation system is setup. For a test case scenario of plasma and ion beam, the typical current waveform is observed to be negative then positive then negative current.

11.4. Conclusions

From the adaptation of the coupled charging model to a pulsed RF bias and conventional ion implantation, the versatility of the coupled charging model approach is illustrated. The pulsed RF bias experiments show that the model can accurately determine the turn-on, steady-state, and turn-off conditions for a RF bias as long as the assumptions of the model are still valid. For the argon plasma conditions used, the model was shown to be valid up to 1MHz for its description of the ion current. The conventional ion implantation model concept shows how the plasma can be made time varying to accommodate the time varying ion beam being generated in the reference frame of the wafer. Thus, two new applications for the coupled charging model are demonstrated.

References

- [11.1] D. J. Paul, V. J. Law, and G. A. C. Jones, "Si_{1-x}Ge_x pulsed plasma etching using CHF₃ and H₂," *Journal of Vacuum Science & Technology B*, vol. 13, no. 6, pp. 2234-2237, 1995.
- [11.2] I. Peres and M. J. Kushner, "Pulsed plasma methods in remote plasma enhanced chemical vapor deposition," *1993 IEEE International Conference on Plasma Science*, p. 226, 1993.
- [11.3] B. A. Smith and L. J. Overzet, "Time-resolved energy distribution of F⁻ from pulsed radio frequency discharges," *Journal of Applied Physics*, vol. 78, no. 8, pp. 5195-5197, 1995.
- [11.4] L. J. Overzet and F. Y Leong-Rousey, "Time-resolved power and impedance measurements of pulsed radiofrequency discharges," *Plasma Sources, Science and Technology*, vol. 4, no. 3, pp. 432-443, 1995.

- [11.5] R. J. Visser, J. A. G. Baggerman, J. P. J. Poppelaars, and E. J. H. Collart, "The time evolution of the ion density and the gas temperature in pulsed radio frequency plasmas," *Journal of Applied Physics*, vol. 71, no. 12, pp. 5792-5798, 1992.
- [11.6] A. Kono, M. Haverlag, G. M. W. Kroesen, and F. J. de Hoog, "Temporal behavior of the electron and negative ion densities in a pulsed radio-frequency CF_4 plasma," *Journal of Applied Physics*, vol. 70, no. 6, pp. 2939-2946, 1991.
- [11.7] M. A. Lieberman and S. Ashida, "Global models of pulse-power modulated high density, low pressure discharges," ERL Memo M95/83, 1995.
- [11.8] R. W. Boswell and D. Vender, "Simulation of pulsed electropositive and electronegative plasmas," *IEEE Transactions on Plasma Science*, vol. 19, no. 2, pp. 141-143, 1991.
- [11.9] S. Samukawa, "Pulse-time-modulated electron cyclotron resonance plasma etching with low radio-frequency substrate bias," *Applied Physics Letters*, vol. 68, no. 3, pp. 316-318, 1996.
- [11.10] T. Kure, Y. Gotoh, H. Kawakami, and S. Tachi, "Highly anisotropic microwave plasma etching for high packing density silicon patterns," 1992 Symposium on VLSI Technology. Digest of Technical Papers USA: IEEE, pp. 48-49, 1992.
- [11.11] J. G. England, C. E. A. Cook, D. G. Armour, and M. A. Foad, "Charged particle energy spectrometers and their applications in fundamental studies of wafer charging and ion beam tuning phenomena," *Nuclear Instruments & Methods in Physics Research, Section B*, vol. B96, no. 1-2, pp. 39-42, 1995.

12 Conclusions

Our study has investigated oxide charging damage in integrated circuit processing with both simulations and experiments. The primary test vehicle used is the PIII process, but the study has been extended to RIE, PECVD, and beam-line implantation. The charging damage induced in thin oxides resulted from the interactions of the plasma currents, device structure, and substrate bias. An analytical model of the plasma currents and their coupling to oxide damage was experimentally verified. From the model a better understanding of charging damage and methods of reducing the damage through changes in plasma conditions, device structure, and bias waveform has been achieved.

To monitor the plasma and determine the physical parameters necessary for modeling the plasma, a variety of different diagnostic techniques were employed. To monitor the plasma parameters for the model, a single cylindrical Langmuir probe was used. The extracted plasma parameters by this technique were: the ion density (n_i), electron temperature (T_e), plasma potential (V_p), and floating potential (V_f). The ion and neutral species in the plasma were monitored using several different mass spectrometers. Moreover, to monitor the run-to-run consistency of the plasmas, Optical Emission Spectroscopy (OES) was used as both a fingerprint of the plasma and as a determination of the species in the plasma from the emission peaks. Finally, a technique for measuring the secondary electron yield of plasma exposed materials as a function of ion energy was developed using the plasma model, which was applied to several materials in an argon plasma.

Using experimental results the coupled charging model was verified. The damage was quantified using test structures such as area capacitors and C-V measurements. From experimental measurements, the model was shown to accurately determine the total

plasma currents and the charging damage trend for variations in the repetition rate of the pulsed bias waveform.

Using the plasma model, the effect of the substrate bias on charging damage was established. For the substrate bias a maximum repetition rate for charging damage concerns, called the threshold frequency, was found. Above the threshold frequency, severe charging damage occurs. The threshold frequency and throughput of PIII is maximized by implanting with short (below $2\mu\text{s}$) rectangular pulses.

The plasma parameters also affect charging damage. A lower electron temperature increases the threshold frequency. Also, plasma non-uniformities can induce charging damage when the non-uniformity is severe. The plasma non-uniformity was modeled using a distributed network of plasma elements.

As many previous experiments have shown, the device structure also affects charging damage. Antenna structures enhance the voltage induced by a PIII voltage pulse. Also the dependence of the antenna structure and the plasma floating potential on charging damage without PIII was simulated. The stressing current through the gate oxide increases with larger antenna ratio. The value of the stressing current is reduced by a lower plasma floating potential for the same antenna ratio. Thus, the charging damage due to the antenna structure is dependent on the plasma condition, illustrating the interaction between the device structure and the plasma.

By extending the charging damage model, pulsed RF bias and conventional ion implantation can be simulated. Using the same model as with PIII, the plasma currents for a pulsed RF bias was shown to be accurately simulated. Also, by allowing the plasma characteristics to vary with time, conventional ion implantation can be modeled. These extensions of the coupled charging model show the versatility of the methodology used.

Additional applications for the model and experiments to investigate additional damage mechanisms can extend the model to more applications and demonstrate other charging issues. By the addition of collisional sheath dynamics to the model, a much wider

range of processing pressures can be modeled. A modified Child Law is available that is valid from a collision-less to fully collisional sheath [12.1]

$$J_i = \frac{4\epsilon_o}{9} \left(\frac{2q}{M}\right)^{1/2} \frac{V_s^{3/2}}{S^2 [1 + (12\pi/125) (S/\lambda_i)]^{1/2}} \quad [12-1]$$

where λ_i is the mean free path of the ion-neutral collisions. Also, the pulsed RF bias simulation can be used to optimize the repetition rate and pulse width, minimizing the oxide charging damage. The effect of the substrate bias can also be explored further. By using an equivalent model of the substrate bias network, the effect of the network components on the charging currents can be determined. For the UC Berkeley PIII system, the high voltage pulsing network equivalent circuit is shown in Figure 12-1. Finally the effect of SOI, flat panel displays, and other insulating substrates on the implantation and oxide charging mechanisms is also an important issue to be investigated.

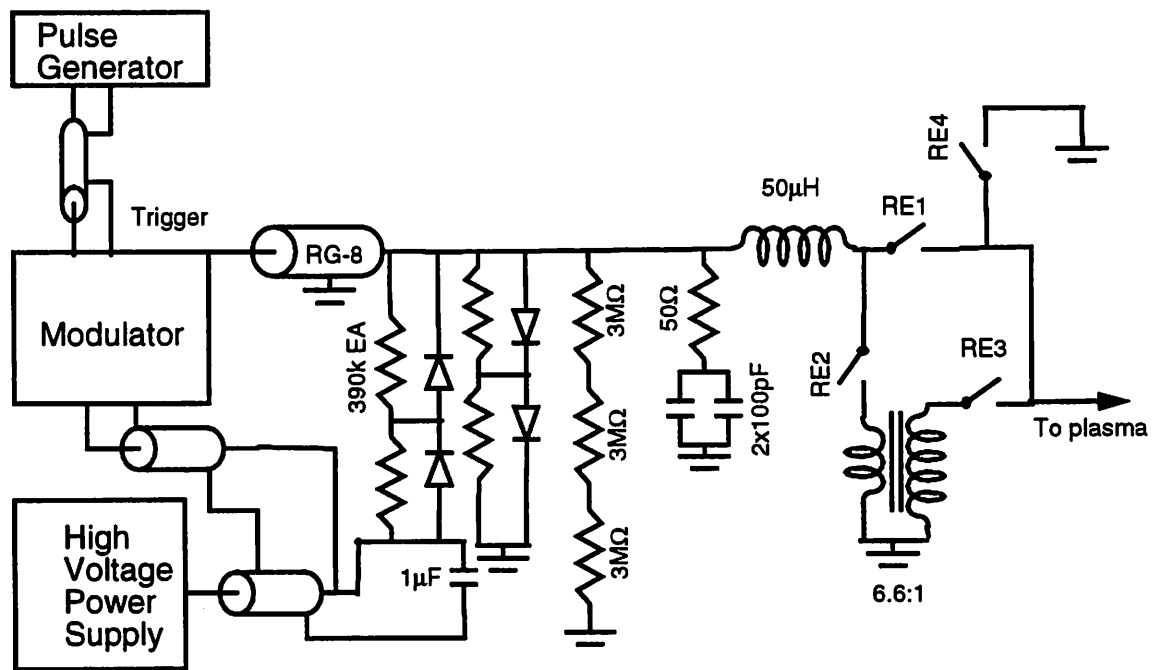


Figure 12-1. Circuit diagram of pulse network for the PIII system

All of the discrete elements used in the pulse network are illustrated. Additional parasitic elements may also play a significant role.

In summary, the coupled charging damage model can provide insight into understanding oxide charging damage mechanisms in a wide range of plasma and implantation processes. The damage model can be used to optimize and tailor the process to minimize the charging damage induced, during an integrated circuit manufacturing process.

References

- [12.1] K. U. Riemann, "Consistent analysis of a weakly ionized plasma and its boundary layer," *Journal of Physics D*, vol. 25, no. 10, pp. 1432-1442, 1992.

Appendix A: OES peaks

A.1 Introduction

A list of neutral and singly ionized OES peaks for Si, BF₃, and all of the decomposed species from BF₃ has been compiled from a variety of sources. The relative intensity of some of the species has also been collected. From these peaks the neutral and ionized species present in a given BF₃ plasma can be found from OES.

$\lambda(\text{nm})$	Species	Intensity	Ref	$\lambda(\text{nm})$	Species	Intensity	Ref
089.0	BF ₃		[A.1]	217.9	B ⁺		[A.6]
094.0	BF ₃		[A.2]	220.7	Si		[A.4]
126.1	Si ⁺		[A.3]	220.8	Si		[A.3]
136.2	B ⁺		[A.3]	221.1	Si		[A.4]
162.4	B ⁺		[A.3]	221.7	Si		[A.4]
180.8	Si ⁺		[A.3]	222.0	B ⁺	70	[A.6]
182.6	B		[A.3]	222.0	BF ₃ ⁺		[A.1]
196.0	BF		[A.3]	229.1	Si		[A.4]
200.8	Si		[A.4]	229.5	Si		[A.4]
201.1	Si		[A.4]	232.3	B ⁺	40	[A.6]
205.5	Si		[A.4]	232.9	B ⁺	40	[A.6]
206.0	B		[A.5]	239.3	B ⁺	40	[A.6]
206.1	Si		[A.4]	239.5	B ⁺	220	[A.6]
206.5	Si		[A.3]	243.5	Si		[A.7]
206.6	B	250	[A.6]	243.8	Si		[A.4]
206.7	B	300	[A.6]	244.3	Si		[A.4]
208.9	B	500	[A.4]	245.0	B		[A.5]
209.0	B	500	[A.4]	245.0	BF ₃		[A.3]
211.5	Si		[A.4]	245.2	Si		[A.4]
212.1	Si		[A.4]	246.0	B ⁺	40	[A.6]
215.0	BF ₃		[A.3]	249.7	B	1000	[A.4]

$\lambda(\text{nm})$	Species	Intensity	Ref	$\lambda(\text{nm})$	Species	Intensity	Ref
249.7	B	1000	[A.8]	288.2	Si		[A.4]
249.7	B		[A.6]	288.2	Si		[A.8]
249.8	B		[A.4]	288.2	Si		[A.7]
249.8	B		[A.8]	289.4	SiF		[A.8]
249.8	B		[A.6]	290.0	Si		[A.9]
250.7	Si		[A.4]	290.4	Si ⁺		[A.7]
250.7	Si		[A.8]	290.6	Si ⁺		[A.7]
250.7	Si		[A.7]	291.8	B ⁺	160	[A.6]
251.4	Si		[A.4]	292.7	F ₂		[A.11]
251.4	Si		[A.7]	295.3	SiF		[A.8]
251.6	Si		[A.4]	296.0	SiF ₄		[A.3]
251.6	Si		[A.8]	296.7	SiF		[A.8]
251.6	Si		[A.7]	297.0	Si		[A.4]
251.9	Si		[A.4]	297.5	BF		[A.10]
252.0	Si		[A.9]	298.8	Si		[A.4]
252.4	Si		[A.4]	300.0	BF ₂		[A.2]
252.4	Si		[A.8]	301.0	SiF ₄		[A.3]
252.4	Si		[A.7]	302.8	SiF		[A.8]
252.9	Si		[A.4]	303.2	B ⁺	110	[A.6]
252.9	Si		[A.8]	304.2	SiF		[A.8]
252.9	Si		[A.7]	305.7	F ⁺	6	[A.7]
253.0	SiF		[A.8]	305.8	F ⁺	7	[A.7]
253.2	Si		[A.4]	306.0	F ⁺	100	[A.6]
253.9	SiF		[A.8]	306.0	SiF ₄		[A.3]
255.6	F ⁺	100	[A.6]	311.8	BF		[A.10]
256.4	Si		[A.4]	312.0	BF		[A.10]
256.5	Si		[A.4]	312.1	BF		[A.10]
257.0	BF ₃ ⁺		[A.1]	312.2	BF		[A.10]
258.4	SiF		[A.8]	312.4	BF		[A.10]
259.5	SiF		[A.8]	315.3	F ⁺	140	[A.6]
263.1	BF		[A.10]	320.3	F ⁺	170	[A.6]
263.1	Si		[A.4]	322.3	BF		[A.10]
264.1	SiF		[A.8]	325.5	BF		[A.10]
265.3	SiF		[A.8]	326.4	F ⁺	140	[A.6]
272.5	BF		[A.10]	332.3	B ⁺	110	[A.6]
275.0	BF ₃		[A.3]	332.4	B ⁺	110	[A.6]
278.0	BF ₃ ⁺		[A.1]	334.0	Si ⁺		[A.7]
280.0	SiF		[A.8]	334.6	SiF		[A.8]
281.3	SiF		[A.8]	336.0	BF		[A.10]
282.4	BF		[A.10]	336.3	SiF		[A.8]
284.2	Si		[A.4]	339.7	BF		[A.10]
284.5	BF		[A.10]	341.5	F ⁺	140	[A.6]
287.1	F ⁺	100	[A.6]	341.6	F ⁺	150	[A.6]
288.0	Si		[A.9]	341.7	F ⁺	160	[A.6]
288.1	SiF		[A.8]	345.0	B ⁺		[A.5]

$\lambda(\text{nm})$	Species	Intensity	Ref	$\lambda(\text{nm})$	Species	Intensity	Ref
345.1	B ⁺	450	[A.6]	408.4	F ⁺	160	[A.6]
347.3	F ⁺	160	[A.6]	410.3	F ⁺	190	[A.7]
347.5	F ⁺	170	[A.6]	410.3	Si		[A.4]
350.1	F ⁺	190	[A.7]	410.3	F ⁺	190	[A.6]
350.1	F ⁺	200	[A.6]	410.4	F ⁺	200	[A.6]
350.2	F ⁺	200	[A.6]	410.9	F ⁺	170	[A.6]
350.3	F ⁺	180	[A.6]	411.7	F ⁺	160	[A.6]
350.3	F ⁺	210	[A.7]	411.9	F ⁺	150	[A.6]
350.5	F ⁺	170	[A.6]	412.2	B ⁺	285	[A.6]
350.6	F ⁺	220	[A.6]	412.2	B ⁺		[A.5]
352.3	F ⁺	160	[A.6]	413.1	Si ⁺		[A.7]
353.7	F ⁺	150	[A.6]	418.3	SiF		[A.8]
354.2	F ⁺	160	[A.6]	419.5	B ⁺	110	[A.6]
355.0	BF		[A.10]	420.0	BF ₂		[A.2]
359.1	F ⁺	160	[A.6]	420.7	F ⁺	140	[A.6]
359.4	F	6	[A.6]	422.5	F ⁺	170	[A.6]
359.9	F ⁺	170	[A.6]	423.0	SiF		[A.8]
360.1	F ⁺	180	[A.6]	424.4	F ⁺	150	[A.6]
360.3	F ⁺	190	[A.6]	424.6	F ⁺	200	[A.7]
370.5	F ⁺	180	[A.6]	424.6	F ⁺	190	[A.6]
371.0	F ⁺	160	[A.6]	424.7	F ⁺	180	[A.6]
374.0	F ⁺	160	[A.6]	427.0	SiF		[A.8]
380.6	F ⁺	140	[A.6]	427.5	F ⁺	170	[A.6]
384.7	F ⁺	270	[A.6]	427.8	F ⁺	160	[A.6]
385.0	F ⁺	260	[A.6]	427.9	F ⁺	160	[A.6]
385.2	F ⁺	250	[A.6]	429.9	F ⁺	200	[A.6]
385.6	Si ⁺		[A.7]	433.4	SiF		[A.8]
389.8	F	5	[A.6]	436.8	SiF		[A.8]
389.9	F ⁺	190	[A.6]	440.1	SiF		[A.8]
390.0	SiF ₂		[A.9]	441.0	SiN		[A.9]
390.2	F ⁺	180	[A.6]	443.0	SiF		[A.8]
390.4	F ⁺	170	[A.6]	444.4	BF		[A.10]
390.6	Si		[A.4]	444.7	F ⁺	170	[A.6]
390.6	Si		[A.8]	444.7	F ⁺	180	[A.7]
393.1	F	8	[A.6]	446.1	BF		[A.10]
393.4	F	5	[A.6]	446.2	SiF		[A.8]
394.9	F	5	[A.6]	446.5	BF		[A.10]
397.2	F ⁺	150	[A.6]	447.2	B ⁺	110	[A.6]
397.3	F ⁺	160	[A.6]	447.3	B ⁺	110	[A.6]
397.5	F ⁺	170	[A.6]	449.6	SiF		[A.8]
401.0	SiF ₂		[A.9]	453.0	B ⁺		[A.5]
401.2	SiF		[A.8]	453.2	SiF		[A.8]
402.5	F ⁺	240	[A.6]	473.4	F ⁺	140	[A.6]
402.5	F ⁺	220	[A.7]	478.4	B ⁺	70	[A.6]
405.0	SiN		[A.9]	485.1	SiF		[A.8]

$\lambda(\text{nm})$	Species	Intensity	Ref	$\lambda(\text{nm})$	Species	Intensity	Ref
485.9	F ⁺	170	[A.6]	597.9	Si ⁺		[A.7]
493.3	F ⁺	160	[A.6]	598.4	BF		[A.10]
494.0	B ⁺	110	[A.6]	599.4	BF		[A.10]
496.1	F	6	[A.6]	599.4	F	50	[A.6]
500.2	F ⁺	140	[A.12]	601.6	F	150	[A.6]
504.1	Si ⁺		[A.7]	603.8	F	80	[A.6]
505.6	Si ⁺		[A.7]	604.8	F	900	[A.6]
510.2	F ₂		[A.11]	606.6	Si		[A.4]
517.3	F ⁺	150	[A.12]	608.0	B ⁺	110	[A.6]
520.2	Si ⁺		[A.7]	608.0	F	100	[A.6]
521.0	BF ₃ ⁺		[A.1]	610.3	F ₂		[A.11]
523.0	F	15	[A.6]	615.0	F	800	[A.6]
527.9	F	12	[A.6]	621.1	F	400	[A.6]
539.4	F ₂		[A.11]	624.0	F	13000	[A.4]
545.7	BF		[A.10]	624.8	F ⁺	140	[A.12]
546.0	BF		[A.10]	627.0	SiF		[A.8]
546.6	Si ⁺		[A.7]	628.5	B ⁺	70	[A.6]
546.7	Si ⁺		[A.7]	633.9	BF ₃ ⁺		[A.13]
547.1	BF		[A.10]	634.7	Si ⁺		[A.7]
551.6	F ₂		[A.11]	634.9	F	10000	[A.4]
554.1	F	18	[A.6]	637.0	BF ₃ ⁺		[A.13]
555.2	F	12	[A.6]	639.7	SiF		[A.8]
557.7	F	10	[A.6]	640.2	BF ₃ ⁺		[A.13]
558.9	F ⁺	160	[A.12]	641.4	F	8000	[A.6]
562.4	F	20	[A.6]	641.6	SiF		[A.8]
562.7	F	12	[A.6]	643.3	BF ₃ ⁺		[A.13]
565.9	F	15	[A.6]	646.4	BF ₃ ⁺		[A.13]
566.4	BF		[A.10]	648.9	F ₂		[A.11]
566.8	F	40	[A.6]	649.2	SiF		[A.8]
567.0	Si ⁺		[A.7]	649.7	BF ₃ ⁺		[A.13]
567.2	F	90	[A.6]	651.9	F ₂		[A.11]
568.9	F	18	[A.6]	653.2	BF ₃ ⁺		[A.13]
570.1	F	25	[A.6]	657.0	F	450	[A.6]
570.7	F	25	[A.6]	658.0	F	300	[A.6]
573.1	F ₂		[A.11]	659.4	SiF		[A.8]
580.4	BF		[A.10]	665.0	F	400	[A.6]
580.7	BF		[A.10]	669.0	F	1800	[A.6]
581.5	BF		[A.10]	670.8	F	400	[A.6]
582.2	BF		[A.10]	677.4	F	7000	[A.6]
582.6	BF		[A.10]	679.6	F	1500	[A.6]
585.1	F ₂		[A.11]	683.4	F	9000	[A.6]
595.0	F	12	[A.6]	685.6	F	50000	[A.8]
595.8	Si ⁺		[A.7]	687.0	F	8000	[A.6]
595.9	F	25	[A.6]	690.2	F	15000	[A.4]
596.5	F	70	[A.6]	691.0	F	6000	[A.6]

$\lambda(\text{nm})$	Species	Intensity	Ref	$\lambda(\text{nm})$	Species	Intensity	Ref
696.6	F	4000	[A.6]	801.6	F ⁺	80	[A.6]
697.7	F ₂		[A.11]	804.1	F	1000	[A.6]
703.0	B ⁺	40	[A.6]	807.6	F	900	[A.6]
703.7	F	45000	[A.4]	807.8	F	350	[A.6]
712.8	F	30000	[A.4]	812.7	F	350	[A.6]
718.0	F ⁺	130	[A.12]	812.9	F	600	[A.6]
720.2	F	15000	[A.6]	816.0	F	300	[A.6]
721.2	F	130	[A.6]	817.9	F	600	[A.6]
724.2	BF ₃ ⁺		[A.13]	819.1	F	300	[A.6]
728.9	Si		[A.7]	821.5	F	2500	[A.7]
730.2	B ⁺		[A.6]	866.8	B		[A.6]
730.9	F	1000	[A.6]	866.9	B	70	[A.6]
731.1	F	15000	[A.4]	873.0	BF ₃ ⁺		[A.1]
731.4	F	700	[A.6]				
733.2	F	5000	[A.4]				
739.9	F	10000	[A.4]				
740.6	Si		[A.7]				
741.6	Si		[A.7]				
742.3	Si		[A.7]				
742.6	F	4000	[A.6]				
748.3	F	2200	[A.6]				
748.5	BF ₃ ⁺		[A.13]				
748.5	BF ₂ ⁺		[A.13]				
748.9	F	2500	[A.6]				
751.5	F	900	[A.6]				
755.2	F	5000	[A.6]				
757.3	F	5000	[A.6]				
759.0	BF ₃ ⁺		[A.13]				
759.0	BF ₂ ⁺		[A.13]				
760.7	F	7000	[A.6]				
762.5	BF ₃ ⁺		[A.13]				
762.5	BF ₂ ⁺		[A.13]				
767.1	Si ⁺		[A.7]				
773.5	BF ₃ ⁺		[A.13]				
775.5	F	18000	[A.4]				
777.5	BF ₃ ⁺		[A.13]				
780.0	F	15000	[A.4]				
784.9	Si ⁺		[A.7]				
785.0	Si ⁺		[A.7]				
787.9	F	300	[A.6]				
789.9	F	500	[A.6]				
793.2	Si		[A.7]				
793.6	F	350	[A.6]				
794.4	Si		[A.7]				
795.6	F	300	[A.6]				

References

- [A.1] C. Creasey, P.A. Hatherly, H.M. Jones, I.R. Lambert, et al, "Vacuum UV fluorescence excitation spectroscopy of BF₃ in the range 45-125 nm. Observation of new electronic transitions in the BF₂ free radical," *Molecular Phys.*, 78 (4), pp. 837-854, 1993.
- [A.2] M. Suto, C. Ye, and L.C. Lee, "Photoabsorption and fluorescence spectroscopy of BF₃ in the extreme-vacuum-ultraviolet region," *Phys. Rev. A*, 42 (1), pp. 424-431, 1990.
- [A.3] J.E. Hesser and K. Dressler, "Radiative Lifetimes of Ultraviolet Emission Systems Excited in BF₃, CF₄ and SiF₄," *J. Chem. Phys.*, 47 (9), pp. 3443-3450, 1967.
- [A.4] C. Candler, *Atomic spectra and the vector model*, Princeton, NJ: D. van Nostrand Co., Inc., 1964.
- [A.5] Th. Glenewinkel-Meyer, A. Kowalski, B. Muller, Ch. Ottinger, and W.H. Breckenridge, "Emission Spectra and electronic structure of group IIIa monohalide cations," *J. Chem. Phys.*, 89 (12), pp. 7112-7125, 1988.
- [A.6] J. Reader and C.H. Corliss, *Wavelengths and transition probabilities for atoms and atomic ions*, Washington: U.S. Govt. Print. Off., 1980.
- [A.7] A.R. Striganov and N.S. Sventitskii, *Tables of spectral lines of neutral and ionized atoms*, Washington: IFI/Plenum, 1968.
- [A.8] R.W.B. Pearse and A.G. Gaydon, *The identification of molecular spectra*, New York: J. Wiley & sons, inc., 1941.
- [A.9] D.L. Flamm, V.M. Donnelly, and J.A. Mucha, "The reaction of fluorine atoms with silicon," *J. Appl. Phys.*, 52 (5), pp. 3633-3639, 1981.
- [A.10] Dull & Strong, *Phys. Rev.*, 47, p. 458, 1935.
- [A.11] Gale, *Astrophys. J.*, 59, p.77, 1929.
- [A.12] A.N. Zaidel, *Tables of spectral lines*, New York: IFI/Plenum, 1970.
- [A.13] C.F. Batten, J.A. Taylor, B.P. Tsai, and G.G. Meisels, "Photoionization processes at threshold. II. Threshold photoelectron photoionization, and coincidence ion-threshold photoelectron spectra of BF₃," *J. Chem. Phys.*, 69 (6), pp. 2547-2552, 1978.

Appendix B: Plasma Model Implementation in SPICE

List of Variables:

j_i	Plasma ion current
j_e	Electron current flowing from the plasma to the oxide surface
q	Unit charge
n_o	Ion density of the plasma
s	sheath thickness also $V_{st\text{thick}}$ and $V(13)$
ϵ_o	permittivity of free-space
M	Ion mass
V_s	Voltage drop across sheath
$V_{s3/2}$	A SPICE voltage equal to $V_s^{3/2}$
I_{s3}	A SPICE current equal to s^3 .
k_1	Constant coefficient for SPICE implementation $k_1 = \frac{9}{4} \sqrt{\frac{M}{2q}} \frac{1}{\epsilon_o} q n_o v_s$
k_2	Constant coefficient for SPICE implementation $k_2 = \frac{4}{9} \sqrt{\frac{2q}{M}} \epsilon_o$
k_3	Constant coefficient for SPICE implementation $k_3 = \frac{1}{4} q n_o v_e$
L_1	Effective inductance for SPICE model which is $L_1 = \frac{3}{4} \sqrt{\frac{M}{2q}} \frac{1}{\epsilon_o} q n_o$
j_{dispa}	Displacement current due to dC/dt
j_{disp}	Total displacement current
C_s	Sheath capacitance ($C_s = \epsilon_o/s$)
j_{dispb}	Displacement current due to dV/dt .
v_s	Sheath edge ion velocity
v_e	Average electron velocity ($v_e = (8qT_e/\pi m_e)^{1/2}$)

V_p	Plasma potential
T_e	Electron temperature in units of Volts
α	secondary electron yield coefficient

B.1 Introduction

Implementation of the analytical plasma model into SPICE requires the re arrangement of the analytical relations into equivalent circuit elements. Each equation can be setup either as a simple element or as a separate circuit that can be solved. After each current component is solved for, they are summed together to determine the total plasma currents. All of the equations are coupled and solved simultaneously, allowing the interactions between the currents to be modeled.

B.2 Model Equation Conversion to SPICE

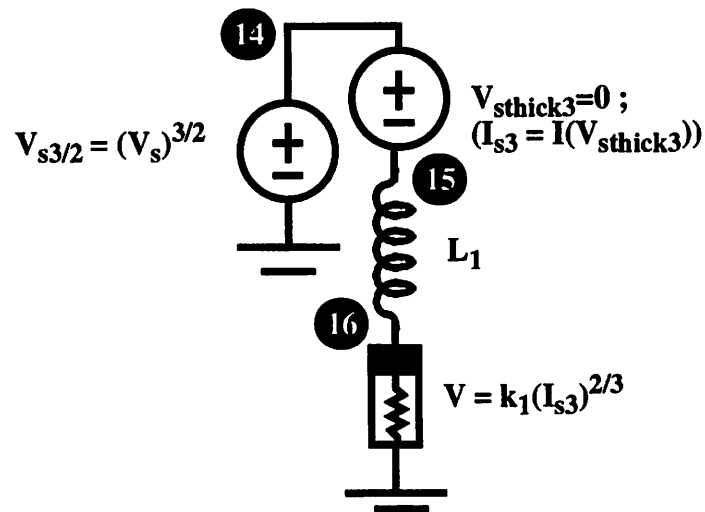


Figure B-1. Sheath thickness circuits

Equivalent circuit for solving the sheath thickness

First the sheath motion during PIII is determined. The sheath motion relation is derived from both the Child law and the relation of the ion flux across the sheath edge:

$$qn_o \left(\frac{ds}{dt} + v_s \right) = \frac{4}{9} \epsilon_o (2q/M)^{1/2} V_s^{3/2} / s^2 \quad [B-1]$$

This relation can be rearranged to a form that can be used in SPICE:

$$V_s^{3/2} = \frac{9}{4} \sqrt{\frac{M}{2q}} \frac{1}{\epsilon_o} qn_o \left(\frac{1}{3} \frac{ds^3}{dt} + s^2 v_s \right) \quad [B-2]$$

In this form Equation B-2 can be converted into an equivalent circuit relation:

$$V_{s3/2} = L_1 \frac{dI_{s3}}{dt} + k_1 (I_{s3})^{2/3} \quad [B-3]$$

where $V_{s3/2} = V_s^{3/2}$, $L_1 = \frac{3}{4} \sqrt{\frac{M}{2q}} \frac{1}{\epsilon_o} qn_o$, $I_{s3} = s^3$, and $k_1 = \frac{9}{4} \sqrt{\frac{M}{2q}} \frac{1}{\epsilon_o} qn_o v_s$. The next step to determining the sheath thickness is to convert the sheath voltage V_s into $V_{s3/2}$ and then convert I_{s3} into the sheath thickness s . The conversion of V_s into $V_{s3/2}$ can be done simultaneously when Equation B-3 is solved as illustrated in Figure B-1.

To determine the actual sheath thickness the current I_{s3} must be cube rooted to convert it to the actual sheath thickness. Figure B-2 illustrates the circuit used to determine the sheath thickness which is set as $v(13)$, the voltage drop from node 13 to ground.

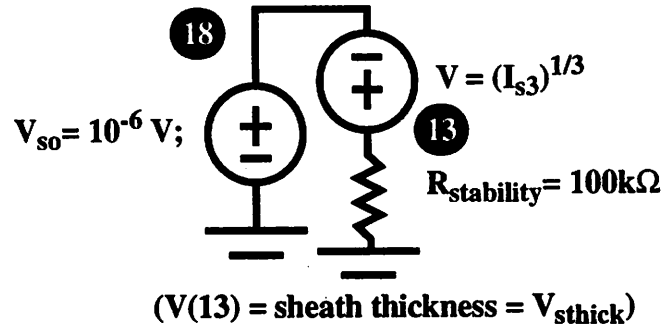


Figure B-2. Circuit converting S^3 to S

Circuit converting the I_{s3} current into the sheath thickness.

From the calculation of the sheath thickness the ion current can be found by using the Child Law:

$$j_i = \frac{4}{9} \epsilon_o (2q/M)^{1/2} V_s^{3/2} / s^2 \quad [B-4]$$

This relation can be directly converted into a circuit element as an arbitrary non-linear element with V_s and s as voltages to be input. The electron current and the secondary electron yield can both be implemented in the same manner since they are also non-linear relations.

Finally, the displacement currents require two separate circuits for each of the components. The displacement current relation consists of displacement due to change in voltage and change in capacitance:

$$j_{\text{disp}} = C_s \frac{dV_s}{dt} + V_s \frac{dC_s}{dt} \quad [\text{B-5}]$$

By rearranging Equation B-5 and using the fact that $C_s = \epsilon_o/s$, the displacement current can be described as:

$$j_{\text{disp}} = \frac{j_{\text{dispa}}}{s} - V_s \frac{j_{\text{dispb}}}{s^2} \quad [\text{B-6}]$$

where $j_{\text{dispa}} = \epsilon_o \frac{dV_s}{dt}$ and $j_{\text{dispb}} = \epsilon_o \frac{ds}{dt}$. Now the relations for j_c and j_v can be solved using the equivalent capacitances and Equation B-6 can be solved as a simple non-linear relation. The two displacement current relations are solved by two separate equations shown in Figure B-3.

So by using these equivalent circuit relations the plasma current model can be implemented within SPICE as a part of the coupled charging model. Attached is a copy of the SPICE input deck for an argon plasma at 1mtorr 900W, with plasma parameters equal to: $n_i = 3.76 \times 10^{16} \text{ m}^{-3}$, $T_e = 4 \text{ Volts}$, and $V_p = 18.23 \text{ V}$.

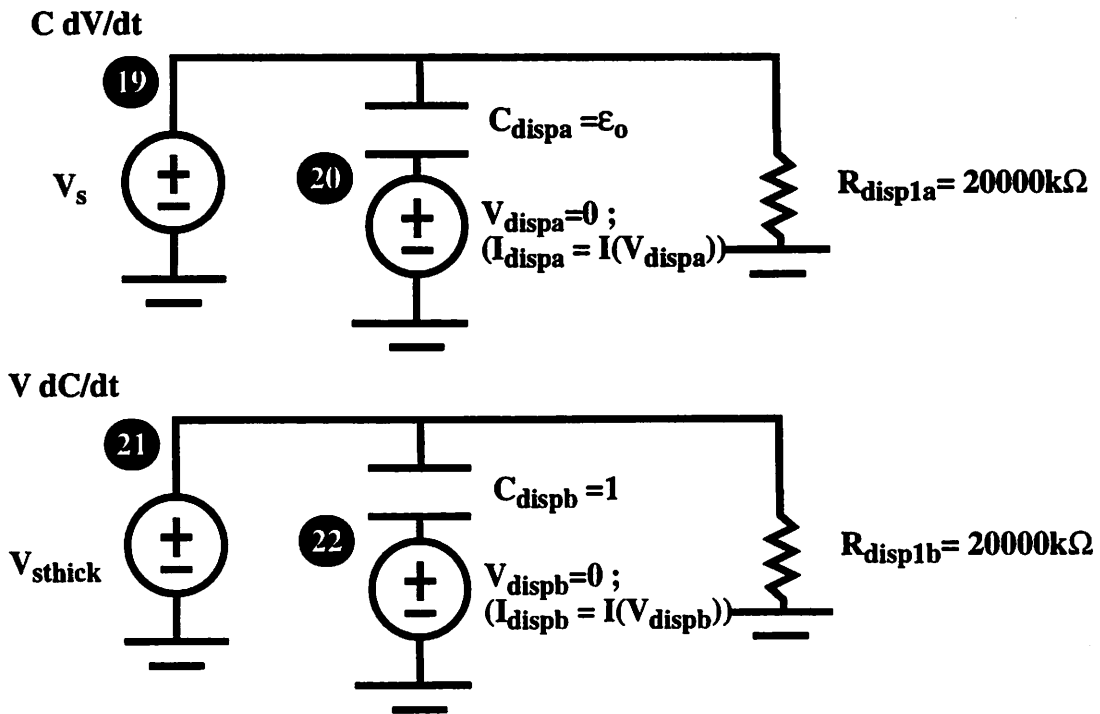


Figure B-3. Circuits solving for the displacement current
 Separate circuits necessary to determine each component of the displacement current

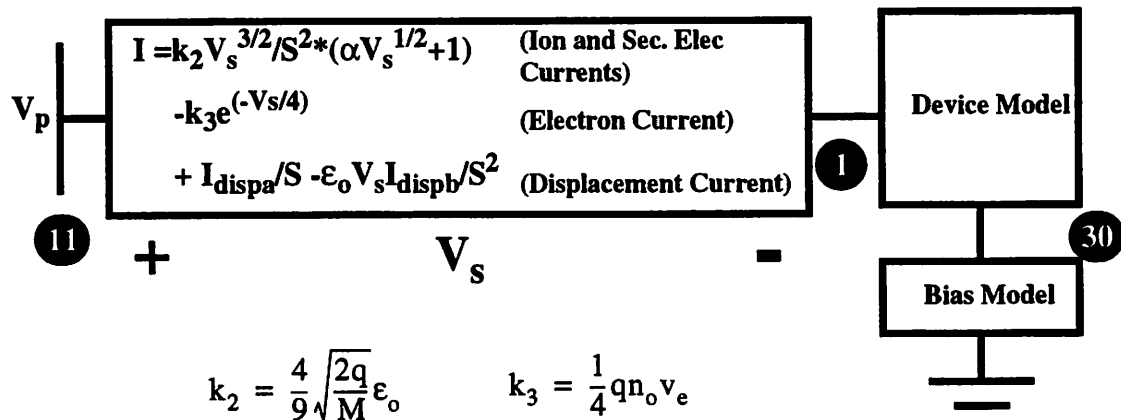


Figure B-4. Total current output of model
 A coupled equation representing the total current output and its connections to the device and bias models

B.3 SPICE Input Deck:

```
A working plasma simulation for short pulse widths (MKS)
* Ar plasma lmt 900W
* K = q*no ; no = plasma density (m^-3)
* A = (4/9)*eo *(2q/M)^0.5 eo = permitivity = 8.854e-12 M =
ion mass
* U = q*no*Ub
* Ub = (q*Te/M)^0.5 = 3095, Ub=Ub*1.1=3404
* Ue = (8q*Te/PI*m)^0.5 = 1.337e6
* Mp = 1.673e-27 kg Me = 9.11e-31 kg
* Te = 4V Vfloating = -0.5V

* Argon M = 40*(1.67e-27)kg at no = 3.76e16 m^-3
* A = 8.612e-9 K = 7.209e-3 U = 22.3

* Bias Model

Vbias 30 0 0 pwl (0 0
+ 2e-5 0)

* Wafer Model (Tox = 150A)
* Assume ESC 1mm of SiO2
* Ring 1

Rox1 30 1 1000k
Cox1 30 1 3.45e-3

* Plasma Models (Area = 88cm^2 = 1/2 wafer)

* Model #1
Vplasma1 11 0 18.23

*Iequil1 12 0 0 pwl (0 0 0 1e-10 -1e4 2e-10 -1e4 5e-10 0 6e-10)
* Main current I = A*(Vsh)^1.5/S^2 *(secele+1) +
0.25*e*ni*Ue*e(-Vsh/Te) + CdV/dt + VdC/dt
Bout1 11 1 i = 8.612e-9*((abs(v(11,1)))^1.5)/
+ (v(13)^2)*(abs(0.0696*sqrt(v(11,1))))+1)
+ - 2.415e3*exp(-abs(v(1,11))/4)+i(vdispla)/v(13)
+ -8.854e-12*abs(v(11,1))*i(vdisplb)/(v(13))^2

BV32 14 0 v = (abs(v(11,1)))^1.5
Vsthick3 14 15 0
* L1 = K/3A = 2.79e5
```

```

L1 15 16 2.79e5

* Bbohm is used to collapse sheath
* k1 = e*no*Ub/A = 2.589e9 (for Vs)
Bbohm1 16 0 v = 2.589e9*(i(vsthick3)^2)/(i(vsthick3)^1.33333)

Bsheath1 13 18 v = (i(vsthick3) + 2e-14)^0.33333
Vso1 18 0 0.0001m
Rstability 13 0 100k

* Displacement Current
* C dV/dt
Edispla 19 0 11 1 1
Vdispla 0 20 0
Cdispla 19 20 8.854e-12
Rdispla 19 0 20000k
* V dC/dt
Edisplb 51 0 13 0 1
Vdisplb 0 52 0
Cdisplb 51 52 1
Rdisplb 51 0 20000k

* Measured current comparison

Vtest 99 0 0 pw1 (0 0
+ 2e-5 0)

Rtest 99 0 1

*.options reltol = 1e-10 itl4 = 1000
.tran 0.01u 10u 0.01u 0.01u UIC
.end

```

Appendix C: Multiple Ion Species Plasma Model

List of Variables:

n_k	Ion density of species k
q	unit electron charge
n_o	Total ion density of plasma
M_k	Ion mass of species k
$u_k(x)$	ion velocity of species k at position x.
v_k	Sheath edge velocity of species k
j_k	Ion current of species k
α_k	Fraction of total ion density for species k ($n_k = \alpha_k n_o$)
f	Voltage in sheath
ϵ_o	Permittivity of free-space
V_s	Voltage drop across the sheath
s	Sheath thickness
T_{on}	Pulse on time
M_{eff}	Effective ion mass
v_{seff}	Effective ion velocity at sheath edge

C.1 Introduction

The addition of multiple ion species in the plasma during PIII requires that the analytical relations describing the plasma currents be changed. Also, additional assumptions about the plasma must be made to generate the modified equations. From the modified plasma relations, a model of the plasma currents from a plasma containing multiple ion species can be obtained.

For the ion current two possible scenarios result from two different assumptions about the plasma. One scenario assumes that in the plasma all of the ion species move together and that the relative ion concentrations remain the same for all time throughout all space. The other scenario assumes that each ion species is semi-independent from each other and has an independent plasma front. Each scenario's assumption has both merits and flaws which will be discussed.

C.2 Multiple Ion Species Derivation

Before differentiating the two different scenarios, a common multiple ion species plasma derivation can be done. Since the pulsing bias does not affect the bulk of the plasma the bulk densities of each species are assumed to remain constant. For each ion species the bulk plasma density is defined as:

$$n_k = \alpha_k n_o \quad [C-1]$$

where n_k , α_k , and n_o are the ion density of species k , a fraction of n_o , and the total ion density. And assuming that the initial ion energy is low compared to the potential across the sheath, the conservation equations for the multiple ion species are:

$$\frac{1}{2} M_k u_k^2(x) = -q\phi(x) \quad [C-2]$$

$$qn_k(x) u_k(x) = j_k \quad [C-3]$$

Solving for $n_k(x)$ by using Equation C-1, C-2, and C-3, we obtain:

$$n_k(x) = \frac{j_k}{q} \left(-\frac{2q\phi}{M_k} \right)^{-1/2} \quad [C-4]$$

Using Equation C-4, the total ion density $n_o(x)$ is:

$$n_o(x) = \frac{(-2q\phi)^{-1/2}}{q} \sum_{k=1}^m j_k M_k^{1/2} \quad [C-5]$$

Using this in Poisson's equation results in:

$$\frac{d^2\phi}{dx^2} = -\frac{(-2q\phi)^{-1/2}}{\epsilon_o} \sum_{k=1}^m j_k M_k^{1/2} \quad [C-6]$$

Multiplying Equation C-6 by $d\phi/dx$ and integrating from 0 to x results in:

$$\frac{1}{2} \left(\frac{d\phi}{dx} \right)^2 = 2 \frac{(2q)^{-1/2} (-\phi)^{1/2}}{\epsilon_0} \sum_{k=1}^m j_k M_k^{1/2} \quad [C-7]$$

using $d\phi/dx = -E = 0$ at the plasma-sheath edge $\phi = 0$ ($x=0$). Taking the negative square root, since $d\phi/dx$ is negative, and integrating Equation C-7, results in:

$$-\frac{4}{3} (\phi)^{3/4} = 2 \frac{(2q)^{-1/4} (-\phi)^{1/2}}{\sqrt{\epsilon_0}} \sum_{k=1}^m \sqrt{j_k} M_k^{1/4} x \quad [C-8]$$

This is as far as the derivation can go without making additional assumptions about the plasma. By making one of two additional assumptions the system can be solved.

C.2.1 Single plasma front model

The first scenario is one where all of the ions are assumed to move with effectively the same sheath edge velocity. Thus, all of the ion species in the plasma will react the same way and at the same time. For multiple ion species plasmas with ions very close in mass, this assumption is valid. Using this assumption a single plasma front can be used to describe the ions.

So using Equation C-8 and setting $\phi = -V_s$ at $x = s$, where s is the sheath thickness and solving for J_k results in:

$$\sum_{k=1}^m j_k M_k^{1/2} = \frac{4}{9} \epsilon_0 \sqrt{2q} \frac{V_s^{3/2}}{s^2} \quad [C-9]$$

Using this equation alone is not sufficient to solve for the sheath thickness. The ion current can also be described as the flux of ions crossing the sheath edge:

$$j_k = q n_k \left(v_k + \frac{ds}{dt} \right) \quad [C-10]$$

Inserting Equation C-10 into Equation C-9 and rearranging for the sheath thickness results in:

$$\frac{1}{3} \sum_{k=1}^m q n_k M_k^{1/2} \frac{ds^3}{dt} + s^2 \sum_{k=1}^m q n_k M_k^{1/2} v_k = \frac{4}{9} \epsilon_0 \sqrt{2q} V_s^{3/2} \quad [C-11]$$

With s as the only unknown in Equation C-11, the sheath thickness can be solved. Using the sheath thickness and Equation C-10, the ion flux of each component and the total ion current can be determined.

By comparing Equation C-11 with the single ion species sheath motion relation, an effective mass and effective ion sheath edge velocity can be extracted. The form of Equation C-11 is the same as the single species equation, except for the constants. Comparing the constants and removing the parts that are the same results in:

$$\sum_{k=1}^m n_k M_k^{1/2} = n_o \sqrt{M_{\text{eff}}} \quad [\text{C-12}]$$

$$\sum_{k=1}^m n_k M_k^{1/2} v_k = n_o v_{\text{seff}} \sqrt{M_{\text{eff}}} \quad [\text{C-13}]$$

Using $n_k = \alpha_k n_o$ results in the effective ion mass (M_{eff}) and ion sheath velocity (v_{seff}):

$$\sqrt{M_{\text{eff}}} = \sum_{k=1}^m \alpha_k M_k^{1/2} \quad [\text{C-14}]$$

$$v_{\text{seff}} = \frac{\sum_{k=1}^m \alpha_k M_k^{1/2} v_k}{\sum_{k=1}^m \alpha_k M_k^{1/2}} \quad [\text{C-15}]$$

Thus using the effective ion mass and effective sheath edge velocity, the single ion species model can be used for multiple ion species.

C.2.2 Multiple plasma front model

The assumption that all of the plasma ions are moving together is not valid in general. When the sheath is expanding into the bulk of the plasma any ion that is swept into the sheath will accelerate into the target. So, during this time regime, the assumption that all of the ions are responding together works. However, when the voltage is turned off, the plasma flows back into the region swept out. Each ion species will flow into the space at a different velocity resulting in a different ion density distribution than the bulk of the plasma until the slowest ions reach the target, which is illustrated in Figure C-1.

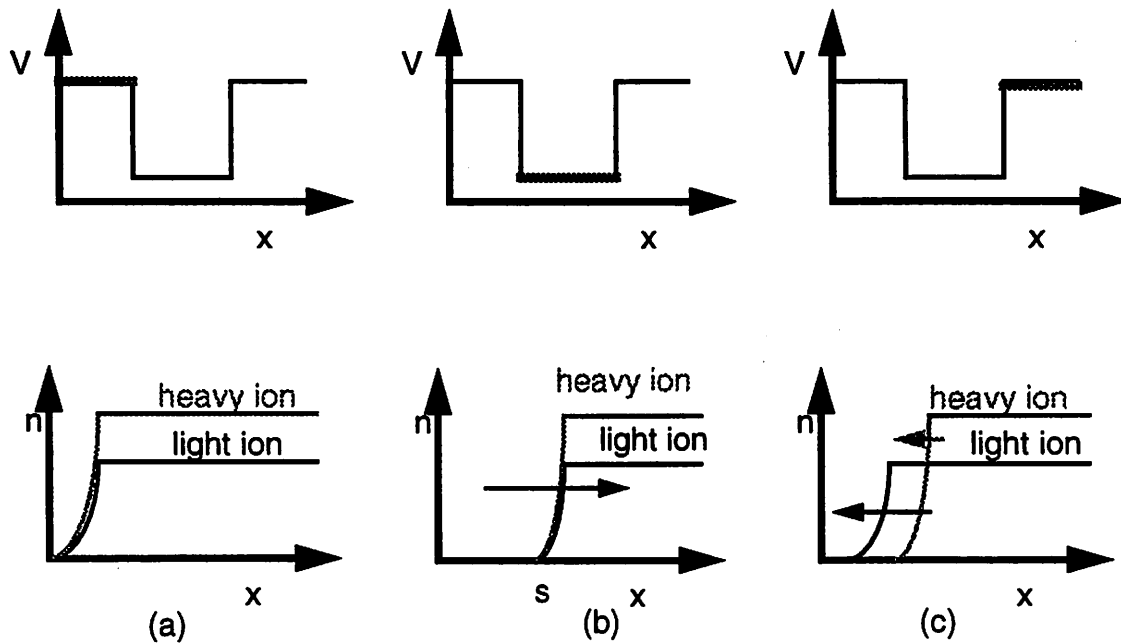


Figure C-1. Dual ion species PIII: ion density variation during an implant pulse

The time variation of the ion density of a two species plasma during an implantation pulse. The dynamics are the same for an arbitrary number of ion species. The voltage applied is shown above the ion density profile. Three regions of operation are shown: (a) initial equilibrium, (b) applied bias is on and sheath is expanding, and (c) bias is turned off and the plasma front of the light ion is moving faster than the plasma front of the heavy ion.

Equation C-10 describes the ion current as a function of the plasma front which is assumed to be at the sheath edge. If the plasma front for a particular ion species lags behind then it can still be described by Equation C-10, but the sheath thickness is replaced by the plasma front of the ion species (s_k):

$$j_k = qn_k \left(v_k + \frac{ds_k}{dt} \right) \quad [C-16]$$

To solve for each of the plasma fronts requires some knowledge of the motion of the system due to a bias. When the sheath is expanding, then any ions crossing the sheath are accelerated and implanted and the plasma fronts are carried along with the sheath. When the sheath collapses, then the sheath collapses at a given velocity, but the plasma

fronts collapse at different rates set by each species' directed velocity (v_k). This formalism can be expressed as a set of conditions:

if $s_k = s$ and $ds/dt > 0$	then	$ds_k/dt = ds/dt$
if $s_k > s$	then	$ds_k/dt = -v_k$
if $s_k = s$ and $-v_k < ds/dt < 0$	then	$ds_k/dt = ds/dt$
if $ds/dt < -v_k$	then	$ds_k/dt = -v_k$

Using this set of conditions the plasma front of each of the ion species can be found and thus the ion currents of each species is known.

C.3 Discussion

The two scenarios for the modeling of multiple ion species have both merits and faults. The first result, which uses a single plasma front and sheath, is accurate for the expanding sheath and for simple rectangular voltage pulses at pulse repetition rates low enough to allow the plasma to flood completely back to the equilibrium sheath thickness, which for a typical plasma takes about $10\mu s$. Thus for the standard pulsing conditions and ideal pulse shapes, the first scenario should be sufficient. However, if the pulse waveform has multiple peaks or the pulse repetition rate is very high, then the second more complex methodology is needed. Basically, for these conditions, the pulsing is such that the sheath expands outward before the plasma has enough time to fully equilibrate and bring all of the ion species back to the wafer. In this case then, the slower heavier ions will remain in the plasma while the lighter ions will move ahead and be swept by the sheath and implanted, resulting in a preferential implantation of the lighter ions. So, a simpler set of relations can be used for a simple bias and implant conditions, but a more complex set of relations is required to fully explain the multiple ion species plasma currents for a more general bias waveform.

Appendix D: Derivation of Equilibration Time After Implant Pulse

List of Variables:

j_{net}	Net current flowing from the plasma to the oxide surface
j_i	Ion current flowing from the plasma to the oxide surface
j_e	Electron current flowing from the plasma to the oxide surface
q	Unit charge
n_o	Ion density of the plasma
v_s	Sheath edge ion velocity
v_e	Average electron velocity ($v_e = (8qT_e/\pi m_e)^{1/2}$)
V_p	Plasma potential
V_{ox}	Voltage drop across the oxide
ΔV_{ox}	Change in oxide voltage drop due to deposition of net charge ΔQ_{ox}
T_e	Electron temperature in units of Volts
Q_{ox}	Net charge on oxide surface
ΔQ_{ox}	Change in oxide surface charge
C_{ox}	Capacitance of the thin gate oxide
δ	Dimension-less number less than unity representing a characteristic fraction of the electron temperature, T_e
t_{equil}	Equilibration time of the gate oxide after deposition of net charge ΔQ_{ox}

D.1 Equilibration Time

Determination of the equilibration time for the floating surface of a thin gate oxide begins with the plasma equilibrium. In equilibrium, no net current flows to the floating electrode. Also, the only current components present are the plasma electron and ion cur-

rents because secondary electrons are not generated without the accelerating bias. Thus the net current to the surface is:

$$j_{\text{net}} = j_i + j_e = qn_o v_s - \frac{1}{4} qn_o v_e e^{-(V_p - V_{\text{ox}})/T_e} = 0 \quad [\text{D-1}]$$

This equilibrium is disturbed when a small quantity of charge is deposited on the surface, due to the implantation voltage pulse. When a small amount of charge, ΔQ_{ox} , perturbs the equilibrated electrode, the voltage on the surface changes by ΔV_{ox} , using $\Delta Q_{\text{ox}} = C_{\text{ox}} \Delta V_{\text{ox}}$ where C_{ox} is the capacitance of the thin gate oxide. This change in surface potential causes a change in the plasma electron current:

$$j_{\text{net}} = qn_o v_s - \frac{1}{4} qn_o v_e e^{-(V_p - (V_{\text{ox}} + \Delta V_{\text{ox}}))/T_e} \neq 0 \quad [\text{D-2}]$$

In this case, a net current from the plasma neutralizes the non-equilibrium charge. Rearranging Equation D-1 and substituting it into Equation D-2, the expression for the net current generated by the non-equilibrium charge simplifies to:

$$j_{\text{net}} = qn_o v_s (1 - e^{\Delta V_{\text{ox}}/T_e}) \quad [\text{D-3}]$$

Since the net current equals the derivative of the surface charge with respect to time, the equilibration time for the gate electrode (t_{equil}) can be found.

$$j_{\text{net}} = dQ_{\text{ox}}/dt = C_{\text{ox}} dV_{\text{ox}}/dt = C_{\text{ox}} d\Delta V_{\text{ox}}/dt \quad [\text{D-4}]$$

$$t_{\text{equil}} = \int \frac{C_{\text{ox}}}{qn_o v_s (1 - e^{\Delta V_{\text{ox}}/T_e})} d\Delta V_{\text{ox}} \quad [\text{D-5}]$$

If the limits of integration are from ΔV_{ox} to zero the integral becomes infinite. To get a good estimate of the time to equilibrate a fraction of the electron temperature, δT_e , replaces the lower limit of zero, where $|\delta|$ is much less than one. δ was chosen because it represents a minimal variation away from the equilibrium. Solving for the integral, the relation for the equilibration time is determined:

$$t_{\text{equil}} = \frac{C_{\text{ox}}}{qn_o v_s} \left(\delta T_e - \Delta V_{\text{ox}} + T_e \ln \left(\frac{1 - e^{\Delta V_{\text{ox}}/T_e}}{1 - e^{\delta}} \right) \right) \quad [\text{D-6}]$$

This relation can be simplified further by considering two cases. In first case the charge deposited on the wafer surface is negative. So ΔV_{ox} and δ are negative. Using the

Taylor series expression for the exponential and taking the first terms, Equation D-6 simplifies to:

$$t_{\text{equil}} = \frac{C_{\text{ox}} T_e}{q n_o v_s} \left(\frac{|\Delta V_{\text{ox}}|}{T_e} + \ln \left(\frac{1}{|\delta|} \right) \right) \quad [\text{D-7}]$$

In this expression, the first term relates the equilibration time to the change in surface potential, and the second term is a constant with respect to the surface charge. The reason t_{equil} is dependent on the surface potential is because a negative surface charge repels the electrons and attracts a constant ion current. Thus with a constant discharge current, the equilibration time is proportional to ΔV_{ox} .

In the second case, when a positive charge is deposited on the surface (positive ΔV_{ox} and positive δ), a different result occurs:

$$t_{\text{equil}} = \frac{C_{\text{ox}} T_e}{q n_o v_s} \ln \left(\frac{1}{\delta} \right) \quad [\text{D-8}]$$

For this positive potential variation, the time to equilibrate does not vary with the deposited positive charge. The exponential dependence of the electron current on the surface potential causes the current induced to increase with the increase in ΔV_{ox} , negating any dependence on deposited charge to first order. In addition, the arbitrary constant α does not affect the equilibration time very much because of the natural log term.

Appendix E: Derivation of Oxide Voltage Dependence on PIII Bias

List of Variables:

$\langle j_i \rangle$	Steady-state time-averaged ion current
$\langle j_e \rangle$	Steady-state time-averaged electron current
$\langle j_{se} \rangle$	Steady-state time-averaged secondary electron current
$\langle V_{ox} \rangle$	Steady-state time-averaged oxide voltage
f	Pulsing repetition rate
q	Unit charge
n_0	Ion density
v_s	Sheath edge ion velocity
v_e	Average electron velocity ($v_e = (8qT_e/\pi m_e)^{1/2}$)
T_e	Electron Temperature in units of Volts
V_f	Floating Potential
T_{on}	Pulse on time
β	Effective secondary electron yield ($\beta \equiv Q_{se}/Q_i$)
Q_i	Ion charge implanted per pulse
Q_{se}	Secondary electron charge generated per pulse

E.1 Oxide Voltage Derivation

The average oxide voltage ($\langle V_{ox} \rangle$) in steady-state derives from the time averaged currents. Three current components determine the new equilibrium, which are the plasma ion current, plasma electron current, and secondary electron current. The time-averaged sum of these three currents in steady-state is zero.

$$\langle j_i \rangle + \langle j_e(V_{ox}, f, T_{on}) \rangle + \langle j_{se}(f, T_{on}) \rangle = 0 \quad [E-1]$$

The time-averaged ion current does not change due to the implantation pulsing. Since, the implantation pulsing does not perturb the bulk plasma, the flux of charge from the bulk of the plasma to the surface remains unchanged. Therefore by charge conservation, the time averaged ion current remains constant for any implantation pulsing.

$$\langle j_i \rangle = qn_o v_s \quad [E-2]$$

On the other hand, the time averaged plasma electron current changes with the implantation pulsing. Two effects change the plasma electron current. First, the plasma electron current falls to zero during the implantation pulse, allowing electrons only during the off cycle. Second, surface voltage variations affect the plasma electron current by modulating the barrier height to electrons. So the time average plasma electron current comes out of the time integral of the electron current over one period divided by the period:

$$\langle j_e \rangle = -f \int \frac{1}{4} qn_o v_e e^{-(V_p - V_{ox}(t))/T_e} dt \quad [E-3]$$

where f is the repetition rate of the pulses.

To understand the implications of this result, Equation E-3 can be greatly simplified. Since the surface voltage does not vary much due to a single implantation pulse, the plasma electron current reduces to a function of the time-averaged surface potential rather than the instantaneous surface potential. In addition, the plasma electron current remains off during the pulse, simplifying the relation further. Using these two approximations, a simplified relation for the time averaged plasma electron current results:

$$\langle j_e \rangle = (1/f - T_{on}) f \frac{1}{4} qn_o v_e e^{-(V_p - \langle V_{ox} \rangle)/T_e} \quad [E-4]$$

The implantation pulsing adds an additional current component: the secondary electron current. The implantation of the ions generates a large number of secondary electrons which accelerate away from the surface. These secondaries leave behind positive charges on the floating surface. The time averaged secondary electron current can then be found from the total number of secondaries generated per pulse averaged over one period:

$$\langle j_{se} \rangle = Q_{se} f = \beta Q_i f \quad [E-5]$$

where Q_{se} , Q_i , β and f are the total secondary electron charge produced per pulse, the total implanted charge, the effective secondary electron yield and the frequency of the pulses respectively.

Substituting Equation E-2, E-3, E-4, and E-5 into Equation E-1 and solving for the time averaged oxide voltage yields an expression that shows the dependence of the oxide voltage on the pulsing and plasma conditions.

$$\langle V_{ox} \rangle = V_f + T_e \ln \left(\frac{1}{1 - fT_{on}} \right) + T_e \ln \left(1 + \frac{\beta Q_i f}{qn_o v_s} \right) \quad [E-6]$$